Final Report: Design Synthesis Exercise Group 10

Mid-flight Aircraft Recharging System

AE3200: Design Synthesis Exercise
2023 D.S.E. Group 10

TU Delft

Final Report: Design Synthesis Exercise Group 10

Mid-flight Aircraft Recharging System

by

2023 D.S.E. Group 10

Student Name	Student Number
Bram Boer	5313457
Charles Cahigas	5283752
Jaap Beckers	4828763
Jacob Elskamp	5053390
Lars Oerlemans	4880110
Paul Dumont	5271053
Patrick Schoots	5309875
Samuel Demian	5250935
Sean Blackmore	5257603
Shawn Tan Zing	5229286

Project Tutor:	Dr. ir. Julien van Campen
Project Coaches:	Ir. Haris Shahzad & Ir. Shyam VimalKumar
Project Duration:	April, 2023 - June, 2023
Faculty:	Faculty of Aerospace Engineering, Delft

TU Delft

Executive Overview

Project Proposal and Objectives

The eCarus project aims at designing and proposing a plan to create an autonomous system capable of recharging all-electric aircraft mid-flight. The mission need statement is given as "*Create an autonomous, in-flight recharging system for carbon-free civil aviation that declutters the airport logistics regarding electrification and hydrogen refuelling, and that can extend the range of all-electric aircraft*" by the project reader (J. van Campen, [1]). The project objective statement is *"Design an autonomous drone system comprised of the ground station, drone and on-aircraft dock for in-flight recharging of carbon-free aircraft in 10 weeks by a team comprising of 10 students"*. In this report the detailed design of the eCarus system is proposed together with outline of our past design steps.

eCarus Design

The design of the eCarus system is divided into multiple subsystems: Payload, Power and Propulsion, Aerodynamics, Structure which are combined in an integration and a full design iteration chpater.

Payload

The battery consists of three components: an anode, a cathode and an electrolyte. For the anode, lithium is selected whereas Nickel Manganese Cobalt (NMC) is used for the cathode. The electrolyte is made out argyodite sulphides. A coating for the lithium is required to prevent a reaction with the electrolyte. The aircraft has a total of three batteries, one payload battery for recharging and two primary batteries for all subsystems of the aircraft. Each battery consists out of 36 modules arranged in series, where each module has 6 cells in series. The modules for the payload battery have 343 cells arranged in parallel, compared to 96 cells in parallel for the modules of the primary batteries.

The eCarus drone electric system will make use of liquid cooling for its battery thermal management. Solid-state batteries have an optimal ΔT ranging from $273\,\text{k}$-$300\,\text{K}$, which should be ensured by the cooling system. As coolant for the BTMS 50% Ethylene Glycol + 50% water is used.
Cruise contributes the most of all flight phases towards the heat flow generated by the propulsion battery. The payload battery results in a heat flow 6.6 times higher than the propulsion battery. This is due to the fact that the drone recharges the Electrifly aircraft battery while simultaneously delivering power to their engines.

Docking Mechanism

The recharge procedure of the eCarus system makes use of an AAR controller with 8 modes that results in the AAR process, visualised in Figure 1 and Figure 2.

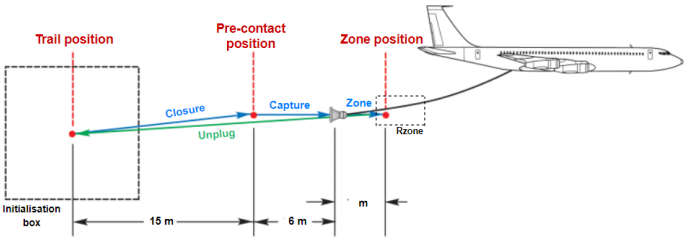

Figure 1: The AAR process [2]

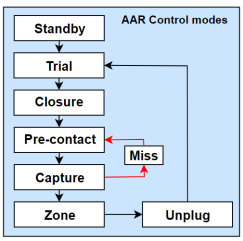

Figure 2: The AAR control modes [2]

When the connection is successful the recharging starts once the drone is within the recharging zone visualised in Figure 3. If the miss mode criteria are met the AAR controller starts the miss mode upon which the drone manoeuvres back to the pre-contact position. The eCarus drone has a total of 5

minutes and 2 attempts to connect with the drogue. If these constrains are exceeded a second drone gets launched from the hub while in the meantime the drone is allowed to perform more attempts. A total cable length of $19\,\mathrm{m}$ and clearance of $15\,\mathrm{m}$ results in a recharging zone of $3\,\mathrm{m}$ with $1\,\mathrm{m}$ for redundancy. The cut-off zone is a redundant zone in which the electric transfer will be cut-off and the drone is commanded to reposition itself within the recharging zone. After recharging the unplug mode is initiated.

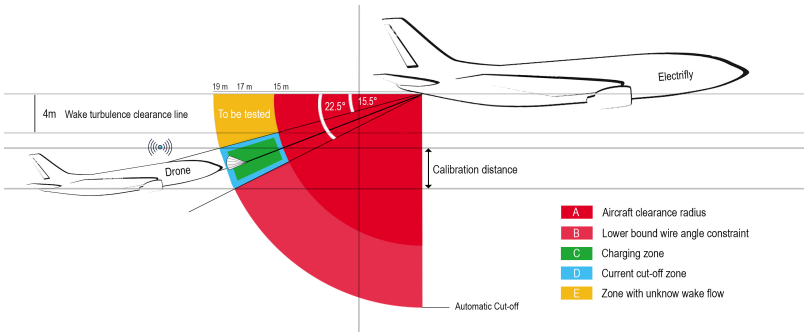

Figure 3: Visualisation of the recharge zone and clearance behind the receiving aircraft[3].

The probe-drogue system consist of a cable drum unit, a drogue, and a probe. The drogue consist of thrusters, a rotate coupling, a ball joint, a coupler and a drogue net equipped with position sensing devices. The general connection makes use of solenoids that connect with the probe upon contact. A general schematic can be seen in Figure 4. The main aerodynamic force directly influencing the connection success is the bow wave effect due to the eCarus drone. Due to this effect a forward position of the probe is chosen for the final design.

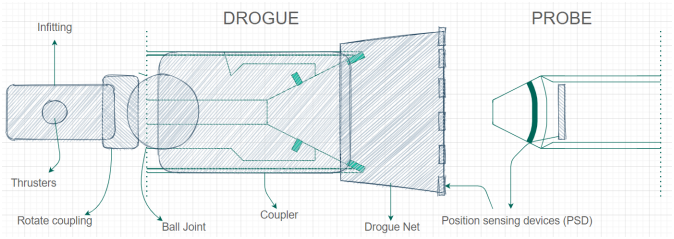

Figure 4: Schematic of drogue-probe system connection with extended view

Power and Propulsion

A trade-off is performed for the thrust generation type and the engine placement as this drives the design of the propulsion system. For the thrust generation type a ducted fan and conventional propeller are considered. These design options are scored against an efficiency, noise, cost and safety criterion. The ducted fan comes out on top of the trade-off. For the engine placement a distinction is made between front and aft placement and the use of distributed propulsion is considered. The options are scored against the same aforementioned criteria. After performing the trade-off, aft non-distributed propulsion is deemed to be the best option for this design.

The MH114 aerofoil is selected for the propeller due to its high $c_l/c_{d_{max}}$ value and a relatively high t/c ratio value. A constant aerofoil distribution is selected to keep cost and complexity at a minimum. For this reason a high t/c ratio is beneficial, because it can carry the high structural load at the propeller root.

For the propeller design, the minimum induced loss procedure is utilised. This procedure specifies the chord and twist distribution along the span of a propeller blade for a prescribed thrust. The propeller design procedure requires some free parameters to be selected. Engine RPM is taken to be 2100, equal to 91.3% of the maximum RPM. The propeller diameter is decided to be 2.20 m, as a result of an analysis on engine power and tip mach number based on 20 reference aircraft. Figure 5 and Figure 6

show the final results of the procedure. A configuration of two propeller blades is chosen as this is able to operate at the highest efficiency of 94.1%.

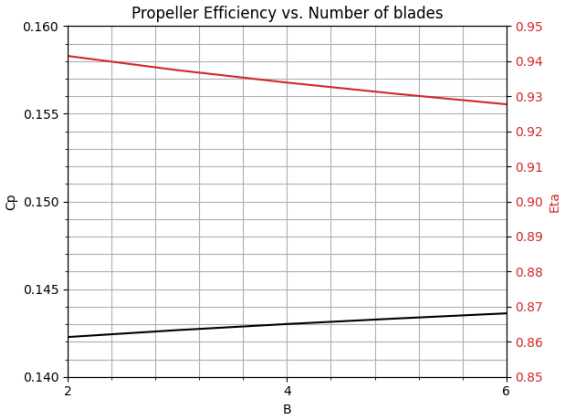

Figure 5: Propeller efficiency versus number of blades

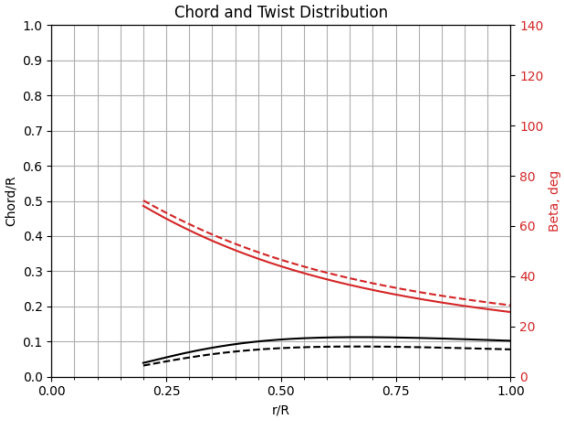

Figure 6: Final chord and twist distribution for a single propeller blade

For the duct, the NACA7312 aerofoil is selected due to its high camber which positively influences duct efficiency. The propeller is located at 30% of the duct chord, which has a length of 1.25 m (equal to half the propeller diameter). Aluminium 6061-T6, the same material for the drone skin, shall be used for the duct because of its similarity in function. A carbon-graphite and Kevlar composite shall be used for the propeller blade because of its light weight, noise reduction and longer service life. The noise generated by the propulsion system is equal to 56.67 dB at cruising altitude.

Aerodynamics

To start off the design of the drone planform and aerodynamics, an initial sizing of the drone is performed. This is done based on the maximum take-off weight and wing loading, resulting in the surface area and span of the drone. Then, a drone volumetric analysis is performed. This is done by making sure that the volume required for the storage of batteries and payload is equal to the available volume in the drone. This analysis provides dimensions for the taper ratio and general shape of the aircraft.

Computational fluid dynamics are used to determine the main force coefficients. The properties of the chosen aerofoil are first analysed on Xfoil. Then, using the aerofoil data, a simulation of the 3d plane is done using the horseshoe vortex lattice method in XFLR5. Only the lift curve and induced drag are used as other outputs from the vortex lattice method are deemed unreliable. The methods described in Roskam are used to determine all stability coefficients for the drone as well as force coefficients which XFLR5 can't predict accurately.

With all aerodynamic coefficients determined, the static and dynamic stability of the drone are determined. For static stability, the sweep angle is modified to satisfy it. For dynamic stability, the linearised equations of motion for an aircraft are used to obtain the eigenmotions of the drone. With the eigenmotions, the stability of the drone can be gauged based onthe MIL-F-94 requirements.
The elevator and rudders are sized to achieve controllability requirements. The rudders are sized as large as possible to provide maximum yaw damping. The elevators are also maximised but split into 2 sections. 1 section is just a regular elevator while the other can be used as a high lift device during take-off to increase $C_{L_{max}}$, as the full elevator surface is not required for controllability during take-off. The controllability of the aircraft at high lift conditions is analysed to make sure that the drone is controllable.

Drone Structure

In the preliminary design phase, a trade-off concludes that a truss structure is preferred over a monocoque or semi-monocoque design. As a starting point of the detailed design a sensitivity analysis is performed for this trade-off, which confirms the design choice for truss structure.

Before the structure is designed, the gust and manoeuvre loads are assessed. For the structural design, a safety factor of 1.3 is used. An extensive trade-off is performed for the material selection of both the skin and the trusses. The chosen materials are aluminium 6061-T6 and aluminium 8089 supported with silicon carbide fibres, respectively.

The skin is assumed to carry only the aerodynamic pressure and is supported by a lattice structure to introduce the loads into the truss structure. Multiple failure modes of the skin are analysed, with the conclusion that yielding in tension is the most critical one. With an initially assumed skin thickness of 1 mm, it is found that the required lattice spacing is 31.9 cm.

The truss structure is designed to support the loads generated by the load factors and safety factors found in the manoeuvre and gust envelope. The trusses are designed to withstand failure in buckling, yield failure, and fatigue. In this truss, a 2D analysis is performed and the trusses are individually sized based on their individual loads. A final configuration of the internal truss structure is shown in Figure 7.

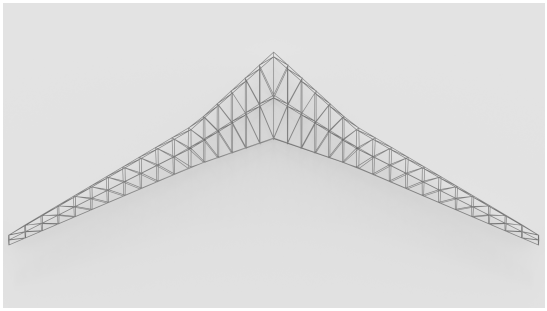

Figure 7: Render of the internal drone structure

System Integration

The method to calculate the centre of gravity of the drone was first presented. The batteries and payload were placed in the drone. The batteries and structures were then integrated over the span to obtain the centre of gravity of the respective components. The total centre of gravity is then calculated by summing up the centre of gravity of the engine, landing gear, tail, structures and batteries.

After finding the centre of gravity, the second moment of inertia about the centre of gravity can be found. All components were assumed to be point masses except for the structure and payload to calculate the second moment of inertia. The batteries and structure were integrated similarly to the method in centre of gravity to obtain the moment of inertia of these components.

With the methods for determining the centre of gravity and moment of inertia established, integration of the entire system can be done. An iteration procedure was implemented in order to place every system correctly, given the constraints by each department. A final configuration of the drone is then obtained show in Figure 8.

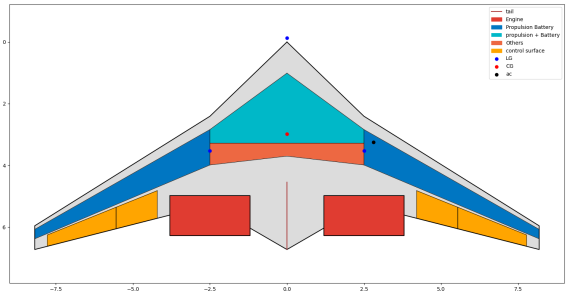

Figure 8: Schematic overview of the entire drone layout. It is to scale in meters.

System Iteration

The iteration procedure is started with a preliminary weight estimation and the wing loading diagram. From this, three key parameters are generated, namely the total weight, required power and surface area of the aircraft. These parameters flow down to the different departments, where a more detailed analysis will be performed. The main results of this analysis are the revised performance coefficients of the aircraft and more accurate subsystem weight estimates. The performance coefficients are used to update the wing loading diagram, where the new weight estimate is used to determine the new required power and surface area through this diagram. This brings the design back to the start of the iteration loop, which can be traversed once more.

Financial Analysis

Including an acceptable profit margin, recharge costs are 3.405 USD. Such a high cost is mainly due to the concept being inherently expensive. A flight from Amsterdam to Madrid takes almost four hours and requires two in-flight recharges which each have their own drone flight time of just over two hours. In the future, efforts could be made to reduce the electricity costs which take up 36.5% of all the direct operation costs. This could be done by securing cheaper PPA contracts. If there is enough capital, investment in purpose-built power generation could also pay off in the long term. The maintenance costs are also a major factor in the high operational costs. Finding ways to streamline the maintenance and simplify the drone could drive down this cost. Over time the drones will be fine-tuned and become more reliable. This could also decrease this cost.

The high price makes the project financially infeasible today without major support. This support could come in the way of subsidies or by way of passengers who are willing to pay a high premium for sustainable air travel. The drive towards sustainability in the aviation industry will surely help.

Operations

For take-off, landing and storage of the drones, regional and local airports are used. Possible airports comply with the following criteria; a concrete or asphalt runway with a length between $1300\,\text{m}$ and $2000\,\text{m}$, and runway altitude below $5000\,\text{ft}$. This leaves around 6600 airports worldwide which is sufficient for initial operations and future-proof regarding the scaling of the system. Airports that are close to the optimal recharge points of popular routes or close to busy international airports are chosen.

In case of a failed docking, a second drone can reach the aircraft within 20 minutes ensuring that the aircraft's flight can continue as planned. This will ensure that the aircraft only experiences an impactful failure once every million recharges.

Sustainability

Throughout the design of the project, a great amount of effort has been put in order to make the design as sustainable as possible. Multiple design choices have been made with as main goal to achieve great sustainability levels. An example of such a choice is the use of a ducted fan in order to achieve high efficiency and low noise levels. Looking at the sustainability requirements it can be seen that the great majority of requirements have been met through those design choices.

Risk Assessment

New risks were defined and risks previously identified were reevaluatedThen, a mitigation plan was developed to reduce the probability or impact of each risk identified together with a pre- and post mitigation risk map was made to analyse the effects these mitigations had. Important risks to note in this report are R-OPE-10-01 and R-OPE-09. R-OPE-10-01 is the risk of the catapult being too expensive to develop. This risk was deemed too critical and thus resulted in the catapult to be changed to a conventional take-off, which removed the risk and caused it to be 0. R-OPE-09 is the risk of the drone being a hazard to the environment. This was a critical risk in the previous report even after mitigation. Extra mitigations were implemented to further decrease the probability of this risk.

Contents

List of Symbols

Abbreviations

Abbreviation	Definition
AAR	Autonomous Airborne Recharging
ACI	Airports Counsil International
AMC	Aluminium Matrix Composite
ATC	Air Traffic Control
BTM	Battery Thermal Management
BTMS	Battery Thermal Management Systems
BWB	Blended Wing Body
CDU	Cable Drum Unit
CFD	Computational Fluid Dynamics
CFRP	Carbon-fibre-reinforced Polymers
DoD	Depth of Discharge
ECU	Electric Control Unit
ETOPS	Extended-range Twin-engine Operational Performance Standards
HDU	Hose Drum Unit
IMU	Internal Measurement Unit
MAC	Mean Aerodynamic Chord
MLG	Main Landing Gear
MMC	Metal Matrix Composites
MRO	Maintenance, Repair and Operations
MTOW	Maximum Take-Off Weight
MV	Machine Vision
NATO	North Atlantic Treaty Organisation
NLG	Nose Landing Gear
PPA	Power Purchase Agreement
PCM	Phase Change Material
PNL	Perceived Noise Level
PSD	Position Sensing Devices
RPM	Revolutions Per Minute
SiC	Silicon Carbide
SPL	Sound Pressure Level
STANAG	Standardisation Agreement
TAW	Tube-and-wing
TiMMC	Titanium metal matrix composite
TOP	Take-off parameter
UAV	Unmanned Aerial Vehicle
US	United States

Key Definitions

Name	Definition
Aircraft Safe-Range	Range the aircraft can safely and constantly fly between recharges
Drone Safe-Range	Range the aircraft can safely and constantly fly between recharges

Name	Definition
Maximum Approach Separation	Maximum radial distance a receiving aircraft can fly away from a hub
Mean Recharge Point	The point near which the aircraft will need a recharge

Symbols

Symbol	Definition	Unit
A	Scaling parameter for drag coefficient and Reynolds number relation of aerofoil	[-]
B	Number of blades per propeller	[-]
C_L	Lift coefficient	[-]
C_D	Drag coefficient	[-]
C_{D_0}	Zero-lift drag coefficient	[-]
$C_{L_{max}}$	Maximum lift coefficient	[-]
$C_{L_{T/O}}$	Take-off lift coefficient	[-]
C_{L_α}	Lift gradient	[1/rad]
C_P	Propeller power coefficient	[-]
C_p	Pressure coefficient	[-]
C_T	Propeller thrust coefficient	[-]
D	Propeller diameter	[m]
D_{duct}	Propeller duct diameter	[m]
D_{hubs}	Maximum distance between hubs	[km]
E_{climb}	Energy used in climb	[Wh]
E_{cruise}	Energy used in cruise	[Wh]
E_{loiter}	Energy used in loiter	[Wh]
E_{total}	Total energy used	[Wh]
F	Propeller tip loss factor	[-]
I_{cell}	Cell current	[A]
J	Propeller advance Ratio	[-]
K_{IC}	Fracture toughness	MPa$\sqrt{\text{m}}$
K_I	Stress intensity factor	MPa$\sqrt{\text{m}}$
L_A	A-weighted sound level	[dB]
L_A	Perceived noise level	[dB]
M_{tip}	Propeller tip mach number	[-]
N	Number of propellers	[-]
P	Power	[W]
P_r	Power required	[W]
$P_{r_{climb}}$	Power required for climb	[W]
$P_{r_{cruise}}$	Power required for cruise	[W]
$P_{r_{loiter}}$	Power required for loiter	[W]
Q	Total torque generated by propeller	[Nm]
Q_{Bat}	Heat flow battery	[W]
$Q_{payload}$	Heat flow generated by the payload battery	[W]
Q_{cruise}	Heat flow during cruise	[W]
R_{design}	Design range of the receiving aircraft	[km]
$R_{errormargin}$	Range needed for a docking time error margin	[km]
R_{int}	Battery internal resistance	[Ω]
$R_{no-headwind}$	Range with no-headwind or tailwind	[km]
$\Delta R_{headwind}$	Decrease in range due to headwind	[km]
R_{DoD}	Range equivalent to the depth of discharge left in the battery of the receiving aircraft	[km]
R_{Drone}	Drone safe-range	[km]

Symbol	Definition	Unit
R_{Safe}	Receiving aircraft safe-range	[km]
S	Surface area	[m^2]
T	Total thrust generated by propeller	[N]
$V_{headwind}$	Velocity of the headwind	[m/s]
V_c =V_{cruise} =$V_{c_{no-headwind}}$	Cruise velocity of the receiving aircraft	[m/s]
$V_{c_{headwind}}$	Cruise velocity of the receiving aircraft when in headwind	[m/s]
$V_{s_{land}}$	Stall speed	[m/s]
V_{tip}	Propeller tip speed	[m/s]
$V_{T/O}$	Take-off speed	[m/s]
V_∞	Free stream velocity	[m/s]
W_{BTMSpl}	Battery thermal management weight for payload battery	[kg]
W_{BTMSpp}	Battery thermal management weight for propulsion battery	[kg]
$W_{B_{total}}$	total battery weight on drone	[kg]
W_{bat}	Battery weight for propulsion system	[kg]
W_{batpl}	Payload battery weight	[kg]
W_{batpp}	Propulsion battery weight	[kg]
W_e	empty weight drone	[kg]
W_m	motor weight	[kg]
W_{pl}	Payload battery weight	[kg]
$W_{B_{aux}}$	Battery weight for auxiliary power system	[kg]
W_{TO}	Take-off weight	[kg]
b	span	[m]
b_b	Transition point between body and wing section	[m]
A	Aspect ratio	[-]
λ	taper ratio	[-]
Λ	Quarter chord sweep	[$^\circ$]
S	Surface area	[m^2]
c	chord	[m]
x_{cg}	x-position of centre of gravity	[m]
C_m	moment coefficient in the y-direction	[-]
$C_{m_{ac}}$	0 lift moment coefficient in the y-direction	[-]
C_l	Moment coefficient in the x direction	[-]
C_n	Moment coefficient in the z direction	[-]
C_{X_u}	Speed derivative of the force coefficient in x-direction	[s/m]
C_{Z_u}	Speed derivative of the force coefficient in z-direction	[s/m]
C_{m_u}	Speed derivative of the moment coefficient in y-direction	[s/m]
C_{X_q}	Pitch rate derivative of the force coefficient in x-direction	[s/rad]
C_{Z_q}	Pitch rate derivative of the force coefficient in z-direction	[s/rad]
C_{m_q}	Pitch rate derivative of the moment coefficient in y-direction	[s/rad]
C_{X_α}	Angle of attack derivative of the force coefficient in x-direction	[1/rad]
C_{Z_α}	Angle of attack derivative of the force coefficient in z-direction	[1/rad]
C_{m_α}	Angle of attack derivative of the moment coefficient in y-direction	[1/rad]
C_{Y_β}	Sideslip derivative of the force coefficient in y-direction	[1/rad]
C_{l_β}	Sideslip derivative of the moment coefficient in x-direction	[1/rad]
C_{n_β}	Sideslip derivative of the moment coefficient in z-direction	[1/rad]
C_{Y_p}	Roll-rate derivative of the force coefficient in Y-direction	[s/rad]
C_{l_p}	Roll-rate derivative of the moment coefficient in x-direction	[s/rad]
C_{n_p}	Roll-rate derivative of the moment coefficient in z-direction	[s/rad]
C_{Y_r}	Yaw-rate derivative of the force coefficient in Y-direction	[s/rad]
C_{l_r}	Yaw-rate derivative of the moment coefficient in x-direction	[s/rad]

Symbol	Definition	Unit
C_{n_r}	Yaw-rate derivative of the moment coefficient in z-direction	[s/rad]
a	Half of crack length	[m]
a	Speed of sound	[m/s]
c_d	Aerofoil drag coefficient	[-]
$c_{d_{min}}$	Aerofoil minimum drag coefficient	[-]
c_{duct}	Propeller duct chord length	[m]
c_l	Aerofoil lift coefficient	[-]
c_{prop}	Propeller chord length	[m]
$c_{l_{(c_l/c_d)max}}$	Aerofoil lift coefficient at location of maximum (c_l/c_d) ratio	[-]
$c_{l_{d_{min}}}$	Aerofoil lift coefficient at location of $c_{d_{min}}$	[-]
c_{l_α}	Aerofoil lift gradient	[1/rad]
d	Lattice spacing	[m]
d_{prop}	Distance from propeller	[-]
e	Oswald efficiency factor	[-]
e	Specific energy density	[Wh/kg]
f	Ratio between take-off weight and landing weight	[-]
k_p	Aerofoil parameter for drag due to lift	[-]
n	Propeller rotations per second	[-]
n_{max}	Maximum load factor	[-]
n_{min}	Minimum load factor	[-]
p	Specific power density	[W/kg]
p_c	Cruise static pressure	[Pa]
r	Propeller radius	[m]
r_{max}	Maximum approach separation	[km]
s_{GR}	Ground roll distance	[m]
s_{land}	Landing distance	[m]
$s_{T/O}$	Take-off distance	[m]
t	Thickness	[m]
t_{charge}	Aerial charging time	[min]
u	Perpendicular gust velocity	[m/s]
w_0	Wake displacement velocity	[m/s]
x	Distance from the hub to the beginning of the charge cycle or distance back to the hub	[km]
α_i	Induced angle of attack	[rad]
α_0	Zero-lift angle of attack	[rad]
α_∞	Free stream angle of attack	[rad]
γ	Power parameter for drag coefficient and Reynolds number relation of aerofoil	[-]
η_{prop}	Propulsive efficiency	[-]
μ	Dynamic viscosity	[Ns/m^2]
ρ	Air density	[kg/m^3]
ρ_c	Cruise air density	[kg/m^3]
ρ_{max}	Air density at maximum hub altitude	[kg/m^3]
ρ_o	Air density at sea level	[kg/m^3]
σ	Stress	[MPa]
σ_{yield}	Yield stress	[MPa]
σ_{max}	Maximum stress	[MPa]
$\sigma_{T/O}$	Ratio between maximum hub altitude air density and sea level air density	[-]
ϕ_{tip}	Propeller blade inflow angle	[rad]
ω	Propeller rotational velocity	[rad/s]

1 Introduction

Sustainable transportation is increasingly becoming a topic of interest in the last few decades. The aviation transportation industry in particular is subjected to criticism and obstacles as a result of its reliance on fossil fuels. At the same time, the demand for transportation has increased rapidly and is expected to increase even more despite of the COVID-19 pandemic. It is therefore essential that a more sustainable approach is taken for the aviation industry. One of the major challenges of transitioning to renewable-energy-powered air travel is the restricted range and size of current electric aircraft.

In order to address this challenge, a group of 10 TU Delft students aim to design and create a network of renewable-energy-powered autonomous drones that are able to recharge an aircraft with renewable energy while in flight. This groundbreaking system is called eCarus. The project primarily focuses on conducting a feasibility study as this pioneering concept has never been attempted before. The key objective is to evaluate whether an optimised design solution is both feasible and realistic as a potential resolution to the problem at hand.

This report aims to present the detailed design study of the autonomous recharging drones and the hubs associated with operating these UAV's. The study primarily centres on the design of a system that exhibits adaptability and compatibility to the 8-passenger aircraft design of the ElectriFly aircraft design group. Next to this, the potential scalability to bigger megawatt-class aircraft is considered. This report is a continuation of the Baseline report [4] and the Midterm report [5] in which the preliminary design for this system has been described.

This report starts off with **??** which states the project requirements generated in the Baseline report. This is followed by chapter 2 where the findings of the Midterm report are summarised, including results of design trade-offs.

Then, the detailed design part of the report is initiated by chapter 3 where the drone's UAV system design is described. This is followed by the detailed design of the battery for both recharging and own operations in chapter 4. The design of the docking mechanism is presented in chapter 5. Subsequently, the detailed design of the power and propulsion system is described in chapter 6. Following this, a detailed aerodynamic analysis is performed in chapter 7. Thereafter, the structural design of the drone is presented in chapter 8. Following from these analyses, the system integration of all drone subsystems is described in chapter 9. The iteration procedure and its results are stated in chapter 10, followed by a detailed design of the operations in chapter 11. The detailed design phase is concluded with the detailed design summary in chapter 12, presenting all obtained results.

Having finished the detailed design, the verification and validation of all used methods is presented in chapter 13. Thereafter, chapter 14 describes the financial analysis. The project organisation is presented in chapter 15. This is followed by chapter 16 which describes the risk analysis. A summary of the sustainability approaches addressed in this report is noted in chapter 17. Following this, the scalability aspect of the project is discussed in chapter 18. The report is finalised by summarising the conclusions and recommendations in chapter 19.

2
Conceptual Design Summary

This chapter aims to summarise the findings of the Midterm report. In this report, the preliminary sizing of multiple components of the drone was performed. section 2.1 describes the initial design trade-offs, followed by the operations and logistics in section 2.2. section 2.3 describes initial payload design and thereafter, section 2.4 presents the preliminary aerodynamic analysis. Subsequently, section 2.5 explains the power and propulsion system design performed in the Midterm report. Following this, section 2.6 describes the initial structural design. Finally, section 2.7 presents the preliminary UAV system design.

2.1. Design Trade-off

The first performed step in the preliminary design was to perform a trade-off on three different upper-level mission aspects; The drone layout, the docking mechanism of the recharging operation and the hub take-off and landing design. In the Baseline Report [4], various design concept options for these aspects were generated before trading them off. Preliminary drawings of the final results of the trade-off are shown in Figure 2.1.

2.1.1. Drone Layout

For drone layout three trade-offs were performed: one concerning the configuration of a single drone, one concerning the aerodynamic layout of the drone and one concerning the scale of one drone.

For the first subject 4 different options were considered: A fixed-wing design, a rotor design, a combination of these two options and a lighter-than-air option. The trade-off concludes that the fixed-wing design option is the most optimal due to its high flight efficiency and accompanying low energy usage and safety.

Following the fixed-wing design selection, a trade-off concerning the layout of this design was performed. For this, 6 designs were considered: A standard layout, multiple wings, a closed wing, a morphing wing, a blended wing and a lifting body. The blended wing layout was considered optimal because it does not require a fuselage and because of the ability to carry the payload within the wing.

The final performed trade-off for the drone layout concerns the scale of one single drone. For this 4 options were considered: A drone charging an aircraft once, a drone charging an aircraft twice, two drones charging one aircraft and three or more drones charging one aircraft. The trade-off concludes that a drone charging an aircraft once is ideal due to the simple recharge operation, sustainability considerations and the efficient energy transfer. However, for scalability to Megawatt-class aircraft, multiple recharging drones are preferred due to size constraints.

2.1.2. Docking Mechanism

The trade-off concerning docking mechanism considered 6 options: Wireless induction charging, a tram-style connection, in-flight battery replacement, drone absorption, an ordinary wired connection and a 'skyhook' system. The trade-off concludes that a cable docking mechanism is ideal as a result of its simplicity and the ability to carry a larger distance between a drone and an aircraft. The type of connection (mechanical or magnetic) was not decided upon yet.

2.1.3. Hub Design

The trade-off for the hub design considered two aspects: take-off and landing. The designs considered for take-off were a gyro launch, a (steam-powered) catapult launch, an ordinary take-off and an electromagnetic catapult launch. The optimal take-off option was considered to be an ordinary catapult

launch mainly due to its efficiency and low complexity.

For landing, the options considered were: A net, a parachute, an arresting wire and a conventional landing. The arresting wire was deemed the best option due to size and complexity considerations.

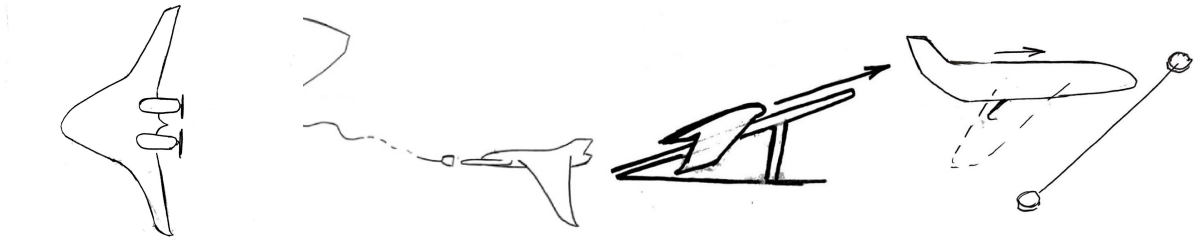

(a) Blended wing layout **(b)** Cable docking mechanism **(c)** Catapult take-off **(d)** Arresting wire landing

Figure 2.1: Preliminary drawings of the design options selected in the trade-off

2.2. Operations and Logistics

For operations, the energy source for the hub was considered. This should provide power to not only the hub, but also the recharging of both the payload and propulsion battery of the drone. For this, energy sources such as solar, nuclear, wind, hydro- and wave power were considered, as well as purchasing green energy through a power purchase agreement. The latter was deemed the optimal solution because this requires the least amount of resources and costs resulting in the most sustainable option.

Furthermore, the hub placement was considered in the preliminary design phase. A program was written which presents the optimal location based on multiple popular flight paths. These flights should span at least 764 km as a result of the 500 km range of the Electrifly aircraft and the recharging distance of 264 km. This program is a useful tool for detailed design to consider exact placement of hubs.

2.3. Payload

Payload design was started by trading off the type of energy source to power the aircraft: A hydrogen fuel cell, an electric battery and a supercapacitor. The electric battery was chosen based on costs and scalablity reasons. The payload battery was then sized based on the required charging energy of 1161.3 kWh for the Electrifly aircraft. Using a battery specific energy of 500 Wh/kg, a payload battery weight of 2903.2 kg was obtained. An initial cable docking design and thermal management design was performed, but shall be further considered in the detailed design.

2.4. Aerodynamics and Flight Performance

The aerodynamic analysis was initialised with a trade-off for the aerofoil to be used in the wing section. The MH91, E186, E230 and MH45 aerofoils are considered of which the MH-91 is considered the best because of its $C_{l_{max}}$ and t/c ratio. Initial wing sizing is performed, resulting in the preliminary parameters as shown in Table 2.1. The wing is decided to be segmented in a body and a wing segment as shown in Figure 2.2. After wing sizing, initial stability and controllability calculations were performed. As shown in Figure 2.2, the drone shall have stabilising surfaces at the wingtips. The preliminary centre of gravity location of the drone was calculated to be at 36.1 % of the total length of the UAV. Further calculations shall be performed in the detailed design

Parameter	Value	Unit
Surface area	81	m^2
Aspect ratio	6	
Sweep angle	38	$^\circ$
Taper Ratio	0.267	
Root chord	5.8	m
MAC	4.08	m

Table 2.1: Calculated drone configuration

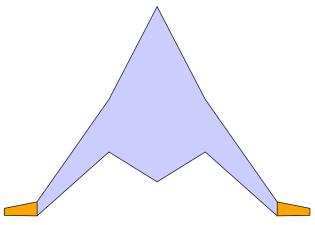

Figure 2.2: The 2-section drone layout along with stabilisers at the wingtips

2.5. Power and Propulsion

The drone utilises electric propulsion powered by an electric battery, due to environmental and social sustainability considerations, as well as because of simplicity. A wing loading and power loading estimate of $2409.01\,\mathrm{N/m^2}$ and $0.050\,\mathrm{N/W}$ were obtained after constructing a wing loading diagram. The required energy per newton of drone weight for one mission was calculated to be $78\,147\,\mathrm{J/N}$. Following this, the Magni650 engine which provides $640\,\mathrm{kW}$ of power was selected. After combining the energy usage of the drone with a battery specific energy of $500\,\mathrm{Wh/kg}$ and the mass estimate of payload and drone structure, a drone weight estimate of $19\,902\,\mathrm{kg}$ was obtained, distributed as shown in Figure 2.3. This means that the drone uses a total energy of $869.82\,\mathrm{kWh}$ per flight. Detailed design will focus on the design of the propulsion system, particularly on the propeller design as well as the integration of this system.

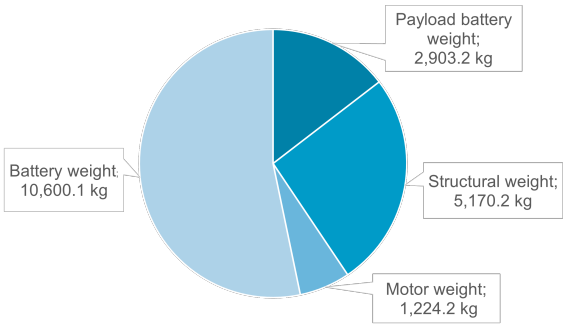

Figure 2.3: Pie chart showing drone component weights

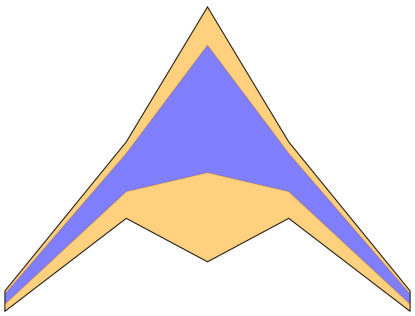

Figure 2.4: Preliminary spar locations in the drone wing

2.6. Structural Design

For the preliminary structural design, a load analysis for one drone mission was constructed, focused on internal forces and moments in the wing. Spars are assumed to be located at 15% and 55% of the chord, as shown in Figure 2.4. Following the analysis, a trade-off was performed on the structural concept where the following designs are considered: Monocoque, semi-monocoque and a truss structure. Because the trade-off does not give a definite winner between the last two options, this shall be further considered in the detailed design. A material selection shall also be performed in the detailed design.

2.7. UAV System

For the UAV system, hardware- and software systems which handle input data have been designed. The subsystems of the architecture of the hardware, software and data handling is shown in Table 2.2.

Table 2.2: Overview of the hardware, software and data handling of the UAV system

Hardware	Software	Data handling
Flight Control System	Flight Control system	Flight Control system
Power system	Mission director	Drone Data input
Sensors (IMU, Prop., Air data etc)	Sensors (IMU, GPS, Air data etc)	Drone processor
Communication Unit	Communication Unit	Communication System
Navigation Unit	Vehicle state estimator	Data Storage

2.8. Sensitivity Analysis Methodology

In the midterm report, the general methodology regarding the trade-off and sensitivity analysis was described [6]. The same approach is used in this report.

The first step is to specify weight ranges for certain trade-off criteria, based upon a proper rationale. Then, a Monte Carlo tool runs through all the different possible score outcomes, resulting in a distribution of which design options win how many times. If this outcome is still not enough to provide closure for the trade-off, a criterion can be added as a final sensitivity analysis step.

3
Detailed Design: UAV System

To achieve a fully autonomous mid-flight drone recharging system, the design of an unmanned aerial vehicle (UAV) system is done. The UAV system encompasses both hardware and software components, depicted in block diagrams in Figure 3.1 and Figure 3.2 respectively. Additionally, a crucial aspect of the system is the communication among UAV drones, hubs, and aircraft, each with its own data handling processes. This process is illustrated in a data handling diagram in Figure 3.3.

3.1. Hardware Design

The hardware design of the autonomous drone comprises various components and systems that enable its autonomous operation are listed below:

- **Power & propulsion** consists of a payload battery, propulsion battery, and thermal control systems with sensors for optimal operating conditions and feedback loops to the onboard computer.
- **Communication system** is equipped with a transmitter and receiver for bi-directional communication, ensuring coordinated operations and the exchange of relevant data.
- **Navigation & positioning** is essential for accurate autonomous flight with a GPS system linked to the onboard computer, providing continuous updates of the drone's position for effective communication.
- **Sensor Integration** into the hardware system enables the system comprehensive data measurements and analysis about the environment and its performance. These sensors provide continuous feedback on altitude, speed, orientation, and environmental conditions. The collected data is processed and utilised by the onboard computer for decision-making and control purposes.
- **flight control** subsystems of the drone executes missions, ensures safe operation, and combines hardware, software and sensors for autonomous decision-making and precise control. It relies on data from the IMU, navigation system, and other sensors to maintain stability and manoeuvre the drone, while detection and avoidance sensors mitigate safety risks.

3.2. Software Design

The software initiates high-level decision-making in the mission director, which is based on mission parameters and additional information communicated from the aircraft and ground system. This decision-making process generates a trajectory that continuously provides information to the flight control system throughout the mission. The flight control software system performs constant feedback processes to monitor the drone's motion in all six degrees of freedom. Consequently, a flight state is determined and used to communicate the required actions to the hardware system in order to achieve the desired flight state. Both the software and hardware systems analyse the flight state using multiple sensors. Within the software system, this analysis forms a feedback loop where various flight dynamics parameters of the drone are estimated. This information is communicated to both the high-level decision-making level and the trajectory planner, leading to an updated desired trajectory and initiating a new iteration of the flight control system.

3.3. Data Handling Design

The UAV system encompasses diverse data streams, as depicted in figure 3.3. During the data handling phase, data from navigation, sensors, and flight control is collected and formatted. Subsequently, the data processor processes and stores the recorded data for future use, or transmits it to the flight control system or communication system. The communication system handles the transmission and reception of data from external entities like other drones, hubs, and aircraft.

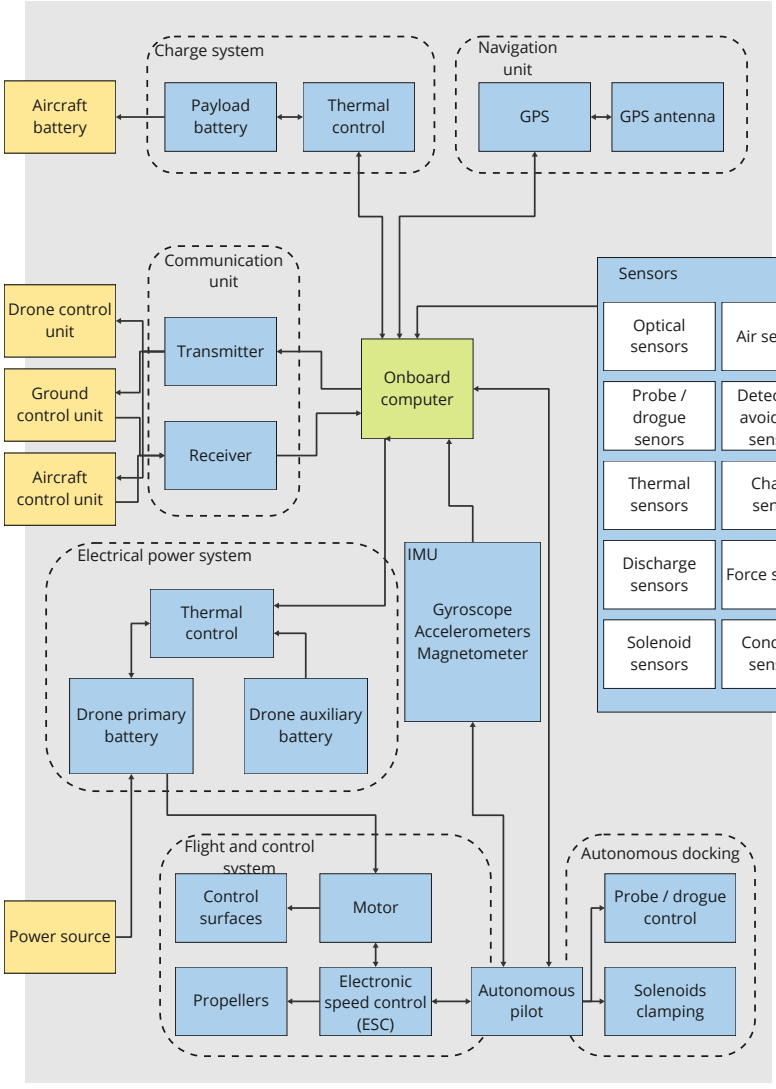

Figure 3.1: Hardware Blockdiagram

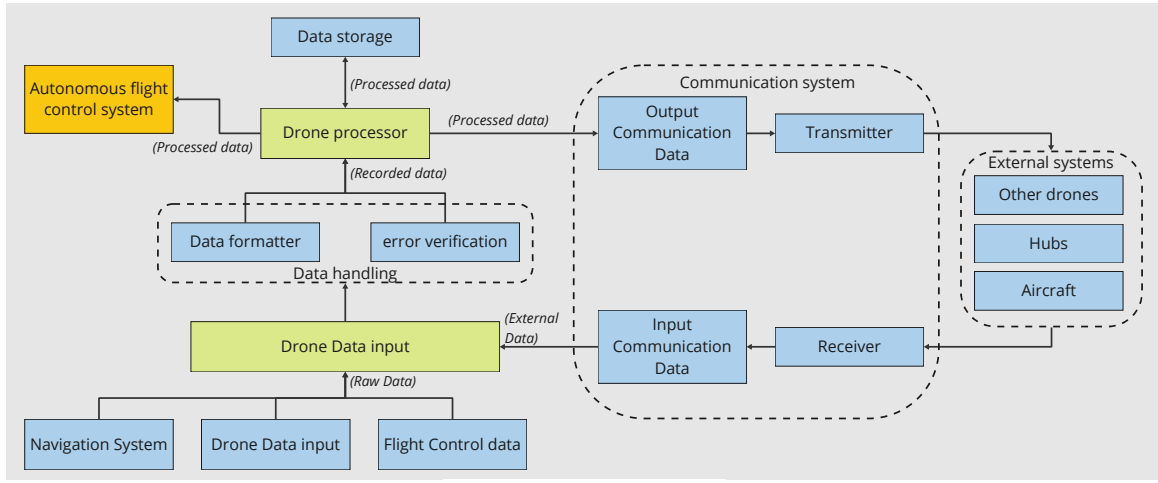

Figure 3.3: Datahandling Blockdiagram

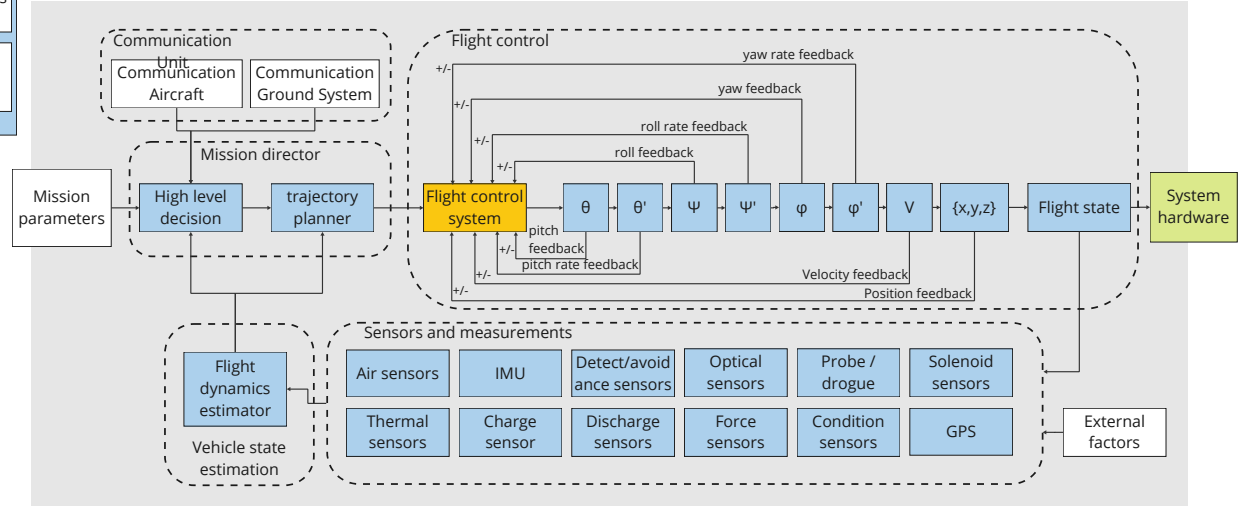

Figure 3.2: Software Blockdiagram

4
Detailed Design: Battery

The energy source of the eCarus system will be in the form of electric batteries. The drone is equipped with 3 major battery segments. Namely the payload battery dedicated for the recharging phase of the eCarus mission and two propulsion batteries in each of the wings. The battery design is performed in close collaboration with the ElectriFly Design Group [3]. First the battery requirements are assessed in section 4.1, after which a battery is selected in section 4.2. The chapter concludes with the thermal management of the eCarus drone is discussed in section 4.3.

4.1. Battery Requirements

To ensure that the entire system can function properly, it is important to define requirements for the batteries of the aircraft. Since this design is integrated with the design of ElectriFly, it is desired to align predicted trends for development of technologies. This also holds for the requirements set on battery performance and therefore a resemblance should be ensured between the two different designs. For the requirements, a distinction can be made between energy density, power density and cycle life.

Energy density

The energy density of batteries is an important criterion when considering battery performance. It directly dictates the eventual weight of the entire aircraft. A higher energy density enables more storage of energy per kilogram of battery weight. Current technology is capable of achieving an energy density of $250\,\mathrm{Wh/kg}$ [7], which results in very heavy aircraft. For the ElectriFly aircraft to adhere to CS-23 requirements, a battery energy density of $570\,\mathrm{Wh/kg}$ is required [3]. Therefore, considering an additional buffer, an energy density of $600\,\mathrm{Wh/kg}$ has to be considered for the design of the Electrifly aircraft to be feasible. For the design of the eCarus system the same energy density is considered for coherence between designs.

Power density

The power density requirement for the battery flows down from the most power demanding flight phase. From Table 4.1, which shows the power demand for different flight phases, it can be concluded that the cruise phase is the most power crucial flight phase. If the considered power density of $500\,\mathrm{W/kg}$ for the ElectriFly design [cite electrifly] is utilised for this design, it can be concluded that this is ample to ensure that the required power during cruise is available through the batteries. This is due to the fact that the energy density is more limiting than the power density.

Cycle life

Cycle life is an important metric for the performance analysis of batteries. An increased cycle life is preferable as it delays the replacement need of the batteries. This is a really important aspect in terms of sustainability, since batteries consist more often than not out of rare earth metals, the use of which should be limited. Ensuring that batteries can be used longer directly implies that fewer batteries have to be used throughout the operation of the aircraft and thus decreases the environmental impact of the operation of the eCarus system. For the design of the ElectriFly aircraft, a cycle life of 6000 cycles is defined to ensure feasible operation of the aircraft [3]. Since per single operation of the ElectriFly aircraft, two recharging cycles are necessary, namely one on the ground and one mid-flight, this infers that the aircraft should perform 3000 flights before maintenance to the batteries is required. Per flight of the ElectriFly aircraft, eCarus' primary battery and payload battery are depleted once. This means that when a similar operational life is considered for both designs, the cycle life requirement for this design should be 3000 cycles. Furthermore, defining a depth of discharge (DoD) also benefits the cycle life of batteries. For this design, a DoD of 80% is used.

Table 4.2 presents the final defined battery requirements which will henceforth be used for the design of the eCarus system.

Table 4.1: Required power per flight phase

Flight Phase	Power [kW]
Climb	388
Cruise	662
Descent	135
Loiter	341
Take-off	618

Table 4.2: Battery requirements

Battery parameter	Requirement
Energy density	600 Wh/kg
Power density	500 W/kg
Cycle life	3000 Cycles
Depth of discharge	80 %

4.2. Battery Selection

Selecting the battery for the aircraft is a crucial part in the design of the entire system. The battery should be able to adhere to the aforementioned requirements in order for the design to be operable. Therefore, a careful consideration of the components of the battery and its specifications is necessary.

4.2.1. Battery Components

The battery consists of three different components: An anode, a cathode and an electrolyte. For the anode, a lithium-metal with polymer coating is selected because of the very high energy capacity of lithium metal. The polymer coating is needed for pairing with the electrolyte. For the cathode, a Nickel Manganese Cobalt (NMC) is chosen because it is already in use in high-energy applications such as the automotive industry. A coating helps increase the electrochemical stability of the cathode. The electrolyte is made out of sulphide because of its high ionic conductivity and because of the less challenging manufacturing process for sulphides in comparison to oxides. More specifically, an argyodite sulphide is selected for the electrolyte because of the high market potential and the suitability as catholyte, anolyte and separator. As noted before, the lithium anode shall have a coating to prevent reacting with the sulphide [3]. Figure 4.1 graphically presents the selected battery components.

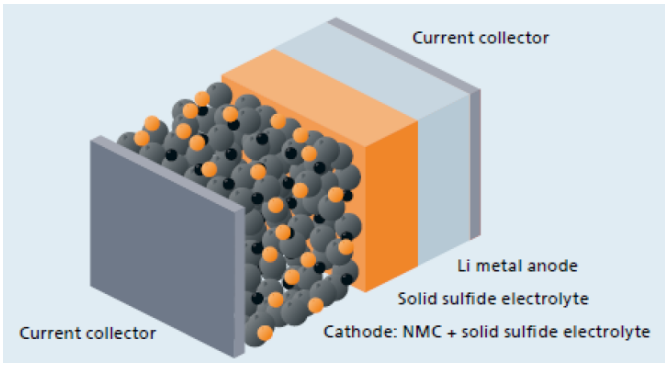

Figure 4.1: Selected battery component layout [3]

4.2.2. Battery Specifications

The specific layout of the battery and the design of each single cell in the battery is an important aspect for the design of the eCarus system. Due to the novelty of electric aircraft there are no references with respect to lithium sulphide battery dimensions, so the battery dimensions of electric vehicles such as Teslas will be used as a reference [3].

The 18650 cell is widely used by Tesla. It has a diameter of 18.4 mm and a length of 65 mm. A major benefit of utilising solid-state batteries is the fact that a casing around each cell is unnecessary, since the electrolyte is solid instead of liquid. A capacity of 5.68 Ah can be achieved by using these solid-state battery cells [3].

The battery cells are divided into modules. The use of modules is advantageous as it enables simpler manufacturing and maintenance. When a cell fails, the entire battery does not have to be taken

out, but instead only a single module containing the faulty cell can be retrieved and mended. It is chosen for the design of the eCarus system to use three battery packs, two battery packs are reserved for the primary battery which powers the entire aircraft and one battery pack is reserved for the payload battery which recharges the ElectriFly aircraft. The voltage per module can be determined with the use of Equation 4.1. Thereafter, the number of modules can be determined based on Equation 4.2 and the voltage requirement of the battery. It is important to note that the modules are arranged in series, such that their joint capacity is equal to the capacity of a single module. Furthermore, the total voltage of the battery is then the sum of all separate voltages of the modules. The total capacity for each battery can be computed using Equation 4.3. Finally, the capacity per module and number of cells in parallel per module can be found with Equation 4.4 and Equation 4.5. The number of cells in series per module is assumed to be equal to 6, since this is coherent with the design of the ElectriFly aircraft [3]. The chosen cell is capable of achieving a voltage (V_{cell}) of 3.8 V and the required voltage for the battery ($V_{battery}$) is equal to 800 V. This flows down from the fact that the selected engines require a voltage of 800 V to operate smoothly. The total energy for the payload battery is equal to 1557.91 kWh and originates from a requirement of the ElectriFly aircraft. The total energy for the primary battery of the eCarus aircraft is equal to 869.82 kWh and flows down from section 6.1.

$$V_{\text{module}} = 6V_{\text{cell}} \tag{4.1}$$

$$N_{\text{module}_{\text{series}}} = \frac{V_{\text{battery}}}{V_{\text{module}}} \tag{4.2}$$

$$C_{\text{total}} = \frac{E_{\text{total}}}{V_{\text{battery}}} \tag{4.3}$$

$$C_{\text{module}} = \frac{C_{\text{total}}}{N_{\text{packs}}} \tag{4.4}$$

$$N_{\text{cells}_{\text{parallel}}} = \frac{C_{\text{module}}}{C_{\text{cell}}} \tag{4.5}$$

Table 4.3: Battery characteristics parameters

Parameter	Primary Battery	Payload Battery	Unit
V_{cell}	3.8	3.8	V
C_{cell}	5.68	5.68	Ah
D_{cell}	18.4	18.4	mm
h_{cell}	65	65	mm
$N_{cell_{parallel}}$	96	343	-
$N_{cell_{series}}$	6	6	-
$N_{module_{series}}$	36	36	-
V_{module}	22.8	22.8	V
C_{module}	543.64	1947.39	Ah

4.3. Thermal Management

The battery power system requires a wide range of recharging and discharging energy which in turn results in large quantities of generated heat. This section starts with an explanation on the effect of thermal management on the battery in terms of life cycle and performance. Furthermore, liquid cooling is addressed and its properties are analysed.

4.3.1. Effect of Thermal Management on Battery Performance

The battery in the drone is required to have a constant and good battery performance. Meaning a steady energy/power density and a long life cycle. Larger energy densities will result in higher temperatures within the battery [8]. High temperatures will accelerate the chemical reactions between the cathode and anode and will result in faster degradation of the battery [8]. In contrary lower temperatures will degrade the battery's capacity and lower the specific energy density of the battery [8]. The thermal management system is also required to regulate a certain uniform temperature distribution. A non-uniform distribution results in different chemical reaction rates which in turn will affect the battery's lifetime and thus the sustainability of the eCarus project [8]. The sustainability of the complete power system is highly dependent on the good functioning of the battery thermal management system (BTMS).

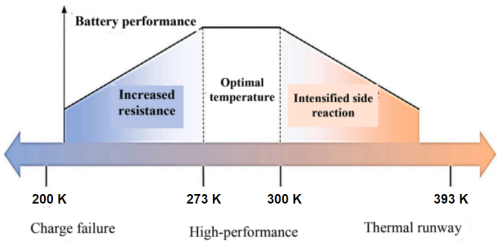

Figure 4.2: Thermal battery range projection of solid-state batteries [8].

The battery thermal spectrum ranges from its lower bound where charge failure occurs to the upper bound where thermal runaway occurs [8]. Within this spectrum, the battery will have an optimal temperature range at which it has its best performance. For Lithium-Ion batteries, charge failure occurs at 233 K, the optimum temperature ranges from 288 K to 308 K, and thermal runaway occurs between 363 K and 393 K [8]. Solid-state batteries operate within a wider range of 200 K to 393 K [9]. By projecting the range of optimal temperatures compared to the failure temperature of Li-Ion batteries onto the solid-state batteries, the following temperature range diagram can be estimated, as shown in Figure 4.2.
The thermal battery range of Figure 4.2 will require a BTMS that is capable of both heating and cooling. This is common in electric aviation as was discussed with Tine Tomažič, Director of Engineering & Programs at Pipistrel. Therefore different BTMS are considered in the next paragraph.

4.3.2. Thermal Management System Types

For the different thermal management systems the most commonly used BTMS are considered and listed below. In general cost, volume, complexity and lifetime are driving factors.

Table 4.4: Overview of the common used BTMS's and their (dis)advantages[8]

Cooling system	Advantages	Disadvantages
Liquid Cooling	Low cost, high efficiency, broad application, heat/cooling capabilities	Requires volume, leakage, pump requires power.
Air Cooling	cheap, simple, low volume	low convection, used for low to moderate cooling
Phase change material cooling (PCM)	constant operating temperature, quick discharge process, great heat expansion	Volumetric expansion, low conductivity

Liquid cooling makes use of a fluid that transfers the heat towards a radiator that dissipates the heat. Liquid cooling can be in the form of direct contact cooling (dielectric liquid) or in the form of indirect contact cooling (conducting liquid) [8]. Dielectric liquid runs through battery cells whereas conducting liquid only cools with the use of conducting the thermal heat. Liquid cooling are often preferred since they are relatively easy to use and cheap. Furthermore liquid cooling has a high efficiency [8]. However it requires a pump system which is prone to leakage, requires some additional spacing and uses energy to function.

Air cooling is the most basic option of a BTMS. It only uses the convection of the heat into the air. This requires a high airflow in order to cool a large amount of heat. These systems are generally used in low to moderate cooling demand systems and its cooling capability is limited to around 1 kW [8]. It should be noted that since the drone is flying at a relative high speed and often in a cold environment this cooling capability could potentially be higher.

Phase change material (PCM) cooling makes use of the fact that changing a materials phase often requires a lot of energy. PCM cooling is capable of having a stable operating temperature of the battery until the point all the energy is absorbed. The main problems of PCM cooling is its low conductivity and its volumetric expansion [8]. This makes PCM cooling not a proper system for aviation applications.

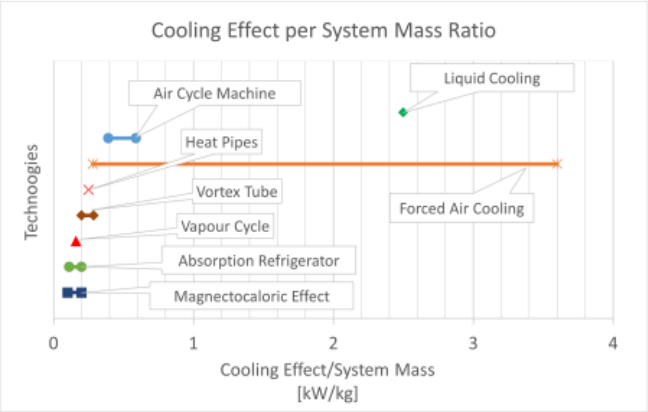

Figure 4.3: Cooling effect of BTMS by system mass ratio [10]

?? shows the system mass relative to its cooling effect. Out of this data can be concluded that liquid cooling has the highest cooling effect compared to system mass which is preferred. Furthermore Figure 4.4 is a visualisation of the cooling effect compared to the electric power consumption used by the system where liquid cooling has a factor of 2.5 approximately resulting in a cruise power usage of $8.2\,\mathrm{kW}$. Figure 4.5 indicates that liquid cooling has one of the highest relative airflow ratio meaning a high heat transfer capability.

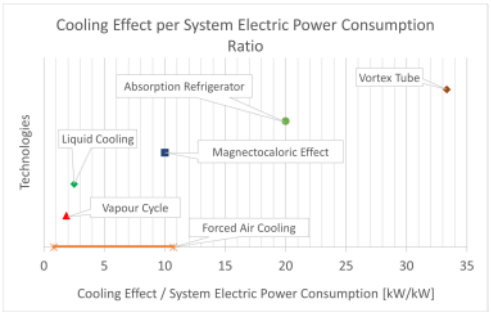

Figure 4.4: Cooling effect of BTMS relative to electric power consumption [10]

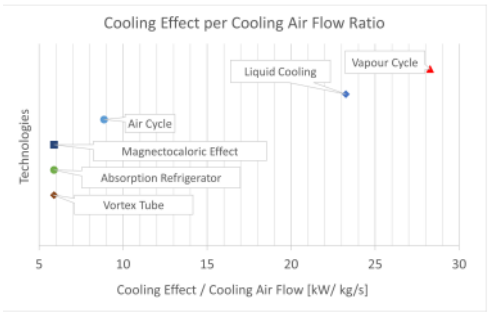

Figure 4.5: Cooling effect of BTMS relative to air flow [10]

Liquid cooling is often used with vapour cooling due to its high thermal absorption as can be seen in Figure 4.5. A conceptual architecture of the liquid cooling used with a vapour cooling system (R134a as working fluid[10] here) is shown in Figure 4.6. The parts that require energy (work) and where the heat is generated is clearly shown. The selection between whether the used liquid cooling is assisted by vapour cooling is not performed in this stage of the design. The BTMS uses 50% Ethylene Glycol + 50% water as coolant.

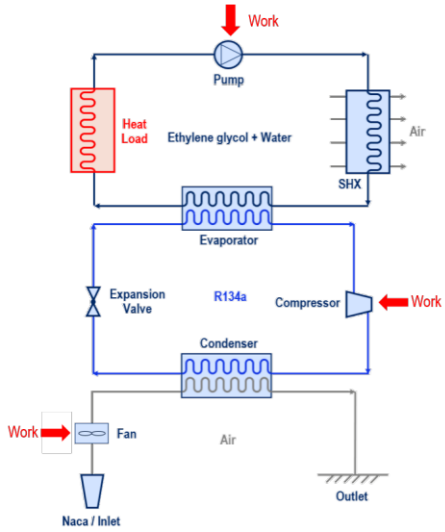

Figure 4.6: Conceptual architecture of a liquid and vapour cooling system [10]

Table 4.5: Heat flow generated by flight phase

Flight phase	Heat Flow [Q]
Take-off	17.9 [kW]
Climb	7.0 [kW]
Cruise	20.5[kW]
Descent	0.8 [kW]
Loiter	5.4[kW]
recharge (payload)	135.5 [kW]

4.3.3. Heat Generation Calculations

For the eCarus drone a heat analysis is performed. The heat flow generated is defined using the following formula.

$$Q_{Bat} = I_{cell}^2 * R_{int} \tag{4.6}$$

An initial heat analysis is performed for both the payload as the propulsion battery. Out of the voltage and required power for the payload batter a current and thus heat flow is determined. The same holds for the heat flow generated by the propulsion batteries. The heat flow is dependent on the different required peak powers for the different flight phases as presented in Table 4.5. The highest heat flow is generated by cruise flight hence the BTMS is designed to handle this heat flow. The payload battery is the most critical battery in terms of heat generation since it requires a high peak power during recharge. To bring it into perspective this is a factor of approximately 10 higher than a Tesla Model 3 [11].

4.3.4. Sizing of BTMS

The sizing of the BTMS is performed in this paragraph. First of all from the heat flow for each flight phase can be calculated using the following formula [12]:

$$Q_{cruise} = \dot{m}_{cool} * C_{Cool} * T. \tag{4.7}$$

Following from temperature range shown in Figure 4.2 the optimal temperature of the battery is set to 286.5 K. With the cruise conditions this will result in an optimal ΔT of 28.24 K wherein the coolant will function. Equation 4.7 also gives an initial indication of the mass flow required by the coolant through the system.

Since there is not yet a good estimation on solid-state battery coolant weight with respect to the battery cell weight, a ratio of current Li-Ion batteries is used. 7.16% of the battery cell weight is used for cooling with a chosen 50% Ethylene Glycol + 50% water coolant [13]. All the coolant specifications are listed in Table 4.6. This will in turn result in a BTMS estimate of 203 kg for the payload battery and BTMS estimate of 92 kg for the propulsion battery which is well with the pre-determined budgets for such a system.

Parameter	Value	Unit
Thermal conductivity coolant	0.38	W/mK
Viscosity coolant	0.00394	$Pa{\cdot}s$
Density coolant	1073.35	kg/m^3
Specific heat coolant	3323	J/kgK
$\dot{m}_{cool}$	0.22	kg/s

Table 4.6: BTMS coolant results

Parameter	Value	Unit
W_{batpl}	2903.0	kg
W_{batpp}	1316.9	kg
$Q_{payload}$	135.5	kW
Q_{cruise}	20.5	kW
W_{BTMSpl}	203.2	kg
W_{BTMSpp}	92.2	kg

Table 4.7: Weights of battery packs and BTMS of the eCarus drone.

4.3.5. Future Thermal Management Steps

Future steps in term of thermal management are needed for the eCarus drone. For a start the sizing of the subsystems i.e. pump, heat exchanger, pipes, coolant and controller units. This can be done by defining the heat exchanger surface area with a certain depth within the RAM air inlet. This RAM inlet can in turn be further analysed in terms of drag loss during flight.

Secondly the battery temperature versus the flight phases will be further analysed by plotting the battery temperature over time. This will give an insight in the temperature distribution over the batteries and possible solutions such as pre-cooling during less intensive phases.

Moreover additional heat dissipates throughout the liquid cooling system which can be used as advantage but also induce extra challenges that will be analysed. By running the liquid cooling pipes close to the skin in the leading edge it may function as additional de-icing system. Furthermore the heat imposed by the batteries could potentially affect other subsystems. This correlation analysis will be performed in a further design phase as well.

In the future one could examine the concept of combined battery recharging. Meaning that in order to minimise the high heat flow concentration around the payload battery some of the transferred energy will flow from the propulsion batteries temporarily. The heat is thus distributed more uniformly around the drone meaning that all the BTMS could cool the drone in correlation.

5
Detailed Design: Docking Mechanism

In this chapter, the docking mechanism is designed. Section 5.1 describes the recharge procedure. Then, in section 5.3, the probe is designed. The aerodynamic effects of the drogue are assessed in section 5.4. An overview of all the assumptions made for the docking mechanism are shown in Table 5.1.

Table 5.1: Overview of assumptions within docking mechanism chapter. (* indicates to be tested in future)

ID	Assumption
AS-PB-01*	small drops of water will not cause connection problems and due to the forward movement there will be minimal water in the drogue.
AS-PB-02*	Small dislocation of the probe will still result in a successful connection.
AS-PB-03	A equal voltage between the receiving and payload battery will result in enough energy transfer.
AS-PB-04*	Bow wave effect is negligible with a probe of 1 meter.
AS-PB-05*	Drogue net is inherently stable
AS-PB-06	The CDU is able to roll the cable on a drum
AS-PB-07	Similar forces during conventional refuelling on the connection are used for the design.

5.1. Recharge Procedure

In this paragraph the determined recharging procedure is described whereas the safety measurements on this procedure are discussed in the next paragraph. In order to ensure the energy transfer to the Electrify aircraft the system makes use of a recharging procedure which is similar to conventional refuelling mid-flight and tested by NASA with autonomous refuelling in 2007. [14, 2]. The different modes and positions during the recharge procedure are visualised in Figure 5.1.

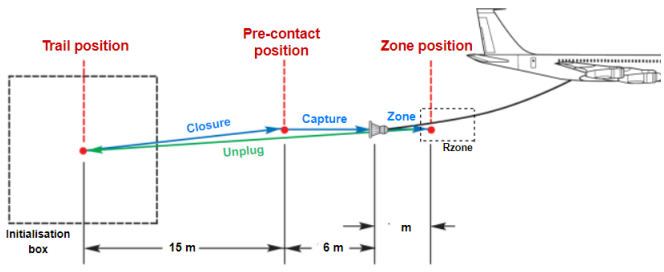

Figure 5.1: The AAR process [2]

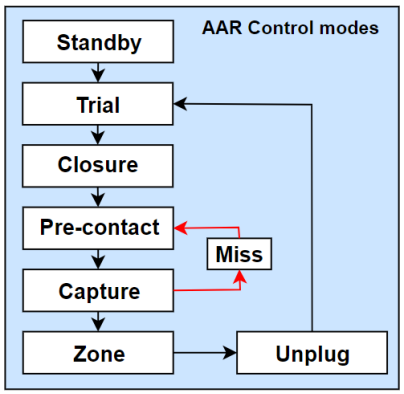

Figure 5.2: The AAR control modes [2]

Standby mode

the autonomous airborne recharging (AAR) controller of the drone starts with the standby mode. the AAR controller is initiated once the drone is positioned somewhere inside the initialisation box. Upon standby mode the receiving aircraft will start its recharge procedure as well. This mode functions as 'zero' and during the complete procedure if there is an error detection in the AAR controller the drone will reposition to this mode.

Trail mode
After the standby mode the trail mode is initiated upon which the drone manoeuvres from somewhere inside the initialisation box to the trail position. trail mode consist of a system/sensor check and if all systems are functioning nominal the drone will start with the closure manoeuvre towards the drogue.

Closure mode
During Closure the drone will move with its programmed velocity towards the pre-contact position. This about 15 m forward in lateral position from the trail position.

Pre-contact position
In the pre-contact position the drone is both lateral and vertical aligned with the drogue. The longitudinal distance from the drogue is fixed at 6 m [2]. This system starts the tracking system where the relative position of the drogue is measured using position sensing devices (PSD). Once the system is locked on the drogue the system starts the capture mode at which the drone connects to the drogue.

Capture mode
In the capture mode the AAR control initiates a closure rate of $3\,\mathrm{m/s}$ in order to successfully connect the probe and drogue. The connection system required success rate is above 99.9% meaning that a miss only occurs ones in a thousand times. If the miss criteria are met the system starts the miss mode upon which the drone manoeuvres back to the pre-contact position. This is visualised in both Figure 5.1 Figure 5.2.

Zone mode
The zone mode is important for the safety of the recharging procedure [14]. This zone mode is designed in close correlation with the Electrifly Design Group [3]. Within the capture mode the probe is connected to the drogue but the drone is not yet in the recharging zone. The drone is required to move within this zone and have a level stable flight.

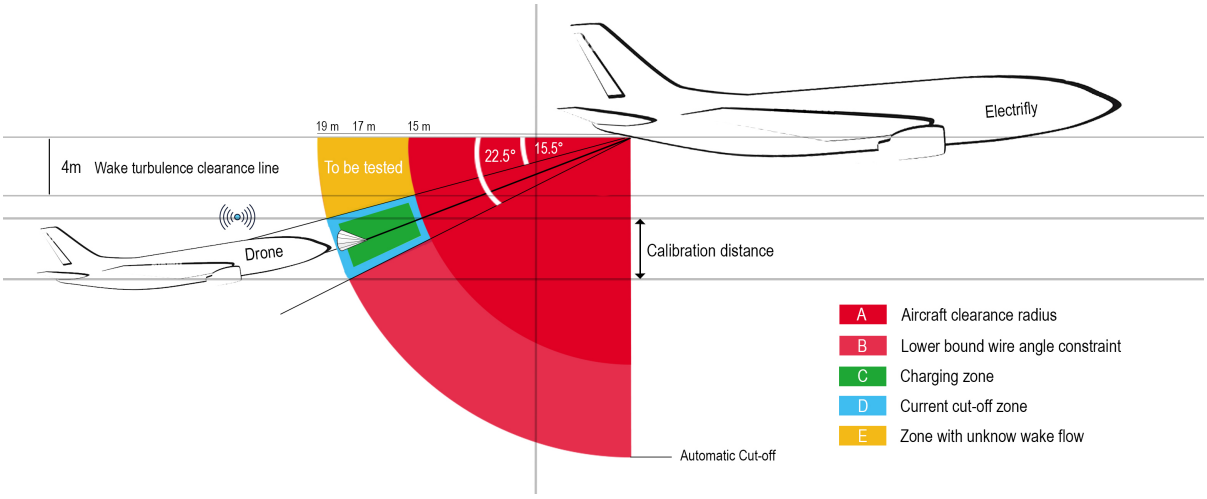

Figure 5.3: Visualisation of the recharge zone and clearance behind the receiving aircraft[3].

Figure 5.3 shows the recharge area. The cable's angular range sets lower and upper thresholds, beyond which it enters the cut-off zone. The front and aft boundaries are determined by the cable length. With a total length of 19 m, a 15 m clearance has been established based on refuelling a KC-46 tanker/receiver plane [15]. This clearance is considered sufficient for ElectriFly [3]. The recharge zone is divided into a 3-meter recharge area and a 1-meter redundancy zone (zones C & D). Additionally, there is a cut-off zone where no charge transfer occurs, used to correct the drone's position towards the recharge zone. If the drone moves outside this cut-off zone, it enters the unplug phase. The region above the upper limit (area E) requires further definition, necessitating CFD analysis and in-flight testing.

Unplug mode

The unplug mode is initiated by either the end of recharging or exceeding the recharge zone limits. It is important that the separation is safely performed. The AAR control will move the drone with a pre-programmed unplug velocity backwards along the longitudinal axis [2]. The drone will manoeuvre back to the trail position upon which it either returns to the hub or starts the reconnecting process due to forced separation.

Miss mode

The miss mode gets initiated if the miss criteria are met. In this case the vertical and lateral positions are fixed to the values just prior to the miss mode initiation [2]. In case of contact between the probe and the drogue the drone will move straight backwards to avoid large imposed stresses on both structures [2]. In case of a second attempt the drone will reposition itself back to the pre-contact position. It is important to note that due to the logistic challenges in terms of docking time described in chapter 11 the total docking time should not exceed 5 minutes and 2 attempts. If these constraints are exceeded a second drone will be launched, in the mean time the current drone is allowed to do more attempts if possible. According to [REQ-US-SR-01] the system shall dock successfully 99.9% of the manoeuvres [16]. In case of 2 attempts this results to a failure once every million. By implementing extra coupling assisting systems such as the PSD and cable thrusters this success rate is assured.

5.2. Safety and Risk Procedure

In this paragraph the safety procedure is discussed and risk are indicated and the performed mitigation is explained. The top level risks are shown in Table 5.2.

Table 5.2: Top level risk table including mitigation.

ID	Risk	Mitigation
RSK-SYS-01	Drone failed to manoeuvre the probe in the drogue (miss mode).	Drone will manoeuvre to pre-contact position and restart coupling procedure.
RSK-SYS-02	Drone inflicts impact damage	Fixed closer rate set to 2-3 m/s [17].
RSK-SYS-03	Tension/Compression forces exceeds maximum	Damping in cable drum unit to mitigate oscillation and the use of recharging zone.
RSK-PD-01	Short circuit in recharge system	Both aircraft are equiped with a ECU consisting of a safety switch and fuses in case of short circuit.
RSK-PD-02	Failure of locking solenoids unable to connect	Use of multiple locking solenoids creating redundancy
RSK-PD-03	Failure of locking solenoids unable to disconnect	Weakpoint in the solenoids resulting in breakage of the solenoids
RSK-PD-04	Discharge effect through other part of the drogue-probe system	ECU will be equipped with discharge wiring switch to the aircraft

These top level risks are all mitigated using either safety procedures or included systems. RSK-SYS-01 is part of the general docking failure in terms of connection. The miss mode procedure is more thoroughly explained in the previous chapter. RSK-SYS-02 is mitigated by fixing the closure speed to a preprogrammed value of $3\,\mathrm{m/s}$[17]. In addition the AAR control system receives continuous feedback on the relative position of the drogue due to the position sensing devices. This feedback is also a driving factor of the closure rate of the drone. A higher closer rate will result in cable whips whereas slower closer rates will result in significant challenges for achieving positive engagement [18][17]. This is mainly due to the fact of bow wash induced by the drone, the high restoring force of the cable and to overcome coupling latch forces [17]. The recharging procedure will come with numerous risks proposed in Table 5.2.

For RSK-SYS-03 the recharging procedure can result in sudden aerodynamic loads which induce compression/tension forces in the cable. During conventional mid-air refuelling the ΔV should be in the range $1 - 1.5m/s$, for the drone a similar ΔV is used[19] [17]. Maximum limit loads of $6.7\,\mathrm{kN}$ and $11\,\mathrm{kN}$ for tension and compression respectively are set for refuelling drogue-probe systems [17]. A safety factor of 1.2 results in maximum loads of $5.6\,\mathrm{kN}$ and $9.2\,\mathrm{kN}$.

For both RSK-PD-01/04 the electric system of the aircraft and the drone are equipped with an electric control unit (ECU) which is equipped with fuses, switches and electric sensors to ensure a reliable energy transfer.

RSK-PD-02 is mitigated by the fact that redundancy is introduced by having multiple solenoids. Since these solenoids have a small cross-section and are easy to replace in the drogue they are introduced as weaklink. If the probe is unable to disconnect the solenoids are designed to fail due to tensile forces (6.7 kN) [17]. The introduced weaklink functions as a mitigation for RSK-PD-03. The probability and impact analysis of the risk and the corresponding pre/post mitigation risk maps are further described in chapter 16.

5.3. Probe-Drogue Design

The probe-drogue system is designed with the use of numerous requirements and criteria. First the receiving drogue is designed in this paragraph after which the connection is designed. The connection design consist of sketches, sensor overviews and concluding a CAD render.

5.3.1. Requirements and Criteria

Sector	ID	Requirement
Mission	REQ-PD-MS-01	The drogue-probe system shall have a communication system in terms of system status to both the drone and aircraft.
	REQ-PD-MS-02	Closing rate drone should be between 2-3 m/s [17].
	REQ-PD-MS-04	The probe/drogue system shall have a clearance of 15 m.
	REQ-PD-MS-05	The drogue-probe system should have a system that allows a discharge of 300 kV between the aircraft and the drone [17].
	REQ-PD-MS-06	The drogue and probe shall have communication in the form of IR sensors and reflectors.
	REQ-PD-MS-07	The drone shall redock in case of tension/compression cut-off.
Probe	REQ-PD-MS-08	The drone shall have 5 minutes to connect.
	REQ-PD-PR-01	The structure of the probe/drogue system shall withstand loads induced during an engagement of 3 m/s.
	REQ-PD-PR-03	The probe nozzle is capable of an off-centre disconnects of 22.5 degrees maximum [17].
Cable	REQ-PD-CB-01	Cable length should provide a stable drogue/cable configuration and shall provide the drone/aircraft of enough clearance.
	REQ-PD-CB-02	The Drogue + Cable should be inherently stable.
	REQ-PD-CB-03	The drogue + coupling should not spin. In addition the coupling swivel ball should not be mechanically clamped [17].
	REQ-PD-CB-04	At full trail the vertical and lateral oscillations should not exceed half the diameter of the drogue canopy. These oscillations should dampen out to 1/3 amplitude after 3 cycles [17].
	REQ-PD-CB-05	The cable tension/compression should not exceed 6.7 kN / 11 kN [17].
Drogue	REQ-PD-DR-01	The drogue shall be aerodynamically stable.
	REQ-PD-DR-02	The drogue shall aim towards the probe using thrusters and or rotary connections.
	REQ-PD-DR-03	The probe/drogue system should not interfere with the air data sensors of the drone.
Cable unit	REQ-PD-CU-01	The cable unit shall provide air/liquid to fulfil thrusters.
	REQ-PD-CU-03	The cable unit shall be able to extend and bring in the cable.
	REQ-PD-CU-04	The cable unit shall include a rotation spring and damper to mitigate oscillations in the distance between the plane and drone.

5.3.2. Drogue Design

The drogue part of the drogue-probe system that is part of the ElectriFly aircraft consist of three major segments namely, the Cable Drum Unit (CDU), the cable and the drogue itself. The CDU is placed in

the receiving aircraft body and its major task is to store the drogue during flight and to reel the cable in/out during the recharging procedure. Figure 5.4 shows an illustration of a Hose Drum Unit (HDU) for mid-air refuelling used by the United States [20]. The HDU consist of the following important parts: **118** pressured air tank, **128** circuitry, **116** cable drum, **130** power supply, **134** storage tube for drogue. The CDU for the probe-drogue system consist of similar parts.

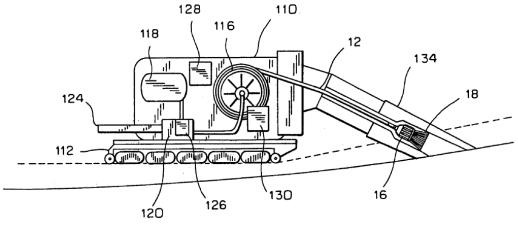

Figure 5.4: Illustration Hose Drum Unit for refuelling mid-air. [20]

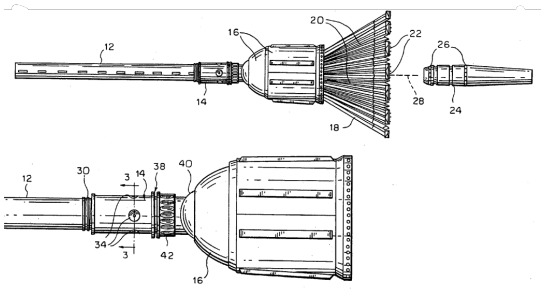

Figure 5.5: Technical sketch of refuelling drogue including cable connection and probe visualization. [20]

The drogue is the most complex system of the docking mechanism. Figure 5.5 is an elevated view of the drogue configuration. **14** is the infitting assembled to the coupler **16** consisting of the ball joint **40** and the connection section described in subsection 5.3.3[17]. **18** is the dragnet consisting of struts **20** with Position Sensing Devices (PSD) **22** linked with PSD **26** on the probe. These infrared sensors allow the drogue to measure its distance relative to the probe both in the longitudinal axis **28** and lateral axis. The drogue is able manoeuvre along the lateral axis with thrusters **34** in the infitting **14** based on the sensor data. The ball joint **40** and the rotate-able coupling allows the drogue to have an angular motion and off-centre (de)connection of 22.5 degrees maximum [17].
The cable used during the recharge is designed in close correlation with the ElectriFly Design Group and is stored in the CDU within the receiving aircraft [3]. The cable is required to transfer a power of 1.7 MW during the recharging time. The cable voltage is chosen to be 800 V in order to be compatible with the voltage of the drone engines and the receiving battery of the aircraft (800 V). The higher the voltage in the cable the lower the cable loss resulting in better efficiency and lower heat generation. With a voltage of 800 V a total current of 2125 A transfers through the cable during recharge.

The length of the cable is designed to minimise the cable loss but allow a safe recharging procedure. Therefore the clearance behind the receiving aircraft is determined and a relative position is estimated. As was described in this chapter the clearance was derived from the boom clearance of a KC-46 refuelling procedure resulting in 15 m [15]. Furthermore a cable length of 3 m is chosen for the charging and cut-off zone with an additional 1 m for redundancy. Concluding the total cable length is 19 m.

For the wire a insulator and conductor has to be selected. XLPE is chosen as insulator. It is common used as insulator and it is applicable in a wide temperature range (363 K-208 K). With a dielectric of 20 kV/mm the thickness is required to be minimum 0.4 mm [21] [3]. Although aluminium and silver were considered as potential conductors, copper is selected as used conductor due to its low resistivity and high thermal conductance. A total wire weight of 50 kg and a efficiency of 99,5% is derived for the cable [3].
The cross-section of the cable is shown in Figure 5.6b. This is a simplified illustration of the copper wiring insulated by XLPE insulation. The middle of the cable consist of air tube which is used for thruster steering by the drogue and pressurised by the CDU. A small benefit of the air tube is that it absorps some of the heat generated by the cable. Figure 5.6a shows a detailed sketch of the air tube and the thrusters indicated by **47** and **50** respectively.

5.3.3. Probe Connection Design

The connection of the drogue-probe system is the most critical part of the system. Failure in the connection will directly result in an emergency procedure. It is thus important to design for redundancy

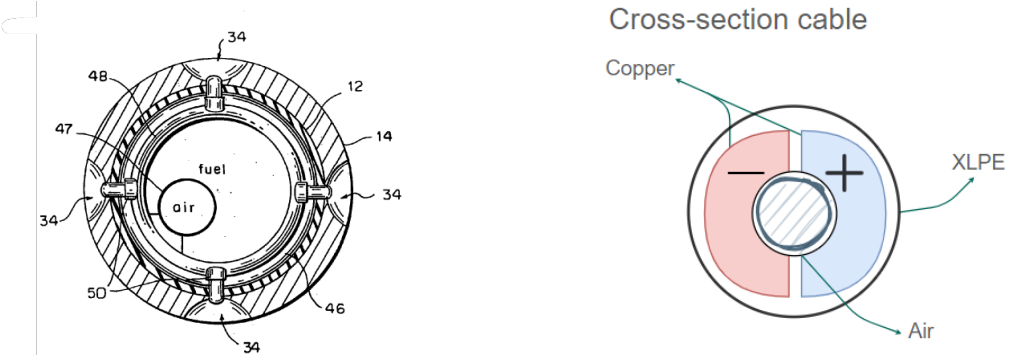

(a) Hose cross-section of conventional refuelling.

(b) Proposed simplified cable cross-section

Figure 5.6: Cross-sections of both the designed cable and a fuel refuelling cable[20].

to meet the requirement of a docking success of 99.9% [REQ-US-SR-01] [4][1]. Since there is no existing drogue-probe system connection a complete new theory is used for the docking mechanism. Figure 5.7 shows a schematic of the drogue-probe connection. The probe makes use of a cylindrical trapezoid configuration which is made from a conductive metal. Since the system makes use of direct current (DC) it has a negative exterior and a positive interior separated with insulation. The cylindrical trapezoid has a locking ridge used for interlocking of the solenoids upon connection. The cylindrical configuration ensures connection for a full 360 degrees of freedom in terms of rotation of the probe/drogue.

The Drogue has a similar positive/negative metal conductor in the core. It consist of 4 locking solenoids which are electrical controlled from the Electric Control Unit (ECU) of the receiving aircraft and will lock the probe in place. The drogue is also equipped with to discharge metals which are in turn connected to the dragnet. As described in Subsection 5.3.3 these metals are responsible for the safe handling of the discharge. A separate wiring is designed to isolate the discharge voltage from the electrical systems within the drogue-probe system.

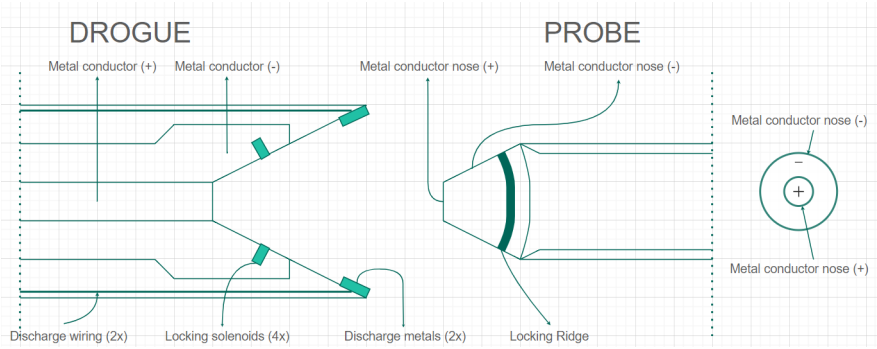

Figure 5.7: Schematic of drogue-probe system connection.

Figure 5.8 gives a schematic extended view of the drogue-probe system. as described in Subsection 5.3.3 the drogue net is equipped with machine vision (MV) or position sensing devices (PSD) which are responsible for close range navigation of the drogue. furthermore the drogue consist of a coupler and a ball joint which allows the system a off-center connection of 22.5 degrees maximum [17]. In addition the rotate coupling allow for 360 degrees radial turning of the drogue with respect to the cable. Finally the infitting is equipped with thrusters that allow the drogue to manoeuvre in the lateral axis to align with the probe. These thrusters are controlled from the ECU in the cable drum unit and perform with air compression. The cable consist of a segment as shown in Figure 5.6b. A similar use of thrusters is shown in Figure 5.6a for conventional refuelling where **50** are the thrusters and **34**the nozzles.

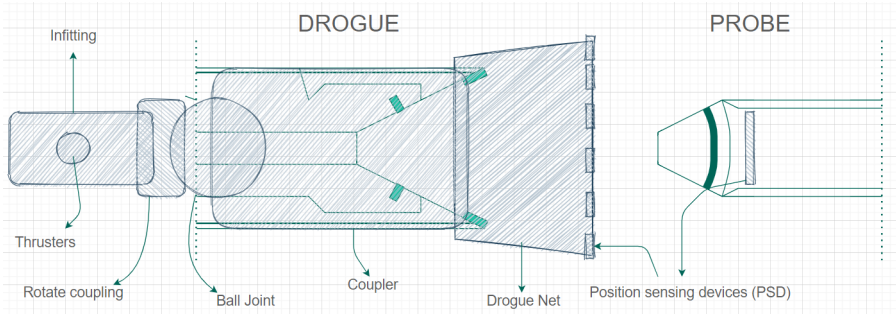

Figure 5.8: Schematic of drogue-probe system connection with extended view

Sensors

The drogue-probe system is completely dependent on sensors in order to function. Sensors can be categorised into sensors with spatial nature used for for tracking and station-keeping tasks [22], electrical sensors and force sensors. UAV related station-keeping sensors are discussed in chapter UAV. The station-keeping sensors w.r.t. the drogue-probe system are used to accurately measure the drogue position with respect to the probe. Current technologies are: GPS, machine vision (MV), radar, electro-optical (laser) [22]. Radar is deemed unfeasible since radar frequencies are easily absorbed by atmospheric conditions (moist etc) resulting in frequencies below K-band 18/24GHz which is considered inaccurate for close range docking [22]. For the drogue-probe system a two stage approach consisting of both a GPS and MV sensors for large and small distance navigation is used respectively [23][24] [25].

The force sensors measure the applied forces on the drogue-probe system once connected. excessive loads are measured by these sensors resulting in forced decoupling and prevent failure in the drogue-probe system. Furthermore the system consist of charge sensors measuring volts and current through the connection. If the probe is not connected properly the recharging of the aircraft stops. All sensors are represented in a sensor diagram of the system in Figure 5.9 and in Table 5.3.

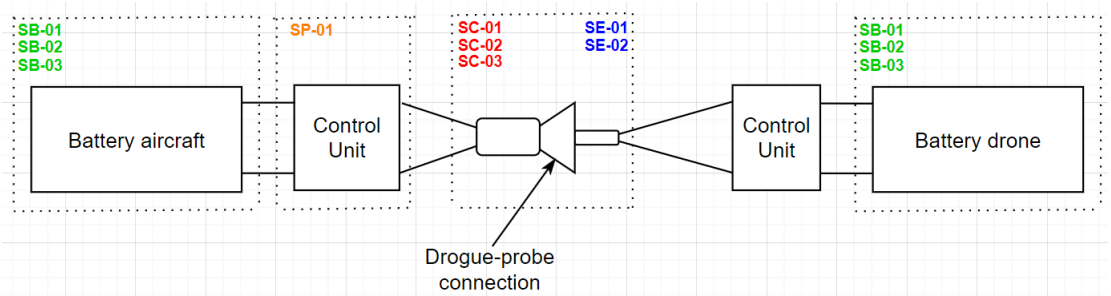

Figure 5.9: Sensor diagram drogue-probe system

Table 5.3: Overview of used sensors for the docking mechanism

ID	Sensors	Application
SP-01	GPS	Large range navigation of drogue-probe system.
SC-01	MV sensors	close range navigation of drogue-probe system.
SC-02	force sensors	used to measure applied load, can result in separation
SC- 03	solenoid sensors	sensors used to verify if solenoids are locked to the probe.
SE-01	Charge sensors	sensors measuring volts and current in connection
SE-02	discharge sensors	sensors measuring the potential discharge in the system.
SB-01	thermal sensor	thermal sensor within the battery.
SB-02	charge sensors	measuring voltage, current, energy capacity of the battery.
SB-03	condition sensors	measuring the battery condition.

Discharge handling

During flight, both aircraft and drone generate static charges from flying through rain, dust, etc. They discharge through built-in structures, but their charges may differ during recharge. The electric systems in the aircraft have to be operable under a discharge of 300 kV [17] To prevent this and potential lightning strikes, a separate conductive path is designed for the drogue-probe system. It's directly connected to the aircraft's static dischargers and assists the ECU with a discharge of 300 kV during refueling.

5.3.4. Probe Placement

The probe placement is mainly dictated by both the aerodynamics of the drogue-probe system and the required clearance from the propeller engines. In chapter 6 a trade-off is performed which results in engines placed on the trailing edge of the drone. Due to this placement the clearance in terms of propeller engines is considered as sufficient.

The aerodynamic effects opposed on the drogue are directly related to the relative velocity of the drogue $W_{rel} \in R^3$ composed as the following [26]:

$$W_{rel} = W_{\infty} + W_{bow} + W_{ac} + W_{atm} \tag{5.1}$$

Where W_{∞} is the free stream velocity, W_{ac} the velocity vector of the aircraft induced by the downwash/vortices, W_{atm} the velocity vector due the experienced atmospheric conditions and W_{bow} the bow wave effect due to the drone [26]. The atmospheric and aircraft vectors are generally small but present hence the bow effect predominantly determines the probe positioning [26]. The bow wave effect of a F-16 reference aircraft from autonomous aerial refuelling (AAR) simulation is visualised in Figure 5.10a [26].

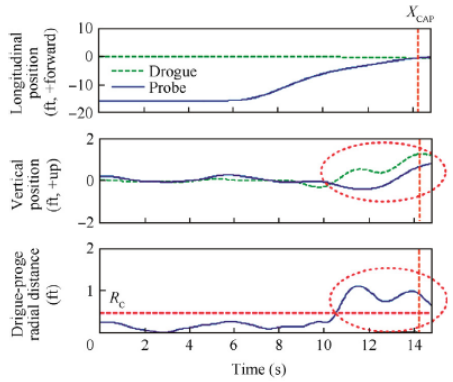

(a) Trajectory curves of drogue and probe position from AAR simulations under bow wave effect of a f-16 reference aircraft [26].

(b) A visualisation of an in front positioned probe on a Global Hawk UAV[27].

As can be seen from the trajectory curves the drogue is in equilibrium position due to atmospheric conditions [26]. As the drogue approaches the probe the drogue vertical position changes upwards. In the last graph a visualisation of the relative change in position between the probe and the drogue induced by the bow wave can be seen. In general the bow wave effect only comes in play a few meters around the forebody of the drone[26]. Introducing a better more forward position of the probe will limit the bow wave effect on the drogue. However a long probe may also impose structural problems such as flutter and other damages. Due to the bow wave effect a probe position of a probe in front of our drone is chosen as can be seen on a Global Hawk inFigure 5.10b.

5.3.5. CAD-Renders

Figure 5.11 gives a CAD render of the drogue-probe system connection used for the recharging procedure of eCarus. Furthermore Table 5.4 gives an overview of all the dimensions for the designed drogue-probe system connection.

Table 5.4: Drogue-probe system connection dimensions

Part	Dimension	Unit
Drogue radius	350	mm
drogue length	400	mm
probe radius	65	mm
probe length	1000	mm
cable length	20	m
cable radius	17.5	mm
Coupler radius	65	mm
rotate coupling radius	65	mm
infitting radius	60	mm
Thruster nozzle radius	15	mm
Ball joint radius	40	mm
solenoid radius	35	mm

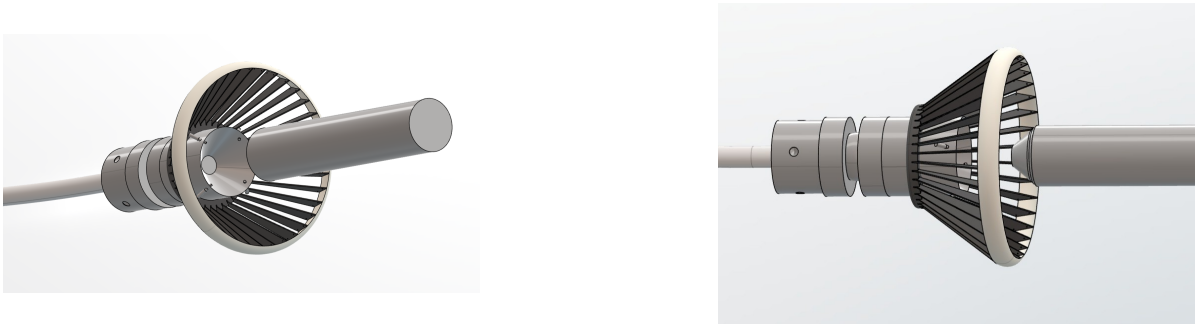

Figure 5.11: CAD Render of the Drogue-Probe System Connection

5.4. Aerodynamic Effects Drogue

The drogue of the cable experiences all kinds of aerodynamic effects when the cable is at full trail.The drone imposes all kinds of forces as well as the induced aerodynamic effects. I.e. the wire centenary curve is something that is important for the safety of the recharging procedure. For stability the lateral and/or vertical oscillations should not exceed a value of $\frac{1}{2} * D_{dc}$ where D_{dc} is the diameter of the drogue canopy. These oscillations should damp out to $\frac{1}{3}$ amplitude within 3 cycles [17]. The dragnet is designed to produce a constant drag force that will make the drogue inherently stable. However this is still to be tested in the next phase of the design. Due to the probe placement described in subsection 5.3.4 the aerodynamic effects of the drogue on the drone will be minimal. This is also proven by CFD modelling of a drogue on a F-16 reference aircraft and shown in Figure 5.12 [26].

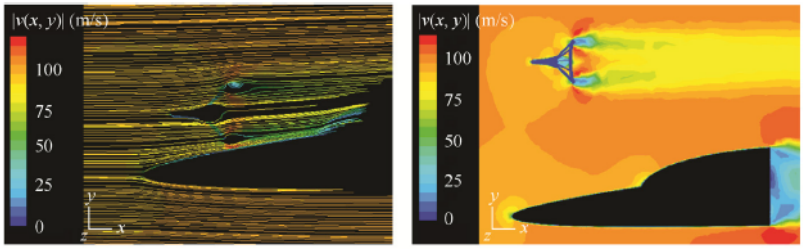

Figure 5.12: CFD modelling of a drogue with respect to reference aircraft forebody[26].

6 Detailed Design: Power and Propulsion

This chapter highlights the detailed design of the propulsion system of the UAV, especially focused on propeller design. The chapter is opened by section 6.1 where changes to the content described in the Midterm report are noted. Following this, section 6.2 describes the trade-off for the type of thrust generation while section 6.3 discusses the trade-off for lateral and longitudinal placement of the system. Subsequently, section 6.4 presents the detailed design of the propeller. Furthermore, section 6.5 describes the design for the duct surrounding the propeller. Thereafter, the material selection for the propeller and duct is described in section 6.6. The chapter is concluded with section 6.7, displaying the final propulsion system design along with the most important parameters. The assumptions made in this chapter are noted in Table 6.1.

Table 6.1: Assumptions made in the Power and Propulsion chapter

ID	Assumption
A-PP-01	The battery is charged to 90% and depleted up to 10%. This extra 10% can be used in case of emergency.
A-PP-02	The approach speed is 1.3 times V_{stall}
A-PP-03	The runway length is 115% of the take-off length
A-PP-04	The take-off length is 1.66 times the ground roll length
A-PP-05	V_1 is 1.1 times V_{stall}
A-PP-06	The propulsion system does not use energy during landing
A-PP-07	There is a correlation between propeller diameter and engine power, RPM and tip mach number
A-PP-08	The tip loss factor is equal to 1 for ducted fans
A-PP-09	Optimality of propeller design is acquired when w_0 is constant
A-PP-10	The most efficient propeller is obtained when the sectional lift coefficient is equal to c_l at $c_l/c_{d_{max}}$
A-PP-11	The duct experiences similar loads to the aircraft skin

6.1. Updates on Midterm Report

Before detailed design for the propulsion system can start, the basis on which the propulsion system design is built must be updated. As described in section 11.1, requirement [REQ-US-PER-05]: *A hub of the system shall be placeable on land and the sea* [4] is relaxed, meaning that hubs on sea are not required anymore. Due to cost and complexity considerations, it is decided that the drone shall take-off and land on ordinary airports. This means that the catapult launch and arrested landing system parameters in the wing loading diagrams are replaced with equations corresponding to conventional take-off and landing. This change influences the design point significantly along with other important characteristics such as stall speed, energy usage and total UAV mass which are described in this section.

6.1.1. Wing Loading Diagram Correction

The new lines in the wing loading diagram that replace catapult take-off and arrested landing are conventional take-off and conventional landing, respectively. Additionally, for manoeuvring a replacement equation is updated.

Conventional Take-off

As explained in subsection 11.1.6, the minimal runway length the drone can be launched from is $1300\,\text{m}$. According to CS25.113, the runway length should be $115\,\%$ of the take-off distance, defined as the distance the aircraft travels before reaching its clearance height of $35\,\text{ft}$. The minimal take-off distance $s_{T/O}$ is $1130.43\,\text{m}$ or $3708.76\,\text{ft}$. This take-off length is used to find the take-off parameter (TOP) from Figure 6.1, which is used to calculate the required wing and power loading for take-off.

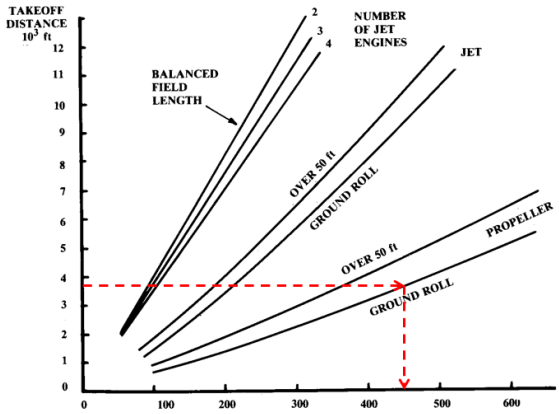

Figure 6.1: Relation between TOP and the take-off distance

Figure 6.1 shows that the TOP value for the corresponding take-off distance of $3708.76\,\text{ft}$ is equal to $450\,\frac{\text{lb}^2}{\text{ft}^2\text{bhp}}$, or $125.58\,\frac{\text{N}^2}{\text{m}^2\text{W}}$ converted to SI values. The TOP value is then used in Equation 6.1 which describes the relation between the wing loading and the weight-to-power ratio [28]:

$$\frac{W}{P} \leq \frac{TOP}{\frac{W}{S}} C_{L_{T/O}} \sigma_{T/O} \tag{6.1}$$

In Equation 6.1, $C_{L_{T/O}}$ is equal to $\frac{C_{L_{max}}}{1.1^2}$ and $\sigma_{T/O}$ is equal to $\frac{\rho_{max}}{\rho_0}$, where ρ_0 is the air density at sea level and ρ_{max} is the air density at the maximal altitude of the hub. In subsection 11.1.6, the maximal hub altitude was defined as $5000\,\text{ft}$ which results in a value of 0.8617 for $\sigma_{T/O}$.

Conventional landing

The maximum wing loading of CS23 aircraft for conventional landing is defined in Equation 6.2 [28]:

$$\frac{W}{S} \leq \frac{\frac{s_{land}}{0.5915}}{2f} C_{L_{max}} \rho_{max} \tag{6.2}$$

In Equation 6.2, f is the ratio between take-off and landing weight, which is 1 for a fully electric aircraft. The landing distance s_{land} is defined as $1130.43\,\text{m}$ similar to $s_{T/O}$ because for landing, one also has to implement a factor of 1.15 with respect to the runway length. A result of the conventional landing is a new stall speed based on the runway length [28], as presented in Equation 6.3:

$$V_{s_{land}} = \sqrt{\frac{s_{land}}{0.5915}} \tag{6.3}$$

This results in a $V_{s_{land}}$ of $43.72\,\text{m/s}$. The approach speed should be 1.3 times the stall speed [28].

Manoeuvring

Due to an error in Equation 7.13 in the Midterm Report [5], the equation accounting for manoeuvring was implemented incorrectly. A correct expression for wing and power loading obtained from the ADSEE-I course is noted below [28]:

$$\frac{W}{P} \leq \eta_{prop} \left(\frac{\rho}{\rho_0}\right)^{3/4} \left(\frac{C_{D_0} \frac{1}{2} \rho V_c^3}{\frac{W}{S}} + \frac{n_{max}^2 \frac{W}{S}}{\pi A e \frac{1}{2} \rho V_c}\right)^{-1} \tag{6.4}$$

Design point selection

The corrected wing loading diagram in Figure 6.2 can now be created. A design point is selected where the W/P and W/S are equal to $0.080\,\mathrm{N/W}$ and $1412.11\,\mathrm{N/m^2}$ respectively, shown with a red dot.

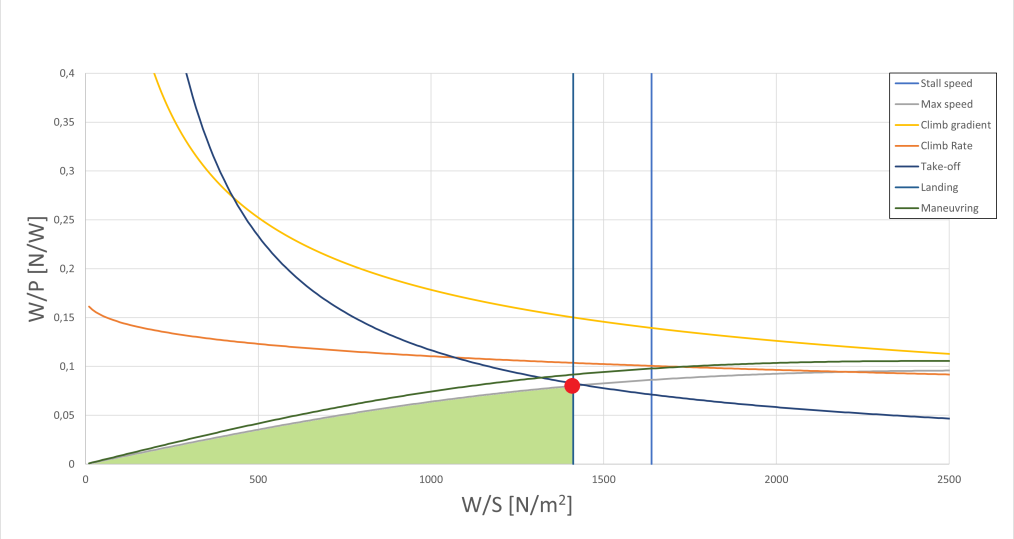

Figure 6.2: Wing loading diagram showing the design space and the selected design point

6.1.2. Energy Usage Correction

The energy usage of the drone throughout its previously determined flight phases climb, cruise and descent changes as a result of the new W/P value. However, due to the change in take-off and landing procedure, the energy usage changes as well.

During take-off, the aircraft accelerates from stationary to its take off speed $V_{T/O} = 1.1V_{s_{land}} = 48.09\,\mathrm{m/s}$ within the ground roll distance s_{GR}. It is assumed that the earlier defined $s_{T/O}$ of $1130.43\,\mathrm{m}$ is equal to a factor 1.66 times s_{GR} [28]. This results in a s_{GR} of $680.98\,\mathrm{m}$. To achieve this, the aircraft must have an acceleration of $1.697\,\mathrm{m/s^2}$ within a time of $28.32\,\mathrm{s}$. Combining the ground roll time with the P/W value during take-off of $9.66\,\mathrm{W/N}$, an E/W value of $273.71\,\mathrm{J/N}$ is obtained. This means that take-off accounts for $0.56\,\%$ of the total energy usage.

It is assumed that the aircraft does not use energy during landing, as the aircraft does not make use of reverse thrust but friction braking. Considering the low total energy usage during take-off, it is safely assumed that energy for landing is even smaller and therefore an insignificant value.

Additionally, it was previously assumed that drones would only operate from hubs designed by eCarus. This meant that loitering was not taken into consideration as it was assumed that a drone would always be able to land on one of the hubs. Also, [REQ-US-SR-06]: *The system shall work in all weather conditions in which the target aircraft can operate* [4] meaning drones would not have to loiter due to bad weather at the hub, as it was designed to withstand this. However, as a result of the change in operating hub (ordinary airfields), loitering must also be taken into account. A loiter time of 10 minutes at an altitude of $1500\,\mathrm{ft}$ is taken for this, for which a P/W ratio of $5.53\,\mathrm{W/N}$ is required, resulting in an E/W value of $3198.5\,\mathrm{J/N}$. This accounts for $6.53\,\%$ of the total energy usage.

6.1.3. Weight Estimation Correction

Based on the new energy usage of the drone, a corrected mission profile can be created, as shown in Figure 6.3. The figure presents the energy usage of each flight phase together with the time and distance travelled by the drone during that phase. The total energy usage of the drone based on the new design point and the alteration of the flight phases is $49\,292.27\,\mathrm{J/N}$. The weight estimation procedure is the same as performed in the Midterm Report, apart from the energy density used for the battery weights. Instead of $500\,\mathrm{Wh/kg}$, a battery energy density of $600\,\mathrm{Wh/kg}$ is used, reducing

the mass of both batteries on board of the drone [3]. This in turn lowers the structural weight and the motor weight. Another factor that contributes to a lower weight is a change in the C_{D_0} and e parameters; As a result of more accurate estimation they changed from 0.03 to 0.012 and from 0.85 to 0.9, respectively. The total drone mass after correction adds up to 6511.83 kg, of which the division between subsystems is presented in Figure 6.4. This is a big decrease in mass compared to the original mass of $19\,897.7$ kg. The battery weight in particular decreased immensely, which is positive in terms of sustainability regarding minimisation of required materials for manufacturing such as rare earth metals.

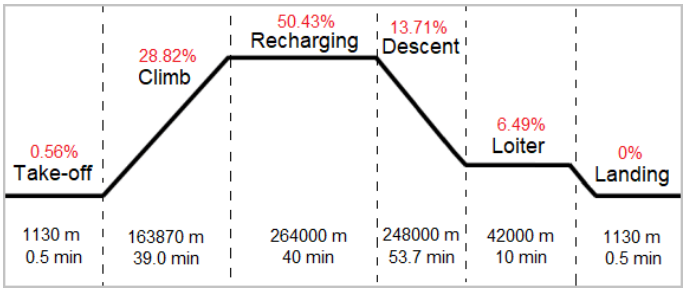

Figure 6.3: Mission profile showing the energy usage percentage, time and distance of each phase

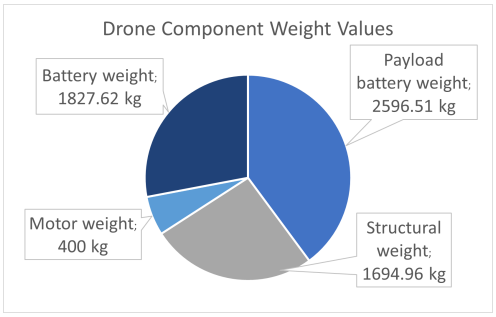

Figure 6.4: Pie chart showing drone component weights after the weight correction

6.2. Thrust Generation Type Trade-off

For the propulsion system, a trade-off is required for the type of thrust-generating device. Performing a trade-off enables the use of the most favourable design for the prescribed mission.

6.2.1. Selection

The following criteria that will have a significant influence on the design choice are defined:

- **Efficiency**: Designing a propulsion system that is as small as possible is desirable, as it decreases the weight and drag of the system itself. The efficiency criterion is therefore given a weight of 5, because it is of utmost importance for the consideration of the thrust generation type.
- **Noise**: Noise production of propulsion systems should be kept to a minimum as much as possible in order to minimise the impact of operating the aircraft on the environment. Due to this reason, it is an important criterion for this trade-off and it is given a weight of 2.
- **Cost**: To make the aircraft economically sustainable, the cost of certain design options should always be kept in mind. This particularly holds for the propulsion system as it is often one of the more expensive subsystems of an aircraft and is therefore defined as a criterion for this trade-off [source]. It is given a weight of 3.
- **Safety**: [REQ-SYS-LEG-02]:*The system shall adhere to safety regulations*, requires the propulsion system to be designed with safety in mind [4]. Therefore, a safety criterion is considered with a weight of 4.

6.2.2. Thrust Generation Type Trade-off

The result of the performed trade-off for the thrust generation type are presented in Table 6.2. It should be noted that the explanation of the score for the ducted fan are given with respect to the propeller as baseline. Hence, the '-' signs for the reasoning of the propeller scores.

Table 6.2: Trade-off Summary Thrust Generation Type

Criteria	Efficiency	Noise	Cost	Safety	
Weights	5	2	3	4	**Total Score**
Ducted Fan	Effective at low speeds, slightly less efficient at high speeds	Duct acts as noise suppressor	Tight tip clearance	Duct provides protection in case of blade separation	45
Propeller	-	-	-	-	39

Legend: Black = Unfeasible (1), Red = Bad (2), Yellow = Moderate (3), Blue = Good (4), Green = Great (5)

The scores awarded for each placement option are discussed and motivated for each viable option.

Efficiency

Adding a shroud which surrounds the blades of a conventional propeller increases the generated static thrust of such a propeller in comparison to one of equal diameter and power loading without shroud. The slipstream contraction of the propeller is reduced due to the presence of the shroud and as a result the mass flow through the propeller disk is increased. This in turn increases the generated static thrust. This large static thrust increase however declines swiftly with increasing flight velocity, since the slipstream contraction also diminishes as the flight velocity increases. When viscous effects are considered, shrouds tend to decrease the efficiency of ducted fans below that of conventional propellers at higher flight velocities [29]. Due to these phenomena, the ducted fan and propeller are both given a score of 3.

Noise

The presence of the duct of a ducted fan has the potential to reduce the noise generated by the propulsion unit, as the duct can effectively act as a suppressor of noise [30]. Compared to an open propeller, a ducted fan has stronger radiation directivity of noise and an overall reduction of noise of up to possibly 50% [31]. It is for these reasons that a ducted fan and propeller are given a score of 4 and 2 respectively for the noise criterion.

Cost

In terms of cost, ducted fans are less desirable than conventional propellers. This is due to the requirement of having tight clearances between the blade tips of the fan and the duct in order to improve the performance of such engines. These tight clearances induce difficult and most importantly costly manufacturing tasks [29]. Due to the aforementioned, ducted fans are given a score of 2 for the cost criterion, whereas propellers are given a score of 4.

Safety

For the safety criterion, ducted fans and propellers receive a score of 4 and 2, respectively. Since the duct of a ducted fan can serve as protection in case of a blade separation, it is deemed to be safer than a conventional propeller. In the event of such a blade separation, the duct can contain the (partly) fractured propeller blade and prevent additional damage to the airframe or ground personnel standing in close proximity to the aircraft [31].

6.2.3. Sensitivity Analysis

Table 6.2 shows that the ducted fan design scores higher than the conventional propeller design. However, before a confident conclusion can be made about the optimal thrust generation type, a sensitivity analysis must be performed. For this, the following ranges of criteria weights are used:

- **Efficiency**: Because efficiency is very important (hence the initial weight of 5), the range of weights is set from 4-5 as weights lower than 4 are considered too low.
- **Noise**: The range of weights is 2-3, because the initial weight of 2 is already relatively low. It is however not deemed more important than a score of 3.
- **Cost**: Cost is an important aspect and should be minimised, but other weights such as safety and efficiency are considered to be more driving. The range is therefore set to 2-4.
- **Safety**: Safety is of utmost importance and therefore a weight lower than 4 shall not be considered. The sensitivity analysis weight range is 4-5.

The sensitivity analysis concludes that the selected weight ranges don't influence the result of the trade-off, as the winner of the trade-off also scores highest for every weight combination.

6.2.4. Trade-off Conclusion

After performing the trade-off for the thrust generation type, it becomes evident for this design it is beneficial to utilise ducted fans. Table 6.2 clearly shows that with a final score of 45, ducted fans outscore conventional propellers with 6 points. It is for this reason that ducted fans are considered for the propulsion system of this design. The sensitivity analysis confirms this outcome.

6.3. Engine Placement Trade-off

Besides the type of thrust-generating device, the optimal placement and layout of this system is also an important aspect which requires a trade-off. Performing such a trade-off in an elaborate way enables

the use of the most favourable engine placement for the specific prescribed mission.

6.3.1. Selection Criteria and Weights

It is important to define criteria that will have a significant influence on the placement of the propulsion system. The following criteria are defined:

- **Efficiency**: Designing a propulsion system that is as small as possible is desirable, as it decreases the weight and drag of the system itself. The efficiency criterion is therefore given a weight of 5, because it is of utmost importance for the consideration of the thrust generation type.
- **Noise**: Noise production of propulsion systems should be kept to a minimum as much as possible in order to minimise the impact of operating the aircraft on the environment. For this trade-off, the is given a weight of 2 as it is important but doesn't outweigh the other criteria.
- **Cost**: To make the aircraft economically sustainable, the cost of certain design options should always be kept in mind. This particularly holds for the propulsion system as it is often one of the more expensive subsystems of an aircraft and is therefore defined as a criterion for this trade-off [source]. It is given a weight of 3.
- **Safety**: [REQ-SYS-LEG-02]: *The system shall adhere to safety regulations*, requires the propulsion system to be designed with safety in mind [4]. Therefore, a safety criterion is considered with a weight of 4.
- **Compatibility**: Optimal integration of the UAV and its propulsion system is important to minimise structural weight of the airframe. Improper placement may induce bending or torsional loads requiring increased wing and structure mass and thickness. Although this criterion is not deemed as important as the criteria safety and efficiency, it is given a weight of 3.

6.3.2. Engine Placement Trade-off

The result of the performed trade-off for the engine placement are presented in Table 6.3.

Table 6.3: Trade-off Summary Engine Placement

Criteria	**Efficiency**	**Noise**	**Cost**	**Safety**	**Compatibility**	
Weigths	5	2	3	4	3	**Total Score**
Front ducted fan	X	X	X	Risk of collission or entanglement with recharging cable	X	X
Aft ducted fan	Boundary layer ingestion has positive effect on aerodynamics	Low noise level due to boundary layer ingestion	Less engines resulting in less costs due to tight clearances in manufacturing	No aerodynamic influence due to casing	Easily embedded in aircraft fuselage	63
Front distributed ducted fan	X	X	X	Risk of collission or entanglement with recharging cable	X	X
Aft distributed ducted fan	Boundary layer ingestion has greater aerodynamic effect when distributed along wing	Combined sound of propellers induce higher noise	Manufacturing costs higher due to more engines as a result of tight clearance	Disturbed airflow in case of engine failure	Increased wingbox thickness due to torsion	49

Legend: Black = Unfeasible (1), Red = Bad (2), Yellow = Moderate (3), Blue = Good (4), Green = Great (5)

The scores awarded for each placement option are discussed and motivated for each viable option. Table 6.3 shows that both the distributed and non-distributed front ducted fan have received a score of 1 once. These design options fall below the threshold score of 2 and shall therefore not be considered further. An explanation for the score is only given at the criterion where they received a 1, as the other criterion scores are considered not relevant.

Efficiency

The efficiency of both distributed and non-distributed aft placed ducted fans is high due to boundary layer ingestion, where slower moving boundary layer air flow is ingested into the engines, resulting in engines having to work less hard which leads to an increased propulsive efficiency. However, for propulsion devices located at the back of a wing the highly distorted boundary layer airflow entering

the engine is a challenge, both aerodynamically and structurally. Specialised inlets and stronger fans are required to efficiently operate the engines [32, 33]. A big advantage of distributed propulsion is the postponement of flow separation and increased high-lift capabilities when it is designed to create a Coandă effect or if it is attached to flaps [34]. Logically, if engines are placed over the whole wingspan, the distributed placement has a greater effect on aerodynamic performance, thus scoring higher on efficiency. Non-distributed and distributed ducted fans are scored 3 and 4, respectively.

Noise

As mentioned before, a great advantage of ducted fans are the low noise levels emitted from the engine due to for example noise shielding of wing-body surfaces and boundary layer ingestion [33]. However, the combined sound of multiple propellers positioned close to each other may induce higher noise as a result of amplitude and phase modulations [35]. A minimal number of propellers is thus ideal in terms of noise and social sustainability, resulting in a score of 4 for non-distributed and a score of 3 for distributed engine layout.

Cost

Although there are few sources mentioning costs of distributed and non-distributed ducted fans, from common sense it can be reasoned that installing multiple smaller engines will cost more than a small number of bigger engines. As mentioned before, the tight clearances require difficult and expensive manufacturing, deteriorating economical sustainability. By having less engines, this time- and cost-consuming task is minimised. For this reason, distributed and non-distributed ducted fans are scored 3 and 4, respectively.

Safety

The forward placement of both types of ducted fans is omitted from the trade-off based on the safety criterion. During recharging, the UAV flies below and behind the ElectriFly aircraft, meaning that the recharging cable comes from the front. If the propellers would be located at the front of the UAV, this imposes an unacceptable risk of collision or entanglement in case of turbulence or other possible failures. [REQ-US-05]: *Under no condition shall a drone collide with an aircraft* and [REQ-US-SR-01]: *A drone shall dock an aircraft successfully 99.9% of all attempts* [4] cannot be assured to be met with the forward placement of the engines. Therefore, both are scored a 1. The aft ducted distributed fan is scored a 2. One of the main disadvantages of distributed propulsion is the safety in case of an engine failure. Malfunctioning engines induce disturbed airflow in the surrounding area, not only affecting the engines close to the failed engine but also the aerodynamic performance of wing and airframe surfaces [33]. Separate bigger ducted fans don't influence each other aerodynamically in case of an engine failure due to the casing surrounding them, resulting in a score of 4 for this placement option.

Compatibility

An advantage of distributed propulsion is the additional bending moment relief as a result of the more distributed weight on the wing. The placement of the engines however induces torsion on the wingbox, resulting in a higher required thickness [36]. Structurally this layout is therefore not ideal, considering the wing already has a bending moment relief due to the battery placement too. Additionally, more pylons are required if the engines are placed far aft of the wing, increasing the wing weight even further [34]. Therefore, the distributed option is scored a 2. A big ducted fan is easily embedded in the aircraft fuselage so that it can be placed at an ideal location, there are more possibilities of placement. They can be designed to take up as less spanwise space as possible, decreasing the loads on the wing [37]. Therefore, it is scored a 4 for compatibility.

6.3.3. Sensitivity Analysis

Table 6.3 shows that the aft-located ducted fan design scores higher than its distributed placed counterpart. However, before a confident conclusion can be made about the optimal engine placement, a sensitivity analysis must be performed. For this, the following ranges of criteria weights are used:

- **Efficiency**: Because efficiency is very important (hence the initial weight of 5), the range of weights is set from 4-5, as a weight lower than 4 is considered not high enough.
- **Noise**: The range of weights is 2-3, because the initial weight of 2 is already relatively low. It is however not deemed more important than a score of 3.

- **Cost**: Cost is an important aspect and should be minimised, but other weights such as safety and efficiency are considered to be more driving. The range is therefore set to 2-4.
- **Safety**: Safety is of utmost importance and therefore a weight lower than 4 shall not be considered. Therefore the sensitivity analysis weight range is 4-5.
- **Compatibility**: Compatibility with the UAV is considered to be very important, and therefore the range is set from 2-4. With this range, it is still about equally important as the cost criterion.

The sensitivity analysis concludes that the selected weight ranges don't influence the result of the trade-off, as the winner of the trade-off also scores highest for every weight combination.

6.3.4. Trade-off Conclusion

After performing the trade-off for the engine placement, it becomes evident for this design it is beneficial to locate the propulsion system at the back of the fuselage with a non-distributed engine design. Table 6.3 clearly shows that, with a final score of 63, aft-located non-distributed ducted fans outscore their distributed placed counterpart with 14 points. The sensitivity analysis confirms this outcome.

6.4. Propeller Design

For the design of the propeller, it is desired to adopt a method which produces a design which is as efficient as possible. An efficient propeller ensures that the size can be limited, which reduces the amount of material required for the production of the propeller itself. Moreover, a smaller propeller enables the use of a smaller duct as well. Most importantly, an efficient propeller reduces the required power of the engines, as there is less power loss through the entire propulsion system. Reducing the required power avoids the necessity of large engines and also decreases the total energy usage of the entire system, decreasing the battery size as a result. These aspects are important considerations in terms of sustainability and efficiency should thus be of prime importance during the design of the propeller. Therefore, a method, described by Traub in [38], is utilised which aims to design a minimum induced loss propeller. For this method, the thrust should be specified as input along with the propeller diameter, angular velocity, sectional lift coefficient distribution along the propeller blade and flight speed. For the latter, it is generally chosen to design the propeller for cruise condition. As such, the flight speed will be set to the required cruise velocity of the aircraft [38].

6.4.1. Propeller Characteristics

Because there are many free design variables in the method described by Traub, values for certain parameters are assumed. For cruise, an engine revolutions per minute (RPM) setting of 2000 is chosen, which is $87\,\%$ of its maximum of $2300\,\text{RPM}$. For the propeller diameter, it is decided to base this on reference aircraft. Unfortunately, very few aircraft exist that use a ducted fan propulsion system. However, as explained in subsection 6.2.2, the efficiency of ducted fans at higher flight velocities is similar and sometimes even lower than normal propellers. Therefore, it is assumed that the diameter of the propeller shall be of similar size to conventional propellers. 20 reference aircraft are selected based on similar maximum take off weight (MTOW), amount of engines and peak power output. For these aircraft, the correlation between propeller diameter and parameters such as maximum power, maximum cruise thrust (based on cruise velocity and maximum power), thrust per blade, number of blades and engine RPM is analysed. Only for peak power and engine RPM a convincing correlation is found, as shown in Figure 6.5.

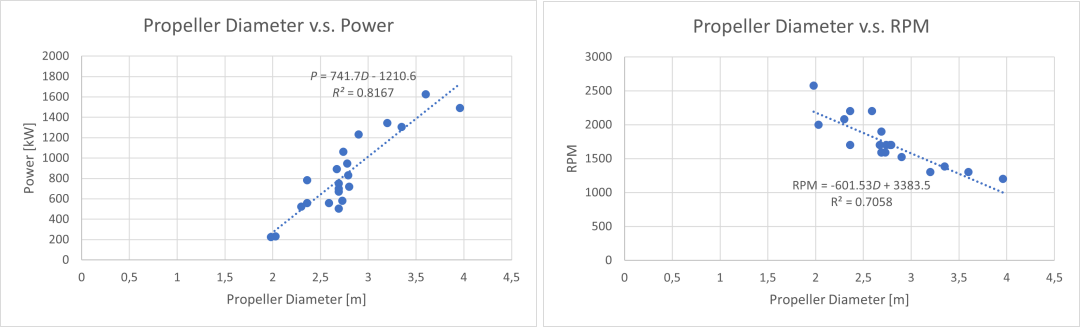

(a) Plot showing the propeller diameter and the maximum power

(b) Plot showing the propeller diameter and the RPM

Figure 6.5: Propeller diameter plotted against the RPM and maximum power output of 20 reference aircraft

Furthermore, an analysis is performed on the tip speed V_{tip} of the propeller aircraft. V_{tip} is related to RPM and the propeller diameter D as presented in Equation 6.5.

$$V_{tip} = \frac{\text{RPM}}{60}\pi D \tag{6.5}$$

Combining V_{tip} and V_∞ with the speed of sound a, the tip mach number M_{tip} is found using Equation 6.6.

$$M_{tip} = \frac{\sqrt{V_\infty^2 + V_{tip}^2}}{a} \tag{6.6}$$

This analysis is performed for every aircraft at sea level and at the cruising altitude of every aircraft, . The average M_{tip} on cruising altitude is calculated to be 0.857 with a standard deviation of 0.037 whereas on ground an average M_{tip} of 0.817 is found with a standard deviation of 0.039. These standard deviations provide confidence in the reliability of the propeller diameter analysis based on tip Mach numbers. All four methods to calculate the propeller diameter are noted in Table 6.4.

Table 6.4: Four methods to calculate the ideal propeller diameter based on 20 reference aircraft

Source	Equation	D
P	$D = \frac{\text{RPM}-3383.5}{-601.53}$	2.495
RPM	$D = \frac{P+1210.6}{741.7}$	2.300
M_{ground}	$D = \frac{60}{\text{RPM}\pi}\sqrt{(M_{tip_{ground}}a_{ground})^2 - V_\infty^2}$	2.481
M_{cruise}	$D = \frac{60}{\text{RPM}\pi}\sqrt{(M_{tip_{cruise}}a_{cruise})^2 - V_\infty^2}$	2.469
Final value		2.450

For P, the Magni650's maximum power output of 640 kW is used, whereas V_∞ is equal to the cruise velocity of 110 m/s. A final diameter value of 2.45 m is chosen based on the four methods which present a relatively similar diameter value.

The desired thrust of the propulsion system follows from the decision to design for cruise conditions. The P/W ratio is 10.357 during cruise, resulting in a P_r of 662.32 kW when combined with the weight estimate of 6519.1 kg. Combined with the V_∞ of 110 m/s, a total required thrust of 6021.12 N is found. As there are two engines being used, each engine must be able to deliver 3011.56 N.

6.4.2. Propeller Noise Prediction

The prediction of noise generated by the propulsion system is important for social sustainability, because the drone should not be a source of noise disturbance. Ideally, the drone should not be noticeable for anyone located beneath the aircraft on cruising altitude. This also follows from requirement [REQ-SYS-FP-08]: *The noise generated shall not be more than 65 dB at places with people present* [4].

A prediction of propeller noise is given by Ruijgrok in "Elements of aviation acoustics" [39]. Equation 6.7 presents the maximum sound pressure level (SPL) based on the influence of a number of factors.

$$\text{SPL}_{max}(r) = 83.4 + 15.3 \log P_{br} - 20 \log D + 38.5 M_{tip} - 3(B-2) + 10 \log N - 20 \log d_{prop} \quad (6.7)$$

In Equation 6.7, P_{br} is engine shaft power in kW, B is the number of blades per propeller, N is the number of propellers and d_{prop} is the distance from the propeller in m. However, as noted in subsection 6.2.2 the ducted fan design reduces emitted sound by 50 %. A decrease of 50 % is equivalent to a decrease of 3 dB, which means that the SPL_{max} for ducted fans is equal to the value of Equation 6.7 minus three.

The value of SPL_{max} occurs at an emission angle of 105 ° as shown in Figure 6.6, where SPL_{max} is about 2 dB higher than its space average. The perceived noise level (PNL) is thus obtained by subtracting 2 dB from the SPL_{max}.

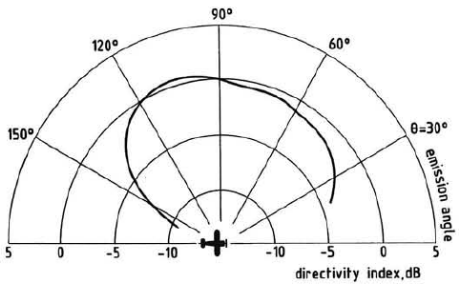

Figure 6.6: Directivity index of the SPL with the PNL at 0 dB [39]

To convert PNL to real sound, an A-weighting filter is often used as it works well for loudness comparisons at all frequency levels. The A-weighted sound level (L_A) is equal to the PNL value (described with symbol L_{PN}) except for a constant 12.5 dB as shown in Equation 6.8.

$$L_A = L_{PN} - 12.5 \quad (6.8)$$

The L_A value in dB which results from Equation 6.8 is representative of the noise received on ground, and is therefore used to check if [REQ-SYS-FP-08] has been met once the required inputs are available.

6.4.3. Minimum Induced Loss Procedure

With the propeller diameter, angular velocity and the desired thrust set, the procedure of minimum induced loss can be carried out. The procedure assumes that optimality of the design is acquired when the wake moves aft as a nondeforming helical surface, inferring that the wake displacement velocity (w_0) is constant [38]. With the wake displacement velocity known, the induced angle of attack is given by the relation presented in Equation 6.9 [38].

$$\alpha_i = \frac{cos(\alpha_\infty)}{\left(sin(\alpha_\infty) + \frac{2\omega r}{w_0 cos(\alpha_\infty)}\right)} \quad (6.9)$$

Where the free stream angle of attack (α_∞) is simply calculated with Equation 6.10.

$$\alpha_\infty = arctan\left(\frac{V_\infty}{\omega r}\right) \quad (6.10)$$

The relation for the induced angle of attack and free stream angle of attack can be used to compute the required chord and twist distribution with Equation 6.11 and Equation 6.12 respectively.

$$c_{prop} = F\frac{\pi}{2}\alpha_i \frac{16r}{Bc_l}[sin(\alpha_\infty) + \alpha_i cos(\alpha_\infty)] \quad (6.11)$$

$$\beta = \frac{c_l}{c_{l\alpha}} + \alpha_\infty + \alpha_i + \alpha_0 \quad (6.12)$$

In Equation 6.11, F represents the tip loss factor, ranging from 1 at the hub of the propeller to 0 at the tip of the blade. This factor accounts for the radial flow of air over the propeller blade due to the tip vertices [38]. According to Tomas Sinnige, an employee at the Power & Propulsion department at the Delft University of Technology and an expert in the field of propeller design, the choice of utilising a ducted fan for the engine configuration implies that the tip loss factor can be assumed to be 1 over the entire length of the blade. It is however still relevant to implement it into the calculations for later verification purposes. F is defined by the following relation [38]:

$$F = \frac{2}{\pi} arccos\left(e^{\frac{-B(1-r/R)}{2sin(\phi_{tip})}}\right) \tag{6.13}$$

Where the inflow angle at the tip (ϕ_{tip}) is defined by Equation 6.14.

$$\phi_{tip} = arctan\left(\frac{J}{\pi}[1 + \frac{w_0}{4}]\right) \tag{6.14}$$

The advance ratio J, presented in Equation 6.15, is a propeller and flight condition specific constant.

$$J = \frac{V_\infty}{nD} \tag{6.15}$$

It is important to note that in Equation 6.11 and Equation 6.12 it is assumed that the sectional lift coefficient distribution along the radius of the propeller is known. This is typically set to the lift coefficient at which the maximum lift-over-drag occurs, as this leads to the most efficient propeller design [38]. Furthermore, the slope of the aerofoil lift curve (c_{l_α}) and the zero lift angle of attack (α_0) are all parameters that are aerofoil dependent and will be presented in subsection 6.4.4.

The calculated chord and twist distributions, given by Equation 6.11 and Equation 6.12, can be used together with the induced angle of attack, free stream angle of attack, lift-over-drag ratio and sectional lift coefficient to compute the generated thrust and torque at each aerofoil section along the radius of the propeller blade. This can then be integrated along the radius of the propeller to acquire the total thrust and torque generated by the propeller, as presented in Equation 6.16 and Equation 6.17 [38].

$$T = \frac{B\rho\omega^2}{2}\int_r^R r^2 c_{prop}\frac{cos^2(\alpha_i)}{cos^2(\alpha_\infty)}c_l\left(cos(\alpha_i+\alpha_\infty) - \frac{c_d}{c_l}sin(\alpha_i+\alpha_\infty)\right)dr \tag{6.16}$$

$$Q = \frac{B\rho\omega^2}{2}\int_r^R r^3 c_{prop}\frac{cos^2(\alpha_i)}{cos^2(\alpha_\infty)}c_l\left(sin(\alpha_i+\alpha_\infty) + \frac{c_d}{c_l}cos(\alpha_i+\alpha_\infty)\right)dr \tag{6.17}$$

The procedure for the propeller design can now be initiated by assuming a value for the wake displacement velocity (w_0) between zero and the free stream velocity ($0 \leq w_0 \leq V_\infty$), where convergence of the design is robust [38]. Hereafter, the induced and free stream angles of attack can be computed. These in turn can be used to determine the chord and twist distributions. For these distributions, the initial sectional lift coefficients are assumed to be constant and set to the lift coefficient for the maximum lift-over-drag ratio. The thrust and torque can then be computed, where after it should be compared to the desired thrust for the propeller. The wake displacement velocity should be varied until the calculated thrust is equal to the desired thrust. For this value of w_0, the chord and twist distribution are calculated to serve as a basis for further iteration of the design.

The Reynolds number, defined by Equation 6.18, has a significant influence on the aerodynamic properties of aerofoils. The Reynolds number is dependent on the local chord length of the aerofoil and the incoming velocity that the aerofoil experiences, which in turn is dependent on the radial position along the propeller blade of the considered aerofoil.

$$Re = \frac{\rho V c}{\mu} = \frac{\rho\sqrt{V_\infty^2 + (\omega r)^2}c_{prop}}{\mu} \tag{6.18}$$

The maximum lift-over-drag ratio and lift coefficient where this occurs changes as a function of the Reynolds number. A circular loop can be identified where the Reynolds number depends on the chord

length of the aerofoil and its radial position, but the chord length depends on the sectional lift coefficient as can be seen in Equation 6.11. The optimal sectional lift coefficient is dependent again on the Reynolds number since the maximum lift-over-drag ratio changes significantly with the Reynolds number. A work around this loop can be achieved by iterating over the design. As previously mentioned, a constant lift coefficient distribution can be assumed initially [38]. Furthermore, the lift-over-drag ratio is initially assumed to scale linearly with Reynolds number. After having performed the procedure, the Reynolds numbers along the propeller blade can be calculated with the found chord distribution. These Reynolds numbers can then be used to calculate a new optimal sectional lift coefficient distribution and lift-over-drag ratio with the use of Equation 6.19, Equation 6.20 and Equation 6.21 [38]. The method to obtain the coefficients A, γ and k_p will be explained in subsection 6.4.5.

$$c_{d_{min}} = A\mathrm{Re}^{\gamma} \tag{6.19}$$

$$(c_l/c_d)_{max} = \frac{\sqrt{c_{d_{min}}/k_p + c_{l_{d_{min}}}^2}}{c_{d_{min}+k_p(\sqrt{c_{d_{min}}/k_p)+c_{l_{d_{min}}}^2}-c_{l_{d_{min}}})^2}} \tag{6.20}$$

$$c_{l_{(c_l/c_d)max}} = \sqrt{c_{d_{min}}/k_p + c_{l_{d_{min}}}^2} \tag{6.21}$$

These newly found optimal sectional lift coefficient and lift-over-drag ratio distributions can be used to calculate a new value for the generated thrust using Equation 6.16. By altering the wake displacement velocity w_0, the calculated thrust should once again be matched to the desired thrust. Thereafter, the chord and twist distributions can be recalculated and the entire iteration procedure can be restarted once more. This iteration is performed until convergence of the design is obtained. After the iteration, the required torque for turning the propeller can be calculated using Equation 6.17. The required power is computed through Equation 6.22.

$$P = Q\omega \tag{6.22}$$

The efficiency of the propeller, which is eventually the most important aspect of the propeller in terms of sustainability, can be calculated using Equation 6.23, Equation 6.24 and Equation 6.25. Maximising the efficiency leads to a decrease of the power loss throughout the propulsion system. This infers that eventually the primary battery size will be reduced by optimising the efficiency of the propeller. Reduction of the primary battery size means that less rare earth metals have to be used for the production of the aircraft, which is a desirable result in terms of sustainability. Equation 6.11, Equation 6.16 and Equation 6.17 show the dependence of the chord distribution, the generated thrust and the required torque on the number of propeller blades (B). In fact, the number of propeller blades directly influences the achievable efficiency of the propeller itself. For this design, the procedure is performed for a range of number of propeller blades. The number of blades is varied from 2 to 6 and for each configuration the theoretical efficiency is computed. These results are then compared and the most efficient configuration is chosen, provided that the given chord distribution is realistic and physically possible.

$$\eta_{prop} = J\frac{C_T}{C_P} \tag{6.23}$$

$$C_T = \frac{T}{\rho n^2 D^4} \tag{6.24}$$

$$C_P = \frac{P}{\rho n^3 D^5} \tag{6.25}$$

The described iterative procedure for a minimum induced loss propeller is programmed into Python. The results from running this programme with the chosen design inputs are presented in section 6.7. Furthermore, the verification and validation of the written code will be displayed in section 13.2.

6.4.4. Propeller Aerofoil Selection

For propeller aerofoil selection, 28 aerofoils are considered and analysed based mainly on their $c_l/c_{d_{max}}$ value, as this is the most relevant for a propeller aerofoil. As noted in subsection 6.4.3, this is because a maximised $c_l/c_{d_{max}}$ value leads to the most efficient propeller design. A list of often used aerofoils on propeller is constructed from the aerofoil database of *airfoiltools.com* [40]. Following this, the same website is used to collect aerofoil data such as t/c_{max}, maximum camber position and the $c_l/c_{d_{max}}$ and its respective α value at a Reynolds number of $1\,000\,000$. The results are noted in Table 6.5.

Table 6.5: Aerofoil selection

Aerofoil	t/c_{max} (%)	max camber (%)	$c_l/c_{d_{max}}$	α (deg)
Clark K	11,70	3,3	121,4	4,75
Clark V	11,60	3,4	129,4	3,75
Clark W	11,20	3,7	116,1	3,25
Clark X	11,70	3,3	122,4	4,75
Clark Y	11,70	3,4	114,8	3,75
MH112	16,20	6,7	147,7	3,75
MH113	14,62	6,4	153,0	3,75
MH114	13,02	6,4	161,0	3,50
MH115	11,10	5,5	158,7	4,25
MH116	9,84	4,1	150,8	4,50
MH117	9,80	2,7	120,1	4,25
MH120	11,57	2,2	124,3	5,25
MH121	8,80	3,0	139,1	3,00
MH122	9,30	3,4	161,2	3,75
E193	10,20	3,0	138,9	5,50
ARA	6,00	5,0	139,7	2,75
ARA	10,00	4,0	100,6	6,75
ARA	13,00	3,6	97,9	7,25
ARA	20,00	3,8	101,1	8,50
E850	8,00	1,8	105,8	2,50
E851	9,00	2,3	122,7	3,00
E852	10,10	2,8	132,1	3,75
E853	11,60	3,1	135,6	4,75
E854	13,40	3,3	136,3	6,00
E855	15,70	3,7	140,5	7,75
E856	18,20	4,2	128,9	8,50
E857	20,30	4,9	110,2	8,50
E858	22,70	4,7	88,1	8,75

The table clearly shows that the MH1xx aerofoils designed by Martin Hepperle score very well, with the MH114 and MH122 aerofoils in particular. The latter is often used for tip sections of propellers as a result of its very low t/c_{max} value, whereas the MH114 is often used for middle sections. However, to reduce design complexity it is decided to use a constant aerofoil distribution throughout the propeller blade. For this reason the MH122 aerofoil with a higher $c_l/c_{d_{max}}$ value is not selected because it is not thick enough for the inboard section of the propeller to carry the accompanied structural loads. The MH144 makes a good compromise as it has a very high $c_l/c_{d_{max}}$ value and a relatively high t/c_{max} value. For these reasons, it is decided to utilise this aerofoil for the propeller design.

6.4.5. Propeller Aerofoil Analysis

After selection, the aerofoil is analysed to find useful parameters for the propeller design. These include the A and γ values as noted in Equation 6.19 and the k_p value as noted in Equation 6.20.
Another article by Traub [41] which presents a simplified propeller analysis describes an approach on how to determine these values. First, the values for A and γ should be estimated using an aerofoil analysis software, for which XFLR5 is chosen. For a range of Reynolds numbers as suggested in the

paper the minimal drag coefficients are determined and then plotted, as shown in Figure 6.7. A power curve is fitted to the data to obtain an estimate for A and γ, which are equal to 35.694 and -0.624, respectively. The R^2 value of 0.9531 indicates high accuracy of the trend line.

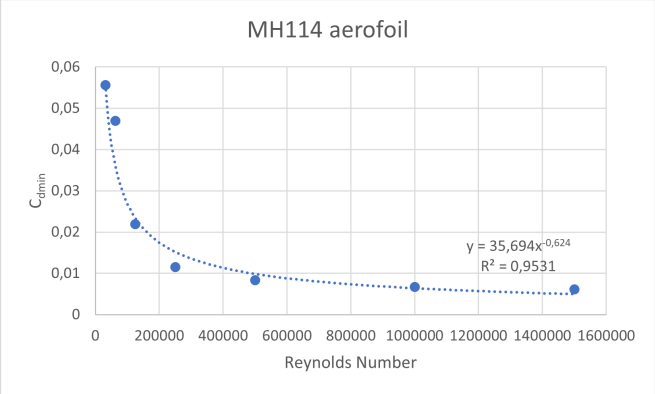

Figure 6.7: Reynolds numbers potted against their respective $c_{d_{min}}$ values to obtain estimates for A and γ

The article by Traub also describes two techniques to find the drag due to lift parameter k_p: Using a formula to calculate the k_p value and by plotting plotting c_d verse $(c_l - c_{l_{d_{min}}})^2$ and determining the slope of this line, which is equal to k_p. Both shall be performed to obtain a reliable estimate for this parameter. The formula to calculate the k_p value is described in Equation 6.26 and consists of the previously determined $c_{d_{min}}$, but also the lift coefficient corresponding to the minimum drag coefficient $c_{l_{d_{min}}}$ and the lift coefficient at the location of the maximum l/d ratio $c_{l_{(l/d)_{max}}}$ [41].

$$k_p = \frac{c_{d_{min}}}{c^2_{l_{(l/d)_{max}}} - c^2_{l_{d_{min}}}} \tag{6.26}$$

The estimation of k_p using the slope of the linearised drag polar is performed on the range of Reynolds numbers suggested by Traub, although a few unreliable results for low Reynolds numbers are omitted. The analysis is performed by determining the drag coefficient for the c_l values corresponding to the linear part of the $cl - \alpha$ curve, which ranges from about 0.4-1.6 for the MH114 aerofoil. A step size of 0.1 is taken for this analysis. The $(c_l - c_{l_{d_{min}}})^2$ values for every c_d are calculated and then plotted. The estimation of k_p for suggested Reynolds numbers by Traub is shown in Figure 6.8a. In the same paper it was also suggested to analyse the propeller at radial stations (r/R) of 0.2, 0.4, 0.6, 0.8 and 0.95. Based on an initial c_{prop} estimate of $0.2\,\text{m}$, a V of $279.15\,\text{m/s}$ and a ρ and μ value based on the cruising altitude of $15\,000\,\text{ft}$, the Reynolds numbers for these r/R can be calculated as shown in Figure 6.8b.

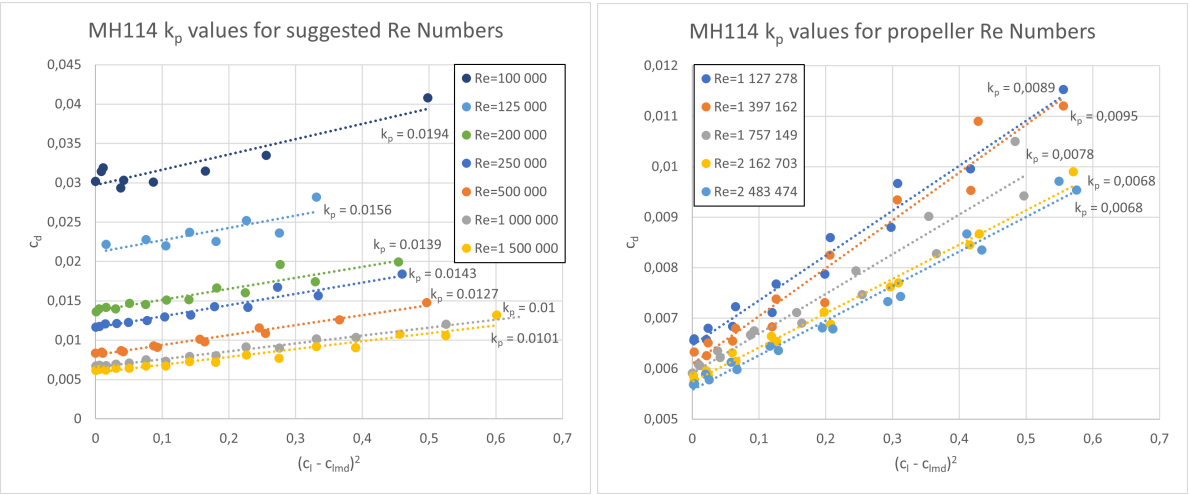

(a) Suggested Reynolds numbers by Traub

(b) Reynolds numbers corresponding to initial propeller estimate

Figure 6.8: Linearised drag polars showing the k_p value for various Reynolds numbers

Table 6.6 shows the calculated k_p values for both methods, the R^2 value corresponding to the trend lines of Figure 6.8 and the average value of the two methods. In Figure 6.9 the k_p values for both methods are plotted with a fifth order polynomial trend line as well as a trend line showing the average k_p values of both methods.

	Calculated	Estimated		Average
Re	k_p	k_p	R^2	k_p
100 000	0.0203	0.0194	0.8455	0.0198
125 000	0.0161	0.0156	0.6403	0.0158
200 000	0.0124	0.0139	0.8814	0.0131
250 000	0.0128	0.0143	0.9458	0.0135
500 000	0.0114	0.0127	0.9823	0.0121
1 000 000	0.0081	0.01	0.981	0.0091
1 500 000	0.0118	0.0101	0.9339	0.0109
1 127 278	0.0086	0.0089	0.9712	0.0088
1 397 162	0.0107	0.0095	0.9529	0.0101
1 757 149	0.0076	0.0078	0.9448	0.0077
2 162 703	0.0054	0.0068	0.9872	0.0061
2 483 474	0.0056	0.0068	0.9798	0.0062

Table 6.6: The calculated and estimated k_p values noted together with their average

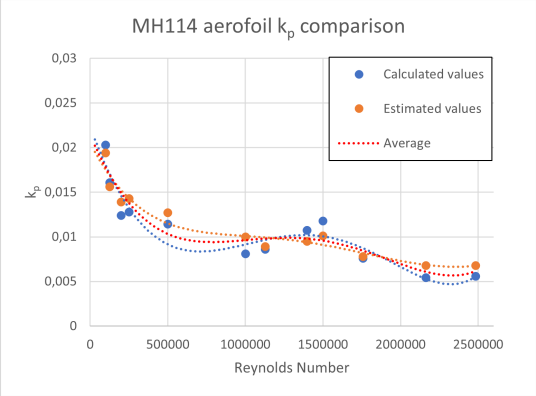

Figure 6.9: The calculated and estimated k_p values plotted against the Reynolds number

The difference in results between the two methods could be explained by the slight inaccuracies involved in both calculation methods. For the calculations based on Equation 6.26, inaccuracies may be induced as a result of $c_{l_{(l/d)_{max}}}$ as this value is often not found at one exact c_l, but at a slight range of c_l values. This is because the maximum l/d ratio is often not at exactly one combination of c_l and c_d values, but on multiple. The same holds for and $c_{l_{d_{min}}}$, where $c_{d_{min}}$ is sometimes the same at multiple c_l values. However, the procedure based on the linearised drag polar also induces inaccuracies as the drag polar is not perfectly parabolic, meaning that there is always a slight offset of values. This can also be seen from the R^2 values in Table 6.6. If the trend line fit would be nearly perfect, the R^2 values would have been higher and the k_p values would be more accurate.
Nevertheless, the trend lines for both k_p calculation methods show a visual resemblance in Figure 6.9, indicating that both procedures are converging to similar values for certain Reynolds numbers. To account for the inaccuracies of both methods, the k_p formula corresponding to the average trend line shall therefore be used for further calculations.

6.5. Duct Design

The duct consists of an aerofoil that is placed with the thick side towards the propeller blades, so that it it is placed ”inverted”. The reason for this is that the inlet area is bigger then the area at the location for the propeller so that the air gets slightly accelerated, which is beneficial at low speeds [42]. For the duct of the propeller, multiple variables have to be determined; the aerofoil of the duct, the longitudinal location of the propeller and the duct chord length.

S. Yilmaz et al performed an analysis on five different duct aerofoils and concluded that a composite aerofoil consisting of NACA7312 and NACA4312 aerofoils performs the best in terms of efficiency [43]. The paper also concludes that high negative camber in the forebody (the part in front of the propeller) affects efficiency positively. However, to reduce complexity, it is chosen not to have a composite aerofoil. The NACA7312 aerofoil is selected for the full duct chord due to its high camber and efficiency.

The longitudinal propeller placement within the duct should now be considered. According to Tomas Sinnige, it should be avoided to place the should rotor too close to the duct inlet to avoid highly non-uniform inflow to the rotor in case of non-axi-symmetric inflow conditions (such as a non-zero angle of attack). On the other hand, he noted that moving the rotor towards the outlet could lead to separation just behind the rotor plane, which should also be avoided. S. Yilmaz et al placed the propeller at the maximum camber position of $30\,\%$ of the aerofoil. Because this complies with the comments made by Tomas Sinnige, it is chosen to locate the propeller on this location.

For the duct chord length, Tomas Sinnige also mentioned that the ratio between duct chord length and propeller diameter is a compromise between duct and rotor performance but also between weight and wetted area (thus friction drag). Often used values for the D/c_{duct} ratio are 0.5 [43, 44]. All things considered, the same D/c_{duct} ratio of 0.5 is selected for the duct design.

The final duct dimensions are obtained based on the placement of the propeller, the chosen aerofoil and the D/c_{duct} ratio. The inner diameter of the duct is equal to the propeller diameter of 2.45 m. The outer diameter is calculated by adding twice the thickness of the duct chord at the longitudinal position of the propeller. The thickness of the chord is 12 % at this point, whereas the chord length is equal to $0.5D$. The duct diameter is then $D_{duct} = \frac{D}{1-0.12}$ = 2.78 m.

6.6. Material Selection

For the propeller blades, a composite material is used. This decision is made because of several considerations:

- Weight reduction: Composites provide the capability of creating thin and lightweight aerofoils for propellers that can can withstand the forces encountered during operation. A reduction of propeller blade weight also influences the engine: By having lighter blades, engine wear may be reduced and propeller efficiency can be increased [45]. This reduces the need for bigger batteries and thus decreases aircraft weight. This is beneficial in terms of sustainability because less rare earth metals and other scarce resources are required for producing the batteries.
- Noise reduction: In composite propeller blades, it is easy to incorporate a foam core which absorbs vibration and is accompanied noise [45]. This creates a more socially sustainable design.
- Longer service life: One of the main advantages of composite propeller blades is their service life, because repairs can be done a great number of times and very easily without affecting the aerofoil shape. Minor repairs could even be performed without sending the propeller to a specialised repair shop [45]. This helps reduce downtime and its associated costs and eliminates environmental impact of transport to a repair shop.

Even though producing composite propellers is more time-consuming and expensive than aluminium blades, the aforementioned advantages outweigh the disadvantages of composite propeller blades. An often used composite in propeller blades is carbon-graphite and Kevlar [46]. Because this is a proven material combination, it is decided to use this composite for the propeller of the UAV, along with a foam core. This also eases manufacturing, as layers of composite prepregs can be put on top of the foam and then cured without having to remove the mould afterwards.

For the material used for the duct, it is decided to use recycled Aluminium 6061-T6, the same material that is used for the skin of the drone. A thorough trade-off and justification on why this material is selected for the skin of the drone is explained in subsection 8.3.3. The duct is very similar to the skin of the drone, as its main function is not carrying structural loads, but providing an aerodynamic shape. Therefore, considering design cost, simplicity and sustainability, the most logical decision is to select the same material for this element.

6.7. Final Propulsion System Design

According to Tomas Sinnige, for propeller design one should consider the Reynolds number with respect to the blade section at $r/R = 0.7$. At this location, the rotation speed corresponding to a diameter of 2.45 m and RPM of 2000 is equal to $0.7V_{tip}$ = 179.59 m/s which results in a total blade speed of 210.60 m/s when considering flight at cruise velocity V_∞ = 110 m/s. Filling in this value in Equation 6.18 together with ρ and μ at $15\,000$ ft and an updated c_{prop} estimate of 0.1 m, a design Reynolds number of $977\,963.85$ is found.

This Reynolds number is used to find the k_p from the trend line of Figure 6.9. Using XFLR5 the c_{l_α}, $\alpha_{c_l=0}$, $c_{d_{min}}$ and $c_{l_{d_{min}}}$ for Re=$977\,963.85$ are found, of which the latter two are put into Equation 6.26 to obtain $c_{l_{(l/d)_{max}}}$. All useful parameters of the MH114 aerofoil for propeller design are noted in Table 6.7.

Table 6.7: MH114 aerofoil parameters for design Reynolds number of $977\,963.85$

Parameter	Value	Unit
A	35.6940	-
γ	-0.6240	-
k_p	0.0096	-
c_{l_α}	0.1073	1/deg
$\alpha_{c_l=0}$	-8.2524	deg
$c_{d_{min}}$	0.0067	-
$c_{l_{d_{min}}}$	0.8692	-
$c_{l_{(l/d)max}}$	1.2062	-

Table 6.8: Propeller design inputs

Parameter	Value	Unit
V_∞	110	m/s
RPM	2000	-
$T_{desired}$	3011.56	N
ρ	0.770 816	kg/m^3
D	2.45	m

The programme, explained in subsection 6.4.3, can be ran with the inputs presented in Table 6.7 and Table 6.8. The theoretical obtainable efficiency by varying the number of blades for the propeller is visualised in Figure 6.10. It is evident that increasing the number of blades reduces the efficiency of the propeller. Therefore, a propeller is chosen where 2 blades are used, which should theoretically be able to obtain an efficiency of 93.6%. This design choice leads to a chord and twist distribution for a single propeller blade as shown in Figure 6.11.

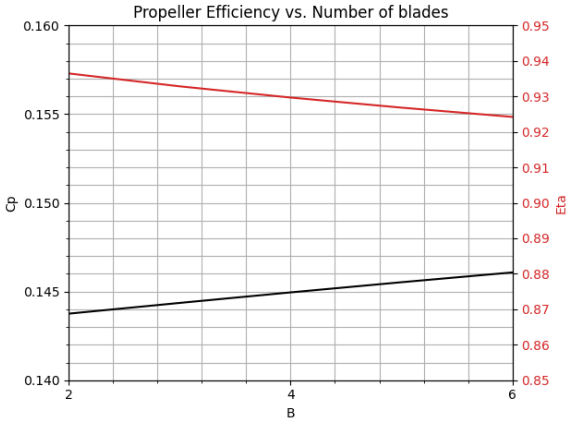

Figure 6.10: Propeller efficiency versus number of blades

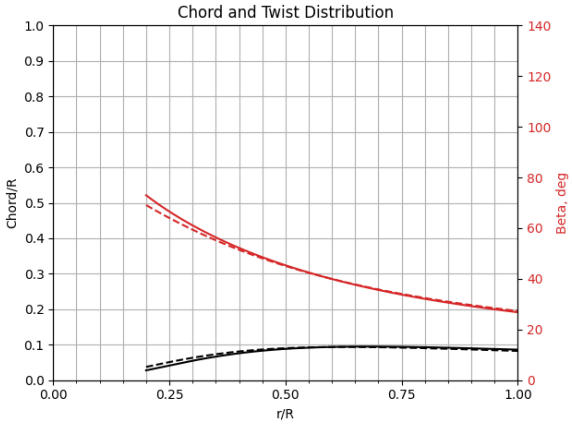

Figure 6.11: Propeller blade chord and twist distribution

Filling in every known parameter into Equation 6.7 and Equation 6.8 together with the 65 dB requirement for L_A from [REQ-SYS-FP-08] gives an r of 3055 m. This means that at an altitude higher than 3055 m, the noise requirement is met.

7 Detailed Design: Aerodynamics

Aerodynamics is an important aspect that has to be done extensively for the drone. Poorly designed aerodynamics of the drone would mean that the aircraft is ineffficient and is wasting resources. An unstable drone would also mean the mission cannot be fulfilled, or even a danger to it's environment.

In section 7.1, preliminary sizing and estimation of the drone configuration is done. Then, an analysis of the volume within the drone is done to check if the payload can be stored within the blended wing body. The tail is then sized in section 7.3. A computational fluid dynamic analysis of the drone is then done to obtain basic force coefficients. The other aerodynamic coefficients like stability derivatives are calculated in section 7.5. With the stability coefficients obtained, a stability analysis is done in section 7.6. Once stability is achieved, the controllability is design with the sizing of control surface and designing of a control system in section 7.7 and section 7.8.

7.1. Preliminary Concepts

At the start of the design, several mission parameters are considered. In this section, preliminary calculations will be executed to constrain the design variables of the aerodynamic shape using those mission and design parameters.

7.1.1. Assumptions

Before starting the design, it is important to define the assumptions of this chapter. In Table 7.1, an overview of all the assumptions can be found.

Table 7.1: Overview of assumptions within aerodynamic design chapter.

ID	Assumption
AS-AE-01	Aerodynamic centre is positioned at the quarter-chord point of the Mean Aerodynamic Chord (MAC)
AS-AE-02	Compressibility of the flow is not considered in the calculations.
AS-AE-03	The lift slope of the vertical's tail airfoil is approximated to 2π.
AS-AE-04	Control surfaces are seen as simple plain flaps in the design calculations.
AS-AE-05	The vertical stabiliser is assumed to have an elliptical wing lift distribution.
AS-AE-06	The control system is assumed to be capable of handling the highest type of workload for a human

7.1.2. Initial values

As the design process is an iterative process, the values of iteration zero were defined. Those originate from literature, preliminary computations or other departments. The values of those parameters can be found in Table 7.2. **ref PP chapter, sensitivity analysis of aspect ratio**

Table 7.2: Initial values for iteration 0

Parameter	Initial value	Origin
A	6	References [47, 48, 49]
$C_{L_{max}}$	1.4	Preliminiary computation Lifting Line Theory
MTOM	$6521.24\,\text{kg}$	PP chapter
V_{cruise}	$110\,\text{m/s}$	Electrifly
h	$4000\,\text{m}$	Electrifly
W/S	$1412.11\,\text{N/m}^2$	ref PP chapter

Several things need to be noted. First, the aspect ratio is an average of the values found in the papers mentioned in the table [47, 48, 49]. This is an educated guess and is submitted to a sensitivity analysis in section 13.5. Second, the values for the cruise speed and the altitude are taken from the mission profile of Electrifly

7.1.3. Preliminary Calculations

In this subsection preliminary calculations will be performed to find design parameters such as surface area and span.

Surface area

The surface area is portrayed with the symbol S and is a basic assessment of the wing surface required to achieve sufficient lift. The surface area can be found using **??**, with the wing loading (W/S) and the Maximum Takeoff Mass (MTOM).

$$S = \frac{\text{MTOM} \cdot g}{W/S} \tag{7.1}$$

Lift coefficient at cruise

The required lift coefficient at cruise will determine the wing characteristics such as the cruise angle of attack. This can be found using Equation 7.2.

$$C_{L_{cruise}} = \frac{W/S}{0.5 \cdot \rho \cdot V_{cruise}^2 \cdot S} \tag{7.2}$$

where ρ is the air density at cruise altitude and V_{cruise} is the cruise speed.

Stall speed

The stall speed of the aircraft is calculated with the estimated maximum lift coefficients ($C_{L_{max}}$). This coefficient value was estimated through lifting line theory computations of a preliminary planform of an MH91 airfoil [4]. The limitations and details of this computational tool are explained in more detail in section 7.4. The relation to finding the stall speed can be seen in Equation 7.3.

$$V_{stall} = \sqrt{\frac{W/S}{C_{L_{max}} \cdot 0.5 \cdot \rho \cdot S}} \tag{7.3}$$

Span

The span of the aircraft is determined through its aspect ratio and its required surface. Equation 7.4 shows the importance of the sensitivity analysis of the aspect ratio as it directly influences the planform of the aircraft.

$$b = \sqrt{S \cdot A} \tag{7.4}$$

7.2. Volume Analysis

The payload and batteries have to be stored within the wing and body section. Thus, an analysis of the volume within the drone has to be done. It was decided that the payload and batteries shall be stored only within 15-55% of the chord, Figure 7.1 shows the available space where blue represents the region where storage of the battery and payload is possible.

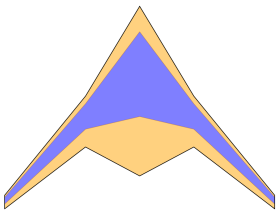

Figure 7.1: Available space for storage of payload

The total volume that needs to be stored consists of the payload batteries, propulsion batteries, and other components of the payload such as computers, thermal management etc. The volume of the other components was assumed to be 0.25 of the total battery volume. Thus, the total required volume to be stored in the wing-body section was found.

Now that the required volume is found, the available volume needs to be defined. The volume within the drone can be calculated with Equation 7.5. A represents the available surface area for the airfoil with a chord of $1m$. A constraint was set where the available volume within the drone has to be equal to the volume required to maximise volumetric efficiency.

$$V = \int_0^{b/2} 2A \cdot c(y)^2 dy \tag{7.5}$$

The main parameters that affect the volume within the drone are the taper ratio and y-position of the transition between the sections. The taper ratio of the wing section is assumed to be constant to maximise aerodynamic efficiency so only the y-position of the transition and the taper ratio of the body is the main variables to manipulate volume.

To get a full configuration of the drone, a second constraint has to be set. The total surface area of the drone has to be equal to the surface area from subsection 7.1.3. Thus, with these constraints, the taper ratio of both sections, the root chord, and the tip chord can be found for a given y-position of the transition. A more in-depth explanation of the equations and the calculations done can be found in [5]

7.3. Stabiliser Sizing

A blended wing body tends to be unstable, therefore, the sizing of the vertical and horizontal stabiliser is investigated in this section. As was discussed in [4], the choice of adding a tail is not considered for the time being. It is believed that the planform possesses a sufficient moment arm in order to avoid adding a drag-increasing tail. If during the investigation it is found that the planform does not possess a sufficient moment arm, the implementation of a tail will be discussed.

7.3.1. Horizontal Stabiliser

As aerodynamic efficiency is seen as a top priority, it was decided to minimise the surface area of the aircraft. Therefore, it is believed that using a dedicated surface in order to stabilise the aircraft is unnecessary. The wing is from this point on designed in order to fulfil the stability requirements. There are other ways to stabilise the aircraft in the longitudinal plane.

7.3.2. Vertical Stabiliser

The design of the vertical stabiliser is driven by two requirements. The first requirement states that the system shall be stable and controllable when one engine fails and the second one states that the system shall be dynamically stable in all conditions. During the first design iteration, two options were considered. The options are a wingtip configuration or a twin vertical stabiliser on the inner part of the body. These options are shown as optimal by G. Larkin and G. Coates [50].

The sizing of the vertical stabiliser has the following structure, first, the moment created by the asymmetric engine thrust is calculated, second the required surface for both the wingtip and the twin-tailplane configuration is found and finally, the arrangement with the minimal surface is chosen. Afterwards the induced dynamic stability coefficient from **??** are analysed. It is important to note that during the design process, the lift slope of the vertical stabiliser was found using Roskam's method [51, p.3], the taper ratio was computed in order to approach an elliptical wing lift distribution

Wing tip

As the wingtip of the aircraft already has a set chord length, the aspect ratio of the stabiliser is the only variable influencing the surface area of the stabiliser. The surface area and consequently the planform of the vertical stabiliser can be found using Equation 7.6.

$$S_{v_{wt}} = \frac{T_{engine} \cdot d_{engine}}{2 \cdot (C_{L_{\beta_v}} \cdot \beta + C_{L_{rudder}}) \cdot 0.5\rho V^2 \cdot l_v} \tag{7.6}$$

Looking at the equation above, T_{engine} is the thrust of one engine, d_{engine}, is the distance of one engine to the centerline of the aircraft, $C_{L_{\beta_v}}$ is the lift slope of the vertical tail, β is the sideslip, $C_{L_{\beta_v}}$ is the increase in lift coefficient caused by the rudder and l_v is the distance between the centre of pressure and the centre of gravity. More information about the change in lift coefficient can be seen in section 7.7.

Twin tail on the body

The second option is a twin vertical tail on the body. Assuming that the end of the root chord of the vertical stabiliser coincides with the end of the body section, the moment arm l_v is limited by the size of the tail. Furthermore, the spacing dy_v between the two vertical stabilisers is determined by the maximum amount of sideslip β_{max}. This relation can be seen in Equation 7.7 and makes sure the wake of one vertical tail does not interfere with another. Finally the roots of Equation 7.8 give the required surface area.

$$dy_v = \tan(\beta_{max}) \cdot c_{r_v} \tag{7.7}$$

$$0 = T_{engine} \cdot d_{engine} - 2 \cdot (C_{L_{\beta_v}} \beta + \delta C_{L_{rudder}}) \cdot 0.5 \rho V^2 S_v \cdot l_v(S_v) \tag{7.8}$$

As the moment arm is depending on the tail size S_v, finding the root of Equation 7.8 is not as straightforward as for a wingtip configuration. The moment of the vertical stabiliser is quadratically dependent on the surface area and creates a parabolic curve. This means that for a given input, the function could have no solution, one solution or two solution. Looking at how the code is constructed, the newton-raphson method will not be able to converge around a root if there is no solution. For this reason it will return that the method does not converge. An example of such a curve is shown in Figure 7.2.

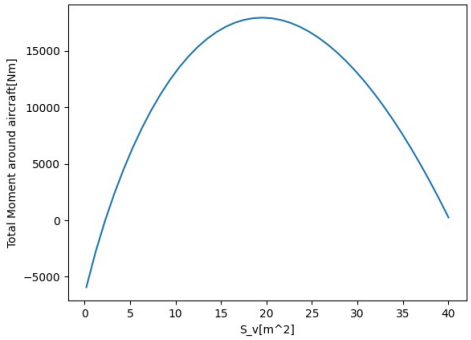

Figure 7.2: Total moment around the centre of gravity of the aircraft

Final configuration

The results of the first iteration show that a wingtip with a high aspect ratio would be necessary to fulfil the asymmetric thrust requirement. However, it is believed that this configuration is structurally unfeasible. Therefore, a combination of wingtip stabilisers and a singular vertical stabiliser on the body was chosen. The aspect ratio of the wingtip stabiliser is set to 2 for structural reasons and the aspect ratio of the body stabiliser is set to 3 to increase the moment arm.

The previous calculations make sure the drone fulfils the asymmetric thrust requirements. This, however, does not mean the aircraft is stable and the values of the previous equations will be used as minimum surface values. Further investigation of the stability requirement is given in **??**.

7.4. Computational Fluid Dynamics

Due to the complex geometry and airfoil of the design, CFD analyses are used to determine the basic aerodynamic characteristics of the drone. The models used to perform the analysis, as well as the outputs and limitations will be discussed in this section. The results will also be discussed briefly.

7.4.1. XFOIL

For the analysis of the airfoils, the 2d CFD program xfoil was used. The program outputs the aerodynamic properties and the curves required for a 3d analysis. It combines an inviscid and a viscous analysis to provide an accurate prediction of the aerodynamics around the airfoil. The accuracy of xfoil was tested in [52] and thus, outputs from xfoil are trusted.

For the inviscid analysis, xfoil uses a vortex sheet on the surface of the airfoil, as well as a source sheet on the surface and the wake for non-penetration conditions. Then, it uses the Kutta condition to solve the strengths of each vortex. Then, using the vortex strengths, the lift and moments can be found.

For the viscous analysis, the compressible integral momentum and kinetic energy shape parameter equations were used. With the viscous analysis, viscous phenomena such as instability, separation, bubble losses etc. can be modelled and thus, stall characteristics and drag can be obtained.

7.4.2. VLM

Initially, the lifting line theory was used to model the 3d plane as the theory is easy to understand and verify, while also being easier to use. Due to the high sweep and low aspect ratio of the design, it was found that lifting line methods do not provide sufficient accuracy for the design. Figure 7.3 shows a comparison of the $C_L - \alpha$ curve for lifting line and vortex lattice methods.

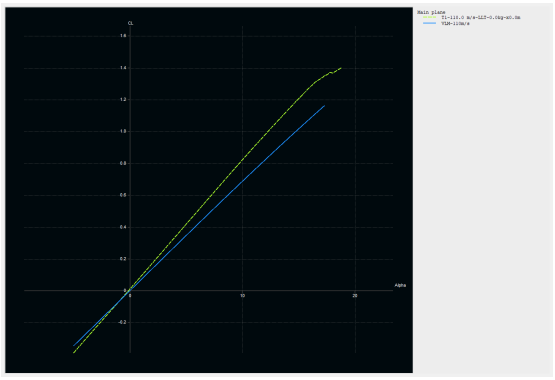

Figure 7.3: C_{L_α} curve results comparison of LLT with VLM

It can be seen that there is a huge difference between the results thus the horseshoe vortex lattice is implemented as it takes into account sweep. But vortex lattice is more complicated and is more difficult to use and thus required more effort to understand and use.
Xflr5 was used as the program for the VLM. It uses the methods from Katz and PLotkin[53] to perform the VLM analysis. The method uses a grid of horseshoe vortices with unknown strengths along the wing as shown in Figure 7.4b. Control points are also set up on the grid where non-penetration conditions are applied. The non-penetration condition, along with the Kutta condition allows the strength of the vortices to be solved. With the strengths of the vortices, the lifts and induced angles can thus be calculated. The program can thus output a reliable lift curve and so a C_{L_α} value.

Before performing the analysis, an appropriate mesh has to be determined. A mesh of 20 points was used for this analysis as shown in Figure 7.4a. A more detailed mesh with mesh points up to 30 points was tested but it gave the same results with a large increase in run time, thus a mesh size of 20 was the optimal number. The mesh is arranged in a cosine function where it is more detailed at the sides. The transition point between the body and wing section, wing tips and root chord are the most critical points as these parts are more prone to errors.
For $C_{L_{max}}$, which is a viscous effect, xflr5 interpolates the viscous results from xfoil at each section given the true angle of attack at each section. This model is not very accurate but is still much more accurate than lifting line. Thus, the $C_{L_{max}}$ from xflr5 is still used for the design. According to Ir. M.T.H. BrownTable 15.1, $C_{m_{ac}}$ predictions in xflr5 is unreliable for a blended wing due to boundary layer interactions. Thus, the $C_{m_{ac}}$ from xflr5 was not used for the design and other methods will be explained in later chapters. For drag, the induced drag output from xflr was used as it is calculated with inviscid methods of VLM. Profile drag however is unreliable due to it being a viscous parameter and results from xflr will not be used. Thus, other methods need to be used to predict the profile drag.

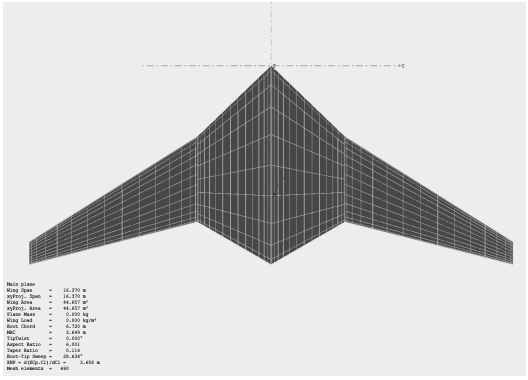

(a) Discretisaton of aircraft planform

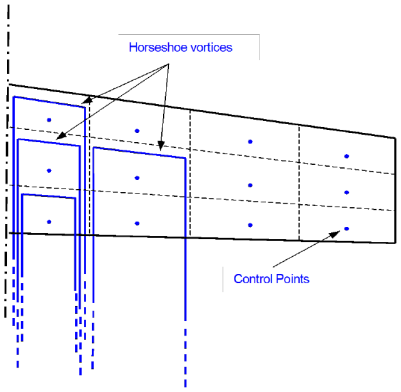

(b) VLM analysis layout

7.5. Aerodynamic Coefficients

To assess the flight characteristics of the aircraft, it is decided to compute the aerodynamic coefficients of the drone. During that process semi-empirical and Computational Fluid Dynamics (CFD) methods are used with adequate reasoning. The limitations of the latter are explained in section 7.4.

For force coefficients, CFD and semi-empirical methods were both used. For symmetric stability derivatives, methods from [54] were implemented while asymmetric were determined by seim-empirical methods in [51].

7.5.1. Main Forces and Moments

In this subsection, the method used to find the zero drag coefficients, the lift slope and the moment coefficient around the aerodynamic centre will be explored in more detail.

Lift slope and maximum lift coefficient

The lift slope is the change in the lift coefficient with the angle of attack. During previous iterations, a preliminary planform is constructed and an airfoil was selected. From this, an estimate of the parameters is computed using the vortex lattice method (VLM). More information about this method is given in subsection 7.4.2.

Zero lift drag

As explained in section 7.4, only results from inviscid analyses are used as viscous analyses are unreliable. Thus, a different method has to be used for the zero-lift drag coefficient(C_{D_0}). The component drag build-up method from [55] was used to estimate the zero-lift drag coefficient.

$$C_{D_0} = \frac{1}{S_{ref}} \sum_c C_{f_c} \cdot FF_c \cdot IF_c \cdot S_{wet_c} + \sum C_{D_{misc}} \tag{7.9}$$

This method uses the skin friction coefficient(C_{f_c}) and the wetted surface(S_{wet_c}) of different components to estimate the friction drag of each component. It also takes into account the effects of shape in the form factor(FF_c) and the effects of interference between components in the interference factor(IF_c). It also takes into account the drag due to other components such as instruments and landing gear.

These values have to be determined for each component c. Three components have been identified for the drone: The wing section, body section, engine nacelle, and vertical tails.

Body and wing section:

Although the body section and wing section of the wing are separate components, the method of calculation is the same. The skin friction coefficient is calculated with Equation 7.10 for both the turbulent and laminar boundary layer contributions.

$$\text{Laminar: } C_f = \frac{1.328}{\sqrt{Re}} \qquad \text{Turbulent: } C_f = \frac{0.455}{(log_{10}(Re))^{2.58}(1 + 0.144M^2)^{0.65}} \tag{7.10}$$

The overall skin friction coefficient of the whole wing can then be calculated by the weighted sum based on how much of the chord is laminar or turbulent. Due to the skin being metal and thus not as smooth, it was found that the transition point would be at 0.3 of the chord. The total skin friction coefficient can thus be calculated with Equation 7.11

$$C_f = 0.3 \cdot C_{f_{lam}} + 0.7 \cdot C_{f_{turb}} \tag{7.11}$$

The form factor of both the wing and body sections was calculated with Equation 7.12. This factor takes into account the thickness of the airfoil and the sweep of the section.

$$FF = \left(1 + \frac{0.6}{(x/c)_m}\left(\frac{t}{c}\right)_{max} + 100\left(\frac{t}{c}\right)^4\right)(1.34M^{0.18}cos(\Lambda_m) \tag{7.12}$$

The interference factor was found using statistical data from literature[55]. Due to the lack of a fuselage, the wing section only interacts with the tail which can be assumed to be a modern blended winglet which has an interference factor of 1.01.

The wetted surface of the wing is given by Equation 7.13. The wetted surface accounts for the extra surface due to the shape of the airfoil by multiplying by 1.07.

$$S_{wet_{wb}} = 2 \cdot 1.07 \cdot S \tag{7.13}$$

Nacelle:
The skin friction coefficient of the nacelle can be calculated in the same way as the wing and body section with Equation 7.9. Due to the shape of the nacelle, the transition point is much earlier and is at 0.1 of the chord. The total skin friction can then be found with the weighted sum similar to Equation 7.11

The nacelle is modelled as a circular cylinder with a diameter and length. Thus, the wetted surface area of the nacelle can be calculated with Equation 7.14.

$$S_{wet_n} = \frac{2\pi d^2}{4} + \pi dl \tag{7.14}$$

Based on [55], the form factor can be found with Equation 7.15. f is the ratio between the length and diameter of the nacelle where $f = \frac{l}{d}$.

$$FF = 1 + \frac{0.35}{f} \tag{7.15}$$

Tail:
The coefficient of friction, wetted surface area, and form factor were calculated in the same way as the body and wing sections. But the interference factor has a different value.

Due to the decision to place the vertical tails on the wing tips as well as on the body, the two different tails have different interference factors. The interference factor for the wing tip tails is the same as the wing-body interference factor of a modern blended winglet interference factor of 0.01.

The vertical tail on the body is assumed to be similar to a conventional tail. A conventional tail has a horizontal stabiliser at the bottom, which in this design is replaced by the wing itself. The interference factor for a conventional tail is 1.05.

Moment coefficient in aerodynamic centre

Although the lift distribution can be reliably computed through lifting line theory or VLM, those methods are not considered sufficient for the moment around the aerodynamic chord. According to Ir. M.T.H. Brown

$$C_{m_{o_w}} = \frac{A\cos\Lambda_{c/4}{}^2}{A + 2\cos\Lambda_{c/4}} \cdot \frac{c_{m_{o_r}} + c_{m_{o_t}}}{2} + \frac{\Delta C_{m_o}}{\epsilon_t} \cdot \epsilon_t \tag{7.16}$$

where $c_{m_{o_r}}$ and $c_{m_{o_t}}$ are the root and tip chord zero lift moment respectively, $\Lambda_{c/4}$ is the quarter chord sweep, $\frac{\Delta C_{m_o}}{\epsilon_t}$ is the effect of linear twist on the moment and ϵ_t is the linear twist

It is important to note that the root and tip chord zero lift moment coefficients are calculated through Xfoil, which is explained in more detail in subsection 7.4.1. Furthermore, Roskam's method also explains in more detail the contribution of other elements of the aircraft such as the fuselage or horizontal tail. However, as the configuration of the aircraft is a BWB, the only contribution to the moment is considered to be the wing.

7.5.2. Angle of Attack (α) Derivatives

C_{X_α}

The angle of attack derivative for the horizontal and vertical forces can be found with Equation 7.17.

$$C_{X_\alpha} = -C_L \left(1 - \frac{2C_{L_\alpha}}{\pi A e}\right) \tag{7.17}$$

$$C_{Z_\alpha} = -C_{L_\alpha} - C_D \tag{7.18}$$

C_{m_α}

Due to the aircraft not having a tail, the wing is the only contribution to C_{m_α}. Thus, with an analysis of the forces, C_{m_α} can be found with **??**

$$C_{m_\alpha} = C_{L_\alpha} \cdot \frac{x_{a.c.} - x_{c.g.}}{\bar{c}} \tag{7.19}$$

7.5.3. Speed (u) Derivatives

The speed derivatives were derived based on a differentiation of the forces on an aircraft with respect to speed. Small angle assumptions were used when doing this and the results are shown in the equations below.

$$C_{X_u} = -2C_D + T_c(2 - k(1 - \frac{\partial C_D}{\partial T_c})) - \frac{\partial C_D}{\partial M} M \tag{7.20}$$

$$C_{Z_u} = -2C_L + T_c((-2 + k)(\alpha_0 + i_p) + k\frac{\partial C_L}{\partial T_c}) - \frac{\partial C_L}{\partial M} M \tag{7.21}$$

$$C_{m_u} = -k \cdot T_c \cdot \frac{\partial C_m}{\partial T_c} + \frac{\partial C_m}{\partial M} M \tag{7.22}$$

k accounts for the type of propulsion the aircraft uses. The propulsion used on the drone is electric propulsion, so k=3 for constant speed propeller aircraft. The compressibility corrections $\frac{\partial C_L}{\partial M}$, $\frac{\partial C_D}{\partial M}$ and $\frac{\partial C_m}{\partial M}$ were assumed to be 0 as compressibility effects are not prevalent in the low mach numbers the drone flies at. Due to the drone having 2 symmetric propellers that counter rotate, the effects of slip-stream from the propellers: $\frac{\partial C_L}{\partial T_c}$, $\frac{\partial C_D}{\partial T_c}$ and $\frac{\partial C_m}{\partial T_c}$ were also assumed to be zero. With these assumptions, the speed derivatives of C_X, C_Z and C_m are given by the equations shown below.

$$C_{X_u} = -3C_D \tag{7.23}$$

$$C_{Z_u} = -2C_L - C_D(\alpha_0 + i_p) \tag{7.24}$$

$$C_{m_u} = 0 \tag{7.25}$$

7.5.4. Pitch Rate (q) Derivatives

C_{X_q}

From cite, a plot of C_X against the pitch rate was done. It was found that C_X has no significant difference when pitch rate increases. Thus, C_{X_q} is neglected and is set to zero.

C_{Z_q}

C_{Z_q} however is non-negligible. A pitch rate induces an angle of attack increase of the wing, causing

an increase of lift ΔC_L. Under small angle assumptions, C_X is assumed equal to C_L. Thus, C_{Z_q} can be calculated with **??**

$$C_{Z_q} = C_{L_\alpha} \left(\frac{x_{c.g.} - x_{a.c}}{\bar{c}} \right) \tag{7.26}$$

$\boldsymbol{C_{m_q}}$
C_{m_q} can be calculated with the same concept as C_{Z_q}. But since m is a moment, the force C_{Z_q} has to be multiplied by the moment arm to obtain the change in moment with pitch rate. Thus, **??** was derived to estimate C_{m_q}.

$$C_{Z_q} = C_{L_\alpha} \left(\frac{x_{c.g.} - x_{a.c}}{\bar{c}} \right)^2 \tag{7.27}$$

7.5.5. Sideslip (β) Derivatives

Sideslip is the angle of the oncoming airspeed relative to the lateral plane of the aircraft. This phenomenon tends to occur often in flight and, therefore, must be carefully considered in aircraft design.

$\boldsymbol{C_{Y_\beta}}$
According to Roskam [51, p.383], the sideforce-due-to-sideslip can be estimated by dividing it into the contribution of the wing, fuselage and vertical tailplane. Because of the BWB configuration, the contribution of the fuselage is assumed to be zero. The sideforce coefficient is calculated by summing the contribution of the wing (Equation 7.28) and the vertical tailplane(Equation 7.29).

$$C_{Y_{\beta_w}} = -0.00573(\Gamma) \tag{7.28}$$

as shown in [51, p.383], where Γ is the dihedral of the wing in degrees.

$$C_{Y_{\beta_v}} = -k_v(C_{L_{\alpha_v}})(1 + \frac{d\sigma}{d\beta})\eta_v(\frac{S_v}{S}) \tag{7.29}$$

As shown in [51, p.386], where k_v is an empirical factor, $C_{L_{\alpha_v}}$ is the tailplane's lift slope, $(1 + \frac{d\sigma}{d\beta})\eta_v$ is a correction factor depending on tail dimensions and $\frac{S_v}{S}$ is the ratio of the tailplane's surface to the wing surface.

$\boldsymbol{C_{l_\beta}}$
Similarly to the sideforce coefficient, the rolling moment coefficient is divided into the contribution of the wing-fuselage group, the horizontal tail and the vertical tailplane. However, as there is no horizontal tail, this contribution is considered to be zero. As a result C_{l_β} can be expressed using Equation 7.30.

$$C_{l_\beta} = C_{l_{\beta_{wf}}} + C_{l_{\beta_v}} \tag{7.30}$$

$$C_{l_{\beta_{wf}}} = 57.3(C_{L_{wf}}((\frac{C_{l_\beta}}{C_L})_{\Lambda_{c/2}} + (\frac{C_{l_\beta}}{C_L})_A) + \Gamma\frac{C_{l_\beta}}{\Gamma} + \epsilon_t \tan\Lambda_{c/4}(\frac{\Delta C_{l_\beta}}{\epsilon_t \tan\Lambda_{c/4}})) \tag{7.31}$$

$$C_{l_{\beta_v}} = (C_{Y_{\beta_v}})\frac{z_v \cdot \cos\alpha - l_v \cdot \sin\alpha}{b} \tag{7.32}$$

Equation 7.30, Equation 7.31 and Equation 7.32 originate from Roskam's method [51, p.389, p392, p.397] where, $C_{L_{wf}}$ is the lift coefficient of the wing-fuselage combination, $(C_{l_\beta}/C_L)_{\Lambda_{c/2}}$ is the wing sweep contribution, $(C_{l_\beta}/C_L)_A$ is the aspect ratio contribution, C_{l_β}/Γ is the wing dihedral effect, $\Delta C_{l_\beta}/(\epsilon_t \tan\Lambda_{c/4})$ is a wing twist correction factor, z_v is the z-coordinate of the centre of pressure of the tail compared to the centerline opf the aircraft, α is the angle of attack, l_v is the moment arm of the tail and b is the span of the wing.

$\boldsymbol{C_{n_\beta}}$
According to Roskam, the main contributors to the static directional stability are the fuselage and the vertical tailplane. However, as the design does not posses a fuselage, only the vertical tailplane needs to be taken into account. Using empirical methods[51, p.398], the contribution of the tail can be estimated using Equation 7.33.

$$C_{n_\beta} = C_{n_{\beta_v}} = -(C_{Y_{\beta_v}})\frac{z_v \cdot \sin\alpha + l_v \cdot \cos\alpha}{b} \tag{7.33}$$

$C_{Y_{\dot{\beta}}}$
The final sideslip derivative is the sideforce-due-to-rate-of-sideslip. It is believed that this value can be neglected for high aspect ratio wings [54].

$$C_{Y_{\dot{\beta}}} = 0 \tag{7.34}$$

7.5.6. Roll rate (p) Derivative

C_{Y_p}
As the sideforce-due-to-roll-rate is primarily influenced by the vertical tail, Roskam's empirical method [51, p.417] can be used in order to estimate its value. As the dihedral is assumed to be really small, the contribution of the dihedral to the coefficient is omitted.

$$C_{Y_p} = 2 \cdot (C_{Y_{\beta_v}}) \frac{(z_v \cos\alpha - l_v \sin\alpha - z_v)}{b} \tag{7.35}$$

C_{l_p}
According to Roskam [51, p.417], the rolling-moment-due-to-roll-rate is influenced by the wing and the vertical stabiliser. Roskam's empirical methods were used once again to find an estimate of the coefficients.

$$C_{l_p} = C_{l_{p_v}} + C_{l_{p_w}} \tag{7.36}$$

$$C_{l_{p_v}} = \frac{2}{b^2} \cdot (C_{Y_{\beta_v}})(z_v \cos\alpha - l_v \sin\alpha)^2 \tag{7.37}$$

$$C_{l_{p_w}} = \frac{\beta C_{l_p}}{\kappa} \frac{\kappa}{\beta} + (\Delta C_{lp})_{\text{drag}} \tag{7.38}$$

Where $\beta C_{l_p}/\kappa$ is the roll damping parameter at zero lift, β is compressibility correction, κ is depending on the theoretical lift slope of the airfoil and $(\Delta C_{lp})_{\text{drag}}$ is the contribution of the drag.

C_{n_p}
The final roll rate derivative is the yawing-moment-due-to-roll. According to Roskam [51, p.421], the main contribution to the yawing-moment-due-to-roll is the wing and the vertical tail. The empirical method can be seen in Equation 7.40 and Equation 7.41.

$$C_{n_p} = C_{n_{p_v}} + C_{n_{p_w}} \tag{7.39}$$

$$C_{n_{p_v}} = \frac{-2}{b^2} \cdot (C_{Y_{\beta_v}})(l_v \cos\alpha + z_v \sin\alpha)(z_v \cos\alpha - l_v \sin\alpha - z_v) \tag{7.40}$$

$$C_{n_{p_w}} = \frac{C_{n_p}}{C_L} C_{L_w} + \frac{C_{n_p}}{\epsilon_t} \epsilon_t \tag{7.41}$$

In the equation above $C_{n_p}/C_L C_{L_w}$ is the lift contribution and can be estimated using the geometry of the wing and C_{n_p}/ϵ_t is the contribution of the twist.

7.5.7. Yaw rate (r) Derivative

C_{Y_r}
The sideforce-due-to-yaw-rate is mainly influenced by the vertical tailplane. As a result, an estimate can be found using Roskam's empirical method [51, p.428].

$$C_{Y_r} = -2 \cdot (C_{Y_{\beta_v}}) \frac{(z_v \sin\alpha + l_v \cos\alpha)}{b} \tag{7.42}$$

C_{l_r}
The rolling-moment-due-to-yaw-rate is influenced by the vertical tailplane and the wing. Roskam's method [51, p.428] is once again used to find an estimate of the coefficient.

$$C_{l_r} = C_{l_{r_v}} + C_{l_{r_w}} \tag{7.43}$$

$$C_{l_{r_v}} = \frac{-2}{b^2} \cdot (C_{Y_{\beta_v}})(l_v \cos\alpha + z_v \sin\alpha)(z_v \cos\alpha - l_v \sin\alpha) \tag{7.44}$$

$$C_{l_{r_w}} = \frac{C_{l_r}}{C_L} C_{L_w} + \frac{\Delta C_{l_r}}{\Gamma}\Gamma + \frac{\Delta C_{l_r}}{\epsilon_t}\epsilon_t + \frac{\Delta C_{l_r}}{(\alpha_{\delta_f}\delta_f)}(\alpha_{\delta_f}\delta_f) \tag{7.45}$$

In Equation 7.45 C_{l_r}/C_L is the contribution of the lift, $\Delta C_{l_r}/\Gamma$ is the effect of dihedral, $\Delta C_{l_r}/\epsilon_t$ is the effect of twist and $\Delta C_{l_r}/(\alpha_{\delta_f}\delta_f)$ is the contribution of symmetric flap deflection.

C_{n_r}
Finally, the yawing-moment-due-to-yaw-rate can be calculated as well using Roskam's method [51, p.432]. Similarly to the previous coefficient, the derivative is also depending on the wing and the vertical tailplane.

$$C_{n_r} = C_{n_{r_v}} + C_{n_{r_w}} \tag{7.46}$$

$$C_{n_{r_v}} = \frac{-2}{b^2} \cdot (C_{Y_{\beta_v}})(l_v \cos\alpha + z_v \sin\alpha)^2 \tag{7.47}$$

$$C_{n_{r_w}} = \frac{C_{n_r}}{{C_L}^2} C_{L_w}^2 + \frac{C_{n_r}}{C_{D_0}} C_{D_{0_w}} \tag{7.48}$$

In Equation 7.48 $C_{n_r}/{C_L}^2$ is the contribution of the lift and C_{n_r}/C_{D_0} is the effect of the zero lift drag.

7.5.8. Coefficients of Final Iteration
In this subsection, the results of the empirical method are given in Table 7.3 and Table 7.4 .

Table 7.3: Symmetric motion derivatives

Coefficient	Value
C_{X_u}	-0.06382
C_{X_α}	0.28922
C_{X_q}	0

Coefficient	Value
C_{Z_u}	-1.0017
C_{Z_α}	-3.9942
C_{Z_q}	-0.53328

Coefficient	Value
C_{m_u}	0
C_{m_α}	-0.53328
C_{m_q}	-0.07158

Table 7.4: Asymmetric motion derivatives

Coefficient	Value
C_{Y_β}	-0.32494
C_{Y_p}	0.0082564
C_{Y_r}	0.10005

Coefficient	Value
C_{l_β}	-0.061509
C_{l_p}	-0.32348
C_{l_r}	0.50876

Coefficient	Value
C_{n_β}	0.05002
C_{n_p}	-0.07764
C_{n_r}	-0.02245

7.6. Stability Analysis
An inherent flaw of a BWB is its subpar stability. To ensure the design is stable, an analysis was performed and added to the design iteration. In this section, the method used to check for stability will be demonstrated.

7.6.1. Static Stability
Static stability is of utmost importance towards the feasibility of the design. As a general requirement, it can be said that static stability is achieved when the centre of gravity is in front of the neutral point. This however can be simplified in the case of a blended wing body. As the aircraft does not possess any form of horizontal stabiliser outside of the wing, the position of the neutral point can be set equal to the position of the aerodynamic chord of the wing. A further requirement states that the moment coefficient at zero lift around the centre of gravity needs to be positive. As a result, it can be said that to achieve static stability the centre of gravity needs to be in front of the aerodynamic centre and that

C_{m_0} needs to be greater than zero.

Knowing this, it is important to understand how to manipulate the positioning of the centre of gravity compared to the aerodynamic centre. Using a python script **??**, different inputs were investigated and their effect on the position of the centre of gravity was assessed. The result of this sensitivity analysis can be seen in the figures below.

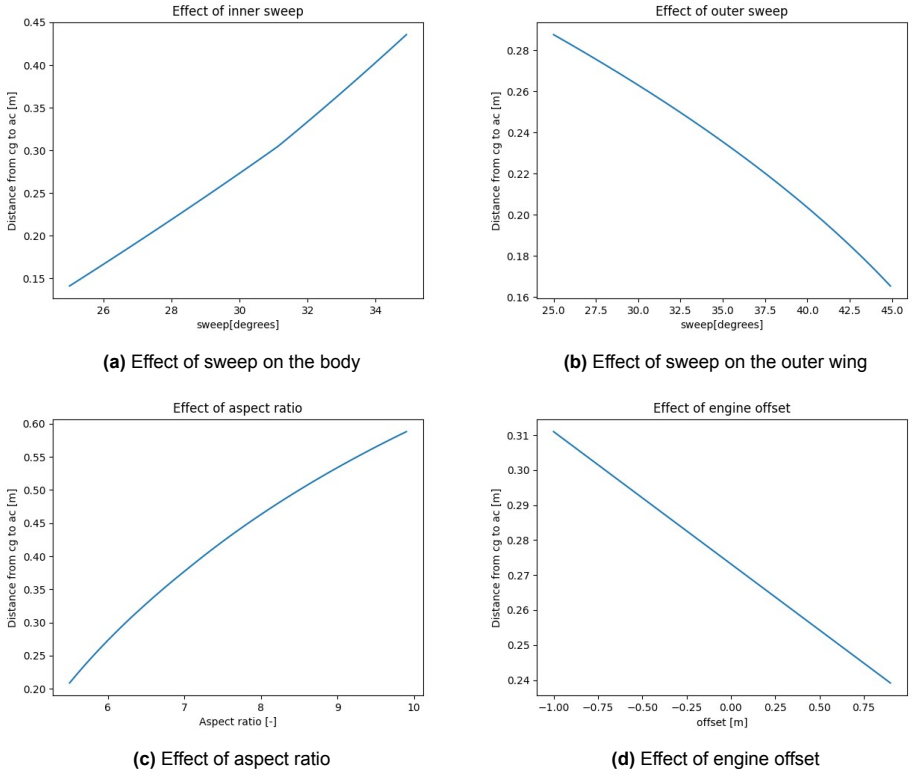

(a) Effect of sweep on the body

(b) Effect of sweep on the outer wing

(c) Effect of aspect ratio

(d) Effect of engine offset

Figure 7.5: Sensitivity analysis of static stability

In Figure 7.5a and Figure 7.5b it can be seen that an increase in the sweep angle of the body will stabilise the aircraft. On the other hand, an increase in the sweep angle of the outer wing destabilises the aircraft. Although an increase in engine offset does stabilise the aircraft, Figure 7.5 shows that its effect is minimal. Finally looking at the aspect ratio, it can be said that a high aspect ratio is preferable as it improves the stability.

7.6.2. Dynamic Stability

Next to the static stability, it is important to assess the dynamic stability of the aircraft. This gives an assessment of how the aircraft will react to disturbance input and what is required to keep the aircraft stable. A way to evaluate the dynamic stability is to analyse the eigenmotions of the aircraft. In this section the eigenvalue corresponding to each eigenmotion will be computed and compared to the stability goals.

Eigenvalue calculation

To analyse the eigenmotion of the aircraft the equations of motion of the drone has ti be defined. The linearised equations of motion of the drone from [54] for both symmetric and asymmetric motions. The equations of motion is in the form shown in Equation 7.49.

$$Ax + Bu = 0 \tag{7.49}$$

Where x is the states and u is the inputs. The behaviour of the drone without input needs to be analysed. To do this, the determinant of the matrix A needs to be 0. This results in a 4 degree polynomial with

variable Λ. Solving for lambda will give an insight on the behaviour of the aircraft in it's eigenmotions. The eigenmotions that will be analysed are the phugoid, short period, dutch roll and spiral motions
The eigenvalues by itself do not say much about the behaviour of the aircraft in its eigenmotions. Thus, the eigenvalues are converted into 2 parameters for analysis: the half time and damping ratio. The half time is the amount of time for that amplitude of the eigenmotion to halve, and the damping ratio gives an indication of how fast the eigenmotions will dampen out. The results of iteration 1 are shown in Table 7.5

Table 7.5: Iterations 1 stability results

Half time $T_{\frac{1}{2}}$	0.952	70.57	13.5	0.446
Damping ratio ζ	0.057	0.042	0.008	1

Stability goals
As the aircraft is planned to be fully controlled by computers, it can safely be assumed that the aircraft is capable of handling a high workload. This, however, has limitations and a good understanding of the computer capabilities is required. However, as proposed by Dr. S.J. Hulshoff **??** in a personal interview, it was decided to design the control system in such a way that it can handle the highest temporary workload for a human.

Looking at the "Military Specifications: Flying Qualities of Piloted Airplane" by the U.S. Military [56], a comprehensive goal for properties of eigenvalues can be set up for the eigenmotions. Assuming that the aircraft behaves like a medium-weight, low-manoeuvrability aircraft in nonterminal flight phases and can be compared to an aircraft causing an excessive but manageable workload for the pilot, the following stability goals can be set up.

Table 7.6: Dynamic stability goals

Eigenmotion	Requirement
Phugoid	$T_2 > 55s$
Short Period	$\zeta > 0.15$
Dutch Roll	$\zeta > 0, \omega > 0.4\frac{rad}{s}$
Spiral	$T_2 > 4s$

T_2 stands for the double amplitude time, ζ is the damping ratio of the eigenvalue and ω is the frequency.

7.7. Control Surfaces

In this section control surfaces are investigated.

7.7.1. Rudders

During the first iterations of the design, the sizing of the rudder is assumed to take a quarter of the chord of the vertical stabiliser. Next to that it is also assumed that the vertical stabiliser spans over the whole surface of the vertical stabiliser. These values can be changed in later iterations if needed. The increase in lift caused by a rudder deflection was computed by assuming it to be a plain flap and by using Roskam's method [51, p.259] to evaluate the change in lift coefficient. This method can be seen in Equation 7.50.

$$\Delta C_{L_{rudder}} = K_b(\Delta c_l)(C_{L_{\beta_v}}/c_{l_\beta})\frac{(\beta_\delta)_{C_L}}{(\beta_\delta)_{c_l}} \tag{7.50}$$

where K_b is the flap span factor, Δc_l is the airfoil lift increment and $C_{L_{\beta_v}}$ is the vertical tail lift curve, $c_{l_{\beta_v}}$ is the vertical tail airfoil lift curve and $\frac{(\beta_\delta)_{C_L}}{(\beta_\delta)_{c_l}}$ is the ratio of the three-dimensional flap-effectiveness parameter to the two-dimensional flap-effectiveness parameter.

7.7.2. Elevators

Before designing the elevators, the available space for the elevators needs to first be analysed. The engine placement will be discussed further in section 9.4 but in short, the engines were decided to be pusher engines, and thus have to be placed at the trailing edge part of the drone. Other than that, the engines are incorporated within the wing, which means that the entire area where the engines are placed cannot be used for elevators, along with a margin of 0.05 of the span. On the wing tips, a margin of 0.05 was also used to prevent interference with the wing tip vertical tails.

There is very little space for control surfaces in the body section due to the engines and the tail. Implementation of control surfaces would also be difficult as the body is more complex with the landing gear, payload, tail and engine all requiring extra space on the body section. Thus, it was decided that elevators will only be on the wing section.

To maximise controllability during flight, it was decided to use all available space on the wing section to as elevators. Thus, the elevators will be from the region where the engine ends + 0.05 span to 0.95 of the space($y_{max} + 0.05 \cdot b \leq y_{elevator} \leq 0.95b$). $y_{elevator}$ is non-dimensionalised to the parameter η and thus ($y_{max}/b + 0.05 \leq \eta \leq 0.95$)

Controllability during take-off and landing

Although the control surface is maximised, all of it it might not be required for controllability during take-off and landing. Thus, an analysis of the moments required in order to achieve controllability during the drone's most critical configurations(take-off and landing) needs to be done.

The most critical condition in which the aircraft has to remain controllable is when $C_L = C_{L_{max}}$. As the configuration chosen does not have a horizontal stabiliser, the moment coefficient can be calculated with Equation 7.51

$$C_m = 0 = C_{L_{max}} \left(\frac{x_{c.g.} - x_{a.c.}}{\bar{c}} \right) + C_{m_{ac}} + \Delta C_m \tag{7.51}$$

ΔC_m is the change in a moment due to the elevators and is the main parameter to size the elevators. Equation 7.51 is a constraint that needs to be satisfied in order for the aircraft to remain controllable, and thus provides the first constraint for the sizing of the elevators.

Control surface analysis

The main parameters to define the elevators are the deflection of the elevators (δ), the fraction of the span where the elevator starts and ends(η_i and η_o) and the proportion of the chord taken up by elevators(c_f/c). Thus, ΔC_m as a function of these parameters need to be found as shown in Equation 7.52

$$\Delta C_m \sim (\delta, c_f/c, \eta_i, \eta_o) \tag{7.52}$$

To find Equation 7.52, the methods of Roskam were used. From [57], it was stated that the elevators and other control surfaces can be modelled as a plain flap and calculated with methods from Roskam 6 [51]. Thus, the ΔC_m created from a plain flap can be calculated with Equation 7.53.

$$\Delta C_m = \Delta C_L \left(\frac{x_{c.g.} - x_{a.c.}}{\bar{c}} \right) + \Delta C_{L_{ref}} \cdot K_\Lambda \cdot (A/1.5) \cdot \tan \Lambda_{c/4} + K_p \cdot (\Delta C'_m / \Delta C_{L_{ref}}) \cdot \Delta C_{L_{ref}} \tag{7.53}$$

ΔC_L and $\Delta C_{L_{ref}}$ can be calculated in the same method as of Equation 7.50 where $\Delta C_{L_{ref}}$ is the ΔC_L for a reference wing with no sweep and aspect ratio of 6. The constants K_Λ and K_p are a function of η and takes into account the effect of sweep and the position of the elevators. $(\Delta C'_m / \Delta C_{L_{ref}}$ accounts for the extra moment of the aerofoil due to elevator deflection and is a function of the elevator chord c_f/c. These constants can be determined from [51].

Elevator configuration

The entire space of the wing section to be used for elevators would most likely be overdesigned to satisfy the constraint of Equation 7.51. Thus, a different configuration was provided for the control surfaces.

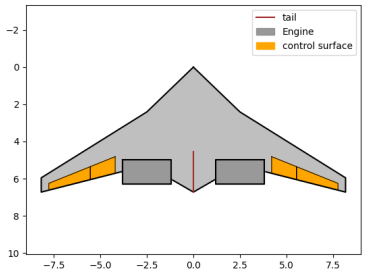

Figure 7.6: Control surfaces on the drone configuration

The control surfaces were split into 2 sections: one for control during take-off, and one that can also be used as high-lift devices during take-off and landing. This way, the controllability to provide more stability for the aircraft can be maximised, and the control surfaces can also be used efficiently during take-off and landing.

The point which separates the 2 sections have to be optimised such that $C_{L_{max}}$ is maximised while keeping the aircraft controllable. The maximum deflection of the elevator (δ) is chosen to be 30°. c_f/c is chosen to be 0.4 of the chord, leaving 5% of the chord between the spar and control surfaces for the mechanism.

$$\Delta C_m = \Delta C_{m_{HLD}}(\delta, c_f/c, \eta_e + 0.05, eta) + \Delta C_{m_{elev}}(-\delta, c_f/c, eta, 0.95) \tag{7.54}$$

Equation 7.54 implies a second constraint on the design of the elevators. It states that sum of the change in moment due to the high-lift devices and the change in moment due to elevators needs to equal the required change in moment ΔC_m from Equation 7.51. These equations cannot be solved analytically and thus a Newton-Raphson algorithm was used to solve for η.

Elevator size

The sizing of the elevator with the methods above can only be done when the planform and the integration of subsystems was done. Unlike the sections, the sizing of the control surfaces was only done in iteration 1 so the configuration and planform used were the ones from iteration 1. The results of the iteration will be discussed more in chapter 10 but the results from iteration 1 were the inputs for the control surface sizing.

Equation 7.54 was solved and η was found to be 0.677. A visual of the control surfaces is shown in Figure 7.6 where the control surfaces are in orange.

7.8. Control System

In Table 7.6.2, it was found that the drone, although stable, does not meet the requirements for stability. Thus, a control system needs to be implemented to stabilise the aircraft further. The main eigenmotions that need to be damped are the short period, phugoid and dutch roll.

7.8.1. Short Period Motion

The low C_{m_q} due to the lack of horizontal stabiliser means the dampening of the short-period eigenmotion is small. The short period is primarily characterised by a change in pitch and high pitch rates. Thus, a pitch damper is implemented in the flight control system to stabilise it.

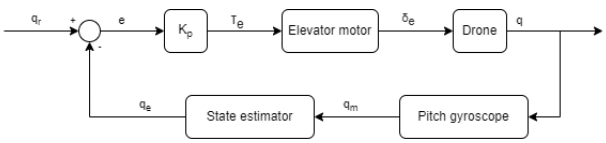

Figure 7.7: Pitch damper control loop

Figure 7.7 shows the control loop for the pitch damper. Firstly, the required pitch rate q_r is defined. The value for pitch rate is usually 0 as this will dampen out any eigenmotions and disturbance during steady flight. But when a change in pitch is required, and hence a non-zero pitch rate, a trajectory can be generated changing the pitch rate to a non-zero value and allowing for a smooth pitch change. The pitch rate at the end of the trajectory where the required pitch is reached, should be set back to 0 so the pitch damper can dampen out the oscillations. The error e is then multiplied by the controller gain K_p. This gain should be negative as a positive pitch rate (negative error) should cause a positive deflection of the elevator, resulting in a negative moment to reduce the pitch rate. The error multiplied by K_p is the required torque τ_e that is inputted into the elevator system, which deflects the elevator. The drone then experiences a new pitch rate which is measured by the gyro obtaining the measured pitch rate q_m. A state estimator can be implemented as the equations of motion of the drone as a function of the inputs are known, thus a model of the system can be created. The state estimator used is a Kalman filter, but the parameters of the Kalman filter are not yet determined as this requires testing of the drone. The estimated pitch rate is then subtracted from the required pitch rate and the control loop continues.

7.8.2. Pitch Control

To maintain pitch at a required value, a pitch controller is also implemented. A pitch controller also acts as a phugoid damper as the phugoid motion has large changes in pitch and low pitch rates which the pitch damper is ineffective. Thus, this controller provides increased resistance to disturbance on pitch, as well as damping for the phugoid eigenmotion. Figure 7.8 shows the control loop for the pitch controller.

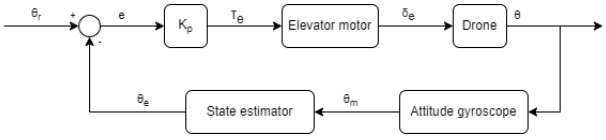

Figure 7.8: Pitch controller

The control loop is generally the same as the pitch damper but the pitch rate is replaced with the pitch of the drone. θ_r is not 0 in this case but is the required pitch according to autonomous flight system. K_p for the pitch controller should also be negative as an increased pitch angle(negative e) would create a negative moment.

7.8.3. Yaw Damper

During a Dutch roll, the yaw and the roll of the aircraft oscillate a lot. Although damping of roll with ailerons is an option, it is more efficient to dampen dutch roll with yaw as less surface needs to be deflected. Thus, a yaw damper is implemented to dampen the dutch roll. Figure 7.9 shows the control loop for the pitch controller.

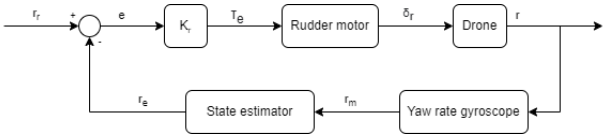

Figure 7.9: Pitch damper control loop

The controller gain for the yaw damper K_r needs to once again be negative. A positive yaw rate(negative error) needs to be counteracted with a negative moment that is caused by a negative deflection of the rudder surfaces.

8
Detailed Design: Structures

This chapter covers the structure detailed design. Firstly the structure type trade-off is confirmed in section 8.1, then in section 8.2 covers the flight envelope generation. The material selection is adressed in section 8.3. section 8.4 covers skin structure design and section 8.5 the truss structure design. The material characteristics summary is in section 8.6 and production and end-of-life procedures are described in section 8.7 and section 8.8 respectively. The assumptions used for structural designed are summarised in Table 8.1.

Table 8.1: Overview of assumptions within the structures chapter

ID	Assumption
AS-SD-01	The skin carries only the aerodynamic loads.
AS-SD-02	The pressure on the inside of the skin will have the same value as the static pressure at cruise altitude.
AS-SD-03	Cracks up to 3 mm are present in the skin.
AS-SD-04	Initial skin thickness is 1 mm.
AS-SD-05	The engines introduce no torsional load into the structure.
AS-SD-06	The weight of the battery and structure vary linearly in the direction of the span.
AS-SD-07	Node connections are neglected in finding the total structural mass.
AS-MA-01	By 2035, recycled aluminium 6061-T6 will have the same mechanical properties as the primary variant.

8.1. Structure Layout Sensitivity Analysis

In the midterm report, a trade-off was performed to choose a structural layout. The options considered were monocoque, semi-monocoque, and a truss structure. They were scored against multiple criteria to select the most suitable design option for the eCarus drone [5]. The trade-off summary table is presented in Table 8.2.

Table 8.2: Summary table of the structural layout trade-off [5]

Criteria	Mass	Life cycle sustainibilty	Subsystem integration	
Weight	**4**	**5**	**3**	**Total score**
Monocoque	Unacceptable skin thickness	X	X	-
Semi-monocoque	Less weight efficient	Good recyclability	Flexible subsystem placement	39
Truss structure	Reduced weight	Ease of assembly and maintenance	Place subsystem at nodes	40

Legend: Black = Unfeasible (1), Red = Bad (2), Yellow = Moderate (3), Blue = Good (4), Green = Great (5)

From Table 8.2, it is observed that the truss structure wins, but only with one point. It is thus important to perform a sensitivity analysis. The weights of the criteria are to be varied to identify the sensitivity of the trade-off to different weight combinations. The weight ranges used are justified below.

- **Mass:** The mass was initially given the weight of 4 as it is an important design-driving system parameter. It is interesting to see what the outcome of the trade-off will be if the mass is deemed a bit more, or less important. The weight range is set at 3-5.
- **Life cycle sustainability:** [REQ-SUS-ENV-01] states that *The system shall have recycling procedures in place for the end-of-life phase* [4]. As the design should be sustainable and minimise

the impact on the environment, this criterion was therefore given a weight of 5. For this sensitivity analysis, it is investigated what would happen if this criterion had been deemed of lesser importance. A weight range of 3-5 is specified.

- **Subsystem integration:** The structure must allow for proper integration of all the subsystems. The weight given was a 3, as it was deemed of lesser importance than the mass. The weight range of this criterion is set at 3-4, to see what the outcome would be if it was deemed of the same importance as the mass.

Running through all the different weight combinations, the output of the sensitivity analysis is that it is a draw six times, the semi-monocoque option wins three times and the truss structure option wins nine times. Thus, for a third of the weight distributions, the trade-off is indecisive on the option to choose. This is deemed too much, thus a further sensitivity analysis is performed by adding a criterion to the trade-off. That criterion is presented below.

- **Design simplicity:** As an additional criterion, the simplicity of designing the structure is used. Because semi-monocoque and a truss structure are this close, it is believed that this criterion can prove to be the deciding factor.

In a semi-monocoque structure, the skin carries a significant part of the load. It is supported by stringers to prevent bucking, using spars and ribs to complete the wingbox. In the thin-walled elements, both normal and shear stresses are present. For a truss structure on the other side, the entire structure consists of simple rods, which are only loaded in tension or compression. Each element can be analysed separately to assess the internal tension or compression. Concluding, the truss structure is considered to be better performing in this criterion. It is thus the final winner of the trade-off.

8.2. Flight Envelope

The first step in designing an aircraft structure is gaining the knowledge of what load factors, defined as the lift divided by the weight, are to be expected during operation. These become apparent by constructing a flight envelope. This is a combination of both manoeuvre loads and gust loads, that need to be withstood at different flight speeds. The loads are set by official regulations like for example the CS-23 regulations, set by the European Aviation Safety Agency. However, eCarus is an unmanned drone and thus these types of regulations do not apply. In the absence of regulations for civil UAVs of this size, a choice is made for Standardisation Agreement 4671 (STANAG 4671). This is a document ”for the airworthiness certification of fixed-wing military UAV Systems with a maximum take-off weight between 150 and 20,000 kg that intend to regularly operate in non-segregated airspace”, made by the North Atlantic Treaty Organisation (NATO) [58]. It should be noted that eCarus is of course not a military drone. Dr X. Wang is active at the Faculty of Aerospace Engineering at the Delft University of Technology and is an expert in aerial robotics. She was consulted on whether using these regulations was the right choice, and stated that in the absence of any civil regulations, the decision was correct.

The input values necessary are presented in Table 8.3.

Table 8.3: Input parameters for flight envelope

Parameter	Value	Unit
W	6521.24	kg
S	45.30	m^2
$C_{L_{max}}$	1.4	[-]
C_{L_α}	3.724	$1/rad$
V_c	110	m/s
ρ_c	$0.770\,816$	kg/m^3

8.2.1. Manoeuvre Loads

The flight envelope consists of 2 types of loads: the manoeuvre loads and the gust loads. Starting at a velocity and load factor of zero, the maximum manoeuvre load factor starts to increase with increasing velocity. It does so following the below relation.

$$n = \frac{L}{W} = \frac{C_{L_{max}} \frac{1}{2} \rho V_c^2}{W/S} \tag{8.1}$$

The maximum load factor increases in magnitude in both the positive and negative direction, until it reaches n_{max} and n_{min}. By STANAG 4671, n_{max} is equal to $2.1 + 10900/(W_{TO} + 4536)$, where W is the drone weight. Then, n_{min} should not be less than $0.4n_{max}$. The dive speed V_d is taken as $1.4V_c$, which is the cruise speed. The results are presented in Figure 8.1.

8.2.2. Gust Loads

STANAG 4671 specifies the positive (up) and negative (down) gust velocities that are to be taken into account. While at V_c, a gust velocity of $15.2\,\mathrm{m/s}$ should be considered. At V_d, the considered gust velocity is $7.6\,\mathrm{m/s}$. The start of the gust envelope is at steady flight, with n = 1. The gust, perpendicular to the airflow, results in a change in the angle of attack. The difference in load factor can then be obtained by the following equation. The results are shown in Figure 8.1.

$$\delta n = \frac{\rho V C_{L_\alpha} u}{2(W_{TO}/S)} \tag{8.2}$$

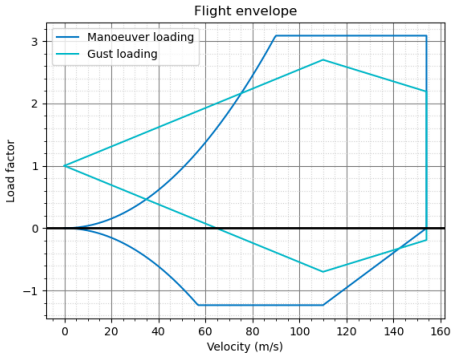

Figure 8.1: Flight envelope

From Figure 8.1, it becomes apparent that for the cruise speed, the manoeuvre loads are limited. Thus, an n_{max} of 3.09 and an n_{min} of -1.23 are to be taken into account.

8.3. Material Selection

In the Mid-Term Report, a trade-off was performed regarding the structural layout of the drone [5]. The conclusion was to go for a truss structure. In this section, a material is chosen for the trusses and for the skin.

8.3.1. Selection Method

For each of the components, first, a list is generated with possible candidates. This list contains groups of materials. The materials are scored based on how well they perform at certain predefined selection criteria. Once a group is selected, a few candidate materials together with their significant properties are stated in a table. Based on these properties, a material choice is then made. It should be noted that for many of the scores awarded, Granta EduPack 2022 R1 is used. This program is a useful tool to generate material bubble charts to aid in the scoring process [59].

8.3.2. Truss Rod Material Trade-off

One of the most important parts of the truss structure is the actual rod elements. This acts as the load-bearing part of the structure so a strong material is desired for example. To select a suitable material, a trade-off will be performed once again. This process is described in this subsection.

Material options generation

According to literature, there are various materials that would be a great fit for the purpose of a truss rod. The first candidate pertains to Silicon Carbide (SiC) fibre-reinforced polymers. Silicon Carbide is a fibre under development that is used for metal matrix composites (MMCs) in the aerospace industry [60].

Table 8.4: Trade-off summary table of truss rod material

Criteria	Fatigue	End of life	Stifness	Strength	Manufacturability	Cost	
Weight	**5**	**3**	**3**	**5**	**3**	**3**	**Total score**
Silicon carbide fibre reinforced polymer	High fatigue strength, low density	Low CO2 footprint, low density	Low density, moderate stiffness	Average strength-to-density ratio	Low density, high CO2 footprint	Most expensive, but expected to improve	82
Aluminium alloy	Moderate fatigue strength, low density	Low CO2 footprint, low density	Low stiffness, low density	Average strength-to-density ratio	Low density, low CO2 footprint	Low density, cheapest material	81
Titanium alloy	X	High CO2 footprint, high density	X	X	High CO2 footprint, high density	X	51
Titanium matrix	X	X	X	X	High CO2 footprint, high density	X	57
Carbon reinforced (CFRP)	Moderate fatigue strenght, low density	Moderate CO2 footprint, low density	Low density, moderate stiffness	Average strength-to-density ratio	Low density, high CO2 footprint	Most expensive, but expected to improve	78

The second and third materials that will be considered are aluminium and titanium alloys as these are conventional structural materials. As for the fourth material, titanium metal matrix composites (TiMMCs) will be considered as they also show great promise for the design according to literature [60]. Lastly, Carbon-fibre-reinforced polymers (CFRP) also show promise and will therefore be considered [61].

Selection criteria and weights

For the trade-off, several selection criteria are considered. A brief description of each is given below with their corresponding weights:

- **Fatigue:** Considering the number of flights the UAV must conduct and its lifetime according to *REQ-US-SUS-02: The nominal lifetime of a drone shall be 30 years*, the structure needs to maintain its performance throughout operational life. This criterion takes a look at the fatigue strength at 10^7 cycles per density In this way, a general indication may be obtained for the life cycle of the material. while taking the weight into account. A weight of 5 is given to this criterion due to the expected large amount of flights.
- **End-of-life:** Looking at *REQ-SUS-ENV-01: The system shall have recycling procedures in place for the end-of-life*, the end-of-life is an important part of the design. This needs to be implemented in a sustainable way. This criterion, therefore, looks at the CO2 footprint per density during the recycling stage of the material. Moreover, a weight of 3 is given to this criterion because it is deemed to be important but still not a driving requirement for the design.
- **Stiffness:** As the truss structure needs to maintain the overall geometry of the aircraft, the stiffness of the rods needs to be considered. However, an allowance for flexibility is needed as well. Therefore, stiffness is not too important for the trade-off. A weight of 3 is therefore given. It is to be noted that this criterion will look at the specific stiffness to account for the weight as well.
- **Strength:** Due to the high loads that the truss structure experiences throughout the mission, the truss rods need to be able to withstand this without going into the plastic region. To be more specific, this criterion will look at the specific strength of the material. A weight of 5 is given as this is deemed to be the most important for the structural department.
- **Manufacturability:** Similar to the end-of-life criterion, the manufacturability of the material needs to be taken into account as well. This again demands a sustainable method. For this criterion, a closer look will be taken at the CO2 footprint per density during manufacturing. A weight of 3 is also given considering the similarities with the end-of-life criterion.
- **Cost:** Considering the limited financial resources available to designs, the cost must certainly be minimised as much as possible. This becomes more important considering that a myriad of UAV drones will have to be manufactured for this mid-air recharging system. Therefore, a weight of 3 is given.

Trade-off summary table

To provide a global overview of the trade-off, a summary table can be found below in Table 8.4. Furthermore, the explanation for the score of each category is also given.

- **Fatigue:** For the fatigue criterion, a bubble chart was generated in Granta Edupack 2022 R1. From this, it is observed that the Silicon Carbide fibre group performed the best by providing high

strength while still being the least dense. 5 is therefore given for SiC fibres. For aluminium alloys, a lower fatigue strength is found but due to their low density, it would still be an acceptable option. A 3 is therefore given for aluminium alloys. For titanium allows, the highest fatigue strength is found but also a very high density. This is therefore given a 3. A similar score for the titanium matrices was given as they still provide high strength but also a high density. For CFRP, a low density was found but the strength is average. So a score of 4 is fitting.

- **End-of-life:** In this criteria, Silicon Carbide and Aluminium alloy perform the best due to their low CO2 footprint and low density. A 5 is therefore given to each. This is the opposite of titanium alloy. Here, a very high CO2 footprint and density are found. A score of 1 is therefore given. Titanium matrix and CFRP fall in between with a score of 2.
- **Stiffness:** Here, the materials perform similarly to each other with a few deviations. SiC and CFPR are given a 3 due to their low density and moderate stiffness. Moreover, titanium matrix is also given a 3. It might have a higher density, but this is compensated for its very high stiffness. Aluminium alloy scores a 2 with its low stiffness and low density. Lastly, titanium matrix also scores a 2 due to its high density and moderate stiffness.
- **Strength:** For strength, most materials perform similarly. CFRP, however, stands out with high strength for a low density. A 5 is therefore given. The rest of the materials are given a 3 due to their strength-to-density ratio.
- **Manufacturability:** When looking at the manufacturability of the materials, aluminium alloy performs by far the best. This is a conventional material which has a low CO2 footprint for low-to-moderate density. A 5 is therefore given. Titanium alloy and matrix perform the worst with a score of 1 due to their high footprint and density. SiC and CFRP both have low density but a high CO2. But due to the expected material improvements in the upcoming years, a 3 is given [60, 62].
- **Cost:** For the cost, the aluminium alloy is by far the cheapest. A score of 5 is therefore given. This is then followed by titanium alloy and matrix which are moderately expensive. A score of 3 is therefore given. CFRP and SiC are the most expensive ones but considering the development in the upcoming years, especially regarding manufacturing, the cost would certainly decrease [60, 62]. A score of 3 is therefore given.

Sensitivity analysis

To perform the sensitivity analysis on the trade-off, some criteria will be given different weights here below to see how much it will affect the outcome.

- **End-of-life:** Considering the subjectivity of the relative importance of end-of-life sustainability to the design, it makes sense to have a weight range for this criterion. A range of 2-4 is deemed to be good.
- **Manufacturability:** Similar to the end-of-life criterion regarding the subjectivity of the relative importance of sustainability, a weight range of 2-4 is given.
- **Cost:** This is another criterion that proves to be quite subjective for relative importance, especially considering the dependency on the entire mid-air recharging system. A weight range of 2-4 is therefore given.

To conclude, with all the adjusted weight ranges, the analysis shows that the silicon carbide design choice wins 2 times more often than the aluminium alloy. This seems to be an indication that the silicon carbide fibre-reinforced polymers may be a good fit even if the relative importance of criteria changes. But a detailed analysis is advised to further comprehend the difference between the two materials.

Specific material selection

According to the trade-off and sensitivity analysis, Silicon Carbide fibre-reinforced polymers seem to be the best material for the selected criteria. This group will therefore be considered for the truss rods. Looking at this family of materials, there are several options for metal matrices which include magnesium, aluminium and titanium. Magnesium matrices are the least dense while titanium matrices are the highest. If the density is not taken into account, however, magnesium would perform the worst and titanium the best. Aluminium matrices fall in between. For this reason, aluminium matrices are considered.

Within this group of aluminium matrices, there are 2 main candidates that perform the best across the criteria. These are the following: Al(8089)-20%SiC(p) MMC powder and Al-47%SiC(f), 0/90/0/90. For all the criteria except the price, Al-47 performs when not looking at the density. However, when it purely

comes to density, Al(8089) wins significantly. As a final choice for the material, Al(8089)-20%SiC(p) MMC powder is chosen due to its overall moderate performance for its low price and density.

8.3.3. Skin Material Trade-off

The second material choice to be made is that of the skin. As the structure has a truss configuration and is not semi-monocoque, the only function of the skin is to transfer the aerodynamic loads into the truss structure. With this, it is crucial that the aerofoil maintains its aerodynamic shape. A material is to be chosen accordingly.

Material option generation

The first candidate entering the trade-off is the group of honeycomb sandwich materials. Because of their core layout, they are light and efficient. They are already applied in the aerospace sector, and are promising for skin panels [63]. The next material group considered is aluminium alloys. It is a light metal with good mechanical properties and is widely used for skin panels. Finally, composites with a polymer matrix are considered in the trade-off. Composites using fibres made of for example carbon or glass are increasingly used in the aerospace sector. As an example, the Boeing 787 Dreamliner uses approximately 35 tonnes of CFRP [64].

Selection criteria and weights

For the skin material, one addition is made to the selection criteria of subsection 8.3.2. Also, the weight distribution is different as the skin has to perform a different function.

- **Fatigue:** The skin is an easy component to inspect for fatigue failures, and if needed replacement is more doable than if a truss is to be replaced. However, it is still important that this is minimised and that the lifetime is as long as possible. Therefore, a weight of 3 is given. As for the previous trade-off, a look is taken at the fatigue strength at 10^7 cycles.
- **End-of-life:** At the end-of-life of the drone, both the trusses and the skin are to be recycled. Thus the recyclability of both materials is of comparative importance. Therefore a weight of 3 is given. Material performance on this criterion is again quantified by looking at the CO2 footprint during the recycling stage.
- **Stiffness:** For the skin, stiffness is a crucial property. As stated earlier, the airfoil must maintain its aerodynamic shape. If subjected to strong aerodynamic loads, the skin is also expected to return to this shape. The highest weight of 5 is given to this criterion.
- **Strength:** In the truss wingbox, the skin does not carry any structural loads. It is assumed that the aerodynamic loads will not be sufficient to approach the failure region. Thus, it is given a 2.
- **Manufacturability:** As for the trusses, the manufacturability of the skin is to be considered. It is deemed to have the same importance, thus a weight of 3 is given to this criterion. Again the CO2 footprint during manufacturing is investigated.
- **Durability:** In contrast with the truss, the skin is an external structure. This means that it is susceptible to environmental factors like the sun and water. It is critical that the skin can handle the environment, thus a weight of 5 is given.
- **Cost:** The cost is the last parameter to consider for scoring materials. As in the previous trade-off, the cost is weighted with a 4.

Trade-off summary table

Table 8.5 presents the trade-off summary table for the skin material selection. Afterwards, a more elaborate explanation is given of the scores of each design option.

Table 8.5: Trade-off summary table for skin material

Criteria	Fatigue	End-of-life	Stifness	Strength	Manufacturability	Durability	Cost	
Weight	3	3	4	2	3	5	4	**Total score**
Honeycomb	Excellent fatigue strength, low density	Low carbon footprint, low density	Low stifness	Low strength	Laborious manufacturing	Problem of fluid intrusion	Laborious manufacturing	72
Aluminium alloy	Okay fatigue strength, moderate density	Moderate carbon footprint, moderate density	Good stifness, moderate density	Good yield strength, moderate density	Relatively low carbon emissions produced	No fluid intrusion, resists UV radiation	Cheapest	81
Polymer matrix composite	Okay fatigue strength, low density	Difficult to separate fibres from resin	Good stifness, low density	Good yield strength, low density	High CO2 emissions	Problem with UV radiation	Most expensive	71

- **Fatigue:** Granta showed that for a lower density, most of the composites had a comparable fatigue strength after 10^7 cycles. For a honeycomb sandwich, it has proven itself to be well-performing in this criterion, proving itself in applications like high-performance yachts [65]. This results in a score of 4, 2 and 3 is given to honeycomb sandwich, aluminium alloys and polymer matrix composites, respectively.
- **End-of-life:** From the bubble chart generated it became evident that honeycomb sandwich structures contain a lot of options with a relatively low carbon footprint during recycling. It is therefore scored with a 4. The carbon emission of recycling aluminium is 2.5 to 3 kg of CO2 for each kg of aluminium. This is a bit higher than most of the honeycomb alternatives, thus it is scored a 3. It is a challenging task to recycle polymer matrix composites. Extracting the fibres from the resin is difficult and results in a lot of waste [66]. It is scored with a 2.
- **Stiffness** To assess the scores for this criterion, a bubble chart is generated in Granta, laying out the Young's modulus against the material density. From there it became evident that honeycomb sandwiches score a 3, aluminium alloys score a 4 and composites a 5. Aluminium has a comparable Young's modulus with fibre composites, but was outperformed because of its higher density.
- **Strength:** For this criterion, the yield strength is considered as the defining material property, taken relative to the material density. Honeycomb structures are favourable because of their low density, but have a yield strength ranging up to 2 Mpa. Compared with aluminium or fibre composites, this is a low value. Thus it is scored with a 2. As for the previous criterion, aluminium alloys and polymer matrix composites have a similar yield strength. Due to its lower density, fibre composites get a score of 4 and aluminium alloys a 3.
- **Manufacturability:** As for the truss material trade-off, for this criterion the kilograms of CO2 that are produced by manufacturing the material are considered. From a bubble chart generated in Granta, it is observed that both polymer matrix composites and honeycomb sandwich materials have a wide range in how much CO2 is produced during manufacturing. For some CFRP configurations, production emissions can go up to 50 kg/kg, while for some glass composites it is only 2 kg/kg. Overall, for aluminium alloys CO2 production is about 10 kg/kg. Honeycomb and fibre-reinforced materials are both scored a 3. Aluminium is scored a 4.
- **Environmental susceptibility:** To get an indication on how well the skin handles environmental factors, both the susceptibility to UV radiation and water resistance are taken to account. Because of their internal hollow layout, honeycomb sandwich materials are very prone to fluid intrusion. This is not desirable as it degrades the material performance [67]. Using the Granta program, it is observed that honeycomb materials perform average on resistance to UV radiation. It is scored a 3. For fibre-reinforced composites, it is observed that it is the other way around. It performs well on water resistance, but is preferable when exposed to UV radiation. It is thus also scored with a 3. Aluminium performs excellently on exposure to UV radiation and is acceptable on water resistance. It is scored a 4.
- **Cost:** Cost-wise, the best option is to go with an aluminium alloy. It is scored with a 4. The most expansive options are polymer matrix composites. They are scored with a 2. In the middle are honeycomb structures. They are also quite expensive as they are highly laborious in manufacturing and quality control is difficult [68].

Sensitivity analysis

A sensitivity analysis should be performed to get an indication of what the result would have been, had another weight distribution been present. Below different weight changes are described.

- **End-of-life:** As for the truss material, it is interesting to see the result if the weight of this criterion is varied. The weight range is set at 2-4.
- **Manufacturability:** As for the previous criterion, the relative importance of sustainability is varied. The weight range is again 2-4.
- **Durability:** It can be argued that durability can be deemed a bit less important. The material can for example be coated to protect it from environmental factors. A weight range of 3-5 is given.
- **Cost:** The cost is influenced by a lot of parameters considering the entire system. A weight range of 3-5 is specified.

With the sensitivity analysis, it was found that aluminium alloys win the trade-off for all of the possible weight distribution. It is thus an insensitive trade-off, and the conclusion can be drawn that an aluminium

alloy will be used for the skin.

Specific material selection

Now that the material group is chosen to be that of aluminium alloys, a choice must be made regarding the specific alloy. Two candidates that are considered are 2024-T3 and 6061-T6. They are both materials that have proven to be very suitable for aerospace applications.

To make a choice between the two, a look is taken again at the trade-off criteria. Aluminium 2024-T3 has better mechanical properties than 6061-T6 like fatigue, stiffness and strength. However it is heavier than 6061-T6, it is cheaper and is more susceptible to environmental factors like water. As the skin does not have to carry any structural loads, the mechanical properties are deemed of secondary importance.

Producing aluminium is an energy intensive process. It is extracted from mined bauxite, and separating the aluminium from the oxides requires extensive power. Thus, it contributes heavily to the yearly global carbon emissions [69]. According to [REQ-US-SUS-01]: *The life-cycle impact of the system must be minimal*. This means that to reduce the environmental impact of eCarus, alternatives must be considered. Recycling aluminium results in a 95% decrease in energy consumption during production [70]. As of now, recycling of aerospace-grade aluminium alloys is at an early stage. As they usually have a relatively high level of alloying, proper separation is needed [71]. However, extensive research has already been performed on the recycling of aluminium. It has been found that recycling does not degrade the mechanical properties a lot, and can sometimes even enhance the material properties using heat treatment [72, 73]. Accounting for the development of the technique over the coming years, it is safe to assume that once eCarus becomes operational in 2035, recycled aluminium 6061-T6 has the same mechanical properties as the primary variant. Thus, the skin material chosen is recycled aluminium 6061-T6.

8.4. Skin Design

Now that a material choice has been made for both the trusses and the skin, it is important to investigate how the skin will transfer the aerodynamic loads into the truss structure. As the truss layout is quite robust, some additional elements are needed to support the skin. The skin is not allowed to lose its aerodynamic shape.

8.4.1. Load Analysis and Support Structure

The loads acting on the skin are to be analysed before any design can be performed on the support structure. From XFLR5, the pressure distribution is derived around the MH91 aerofoil at cruise conditions. The result is presented in Figure 8.2.

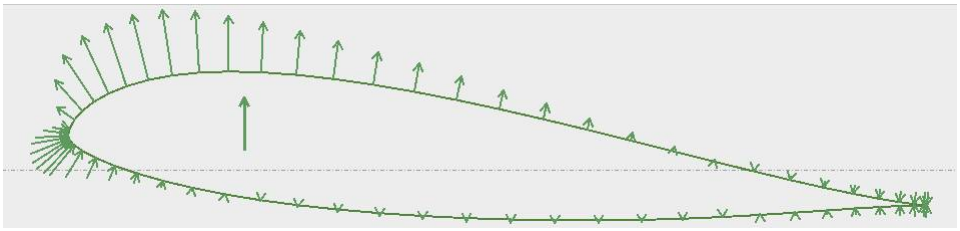

Figure 8.2: Visualisation of pressure distribution around aerofoil at cruise

The figure presents the aerodynamic loads that will act on the skin. It can be seen that the loads at the leading edge will be the most severe. It is thus important that sufficient skin stiffening is present there. To get an indication of what Figure 8.2 means in terms of forces, the pressure coefficients found with XFLR5 are to be transformed into the actual pressure, using the equation stated below.

$$p = \frac{1}{2} C_p \rho_c V_c^2 + p_c \tag{8.3}$$

As the eCarus drone is not pressurised, it can be assumed that the pressure on the inside of the skin will have the same value as the static pressure at cruise altitude. To assess the load acting on the skin,

the differential in pressure is to be used. Thus, the p_c term can be omitted in Equation 8.3. With a cruise velocity and density of $110\,\mathrm{m/s}$ and $0.771\,\mathrm{kg/m^3}$ respectively, Figure 8.3 is generated.
In Figure 8.3, the upper line presents the upper surface of the aerofoil, and vice versa. It is evident that the maximum pressure the skin has to withstand is directed outward and has a magnitude of $7290\,\mathrm{Pa}$.

To support the skin, a certain underlying structure should be present. From literature it has been found that for a truss wingbox configuration, a lattice promises to be a good skin stiffening method [74, 75]. It consists of stiffening elements at $45°$ and $-45°$, with respect to the truss wingbox. Figure 8.4 presents an indication of what this lattice looks like.

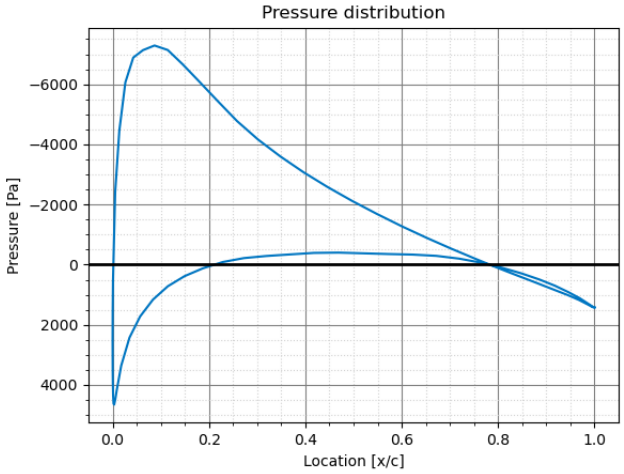

Figure 8.3: Pressure distribution around aerofoil at cruise

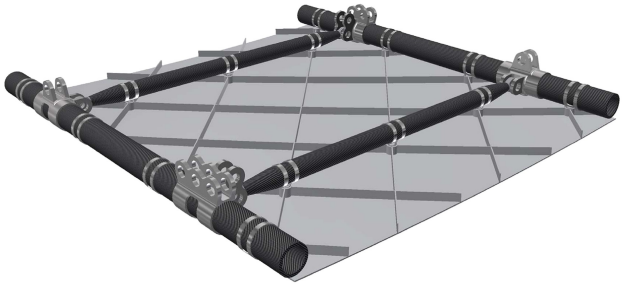

Figure 8.4: Visualisation of lattice layout [75]

8.4.2. Support Structure Attachment

Before the internal stress is analysed, it is chosen how the lattice elements are connected to the skin. Two options that can be considered are conventional rivets or adhesive bonding. The advantages of rivets are their simplicity in manufacturing and attaching parts. However, they can be quite heavy and they result in stress concentrations.

Adhesive bonding is a solution to the beforementioned problems. A discussion was held with Dr S. Teixeira de Freitas, a specialist in adhesive bonding, active at the Delft University of Technology. She stated that adhesive bonding has significant advantages with respect to rivets. Weight reduction is the first important one. Also, due to the adhesive polymer between the two elements, the joint allows for a lot of flexibility. Finally, adhesive bonded joints limit stress concentrations [76, 77]. From all these advantages, it is clear that adhesive bonding promises significant benefits against conventional rivets. Therefore, it is chosen to attach the lattice to the skin.

8.4.3. Internal Stress Analysis

A metallic sheet can undergo many different failure modes. It is important to assess what will be the most critical one, under the stresses applied to the skin. Possible failure modes for a thin sheet are listed below.

- Buckling in compression
- Bucking in shear
- Yielding in tension
- Fracture in tension

Buckling in compression is a failure mode that occurs when a thin sheet is exposed to a compressive load and deforms out-of-plane as a result. As the aerodynamic load is transverse, no severe compression is expected in the skin. Thus, this failure mode is not deemed to be the most critical one.

For shear buckling, the same argument as for the previous failure mode holds. The truss structure will carry the shear loads generated by the lift and drag. The skin will only hold the aerodynamic pressures, thus the most severe internal load in the skin will be tension. The last two failure modes should be considered.

For both yielding and fracture, tension is the internal load leading to failure. Yielding in tension happens if the internal tensile stress exceeds the material yield strength σ_{yield}. The skin will deform plastically, meaning it is irreversible and the skin has failed. The tensile yield strength of aluminium 6061-T6 is 276 MPa. Thus, including the factor of safety of 1.3, the maximum tensile stress present in the skin may be 212.3 MPa.

Crack propagation is the phenomenon that results in the fracture of a material. It must be assessed whether this will occur before yielding of the plate. The material parameter that is important for this is the fracture toughness, or K_{IC}. For aluminium 6061-T6, this is 29 MPa$\sqrt{\text{m}}$. Including the factor of safety of 1.3, it is 22.3 MPa$\sqrt{\text{m}}$. Initial cracks present in the aluminium grow with the cycles the skin is subjected to, eventually growing so large that the internal stress causes fracture. To size for fracture, an input is the length of cracks that are present in the skin. Some non-destructive techniques are present to find these crack sizes. A tool that is used widely is ultrasonic inspection. It can detect cracks under 1 mm, and size cracks under 3 mm [78]. To go for a conservative approach, it is assumed that cracks up to 3 mm can be detected upon inspection. The stress intensity factor at the crack is given below [79].

$$K_I = \sigma\sqrt{\pi a} \tag{8.4}$$

With cracks assumed present of 3 mm and the beforementioned fracture toughness of aluminium, using Equation 8.4 it is found that the internal skin stress may not exceed 324.96 MPa. From this value, it can be concluded that the panel will yield before fracturing, thus the sizing should be done regarding the yield strength. It is noted that for this to hold, regular inspection is necessary to ensure that the crack length does not exceed 3 mm.

To find the internal shear stresses, the skin is modelled as a collection of flat plates. A transverse distributed load acts on them from the pressure described in subsection 8.4.1. They are simply supported at the edges, where the supporting lattice structure is present. Dr Calvin Rans was consulted if this approach was a valid one, and he stated that is a good, conservative approach. A visualisation of the model is given in Figure 8.5.

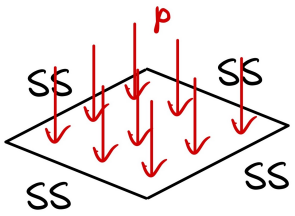

Figure 8.5: Representation of how the skin elements are modelled

The internal stress depends on two parameters: the skin thickness and the lattice spacing. The lattice spacing determines the width of the flat plates. The formula to calculate the maximum stress in the panel is given below [80].

$$\sigma_{max} = 0.287p\frac{b^2}{t^2} \tag{8.5}$$

A skin thickness of 1 mm is assumed. This is an initial assumption and should be iterated on later. Now, using the maximum allowable stress equal to 212.3 MPa and the maximum encountered pressure of 7290 Pa, Equation 8.5 is used to evaluate the required lattice spacing. It is found that for the skin to withstand the pressure, the lattice spacing should be 31.9 cm.

8.5. Truss Wingbox Design

The wingbox of the drone is a truss structure. Functionally, the truss is a load path for the weights attached to it and the engine's trust up to the aerodynamic skin pressure forces. This section highlights the steps taken to design the geometry of the truss structure inside the wing and the truss-specific loading analysis.

8.5.1. Axis System

The axis system defined follows the body-fixed reference frame convention illustrated in Figure 8.6 as x_B, y_B, z_B. As the aircraft is symmetrical on the Ozx plane, the right wing and side of the aircraft will be designed and the left side follows from symmetry.

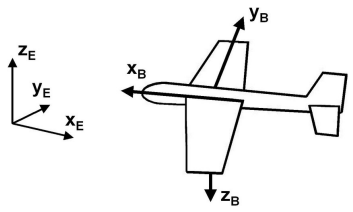

Figure 8.6: body fixed reference frame

8.5.2. Load Analysis

In a truss structure, the primary convenience is that all truss elements are loaded axially. This allows a designer to choose a material and structural design optimised for one type of loading. In order to not introduce any shear or moment forces into the truss elements, all loads must be applied at the truss nodes. The loads will be analysed as applied at the nodes. The aerodynamic forces are assumed applied at the node closest to their point of application on the skin.

In section 8.2 it is found that the necessary load factors that are designed for are $n_{max} = 3.09$ and $n_{min} = -1.23$. The sum of loads on the x and z axes and the sum of torques on the y-axis are multiplied by these factors to generate two extreme load cases the structure must withstand.

The current loading case comprises a lift distribution along the span, a drag distribution and an aerodynamic distribution at the quarter chord all generated by a horseshoe vortex and vortex lattice CFD method from xflr5. The weights of the structure comprise of engine weight and thrust positioned at a 1.47m y coordinate in both directions for the two engines. The engine is assumed to generate no torsional force on the airframe. The weights of the batteries and of the structure are assumed to vary linearly with local chord lengths along the span as in. The Python implementation of the load distribution into node forces has for output a force in newtons applied to each node point. Figure 8.7 shows the combined distributed load from lift and weight without engine mass point load and the force applied at the nodes at n = 1. The example is for a truss with 20 evenly separated nodes.

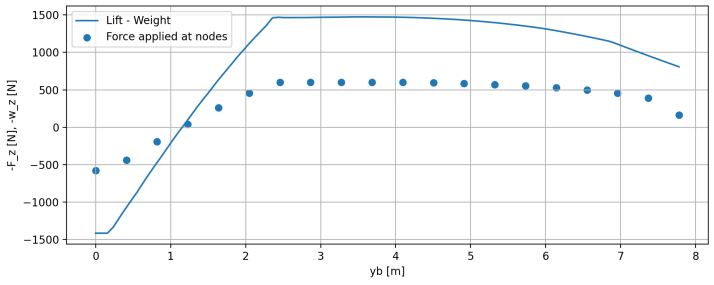

Figure 8.7: Node forces due to distributed loading in the z direction along the half-span

8.5.3. Failure Modes

In order to size and design the truss elements, the different failure modes bounding the design are analysed. The failure modes analysed are:

- axial tension yield failure: at the elastic limit of the material when loaded in tension.
- axial compression yield failure: at the elastic limit of the material when loaded in compression.
- column buckling failure: modelled as Euler buckling of a simply supported beam. The critical loading is given by Equation 8.6 from [81].
- fatigue failure: with an assumption of four flights a day and 300 days of flight in a year, during the 30 years of nominal operation, 36000 flights are expected in the nominal lifetime of the drone.

$$P_{crit} = \frac{\pi^2 n^2 E I_{xx}}{L^2} \tag{8.6}$$

Where n is the buckling mode, with n=1 considered a failure, E the modulus of elasticity, I_{xx} the second moment of area of the cross-section and L the length of a truss.

8.5.4. Cross-sectional Design of the Truss Elements

In order for the truss elements to be lightweight while retaining high I_{xx} on all axes for buckling performance, a tubular truss cross-section is chosen as it is a lightweight point symmetrical cross-section. It is defined with an external diameter and a thickness of D and t. Without a thin-walled assumption, the cross-sectional properties of Equation 8.8 and Equation 8.7 follow from the cross-sectional parameters.

$$I_{xx} = \frac{\pi}{4}\left(\left(\frac{D}{2}\right)^4 - \left(\frac{D-2t}{2}\right)^4\right) \tag{8.7}$$

$$A = \pi(D^2 - (D-t)^2) \tag{8.8}$$

As a limit yield stress and a limit buckling forces are determined, The cross-section parameters are chosen from the system of equations determined by the A and the I_{xx} required.

8.5.5. 2D Truss Design on the Oyz Plane

The design of the truss geometry is done in two steps. First, a truss type is chosen, and then the geometric parameters of the truss are altered to optimise performance in the given load case. The parameters of the truss are kept constant along the span in this analysis of design options.

The design of the truss geometry is done by comparing the performance of different truss types used for bridge design by civil engineers. They are geometries adapted for high aspect ratios and for the support of distributed loads. The following truss types are analysed:

- A: Warren truss. This type of truss is used in civil applications where long spans must be supported under distributed loads as the loads spread evenly in the truss members as described by SkyCiv Engineering [82].
- B: Pratt truss. This type of truss is equally used for long horizontal spans with vertical applied forces. According to SkyCiv Engineering [82], it is a proven design that has the advantage of having a predictable loading behaviour in the diagonal members always in tension.
- C: Warren truss with added horizontal members. This is a hybrid of type A and type B, the tension and compression loads are supported by additional vertical members
- D: A Pratt truss with two diagonal members crossing. This type of truss has the added benefit of adding redundancy to the diagonal truss members and spreading the loads between the diagonal members.

For this analysis, the truss is simplified to a rectangular parallepiped sized for the MAC airfoil. The loading used is the upper loading factor case with a safety factor of 1.3. The cross-sectional area used is of $A = 600\text{mm}^2$ and using the elastic properties of the material chosen in section 8.3. The A,B,C and D 2D truss types are depicted in Figure 8.8.

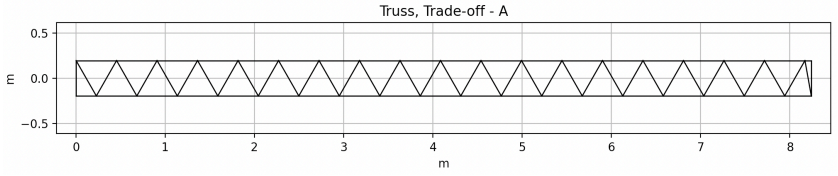

(a) Truss type A geometry

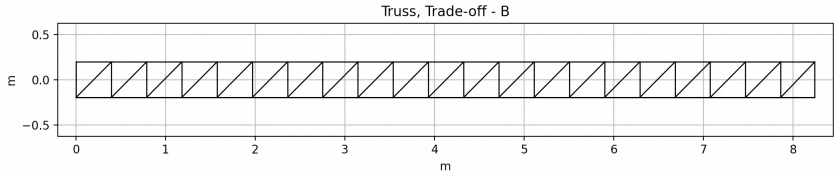

(b) Truss type B geometry

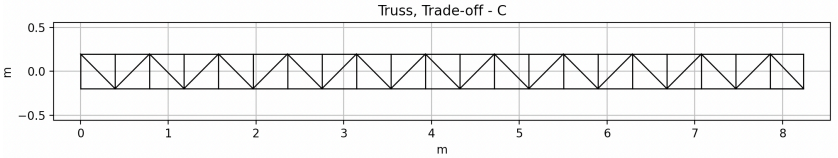

(c) Truss type C geometry

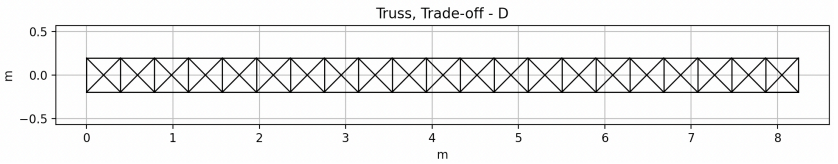

(d) Truss type D geometry

Figure 8.8: Types of truss geometries traded off.

These trusses are analysed through the 1D member structure analysis software frame3dd [83]. This analysis software outputs the axial forces in each member and the deformation of each node under the applied loading generated in subsection 8.5.2. This analysis provided as metrics for comparison the distribution of axial loads in the members, the total truss length needed in the structure (proportional to weight at same cross-sectional area), the deflection of the structure at the tip. Histograms showing post-analysis data on axial loading distributions in the truss are presented in Figure 8.9.

These histograms are taken as an indication of the capability of optimising the truss for weight by lowering the cross-sectional area of less loaded trusses compared to their high-loaded counterparts. Truss D has a high largest normal force however the majority of trusses (83) are only loaded between -4.41 kN and 10.59 kN suggesting large decreases in thickness can be done. This must however be studied further as changing individual truss elastic properties has an effect on the load distribution and deflection of the truss in a statically indeterminate system. They are ignored in the choice of a truss type at this point in the design.

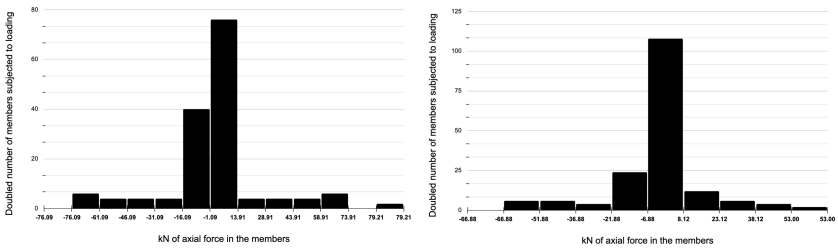

(a) Truss type A axial force distribution in the members

(b) Truss type B axial force distribution in the members

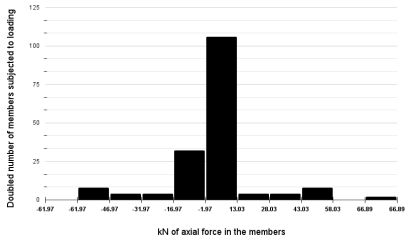

(c) Truss type C axial force distribution in the members

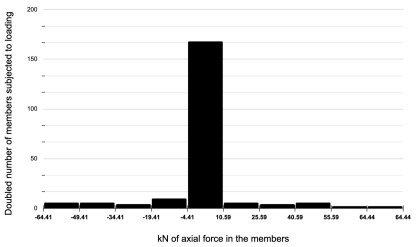

(d) Truss type D axial force distribution in the members

Figure 8.9: Histograms of axial force distribution in truss members

Figure 8.10 presents the deflected trusses with deflections exaggerated by a factor of 10 for the different trusses.

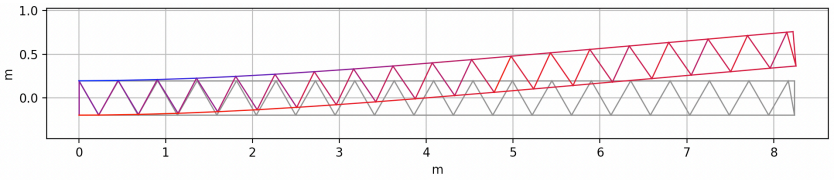

(a) Truss type A deflection

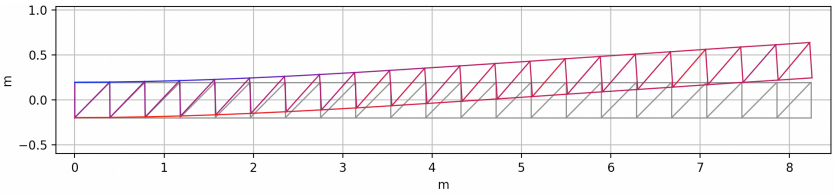

(b) Truss type B deflection

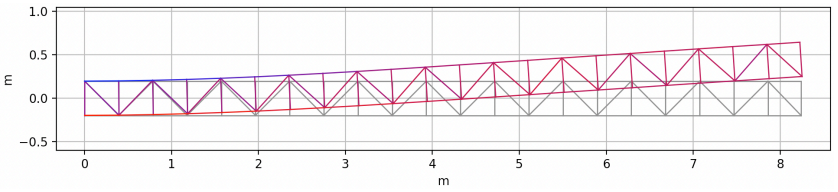

(c) Truss type C deflection

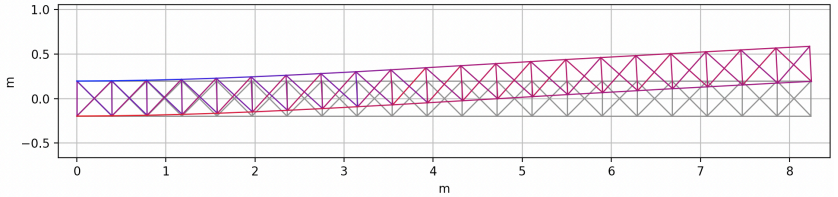

(d) Truss type D deflection

Figure 8.10: 10x exaggerated deflection of the truss types under the load case

Table 8.6 shows the values of the deflections at the tip.

Table 8.6: Deflection at the tip of the trusses (upwards)

Truss type	Deflection in meters	Deflection as percentage of half-span
Truss A	0.0562	0.682 %
Truss B	0.0442	0.536 %
Truss C	0.0446	0.541 %
Truss D	0.03897	0.4729 %

To compute the mass of the structures, the area of material needed to support the highest axial truss force is determined for each truss type to account for trusses spreading the loads more evenly. This area is applied to the total length of the truss. The calculations are summarised inTable 8.7 where a density of 2780 kg/m^3 and maximum stress of 469 MPa are used for the silicon carbide fiber reinforced polymer. It is assumed that the node connections do not contribute to the mass and an upper maximum stress bound is used for compressive and tensile stress based on the lower compressive failure stress.

Table 8.7: Weight of the structure for different truss types

Truss type	Length of truss [m]	Peak axial force [kN]	Area necessary [m^2]	Volume of truss [m^3]	Mass [kg]
A	34	79.21	0.0001689	0.005742	15.96
B	37.16	-66.88	0.0001426	0.005246	14.58
C	37.16	66.89	0.0001427	0.005250	14.61
D	48.83	64.44	0.0001374	0.006709	18.65

To conclude this analysis of truss types A through D, truss type B and truss type D remain preferred for a good performance in deflection and in the total mass of truss B with all diagonal members loaded in tension with positive load factors. For truss D, it is the redundancy offered by the doubled diagonal members that makes it a good choice. To continue with design, it is decided by team eCarus that a structure must have redundancy. In trusses, A through C, failure of any truss members means structural collapse whereas truss D offers redundancy in all truss members. Although a heavier option, truss D is chosen for its redundancy capabilities and superior stiffness.

This concludes in the choice of structure type D pictured in Figure 8.8d for its low deformation properties and for its redundancy in all trusses. This has a significant effect on the safety of the structure at a cost of a 27% weight increase from other types.

8.5.6. Preliminary Estimate of Truss Cross-section

In order to get an upper-end estimate on I_{xx}, it is going back to Equation 8.6, Equation 8.7 and Equation 8.8, using the values of truss type B, with a necessary area of 0,0001426 m^2 and the maximal compressive force of 68.88 kN, from equation Equation 8.6, the critical I_xx necessary is of 1.1457e-5 m^4. Taking for L, the maximal possible thickness of chord length at the root of L = 0.8722.

$$68880 = \frac{\pi^2 1^2 469000000 I_{xx}}{0.8722^2}$$

Solving for D and in Equation 8.7 and Equation 8.8 using the limit I_xx and A calculated, the parameters found are t = 0.00002 m and D = 1.1338 m. These values are not suitable to the wingbox design, thus a more suitable higher cross-sectional area solution is used where A = 0.01 m^2 with D = 0.148 m and t = 0.011 m.

As such an increase of cross-sectional area is inadmissible in terms of mass performance of the structure, these results motivate the need for further design in the trusses of the highly buckling-susceptible region at the wing-root or a rethinking of the truss layout at this section to make the trusses shorter. Buckling is a mode of failure that must not be assumed negligible for the long and high compression loaded members in the en design.

8.5.7. Geometry Definition to Fit the Planform

In order to support the internal bending loads of the structure best, provide useful attachment points for the skin and maximise internal volume for storage of subsystems, the truss is chosen to span the

full height (z-dimension) of the aerofoil along the span. The truss is composed of diagonal vertical members. In order to fit in the trapezoidal platform, they are calculated by the geometrical model in Figure 8.11 to keep the angle of the diagonals constant with the horizontal. The truss shown is of type A however this model is used to determine node locations in other trusses by varying angle beta.

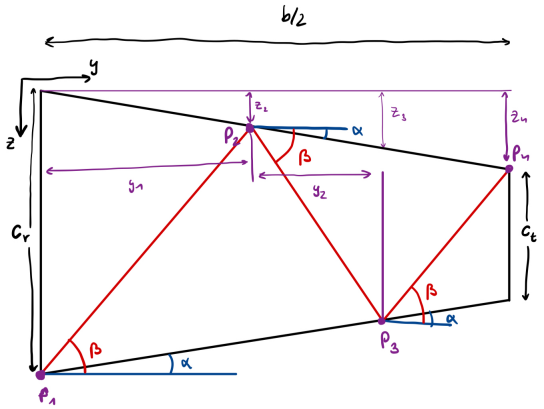

Figure 8.11: Geometry of node locations for a truss of type A

The parameters y_n and z_n give the coordinates of the nodes of the truss along the span to fit inside the aerofoil with an angle β at the base of the triangles. β = 45° for truss D case. The mesh is defined by Equation 8.9 and Equation 8.10 while the aerofoil boundaries define the α by Equation 8.11.

$$\frac{c_r}{tan(\alpha) + tan(\beta} = y_1 \tag{8.9}$$

$$z_2 = tan(\alpha) \cdot y_1 \tag{8.10}$$

$$\alpha = tan^{-1}\left(\frac{c_r - c_t}{b}\left(\frac{t}{c}\right)\right) \tag{8.11}$$

A numerical implementation generates meshes with varying angles β. The mesh of the body and wing section is generated as in Figure 8.12. where the taper of the planform is respected. The body mesh

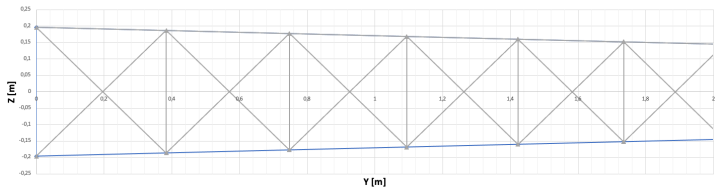

Figure 8.12: Truss mesh on planform of the body from front Oyz plane, beta = 60°

is refined such that at its extremity where it is connected to the wing truss at y = 2.52 m, the truss node angle is adjusted such that the node coincides with the connection. The same is done at the tip of the wing mesh.
The validation of the mesh is done by visual inspection of graphing the points generated. Randomly selected angles were verified to be equal to β and the position of the points at the tip and root were verified with the planform data.

8.5.8. Individual Truss Sizing

For the final report, the additional design will be conducted where the generated planform-sized truss is analysed using frame3dd. The truss axial force results will be used to determine the mode of failure of each individual truss and the cross sections of the individual trusses will be designed depending on these to optimise the structural weight.

8.5.9. 3D Truss Design
For the 3d truss design, cross trusses are added to give stiffness to the truss structure in the xz plane. This is a part of the design to be addressed in further design from the torque load analysis.

8.5.10. Numerical Method
The truss is generated using a spreadsheet and formatted into input for the frame3dd software [83]. Frame3dd conducts a static analysis of the structure as a mesh connected at nodes where moments are not transmitted.

8.6. Material Characteristics
Now that all subsystems and the necessary structural elements have been established, the material needs to be determined for these elements. For most structural elements, the material has already been chosen which is summarised below in Table 8.8. The material for the propeller can also be found in Table 8.8, but this is slightly different from the kevlar/graphite composite with foam core that was chosen in section 6.6. The closest material kevlar 49 is included instead in the material list as exact material properties of the initial chosen composite is hard to find. Also considering that there was no exact trade-off done on the exact kevlar/graphite composite of the propeller, the inclusion of Kevlar 49 for now is justified. It is to be noted that some elements are omitted like the electrical wiring and computer hardware. The material of these elements are deemed non-essential for the design and therefore not considered. All material properties are once again obtained from Grante Edupack 2022 R1 [59].

Table 8.8: Table of essential materials used with relevant properties

Material name	Al(8089)-20%SiC(p) MMC powder	Aluminium, 6061, T6	Kevlar 49
Department	Structures	Structures, Payload and Power & Propulsion	Power & Propulsion
Component	Truss rod	Probe exterior, engine duct, skin and skin reinforcement	Propeller
Location	Body and wing	Body, wing and engine	Engine
Density	2.66×10^3	2.69×10^3 - 2.73×10^3	1.44×10^3 - 1.45×10^3
E (Youngs modulus)[Pa]	1.04×10^{11}	6.66×10^{10} - 7×10^{10}	1.25×10^{11} - 1.35×10^{11}
Yield strength [Pa]	3.1×10^8 - 4.7×10^8	2.4×10^8 - 2.8×10^8	2.25×10^9 - 2.75×10^9
Tensile strength [Pa]	4.8×10^8 - 5.7×10^8	2.9×10^8 - 3.38×10^8	2.5×10^9 - 3×10^9
Compressive strength [Pa]	3.1×10^8 - 4.8×10^8	2.4×10^8 - 2.8×10^8	2×10^8 - 3×10^8
Fatigue strength at 10^7 cycles [Pa]	2.4×10^8 - 2.85×10^8	1.12×10^8 - 1.31×10^8	2.25×10^9 - 2.75×10^9
CO2 footprint, primary production (typical grade) [kg/kg]	12.8 - 14.1	8.16 - 9.53	12.5 - 13.7

8.7. Production Plan
Considering the myriad components within the design, a production plan should be established to manufacture, assemble and integrate all the subsystems. This section will cover the fabrication process from components to final assembly. In addition, purchasing components will also be considered throughout the production process.

8.7.1. Production Flow Diagram
To visualise the production plan, a flow diagram is provided below in Figure 8.13. Here, the production and assembly phase can be seen in the sections coloured in red on the top half of the diagram. This red section is then divided into multiple groups which are parts, sub-assembly, assembly and final assembly. These groups essentially indicate the stage of the production. Within these groups, several elements can be found that need to be either manufactured or assembled from components from the previous stages. Boxes coloured in orange in this production flow diagram means that they are parts

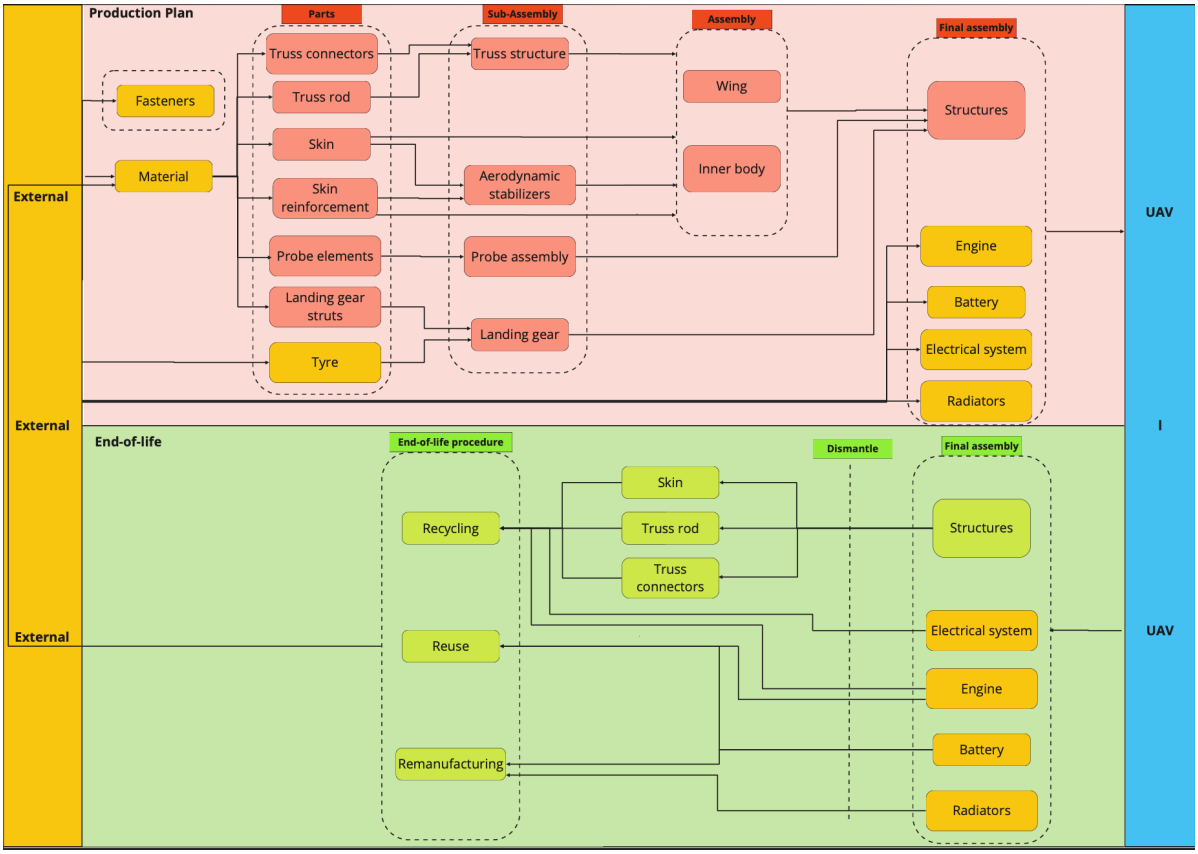

Figure 8.13: Flow chart of production and end-of-life phase

or assemblies purchased from external parties, hence the orange ”external” block found in the left part of the diagram. Lastly, once all the components have been assembled, the designed unmanned aerial vehicle (UAV) is created. This can be seen by the blue ”UAV” block found on the right side of the diagram. To provide more explanation on specific components, a short description is be provided.

Truss structure

One of the most essential parts of the truss structure is the truss rods. This is created by buying material (i.e. Al(8089)-20%SiC(p) MMC powder) from external parties and processing this with for example pultrusion. Another part for the truss structure pertains to the truss connectors. The connectors can be produced by purchasing external metal and can be manufactured by for example casting.

Landing gear

The landing gear sub-assembly relies on the struts and the tyre. For the struts, these can easily be manufactured by extrusions with purchased metal. For the tyre however, it is best to purchase this from external and more knowledgeable parties that can optimally design and have the production infrastructure for this complicated process.

Probe

For the probe design, there are several elements that are required. These elements tend to be made from metals which can easily be purchased. Processing methods can either be casting or extrusion.

Structures final assembly

Once all the sub-assemblies have been produced, the sub-assembly can be combined into two bigger assemblies. One of these assemblies is the wing, which as the name suggests contains all the structural components in the wing sections. For this, the truss structure, skin, skin reinforcements and stabilizers need to be incorporated. The second bigger assembly pertains to the inner body and is very similar to the wing in terms of process and required elements. Combining these two assemblies results in the final structures assembly of the UAV.

Purchased part

To further improve production times and quality, purchasing components is considered. Essentially, when components require manufacturing infrastructure too complex and impractical to implement, then the component will likely be purchased. For the production plan of eCarus, the starting material for the part manufacturing stage can be bought as this is the starting point of the production process. Another important parts to purchase are fasteners. As can be seen in Figure 8.13, it is indicated as a special group on its own as fasteners is involved in many stages of the production, particularly when assembling. So although the fasteners are indicated at the beginning of the flow diagram, it is a component that is relevant throughout the production stage. It is only positioned there due to practical graphic reasons. Furthermore, these fasteners are purchased as there are a myriad companies that can mass produce this with good quality and price. Lastly, tyres are also purchased as discussed before.

Purchased assemblies

Similar to the purchased parts, some assemblies are also purchased. This is done for the engine, battery, electrical system and radiators which are used for the thermal management of the battery. These assemblies are deemed to be too complicated to be manufactured. Opting for external parties is a good choice for quality and cost.

Reused materials

Another aspect to consider for the production is the use of reused materials. This can either be done by reusing materials from retired UAVs or materials from other designs meant for a totally different purpose. As an example, some materials like aluminium can be easily recycled. In this way, the production cost can be lowered. As a result, an end-of-life procedure is also included in the flow diagram. More information on this can be found below in section 8.8.

8.8. End-of-life

To ensure sustainability of the drone and to minimise environmental impact, it is crucial to have a proper end-of-life procedure. In Figure 8.13, the flow is presented that indicates how the drone goes from the production and assembly into the final design. Afterwards, the drone flows into the end-of-life phase. The first step here is to dismantle the drone. This ensures that different important components are separated to efficiently address the end-of-life procedure for each.

Now that the drone is dismantled, three approaches can be taken to close the loop of the circular economy. The first is to recycle the component. In this approach, raw materials are extracted from the component to reform an reuse. Another approach is to reuse the component. This can be done if the drone has reached its end-of-life, but the component is still of sufficient quality. A compromise between the two is remanufacturing of the component. The degradation is too much for immediate reuse, but with addition of some reused or repaired parts, it can perform its function again.

8.8.1. Trusses

The trusses are made of an aluminium reinforced composite (AMC). The fact that it is reinforced with silicon carbide particulates adds some complexity in the end-of-life. As the trusses will have endured many cycles once the drone is retired, recycling is preferred over reuse. For the AMC trusses, two recycling strategies exist. The matrix and particulate can be separated or not. If they are not separated, the trusses are molten and recast. For silicon carbide reinforced AMC, research has proven that up to two times of remelting does not severely degrade the mechanical properties [84]. As the recycling with separation is complex and costly, the trusses will be molten and recast.

8.8.2. Skin

Recycling of aluminium can be a challenge for aerospace applications, as many different alloys are mainly used [71]. As the skin consists only of aluminium 6061-T6, sorting is not necessary and the skin can be recycled immediately. This material can then be used for the skin of new eCarus drones. Following this procedure instead of using primary aluminium 6061-T6, results in a skin production energy decrease of 95% [70].

8.8.3. Batteries

Batteries are complex components, consisting of many interconnected materials. As stated in section 4.1, the battery should be replaced after 3000 cycles. The recycling of batteries poses numerous challenges. It must be disassembled to get the valuable metals, but before that it must be discharged. This can be be a dangerous and labour intensive procedure [85, 86].

Because of the aforementioned challenges, another approach will be taken for the batteries. Some of the batteries will be reused for less critical components of the system. For this one can think of green energy storage at the hub. Batteries that are to be reused in the eCarus drone will require remanufacturing. It has been proven that the state of health of a battery pack can be increased to almost 100% again by replacing the worst aged cells [87].

9 Detailed Design: System Integration

Within this chapter of the detailed design the complete coherence between the subsystems is addressed. First a general overview of the electrical, sensor and thermal management is shown in a diagram in Figure 9.1. Secondly the centre of gravity is determined in section 9.1, after which the second moment of inertia is determined in section 9.2. The full system integration is described in section 9.3. Then, the iteration procedure is layed out in section 9.4. Finally, in section 9.5 an N2 chart is presented.

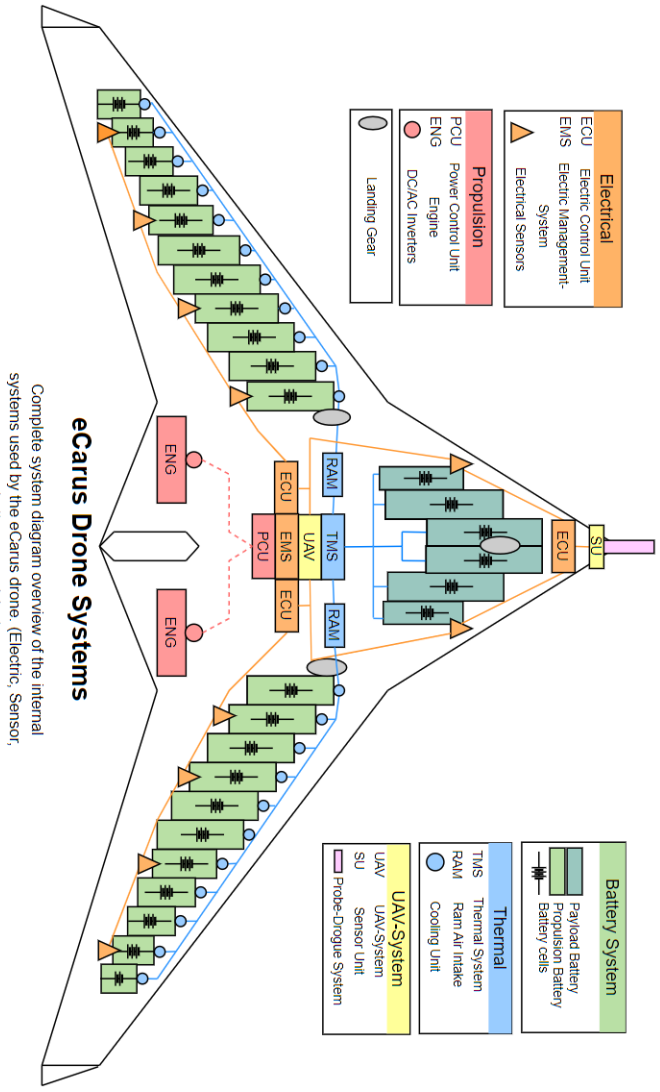

Figure 9.1: eCarus system diagram

9.1. Centre of Gravity Determination

The centre of gravity is an essential part to measure the stability of the aircraft. In section 7.5, most of the stability coefficients are affected by the position of the centre of gravity. Thus, the centre of gravity

needs to be analysed accurately in order to further design the drone. The centre of gravity will be abbreviated as cg in this chapter for simpler.

The main reference point where the cg position is from the leading edge of the root chord. All x in this chapter are defined as the distance from the nose of the drone in the chord-wise direction. The cg in the y-direction is not considered as the drone is assumed to be symmetrical in the xz plane.

9.1.1. Structure

The structure of the drone is split into 4 parts: the landing gear, vertical tail, pylons, and the structure of the wing and body of the drone. The weight and position of all these parts need to be found to get the overall structural cg.

For the centre of gravity of the wing-body structure, the weight distribution needs to be determined. The cross-sectional area of the structure is assumed to be directly proportional to the chord squared. Thus, the centre of gravity of each section can be calculated with **??** where $x_{cg_c}(y)$ is the x-position of the cross-sectional cg in the global coordinate, and c(y) is the chord length of the cross-section. The structure is also assumed to have uniform density, in both the body and wing sections, so only the structural volume needs to be analysed.

$$x_{cg_i} = \frac{\int_0^{b/2} c(y)^2 \cdot x_{cg_c}(y) dy}{\int_0^{b/2} c(y)^2} \tag{9.1}$$

The cross-section is also assumed to be symmetric and for most of the structural weight be from 15% to 55% of the chord. The skins at the outer parts are assumed to be of equal mass on each side of the chord and thus not affect the position of the cross-sectional cg. These assumptions mean that from the leading edge, the cross-sectional cg is thus at 35% of the chord from the leading edge of the section.

To find the position of the cross-sectional cg relative within the coordinate system, the effect of sweep has to be taken into account. Taking these effects into account, the cross-sectional cg ($x_{cg_c}(y)$) can be found with equation Equation 9.2.

$$x_{cg_c} = 0.25 \cdot c_r + y \cdot tan(\Lambda) + 0.1c(y) \tag{9.2}$$

Due to the trapezoidal shape of the sections, c(y) can be calculated easily. The total cg of the wing-body structure(x_{cg_s}) can thus be found with Equation 9.3.

$$x_{cg_s} = \frac{\int_0^{b_b/2} c(y)^2 \cdot x_{cg_c}(y) \cdot dy + \int_{b_b/2}^{b_w/2} c(y)^2 \cdot x_{cg_c}(y) \cdot dy}{\int_0^{b_b/2} c(y)^2 \cdot dy + \int_{b_b/2}^{b_w/2} c(y)^2 \cdot dy} \tag{9.3}$$

The structure of the other components is taken as a point mass on the centre of the component. Since these components are already placed and sized, the weight and position are known. Thus, the overall cg of the structure can be found.

9.1.2. Payload

To find the cg of the payload, the battery needs to first be placed. There are 2 types of battery that need to be carried by the drone: the batteries required for the payload, and the batteries required for propulsion. There are no constraints that are required for the propulsion batteries. The payload batteries, however, need to be at the front of the drone, to minimise the wiring required when recharging as the probe is at the nose of the drone. The constraint where all batteries and payload have to be within 15-55% of the drone remains.

The propulsion battery was decided to be placed at the wing section, to provide bending relief for the structure. An analysis is done to see if there is sufficient volume within the wing to accommodate all propulsion batteries. In the case where it's not enough, the rest of the propulsion batteries will be placed where the payload battery is, to move cg as forward as possible, which is beneficial from a stability point of view. Figure 9.1 shows a visual representation of the configuration.

The available volume within the wing section can be done in a similar way to section 7.2. The area is integrated over the span and the volume was calculated. For the volume in the body section, integration of the thickness in the x and y direction has to be done to determine the dimensions of the batteries in the body section.

With the placement done, the cg of the batteries can be found in a similar way to the structure of the wing-body section. The density is assumed to be constant and is integrated over the span to find the cg of the batteries in the wing section. For the body section, the cg for the triangle part is assumed to be in 0.66 of the height of the triangle. For the rectangular section, the cg is assumed to be at the centre. Then, by performing a weighted sum based on the volume of the triangular, rectangular and wing sections, the overall battery cg is found.

9.1.3. Other Components

For the cg of the engine and systems, the position is just taken as a point mass in the centre of where it is positioned. With the cg of all different components, the cg of the drone can be found.

9.2. Drone Second Moment of Inertia

The second moment of inertia is required to analyse the equations of motion of the drone and simulate the aircraft dynamics. The required second moment of inertia for stability analysis is I_{xx}, I_{yy}, and I_{zz}, as well as one product of inertia I_{xz}.

The drone design is not detailed enough such that integration over the whole drone can be done, thus a lot of assumptions have to be made. The components where the mass is not distributed over a large space and components that do not weigh a big fraction are assumed as point masses around the centre of gravity of the component. These components are the landing gear, tail, payload, and the propulsion systems. Although the engines are quite heavy(10% of the MTOW) and the propeller takes up a large space, the weight is mostly concentrated around the engines of the propulsion system and thus is taken as a point mass around that point. The MOI contribution of each component can thus be calculated with Equation 9.4. ϕ is the axis where the moment of inertia has to be defined and d_{c_ϕ} is the distance of the component to the axis.

$$I_{\phi\phi} = m_c |d_{c_\phi}|^2 \tag{9.4}$$

For the batteries and structures, the assumption cannot be made. Thus, an integration needs to be done to find MOI. The assumption that the area of the structures and batteries increases linearly with the chord squared is once again applied to find MOI. The MOI can thus be found with Equation 9.7.

$$I_{\phi\phi} = \int_0^{b/2} \rho(y) c(y)^2 A |d_{c_\phi}|^2 dy \tag{9.5}$$

ρ is the density of the structure or battery and is unknown as the structure has not been designed fully at this point. A is also unknown as the area of the structure is also not known. Another assumption has to be made where the density is uniform everywhere. This is applied to both the batteries and structures. With this assumption, Equation 9.6 can be formulated

$$\rho = \frac{m}{V} = \frac{m}{\int_0^{b/2} A \cdot c(y)^2} \tag{9.6}$$

Substituting this into Equation 9.7 gives:

$$I_{\phi\phi} = \int_0^{b/2} \frac{m}{\int_0^{b/2} A \cdot c(y)^2} c(y)^2 A |d_{c_\phi}|^2 dy = \int_0^{b/2} \frac{m}{\int_0^{b/2} \cdot c(y)^2} c(y)^2 |d_{c_\phi}|^2 dy \tag{9.7}$$

This eliminates the unknown variables and thus the integral can be evaluated numerically. Summing the contributions of all the components will result in the full moment of inertia of the aircraft.

9.3. Full System Integration

The sizing of each subsystem was done in their respective chapters, but these subsystems need to be combined to create the full system. The main subsystems to be integrated are the tail, wing and body, landing gear, engines, batteries, payload, and electrical and thermal management systems. These subsystems are heavily interconnected and the interactions between the subsystems need to be analysed, and an optimal configuration for the placing of these subsystems is required.

The integration of the tails, batteries, payload, and electrical and thermal management systems were done in section 7.3 and section 9.1. But the integration of other subsystems still needs to be done.

9.3.1. Planform

The aspect ratio, span and surface area of the planform were already determined in section 7.1. With the volumetric analysis in section 7.2, the taper ratio of the body can also be found, for a given transition point of the wing and body. Although these parameters have been defined, they are insufficient to define the entire shape of the planform.

The parameters that are still required are the sweep of the wing and body section, as well as the transition point of the body and wing. These parameters are heavily interconnected with the integration of the other subsystems as it defines the limits where subsystems can be integrated, but the integration of subsystems also affects parameters like cg which impose constraints on the sweep. Thus, the planform should be defined simultaneously with system integration.

9.3.2. Landing Gear

In this section, the approach is laid out on how the landing gear placement and its height are determined. During a discussion with Malcom Brown, an expert in blended wing body (BWB) aircraft and active at the Delft University of Technology, he mentioned that landing gear placement can be a difficult task. Malcom Brown works on the Flying V and stated that for the project landing gear sizing turns out to be one of the biggest issues. The original Flying V has a landing gear height of about $6\,\mathrm{m}$, a heavy construction. It is thus important that proper landing gear placement and sizing are performed.

Landing gear disposition

The methodology used for the design is taken from Roskam [88]. It is noted that this methodology is meant for the design of tube-and-wing (TAW) aircraft. However, Malcom Brown and Dr Roelof Vos stated that it is also applicable to BWB aircraft, as they need to comply with the same ground handling and clearance regulations as TAW aircraft [89].

The first step is to opt for a configuration to use. For the eCarus drone, a conventional retractable tricycle configuration is chosen. Non-retractable landing gear would result in an unacceptably high drag penalty with the drone's cruise speed. Then the location of the main landing gear (MLG) is assumed to be 15% of the mean aerodynamic chord (MAC) behind the centre of gravity. The nose landing gear (NLG) is then placed such that it carries 15% of W_{TO} [90].

Three criteria regarding angles must be fulfilled. The longitudinal and lateral clearance criteria state the angle of the line from the outer MLG to the first component it reaches must not be larger than $15°$ and $5°$, respectively. The lateral tip-over criterion is a bit more difficult to explain, thus a visualisation is presented in Figure 9.2.
First, a landing gear height is chosen such that the longitudinal clearance criterion is fulfilled. Then, the angle of $55°$, shown in Figure 9.2, is used to assess the track width of the MLG with some simple geometric relations. Once the track width is obtained, a check must be performed if the lateral clearance criterion is fulfilled.

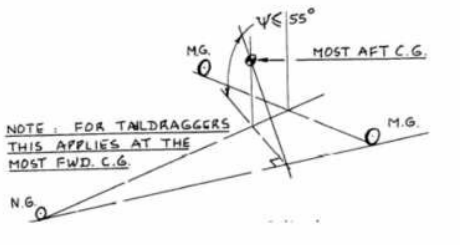

Figure 9.2: Lateral tip-over criterion [88]

Landing gear integration with other subsystems

Although the landing gear positioned would meet all the requirements stated before, the design might not be feasible

when combined with other subsystems. The position could be outside the bounds of the planform, or might coincide with elements of other subsystems. This has to be verified and change accordingly.

It was decided, that the position where the body section transitions to the wing, will be where the landing gear is placed. This is done for structural reasons as the transition point would have a strong structure and thus can accommodate the load from the landing gear. This constrains the position of the transition point as it has to be where the landing gear is required to be.

The landing gear also has to be within the bounds of the planform. This is a strict requirement on the main landing gear as the main landing gear holds most of the load. It could be solved by changing the sweep, the cg, or the

The nose landing gear, however, could be slightly positioned in front of the nose. This would mean the nose landing gear has to be at an angle with the drone as shown in fig. This would impose increased structural requirements as a stronger structure would be required to maintain the loads. Another alternative would be to increase the loads on the nose landing gear, bringing the landing gear inwards. This would mean that more force would be required to turn the nose landing gear as well as a smaller normal force for braking on the main landing gear. Both solutions would solve the problem where the nose landing gear is outside the bounds of the planform but comes with its own drawbacks. In the case this happens an analysis of which solution should be done.

The ability for the landing gear to be stored is also something that has to be checked. This could be solved by, for example, creating fairings or decreasing the landing gear height by increasing sweep. In the case this happens, an optimal solution has to be chosen to provide space for the storage of the landing gear.

9.3.3. Engine

For the placement of the engines, it was decided to place the middle of the engine on the transition point, similar to the landing gear. This is done to maximise structural efficiency as the structure already has to be stronger at that point, so incorporating the engines at this point would be more efficient.

The placement of the engines also affects the sizing of the tail. An engine that is placed too far would mean that a large tail size is required for a feasible design, or there might even be no feasible tail size. Thus, this condition has to be checked within the iteration.

9.4. Iteration Procedure for Systems Integration

As mentioned above, the subsystems are highly interlinked. For example, the landing gear design depends on the cg, but the cg also depends on the landing gear. Thus, an iteration procedure needs to be implemented to find a converged design. The iteration consists of 2 loops, the integration loop and the aerodynamics loop. The integration loop is to verify that physical constraints are not violated and to converge on a configuration. The aerodynamic loop is to ensure aerodynamic constraints, such as static and dynamic stability, are not violated.

The physical constraints ensure that the configuration is physically feasible and does not collide with each other. The physical constraints are as follows:

- The subsystems should not coincide
- Moving mechanisms of subsystems should not collide with others.
- There is a feasible planform where there is enough volume to store the payload.
- The region where the batteries need to be stored should not contain any large volume subsystems such as the engines and propellers.
- The tail should be a set distance away from the engines as explained in section 7.3
- There is a feasible landing gear sizing to meet landing gear requirements in subsection 9.3.2
- The main landing gear should be within the bounds of the planform

- The nose landing gear should be close to the bounds such that feasible solutions can be implemented as explained in subsection 9.3.2.
- There is sufficient space for the landing gear to be stored
- The main landing gear should be at least 5m apart as the body section cannot be too small

The aerodynamic constraints ensure that the configuration is feasible in an aerodynamic point of view and ensures the integration does not disrupt the aerodynamic functioning of the drone. The aerodynamic constraints are as follows:

- The cg should be in front of ac for static stability
- The ac of the vertical tail should be behind cg for directional stability
- All eigenmotions should be stable except for the spiral motion, but the double time should be above accepted values.
- There is a feasible tail size where the drone can operate on one engine
- There is enough space for control surfaces for the drone to be controllable in all configurations

With the constraints set, the iteration can then be done.Figure 9.3 shows a general diagram for the iteration procedure.

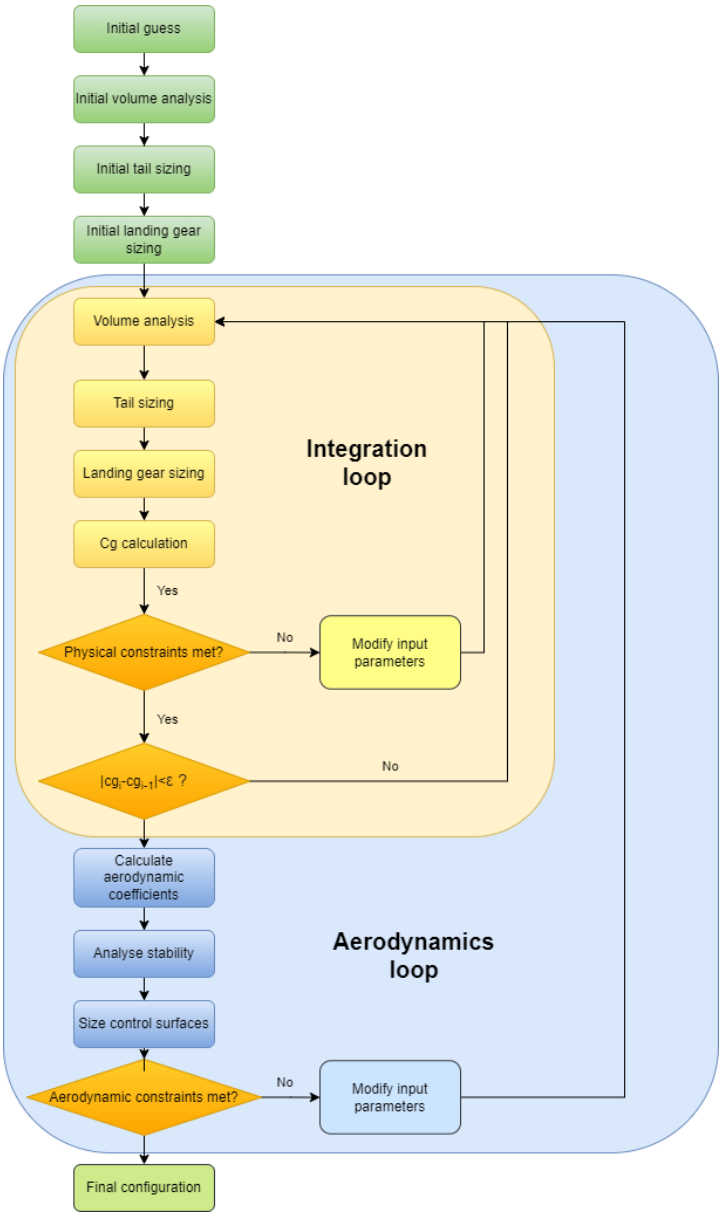

Figure 9.3: Iteration procedure flow diagram

Decision variables

Before performing the iteration, the decision variables need to be identified. These are variables that can be changed and are iterated on. The main decision variables are:

- Sweep of the body and wing section(Λ_w and Λ_b)
- The surface area of the tail (S_v)
- Aspect ratio of the body tail and wing-tip tails($A_{v_{wt}}$ and A_{v_b})
- x-position of the engines
- Proportion of load the nose landing gear takes

These variables are not the only variables that could be changed during the iterations but are the main parameters to be iterated upon. Other variables could also be changed if needed but these will be explained during the design.

There are also variables that need to be iterated upon. These variables have cross dependencies and thus cannot be calculated with just 1 iteration as explained at the start of the subsection. These variables are:

- The cg
- The transition point between the wing and body section(b_b)

Initial guess

An initial guess of the decision and iterated variables were done. These were either based on literature or were from previous calculations done in the midterm report[5]. A good initial guess is beneficial, as the iteration might converge toward different solutions that are unfeasible with bad initial guesses. The cg would also be guessed at this stage as cg is a required input.

After the guessed decision variables are determined, an initial volumetric analysis, followed by an initial tail sizing and landing gear positioning can be done. Since the transition point needs to be on the landing gear, this provides an initial value for the transition point where Landing gear track width = b_b

Volume analysis

The volume analysis ensures there is enough volume within the drone to store the payload. The method to do this is explained in section 7.2. It takes as input the transition point and outputs a planform that is optimised for volume. This analysis does not calculate sweep but does calculate all other parameters required to describe the 2-section planform. The planform created here uses the same sweep as before but calculates other parameters like taper ratio.

Tail sizing and landing gear positioning

The tail is then sized and positioned with methods from section 7.3. It takes as input the planform of the drone and the position of the cg, and outputs the full tail position, dimension and size.

The landing gear is placed with methods from subsection 9.3.2. It also takes as input the cg and planform of the drone but also requires the placement and diameter of the engine. It outputs the landing gear position in both the x-direction and the y-direction, and the transition point b_b.

Cg calculation

The cg can then be calculated based on the landing gear position, as well as the tail size and position. The cg also depends heavily on the planform as the battery positioning depends on the planform.

Physical constraints

The current configuration is then checked to see if the physical constraints are met. If they are not met, the decision variables can be modified and the integration loop is redone with the new decision variables.

An analysis should be done to find the variable which has the largest impact on solving the violated constraint, while not violating the other constraints. For example, increasing the sweep to move cg backwards would decrease the length of the landing gear and thus reduce the required volume to store the landing gear. This is a much better alternative than incorporating fairings for the landing gear which would reduce aerodynamic efficiency.

Convergence check
If the constraints are met, the convergence of the iterated variables still has to be checked. The difference between the values of the current iteration and the previous one should be smaller than an error margin to confirm that the iterated variables have converged toward a value. If not, the new cg and b_b calculated are used as inputs in the first 3 steps and the integration loop is redone.

This is necessary as the cg depends on the planform and the position of the tail and landing gear, but the position of the tail and landing gear also depends on cg. Whereas b_b depends on the landing gear position, which depends on the planform and cg, which once again circles back to b_b. This cross-dependency thus requires iteration to find the correct value.

Aerodynamic coefficients
Once the physical constraints and the iterated variables have converged, a full configuration of the drone is obtained. With the full planform and configuration of all subsystems, the drone can then be modelled and analysed with CFD, and the stability coefficients can be calculated with methods described in section 7.5.

Stability
With the aerodynamic coefficients calculated, the eigenvalues of the drone's equations of motion can be calculated. This estimates the eigenmotions and gives an idea of the behaviour of the aircraft under disturbances or inputs.

Control surface sizing
With the full planform sized and aerodynamic coefficients determined, a $C_{L_{max}}$ should be obtained. Thus, the controllability of the aircraft can be analysed and the control surfaces can be sized with methods from section 7.7. The high-lift devices are also sized here for better take-off and landing performance.

Aerodynamic constraints
With the eigenvalues and aerodynamic coefficients determined, as well as the centre of gravity and aerodynamic centre, the stability of the drone can be found and analysed. Thus, the drone can be checked if the aerodynamic constraints are fulfilled.

If the drone is statically unstable longitudinally, it was found that changing the sweep of the drone will change the stability. Increasing the sweep of the wings have a stabilising while increasing the sweep of the wing section is destabilising. While this property is ultimately determined by the configuration of the batteries and other subsystems, this general rule will be helpful in the case of static instability.

For dynamic stability, it was found that the dutch roll was the least stable eigenmotion due to the small tail size and moment arm. Increasing the tail size manually can bring the eigenmotion stable. But this is not guaranteed as if the body is not long enough, no tail size will be stabilising, and thus the planform has to be changed.

The new inputs will then be put back into the integration loop, where the integration loop will be redone. The integration loop constraints and convergence has to be rechecked and iterated creating a new planform. Then, the stability is rechecked and the iteration goes on until a converged configuration, that meets all physical and aerodynamic constraints is found.

9.5. N2-Chart
The N2-chart is divided into the following segments: flight control, control tools, structural, electrical, intra-aircraft and hub. The interrelation between these segments is described using inputs/outputs in the form of raw data, electricity, controls, forces, heat and airflow interference. It can clearly be seen that the electrical component main influential factors are controls and thermal management whereas for structures the forces play a significant role. The external factors are shown with environmental circles outside of the N2-chart. The N2-chart can be found at the end of this chapter.

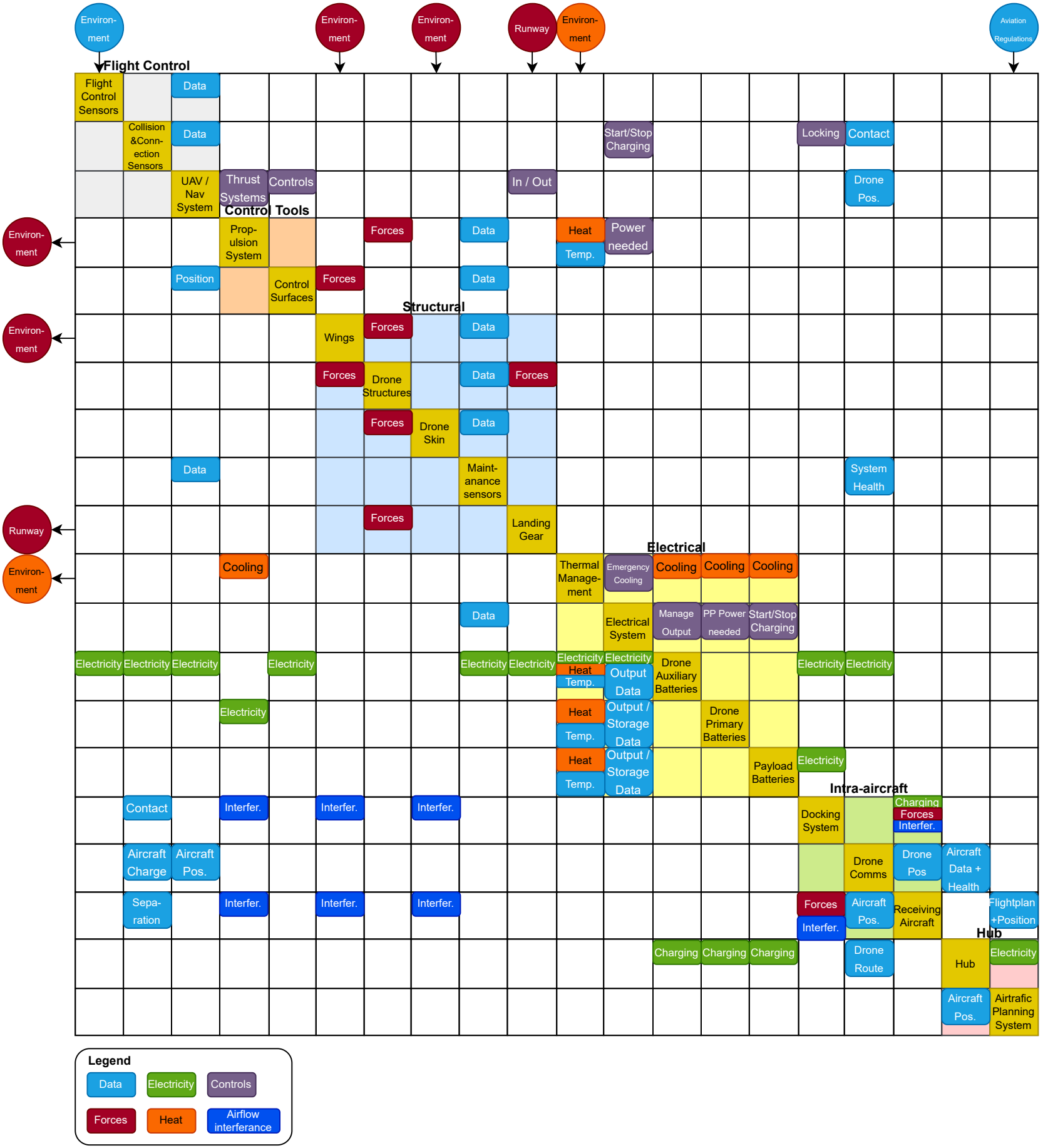
Environ-ment
Environ-ment
Environ-ment
Runway
Environ-ment
Aviation Regulations
Flight Control
Flight Control Sensors
Data
Collision &Conn-ection Sensors
Data
Start/Stop Charging
Locking
Contact
UAV / Nav System
Thrust Systems
Controls
In / Out
Drone Pos.
Control Tools
Environ-ment
Prop-ulsion System
Forces
Data
Heat
Temp.
Power needed
Position
Control Surfaces
Forces
Data
Structural
Environ-ment
Wings
Forces
Data
Forces
Drone Structures
Data
Forces
Forces
Drone Skin
Data
Data
Maint-anance sensors
System Health
Runway
Forces
Landing Gear
Electrical
Environ-ment
Cooling
Thermal Manage-ment
Emergency Cooling
Cooling
Cooling
Cooling
Data
Electrical System
Manage Output
PP Power needed
Start/Stop Charging
Electricity
Electricity
Electricity
Electricity
Electricity
Electricity
Electricity
Heat
Temp.
Output Data
Drone Auxiliary Batteries
Electricity
Electricity
Electricity
Heat
Temp.
Output / Storage Data
Drone Primary Batteries
Heat
Temp.
Output / Storage Data
Payload Batteries
Electricity
Intra-aircraft
Contact
Interfer.
Interfer.
Interfer.
Docking System
Charging Forces
Interfer.
Aircraft Charge
Aircraft Pos.
Drone Comms
Drone Pos
Aircraft Data + Health
Sepa-ration
Interfer.
Interfer.
Interfer.
Forces
Interfer.
Aircraft Pos.
Receiving Aircraft
Flightplan +Position
Hub
Charging
Charging
Charging
Drone Route
Hub
Electricity
Aircraft Pos.
Airtrafic Planning System
Legend
Data
Electricity
Controls
Forces
Heat
Airflow interferance

10
Detailed Design: System Iteration

This chapter aims to describe the iteration procedure of the eCarus design. Performing iterations is a crucial part in ensuring a feasible design, as more accurate values for key parameters can be obtained. section 10.1 explains the general iteration procedure that is used throughout the design of the eCarus system. Hereafter, in section 10.2, the generated engineering budgets are discussed for the primary ánd secondary parameters that influence the design. Finally, section 10.3 presents the results of the performed iteration procedure and discusses the found values with their respective engineering budget.

10.1. General Iteration Procedure

The general iteration procedure is commenced with the corrected preliminary weight estimate and wing loading diagram found in section 6.1. These lead to three key parameters for the design of the eCarus system, namely the total weight, surface area and required power for the eCarus aircraft. These key parameters then flow down to the different departments, where a more detailed analysis will be performed on the field of expertise allocated to each department. More accurate results will be acquired from this, which can then be used to get a more reliable estimate for the three aforementioned key parameters.

First of all, the Aerodynamics department will use the estimated total weight, surface area and required power to generate a preliminary wing planform. Analysis of this planform will generate a more accurate prediction for the aerodynamic coefficients of the aircraft, such as the zero-lift-drag coefficient (C_{D_0}) and the maximum lift coefficient. Moreover, a preliminary tail can be sized, where after an estimate can be made on the position of the centre of gravity. Finally, all aerodynamic load distributions can be computed for the generated wing planform.

The Operations department can use the estimations for weight, surface area and required power to assess if the operational range is still feasible and achievable. Possible revision of the operational range can be performed.

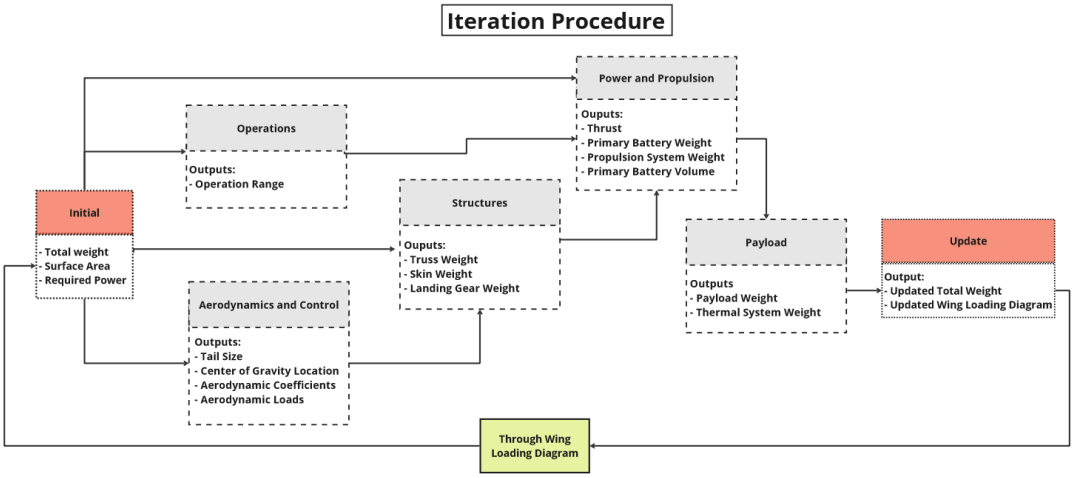

Figure 10.1: Schematic of the iteration procedure

The aerodynamic load distributions, centre of gravity location, wing planform and overall weight of the aircraft enable the Structures department to size and optimise the internal structure of the aircraft. From

this sizing, a weight for the truss structure, skin and landing gear originates. These weights can be used later on to obtain a more accurate estimation of the total take-off weight of the eCarus aircraft.

The Power and Propulsion department can, with the required power, compute the required thrust for the aircraft. This enables a more reliable determination of the weight of the propulsion system. Moreover, using a more accurate estimation for the structural weight and an updated operational range, a revised weight of the primary battery can be calculated accompanied with its respective volume.

Hereafter, the Payload department can design an improved thermal system with the latest primary and payload battery sizes. From this, a more accurate prediction of the thermal system weight will flow down.

Finally, all updated weight estimates can be combined to acquire an iterated total weight estimate. Furthermore, with more reliable values for aircraft performance parameters obtained during the iteration procedure, the wing loading diagram can be updated. Combining this diagram with the newly found weight estimate generates a revised surface area and required power for the eCarus aircraft. This brings the design back to the beginning of the iteration loop, enabling the departments to iterate once more over the newly found values. This entire iteration procedure is schematically presented in Figure 10.1.

10.2. Engineering Budgets

For the iteration to work properly, the use of engineering budgets is of great importance. Engineering budgets are set in place such that a guideline is created for the magnitude of key parameters. Different departments can use these budgets to assess whether their acquired values throughout the iteration are feasible and it is crucial that the found values lay within the allocated budget to ensure smooth progression of the iteration. Iteration values that are outside of the allocated budget should be discussed before continuation of the design. Table 10.1 presents the allocated budgets for all primary parameters that drive the design of the eCarus system the most. The budgets are initiated with an initial estimate based on the results obtained in the midterm report [6]. Thereafter, for each consecutive iteration, the budgets are refined and the range between the maximum and minimum acceptable value is decreased.

Table 10.1: Primary system engineering budgets

Primary System Budgets	Pre-midterm		Iteration 0		Iteration 1		Iteration 2	
Parameter	Max	Min	Max	Min	Max	Min	Max	Min
Total Weight	20 000 kg	19 000 kg	7000 kg	5000 kg	6000 kg	5000 kg	5500 kg	5000 kg
Required Power	4.0 MW	3.3 MW	1.0 MW	400 kW	700 kW	400 kW	600 kW	400 kW
Primary Battery Weight	12 000 kg	10 000 kg	2000 kg	1200 kg	1600 kg	1200 kg	1400 kg	1100 kg
Payload Battery Weight	4000 kg	2000 kg	3000 kg	2000 kg	2800 kg	2200 kg	2700 kg	2500 kg

Table 10.2 shows the allocated budgets for all secondary parameters, which are more department specific. These parameters are updated within the detailed design of each specific area of expertise whereas the evolution of the primary parameters is mostly the consequence of the entire iteration loop. For this reason the secondary parameters are divided per department. For the secondary parameter budgets, the same reasoning applies as for the primary parameter budgets. The range of the budget is decreased with each consecutive iteration and compliance with the budget throughout the iteration is vital. An additional note is for the rows that show '-' signs. These are not appointed a budget at that corresponding stage of the design, as by then no detailed design was performed on said parameters yet.

10.3. Iteration Results

After performing the entire iteration procedure, the development of all values throughout each iteration should be gathered. This makes it such that a general conclusion can be made about the nature of the values, i.e. if a converging or diverging behaviour can be observed. Furthermore, throughout the iteration procedure, the adherence to the set engineering budgets should be checked. Table 10.3 aims to provide all necessary information to first of all highlight the nature of the evolution of the key param-

Table 10.2: Secondary system engineering budgets

Secondary System Budgets	Pre-midterm		Iteration 0		Iteration 1		Iteration 2	
Parameter	Max	Min	Max	Min	Max	Min	Max	Min
Power and Propulsion								
Cruise Thrust per Engine	-	-	-	-	4000 N	1800 N	2500 N	1800 N
Max Thrust per Engine	-	-	-	-	6000 N	4000 N	4900 N	4000 N
Number of Engines	8	6	2	2	2	2	2	2
Engine Weight	1400 kg	1100 kg	500 kg	200 kg	350 kg	200 kg	300 kg	200 kg
Diameter Engine	-	-	-	-	2.9 m	2.4 m	2.7 m	2.4 m
Structures								
Total Structure Weight	6000 kg	4500 kg	2500 kg	1000 kg	2000 kg	1000 kg	1500 kg	1000 kg
Aerodynamics and Control								
$C_{l_{max}}$	1.6	0.8	1.6	1.0	1.5	1.1	1.3	1.1
C_{D_0}	0.04	0.02	0.015	0.006	0.01	0.006	0.009	0.006
e	1.0	0.8	1.0	0.85	1.0	0.85	1.0	0.9
Payload								
Thermal System Weight	-	-	-	-	-	-	300 kg	150 kg
Operations								
Operational Range	750 km	650 km	700 km	650 km	680 km	655 km	675 km	660 km

eters of the design. Secondly, the margin percentages are presented with respect to the boundaries of the set engineering budget for each parameter to assess if the budget is met. All margins presented in green point towards the fact that the budget is adhered, whereas the margins showed in yellow should be opened up to a discussion.

The first debatable margin presents itself for the number of engines. This is rather logical however, since the budget does not specify a range but a set value. This is however acceptable, as the prescribed number of engines can be retained with changing power requirements by changing the selected engine for the design. A decreasing required power and constant number of engines infers that a less powerful but possibly lighter engine can be selected.

The second debatable margin can be seen in the budget for the Oswald efficiency factor during the pre-midterm iteration. This appearance was discussed with the Aerodynamics department, where after it was concluded that it would not pose a risk to the design. Since the Oswald efficiency factor is a parameter that is preferred to be optimised, the lower limit of 0.8 was deemed to be acceptable as the value would most definitely increase with following iterations. In hindsight, it can indeed be seen that the value increased with following iterations.

To conclude the system iteration procedure, Figure 10.3 presents a visual representation of the evolution of the primary parameters throughout consequent iterations. It aims to clarify the converging nature of the primary parameters, which is a desirable result.

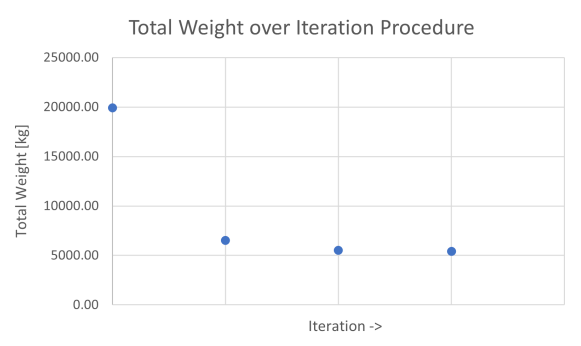

(a) Total weight evolution throughout subsequent iterations

(b) Required power evolution throughout subsequent iterations

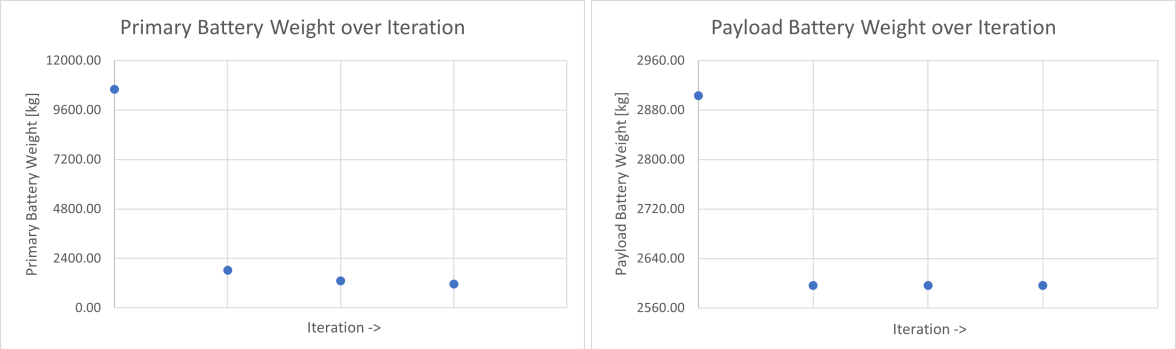

(a) Primary battery weight evolution throughout subsequent iterations **(b)** Payload battery weight evolution throughout subsequent iterations

Figure 10.3: Primary parameters evolution throughout subsequent iterations

Table 10.3: Evolution of the primary and secondary parameters during the iteration procedure

Iteration Evolution	**Pre-midterm**	**Unit**	**%Margin to Budget**		**Iteration 0**	**Unit**	**%Margin to Budget**	
Primary System Parameters			**Upper**	**Lower**			**Upper**	**Lower**
Total Weight	19 902.00	kg	0.49	4.53	6511.83	kg	7.50	23.22
Required Power	3920.60	kW	2.03	15.83	797.74	kW	25.35	49.86
Primary Battery Weight	10 600.10	kg	13.21	5.66	1822.50	kg	9.74	34.16
Payload Battery Weight	2903.20	kg	37.78	31.11	2596.50	kg	15.54	22.97
Secondary System Parameters								
Power and Propulsion								
Cruise Thrust per Engine	-	N	-	-	-	N	-	-
Max thrust per Engine	-	N	-	-	-	N	-	-
Number of Engines	7	-	14.29	14.29	2	-	0.00	0.00
Engine Weight	1224	kg	14.38	10.13	400	kg	25.00	50.00
Diameter Engine	-	m	-	-	-	m	-	-
Structures								
Total structure weight	5175.00	kg	15.94	13.04	1693.08	kg	47.66	40.94
Aerodynamics and Control								
$C_{l_{max}}$	1.400	-	14.29	42.86	1.400	-	14.29	28.57
C_{D_0}	0.030 00	-	33.33	33.33	0.012 00	-	25.00	50.00
e	0.80	-	25.00	0.00	0.95	-	5.26	10.53
Payload								
Thermal system weight	-	kg	-	-	-	kg	-	-
Operations								
Range	734.81	km	2.07	11.54	688.20	km	1.71	5.55

Iteration Evolution	**Iteration 1**	**Unit**	**%Margin to Budget**		**Iteration 2**	**Unit**	**%Margin to Budget**	
Primary System Parameters			**Upper**	**Lower**			**Upper**	**Lower**
Total Weight	5514.97	kg	8.79	9.34	5413.76	kg	1.59	7.64
Required Power	610.00	kW	14.75	34.43	598.99	kW	0.17	33.22
Primary Battery Weight	1316.92	kg	21.50	8.88	1153.70	kg	12.68	4.65
Payload Battery Weight	2596.50	kg	7.84	15.27	2596.50	kg	3.99	3.72
Secondary System Parameters								
Power and Propulsion								
Cruise Thrust per Engine	3011.56	N	32.82	40.23	2024.15	N	23.51	11.07
Max thrust per Engine	5534.34	N	8.41	27.72	4634.61	N	5.73	13.69
Number of Engines	2	-	0.00	0.00	2	-	0.00	0.00
Engine Weight	223	kg	56.95	10.31	223	kg	34.53	10.31
Diameter Engine	2.78	m	4.32	13.67	2.5	m	8.00	4.00
Structures								
Total structure weight	1378.55	kg	45.08	27.46	1145.55	kg	30.94	12.71
Aerodynamics and Control								
$C_{l_{max}}$	1.200	-	25.00	8.33	1.269	-	2.44	13.32
C_{D_0}	0.008 02	-	24.69	25.19	0.008 13	-	10.70	26.20
e	0.95	-	5.26	10.53	0.95	-	5.26	5.26
Payload								
Thermal system weight	-	kg	-	-	295	kg	1.69	49.15
Operations								
Range	665.00	km	2.26	1.50	665.00	km	1.50	0.75

11 Detailed Design: Operations

This chapter aims to provide an overview of the operations and logistics of eCarus. The launching and landing system is analysed a redesign is proposed. Secondly, Hub placement is designed. Finally, what happens during emergency situations, and the operations concerning maintenance are analysed.

11.1. Launching and Landing System

There are four user requirements which drive the launching and recovery system of the drone and thereby the entire hub design:

- **[REQ-US-09]**:*The system shall declutter recharge logistics of electric aircraft at airports.*[4]
- **[REQ-US-PER-05]**:*A hub of the system shall be placeable on land and the sea.*[4]
- **[REQ-US-SUS-03]**: *The hub shall be capable of producing its renewable energy when placed at a remote location.*[4]
- **[REQ-S-MSC-03]**: *The system shall be extendable to worldwide coverage*

Using these requirements, a trade-off on the launch and recovery methods was conducted in the midterm report [6] which resulted in an electromagnetic catapult launch (CD-TO-04) and an arresting cable for landing (CD-LA-03). A preliminary estimate of cost was used in the trade-off where the arresting cable scored well (4/5) on cost and complexity, and the electromagnetic launch did not score well (2/5). In the detailed design phase, the exact prices of such a system are further investigated.

11.1.1. Costs of an Arrested Landing System

The electromagnetic launching of aircraft and their retrieval by arresting wire is almost exclusively used by the military making information on the system and its costs hard to find. However, the following conclusions can be drawn from research:

- The cable is hard to source. The cable is so advanced that only the United States and China are capable of producing such cables [91].
- Multiple cables are needed. The Nimitz class aircraft carrier uses 4 and the Gerald R. Ford carrier uses 3 [92].
- The price of the cable is extremely high. Each cable is rumoured to cost around 1.5 million US dollars [91].
- The operational life is relatively small. The operational life of the cable that makes contact with the landing aircraft, called the cross-deck pendant, is 125 arrestments. The operational life of the rest of the cable, called the purchase cable, is 1,400 arrestments [93].

The most common arresting gear used is the MK-7 hydraulic arresting gear on the Nimitz class aircraft carrier. Although little information is available it is clear that the system is large, complex, and likely very expensive [94]. Together with the high costs of the arresting cable, the price of such a system is extremely expensive. The costs of building an aircraft carrier-sized runway on water also exacerbate the financial problem. Designing an overly expensive system poses a major risk to the feasibility of the system. Therefore potential alternative solutions must be revisited and the added benefit of placing hubs on water must be compared to the added costs. This is done to mitigate the risk of a future implementation of eCarus becoming a financially unsustainable system.

11.1.2. Alternative Solutions

Without an arrested landing, landing on water also becomes infeasible. The options considered in the midterm report were a net, parachute, arresting cable, and conventional landing [6]. At this stage of the design the drone weighs roughly 7 tons meaning that parachute landing is not feasible. Even if the system was redesigned to smaller drones, parachutes could not guarantee a sufficiently short landing distance to significantly decrease the costs of building multiple aircraft carrier-sized floating hubs. A net was discarded in the midterm report for being too slow to cycle to the next drone. This reasoning is still

valid now. Therefore conventional landing becomes the only feasible option. However, conventional landing is not compatible with hubs on water. Therefore the impact of only placing hubs on land must be analysed.

11.1.3. Comparing the Costs and Benefits of Placing Hubs on Water

The predominant negative impact of building only land-based hubs is the decrease in the number of serviceable flights. However, the market for flights that only need recharges on land is still large. Due to the large infrastructure requirements needed for eCarus to function, it will take a long time before the market of in-land recharges is saturated. This means that eCarus can expand at maximum speed for a long time before it would start to feel the decrease in market size due to the lack of on-sea hubs. This makes it an acceptable decision for the initial implementation of the system. For later expansion to on-sea hubs, lessons learned from many years of operating on land can be used. An analysis of flights serviceable by placing hubs on the sea can be done using the land-based procedure, this analysis can be conducted in further design.

Considering the large price associated with the technology required to fully operate from seaborne hubs, and the minimal effect it will have on the perceived market size of eCarus during its initial phases and intermediate phases of the business, it is decided to only place hubs on land. This has an effect on the design of the eCarus system and drone. It however introduces a new risk that if hubs are placed on water in the future, the drone will likely need an extensive overhaul to be compatible with the launch and recovery requirements of such a hub.

11.1.4. Changing the Launching and Recovery Solution

The choice for electromagnetic launch and arresting wire recovery was a good choice assuming that [REQ-US-PER-05] could not be changed. However, leaving out sea-placed hubs changes the trade-off for the launching and recovery system. Conventional landing and take-off become the preferred configuration due to its simplicity, low costs, lower power loading, and the possibility to use existing infrastructure. Drawbacks such as a lower wing loading are considered acceptable.

Using conventional landing naturally leads to using conventional take-off due to the landing often being more sizing for the aircraft than take-off, and due to the compatibility of the two solutions. In summary, the drone will be us conventional take-off and landing.

11.1.5. Purpose-built Hubs Versus the Use of Existing Airports

Using conventional landing and take-off completely changes the hub aspect of eCarus. Using existing airports and their infrastructure suddenly becomes possible. Therefore analysis is done on whether or not to use existing airports and if so, what are requirements there are for selecting suitable airports. This section elaborates on the operational decision regarding the use of purpose-built hubs versus the use of existing airports. First, a suitable airport category is selected where after the feasibility of building and operating purpose-built hubs is compared to using existing airports is discussed

To make a proper comparison, it is important to define the different airport categories. The FAA classifies airports into 5 categories: national, regional, local, basic, and unclassified [95]. For context, in the Netherlands such a system would classify Amsterdam Schiphol and Rotterdam the Hague Airport as national airports, Lelystad and Groningen Eelde Airport as regional, Den Helder de Kooy and Seppe Breda Airport as local airports, and Hilversum and Midden Zeeland Airport as basic airports.

International airports are extremely busy and adding many drone flights to their roster will be expensive, logistically hard, and will clutter the airspace. This is in conflict with [REQ-US-09]: *"The system shall declutter recharge logistics of electric aircraft at airports"* [16]. Local and unclassified airports are omitted as these airports often have grass runways which would require strong landing gear and impose a weight restriction on the drone. Regional and local airports, however, are not nearly as busy as international airports and do have asphalt or concrete runways. In addition, there are many of these airports scattered around the world allowing for easier optimisation of hub placement.

As the purpose-built hubs do not have an existing design, literature on regional and local airports is

used for comparison. According to Director General ACI EUROPE Oliver Jankovec, ”61% of airports handling less than 5 million passengers per year are loss-making – with that percentage rising to 71% for those with less than 1 million passengers” ACI (2019) According to research on regional airport profitability [96], airports that handle below 500,000 passengers annually are all assumed to be unprofitable. This implies that regional and local airports are unprofitable even though these airports have multiple income-generating activities that the purpose-built hubs would not have. These activities include, but are not limited to; passenger airline landing fees (17.2%), passenger airline terminal arrival fees, rents and utilities (24.0%), parking and ground operations (18.6%), and rental cars (8.8%) [97]. The hubs would only generate income from the aircraft clients, which in turn would mainly come from the increase in cost for the passengers. Designing the hubs to operate as regional hubs to be able to gather the aforementioned income streams would be illogical compared to using the vast network of existing regional airports.

Considering the scope of the project and the economic viability. It is decided to only use existing regional and local airports by renting hangars and renting landing and take-off slots. This operational decision has various implications for external parties. The main one is for the regional and local airports. Most important is deemed the sustainability effects and the scheduling of the airports. In this stage of the project, it is assumed that the airports can handle the extra take-offs and landing as the airports are not busy. The addition of electric drones to the flights of a regional airport will cause far less noise pollution to the surrounding environment than if the airport were to expand with conventional flights. Noise pollution to the surrounding environment will still have to be considered carefully when selecting actual airport locations.

11.1.6. Regional and Local Airport Hub Selection

Having chosen to use regional airports, requirements must now be set up to filter through all airports to find which airports are suitable to be chosen as a hub. Data on the classification of airports is sparse and inconsistent but data on the runway lengths of airports is not. There is no explicit correlation between runway length and airport size and classification but in general, the larger the runway, the larger the airport. Therefore a runway range needs to be decided.

The runway length is sizing for the redesigned drone power loading and wing loading which is used to determine the design point. The runway must be large enough that the design of the drone is not too restricted, but small enough that the airport is a regional airport with comparatively low costs.

With regard to the target of regional and local airports, a maximum runway length of 2,000m is determined based on observations of multiple airports. The minimum runway length is determined to be 1,300 meters. This value is determined to be not excessively limiting by the propulsion and power department, and not too small by the operations department.

The maximum altitude of an airport must also be decided due to the varying air density being an important factor for the power and propulsion design team. As can be seen in Figure 11.1, 96% of airports are below 5,000 ft in altitude. This value is a compromise between necessary take-off performance and availability of airports.

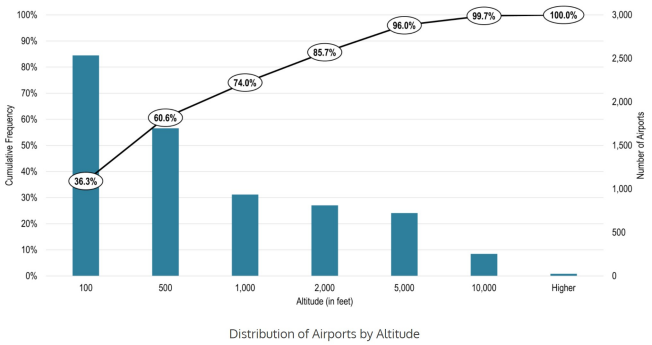

Figure 11.1: Percentage of airports below different altitudes [98]

To check the accuracy of the assumption that 1,300m to 2,000m is not too limiting a filter was conducted on global airports with the requirements that the runway must be between 1,300m and 2,000m and that the runway type must be asphalt or concrete. From the 44,853 runways worldwide [99], 6676 runways meet this requirement which is abundant. When actually selecting hubs consideration should be given to if the local amenities such as electricity supply and hanger availability are compatible with the requirements of eCarus. This is not factored into the code due to the lack of available data. This must therefore be treated on a case-to-case basis.

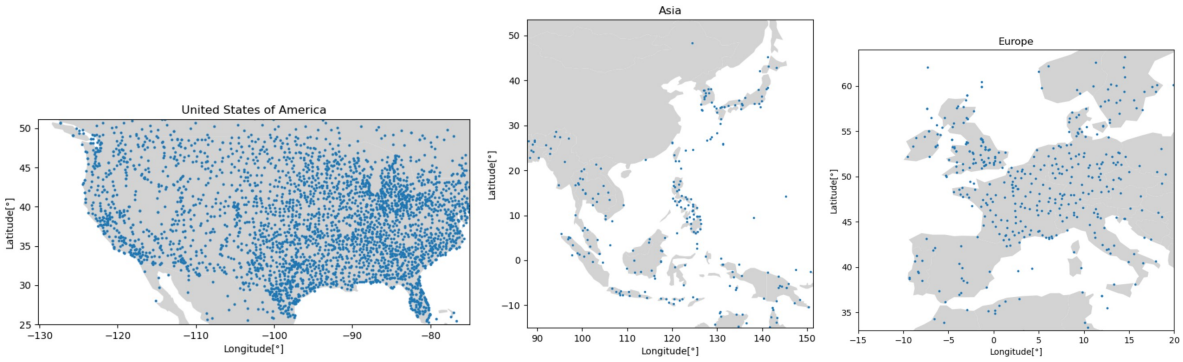

(a) Suitable airports in the USA **(b)** Suitable airports in Asia **(c)** Suitable airports in Europe

Figure 11.2: Suitable airports around in Europe

To visualise if this is sufficient, Figure 11.2 shows where they are in three key continents. It is clear that hub placement in the United States can be extremely optimised since there are so many available airports. In Asia, there is a distinct lack of suitable airports in China. This could be because the data on Chinese airports is less available. The yellow sea and the south china sea also limit optimal hub placement. Europe has a lot of suitable airports. Especially in France which is beneficial due to its central placement.

11.1.7. Combining the Results

The analysis of suitable airports can be overlayed on top of the hub placement results done in the midterm report. The top 50 busiest flightpaths in 2021 in Europe is used as the data [100]. The result is shown in Figure 11.3a. The hub placement code uses the inputs of a maximum hub separation of 620km and a maximum separation distance between hub and plane of 118km. It has been upgraded to show ovals for the hub range since spherical stretching of the map becomes significant in regions such as Europe.

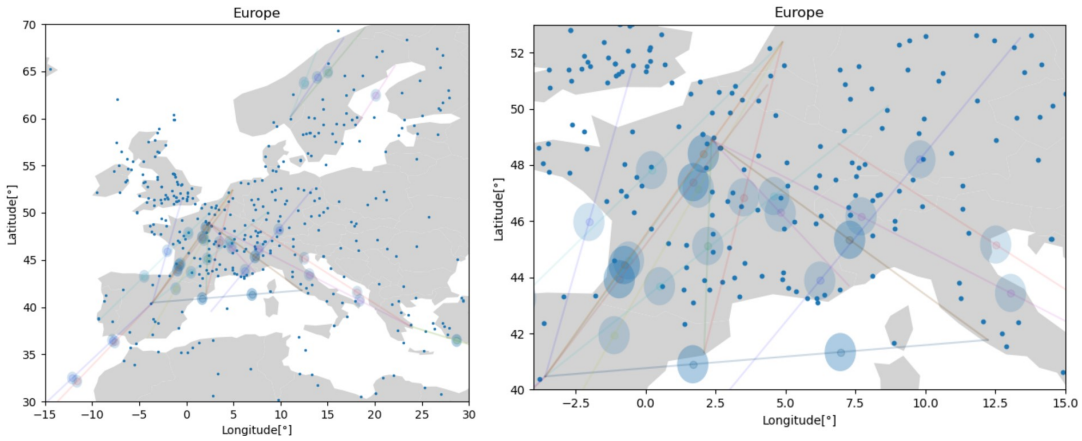

(a) Hub placement code combined results

(b) Hub placement code combined results, zoom in

Figure 11.3: Hub placement code results

Flights to the outside edges of Europe tend to require a recharge point over water or in an area where there is no suitable airport. All flights that can be serviced go through central Europe, especially France. Therefore a zoomed-in part of the results is shown in Figure 11.3b. What should also be noted is that Amsterdam, Paris, and Madrid are almost perfectly on one line with Paris being located so proportionally that recharge points from Madrid to Paris match up with the second recharge points from Amsterdam to Madrid. Such overlaps are ideal for hub placement and should be sought for in future hub placement.

Of the top 50 flights within the EU, there are 44 unique connections between airports. Of these 44, only 24 need at least one recharge. The 24 remaining flighpaths need a collective 42 recharges. Of these flightpaths, only 9 can be serviced using existing suitable airports. These flightpaths collectively need 14 recharges. By optimising hub placement by placing hubs in overlap zones these 14 recharges can be serviced by 9 hubs.

It is key to note that all of the top-50 routes in Europe could be serviced but that they would require more than an optimal number of recharges and thus hubs, and sometimes detours from the ideal flightpath. Also, if the number of recharges required for a flightpath is not an integer, then the program rounds up to ensure that the aircraft can reach each hub. The hub placement code then breaks up the flightpath into equal sections of flight which could therefore be smaller than the maximum distance the receiving aircraft can safely fly between hubs. Therefore there is some variability in the spacing of recharge points along a flightpath. The spacing is dependent on where the previous recharge point is placed making the spacing dynamic. For this project such an expansion is deemed too in-depth however this could be explored further in a future extension of this project.

Looking at the Figure 11.3b two very interesting hub locations are the local airport near the south-east edge of France (47.8984° N, 2.1608° E) and the local airport just south of Paris (44.5974° N, 1.1139° W). These are interesting due to their placement inside overlap zones allowing them to service multiple routes. This would optimise the hub placement resulting in fewer hubs needing to be built thereby reducing the actual surface footprint of eCarus. A test flight using these two hubs is analysed in section 14.1.

11.2. Operational Requirement Compliance

To complete the operational part of the final design, the key requirements that dictate the operations of eCarus must all be finalised and complied with. The full list of requirements and eCarus' compliance with each one is listed in section 13.6. Many of the requirements dealing with operations have already been satisfied. However, two key requirements remain which will be investigated in this chapter.

11.2.1. Emergency Handling

The first requirement that is yet to be properly satisfied is requirement [REQ-US-PER-03] which states that *A drone shall reach the aircraft within 20 minutes in case of an emergency*[16]. The goal of this requirement is two part. Firstly, it aims to ensure that the receiving aircraft can safely rely on recharge so that it will not crash. However, due to the use of regional airports, the aircraft will always be relatively close to a regional airport when the charging has failed. It will therefore almost always be able to turn and land at that regional airport. The second goal of this requirement is to ensure that the quality of the service for the client, the receiving aircraft, is high. This means that the disturbance to the aircraft from the eCarus system should be minimal. Since a docking failure is allowed once every 1000 recharges [REQ-US-SR-01], this will occur enough times over many flights to cause a nuisance. However, sending a second drone that must reach the aircraft within 20 minutes also comes with limitations for the system.

Fixed and variable parameters

To investigate the limitation of sending another drone a model is constructed where the key variables can quickly be changed. The key variables are:

- How long after a declared changing failure must a new drone arrive
- Does the receiving aircraft continue on its original flightpath
- How fast does the receiving aircraft fly
- At what altitude does the receiving aircraft fly
- How long is docking attempted before it is declared a failure
- How far away is the hub from the aircraft's flightpath. This is also known as the maximum separation distance r_{max}.
- How fast does the drone fly towards the aircraft

The first point is fixed at 20 minutes by requirement [REQ-US-PER-03].

The second, the flightpath, is kept straight since a solution is aiming at minimal disturbance to the aircraft's normal operations. In an absolute emergency, the aircraft could turn towards the hub to land.

The aircraft speed is preferably also not altered. However, a slight decrease in airspeed will have minimal impact thus this option is still considered. In normal conditions will remain at cruise speed during recharging. Therefore the velocity that will be varied is the velocity from when the first charge has been declared a failure to the end of the second emergency recharge. This is thus 20 minutes of time for the emergency drone to arrive plus 40 minutes for recharging. The recharge time cannot be altered. This is therefore fixed at 60 min.

The fourth point on the aircraft's altitude is preferably kept constant due to the extra energy and hassle the aircraft would have to use to climb back up. When decreasing the altitude of the models in [autoref] so that the drone can reach the aircraft faster, the largest effect it has is to allow the maximum separation from the hub to increase by 15 km. This is not significant enough to justify the extra hassle of changing altitude. Therefore the altitude is fixed at $15\,000$ ft

For the fourth point, the time after which a charging failure is declared is a trade-off between having enough time to rule out simple solvable problems with docking against giving the emergency drone enough time to reach the aircraft. The time needed for the hub to receive the failed charging signal and deploy another drone must also be factored in. In discussion with the payload department, this value was set at 10 minutes. Within 5 minutes of docking, at least 2 complete docking attempts can be conducted which should rule out most errors. After the drone is launched the failed drone can still attempt docking if the source of the problem is still unknown. The other 5 minutes are to consider the time the emergency drone needs to taxi and take off. This is very fast but regional airports are not very busy and such a rapid take-off is only needed once in a thousand times meaning options like paying a premium for rapid departure could also be considered. Just as importantly, the time is also set to 10 minutes because of the 10-minute safety margin for the drone coming late to recharging. These two margins must be set equal to each other so that they are both optimised.

The fifth point has been sized at 149 km by investigating the drone range, safety margins, and wind

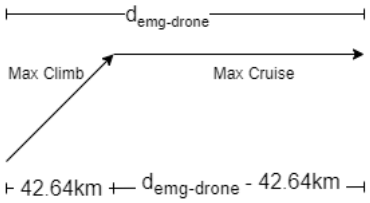

Figure 11.4: Emergency visualisation

conditions in the midterm report [6]. This value is a variable of the design.

The last point on the drone speed is preferably maximised. This analysis investigates the sizing worst-case scenario where the aircraft is flying as far away from the hub as it can while most of the time the aircraft will fly closer to the hub. In such an extreme situation it is decided that the drone must fly as fast as possible towards the aircraft to give the other parameters more breathing room. The main drawback of this is the extra battery usage that the drone will use up when climbing and cruising as fast as possible. This however could be compensated for on a slower and more efficient return journey.

The fastest way for the drone to reach the aircraft at cruise altitude is to first climb as fast as it can and then fly towards the aircraft as fast as it can. The maximum rate of climb of the drone is derived from the maximum available power of the drone to be $7.5\ \frac{m}{s}$ with a $69.95\ \frac{m}{s}$ over the ground speed The total distance that the drone must fly varies and is thus represented by the variable $d_{emg-drone}$.

$$V_{drone} = \frac{251.8 \times 42.64 + 396(d - 42.64)}{d} \tag{11.1}$$

Visualising and analysing different scenarios

Below different scenarios are investigated. In black the nominal flightpath of the drone is shown in case of no failures. Red signifies the aircraft and the emergency drone's flightpath and location are shown in green. Note that the drone always flies towards the actual meet-up point.

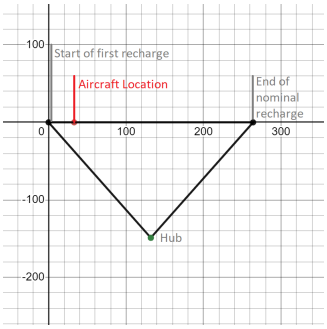

Figure 11.5: time = 0 min, r= 149 km

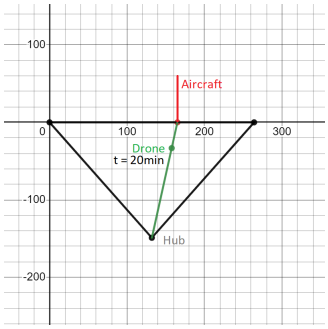

Figure 11.6: time = 20 min, r= 149 km

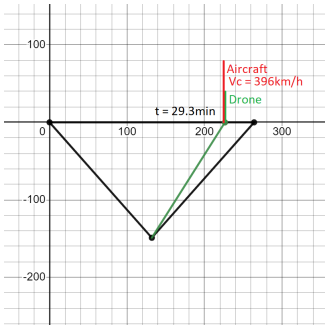

Figure 11.7: Time = 29.3 min, r = 149 km

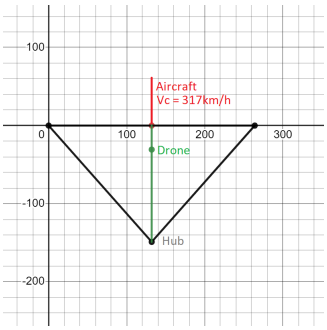

Figure 11.8: Time = 20 min, r= 149 km

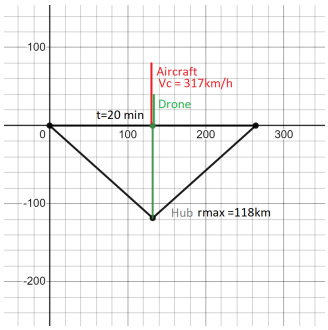

Figure 11.9: Time = 20 min, r = 119 km

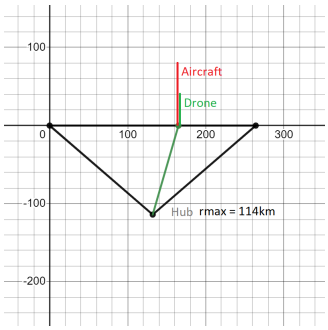

Figure 11.10: Time = 20 min, r = 114 km

Figure 11.5 shows the aircrafts location 33 km further along after 5 minutes of failed docking. This is the moment when at which the emergency drone is launched. This means that there must always be a drone ready to take-off quickly which comes with its own operational limitations. After 20 minutes of flying the drone is still 34 km away from the aircraft as shown in Figure 11.6. It only meets up with the aircraft after 29.3 minutes as shown in Figure 11.7 which shows that parameters must be changed in order to comply with the 20-minute requirement. The parameters used for Figure 11.5 and Figure 11.6 is a r_{max} of 149 km, an aircraft speed of 396 $\frac{\text{km}}{\text{h}}$. The calculated maximum drone speed in Figure 11.6 situation is 355 $\frac{\text{km}}{\text{h}}$ and in Figure 11.7 is 361 $\frac{\text{km}}{\text{h}}$.

The drone speed is already maximised, and the time before declaring a charging emergency is already minimised leaving only r_{max} and the aircraft velocity. If just the aircraft's speed is decreased to the optimal 317 $\frac{\text{km}}{\text{h}}$, the speed at which the distance to the hub at the 20-minute mark is smallest, the drone still has a separation of 31 km away from the aircraft at the 20-minute mark as shown in Figure 11.8. Therefore r_{max} must also be decreased to 118 km as is shown in Figure 11.9. A decrease in r_{max} also has the effect of decreasing the nominal drone range that a successful charging mission would have from 663 km to 616 km.

Adjusting the two variables the other way is also possible. In this case, the aircrafts velocity is kept at 396 $\frac{\text{km}}{\text{h}}$ which forces r_{max} to be 114 km as shown in Figure 11.10. This also reduces the nominal drone range to 613 km.

In the latter case the aircraft can remain flying at its cruising speed. By itself, the 4 km decrease in r_{max} is definitely worth it for the added service quality for the client, the aircraft. However, consideration must also be given to that the emergency drone must return home to the hub after recharging. In Figure 11.9 the total range that the emergency drone must fly after completing its full 40-minute charge is 672 km. In Figure 11.10 this total range is 701 km.

If the first drone is more than 10 minutes late an emergency drone will be launched. However, if the drone is just under 10 minutes late and it fails to successfully recharge then the charge in failure will effectively be declared 15 minutes late. In Figure 11.9 this would yield a total drone range of 799 km. In Figure 11.10 this would yield a range of 829 km. Such a situation would be to containing on the design. Therefore if the drone is 10 minutes late and fails charging, the aircraft must deviate from its flightpath towards the incoming emergency or towards a suitable nearby airport.

A faster aircraft speed also means that the aircraft will have to fly further on its own after a failed initial recharge. This requires the aircraft to reserve a large portion of its battery for this emergency situation. This is thus a trade-off between the comforts and lack of delay due to continuing to fly at cruise speed versus the weight penalty of the extra battery safety margin. Therefore, in agreement with the Electrifly design group, the aircraft will decrease to 317 $\frac{\text{km}}{\text{h}}$ after declaring a failed docking. This results in a delay of 12 minutes.

Using this new ideal mission profile range of 616 km a new drone range can be calculated to be used in the next iteration of the drone. Firstly, the range is increased to 622 km to account for a drone that arrives 10 minutes late to recharge. Then a safety factor must be applied for unforeseen delays and disturbances.

Drone range safety factor

The last reserve of fuel in a modern airliner is called the *Final Reserve Fuel* and should only be used in case of an emergency. For jet engines, it equals 30 minutes of flying at a holding speed of $1500ft$, while for propeller aircraft, it is 45 minutes at the same altitude [101]. Since the drone is unmanned, safety margins can be reduced as no human lives are at stake. Additionally, the waiting time for landing is typically minimal at regional airports and purpose-built hubs. Thus, the fuel needed for non-range extending flight can be further reduced. The margin can safely be reduced to $10min$ of flying at a holding speed of $1500ft$.

As a check, the flight time of a perfect mission at maximum distance is 129 minutes. With a 10-minute

margin, the safety factor becomes 1.07. The drone's range already includes another safety factor for the possibility of being 10 minutes late for recharging, which requires an extended range. The safety margin for this situation is calculated at 1.018. Combining the two safety factors results in a total flight time of 141 minutes.

The battery is charged from 10% to 90% of its maximum capacity. It always keeps a 10% charge to avoid damage to the battery. This can be considered the final safety factor, as in absolute emergencies, the drone's battery can be sacrificed for an additional 11.1% charge.

In terms of range, the safety factor of 1.07 is applied to yield a new drone range of 665 km in ideal conditions for the next iteration of the design.

11.2.2. Flying from Hub to Hub

The drone range is one of the key starting parameters for the design iteration. Therefore, before submitting it to the iteration process, the effects of decreasing the drone range must be analysed.

A decrease in drone range is preferable for almost every part of the drone since it allows the drown to be scaled down and lighter. The drone range thus mainly impacts the operational aspect of eCarus. Its effect on the quality of the service and on safety has been analysed. However, its effect on the logistics of the eCarus system as a whole can still be investigated.

This section will thus analyse the possibility and benefits of drones flying from hub to hub to recharge aircraft. The three primary benefits are the ability to adjust to demand quickly, streamline maintenance, and fly to another hub in case of an emergency. These all benefit the logistics of the eCarus. The main drawback is the potential decrease in hub spacing that it drives.

A hub-to-hub model can be beneficial since it would allow the drone density per hub to be quickly altered to meet demand. The busyness of flight routes changes a lot with the seasons, vacation weeks, and even which day of the week it is. Drones can therefore be moved around quickly to meet the predicted demand at routes.

Maintenance operations could also be streamlined by implementing a hub and spoke model. This would mean that only a few hubs will be capable of proper maintenance. If a drone requires maintenance, then it could fly from hub to hub towards such a central maintenance hub. This would of course only work if the aircraft can fly. If the aircraft is grounded, a team might need to be sent out to the drone's local hub, or the drone must be transported by truck or rail.

Flying from hub to hub could also be used in emergency situations where the drone is outside the hub's normal operating area. Flying any further outside this area would usually result in the drone not being able to return home due to its limited range. However, using this model, a drone could then reach outside of this area by flying towards a neighbouring hub and landing there. This would decrease the chance of a drone having to be sacrificed to save an aircraft.

The drone's range is 665 km and the maximum hub spacing is currently 670 km [6]. If the hub spacing is done optimally, and not restricted by such a hub-to-hub system, then the drone will just barely not reach a neighbouring hub. However in reality hubs will not always be placed at the maximum distance from each other due to factors such as the location of popular flight paths, geopolitical factors, or the presence of hard terrain just to name a few.

Extending the drone's range means larger batteries and thus a heavier drone. Thereby starting a worsening snowball effect. The small decrease needed in the hub spacing is considered worth it for the added benefits of hub-to-hub flight. Therefore the maximum hub separation is set at 620 km to allow for drones to fly from hub to hub safely. The drone range is now also set at 665 km and is submitted to the next iteration of the design which is shown in Table 10.3.

11.2.3. Maintenance

The second requirement that needs to be explicitly addressed is [REQ-SYS-OP-1] which states that ”The system shall allow maintenance facilities at the hub”. This is an important aspect of operations and logistics and thus must be accounted for in order to have a safe and reliable system. Maintenance, repair, and overhaul (MRO), refers to a comprehensive set of tasks with the primary objective of ensuring the flight readiness of the drones at all times. Considering the scope of the project and the top-level requirements, it is decided to outsource the majority of the MRO tasks. This enables the team to focus on the design of the drone and mission-critical operations. For now, various MRO organisations are recommended. For MRO software, Aerotrac or Ramco could be interesting partners as they are among the industry’s leading MRO software companies. For larger one-stop-shop European MRO organisations, Air France Industries and KLM Engineering & Maintenance, Lufthansa Technik can be considered. Possible partners from the United States of America are Delta TechOps and AAR Corp.

Important to note is that most MRO organisations are not yet specialised in maintenance tasks for autonomous drones. Therefore various crucial human-UAV maintenance interactions are identified and listed below [102].

- **Battery maintenance requirements**: The batteries form a crucial part of the mission and of the drone. It is of utmost importance that during maintenance the batteries are properly checked, including the charging/discharging cycles.
- **Distinguishing between payload and aircraft**: As stated in [102], ”In contrast to conventional aircraft, the payload on board a UAV is more likely to be integrated with the UAV structure and power supply”. This implies that MRO organisations should be able to account for the payload and structure and power dependencies. This may be different than for conventional aircraft.
- **Autopilot software management**: As the system is fully autonomous it is important that the MRO organisation is highly skilled in updating and verifying the software.
- **Lack of direct pilot reports**: As the system is fully autonomous, no pilot reports will be available. These reports are often used for conventional aircraft inspection and maintenance. MRO organisations should account for the lack of these reports.

Note that the list above is not comprehensive and only some of the most important factors are included. For more considerations refer to the Federal Aviation Administration (FAA) report, Human Factors in the Maintenance of Unmanned Aircraft [102].

12
Detailed Design Summary

In chapter 3 to chapter 11, the detailed design of the eCarus system is explained. In this chapter, all those chapters are summarised to present the final design in this detailed design summary. First, section 12.1 presents a visual representation of the drone. Then, in section 12.2 the final technical specifications of the drone are summarised. Finally, section 13.5 presents a sensitivity analysis for some important design parameters.

12.1. Visual Representation

In this section four renders are presented of the drone design. In Figure 12.1a a render is presented of the eCarus drone. Figure 12.1b also shows a render, but here a part of the internal structure is exposed. Finally, Figure 12.2, presents the render of the new designed connection system.

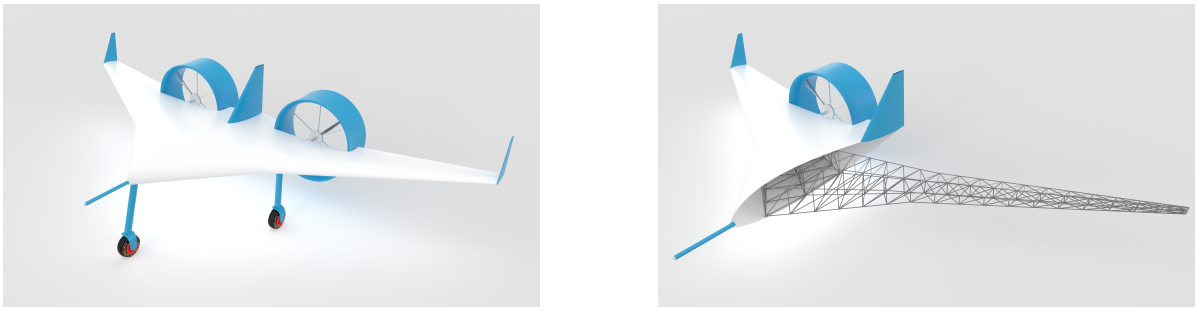

(a) General render

(b) Render exposing internal structure

Figure 12.1: Renders of the eCarus drone

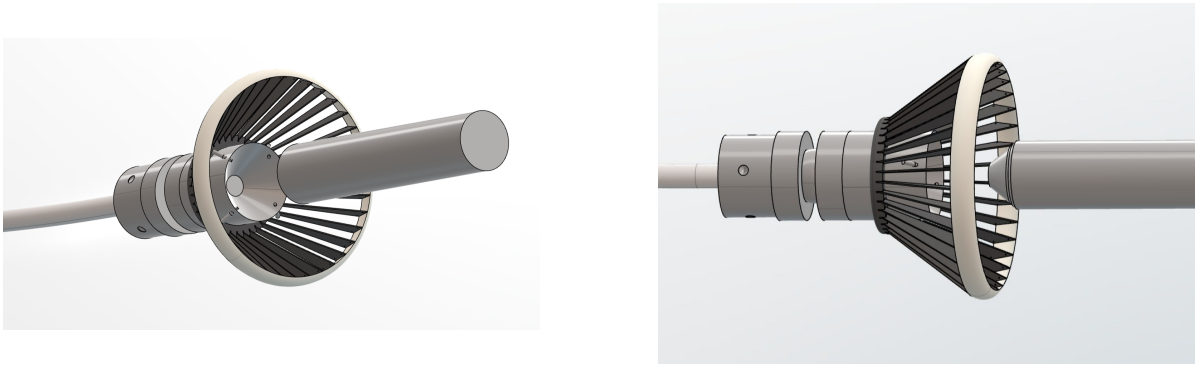

Figure 12.2: CAD Render of the drogue-probe system connection

12.2. System Specifications

This section summarises the key parameters of the design. First general mission characteristics are presented in Table 12.1. Then, Table 12.2 presents the technical specifications of the drone.

Table 12.1: General characteristics of the eCarus drone

General system characteristics	General system characteristics
Operations	**UAV System**
Hubs at regional airports	Probe / drogue senors
Conventional take-off and landing	Detect and avoidance sensors
Docking mechanism	Thermal sensors
Drogue/probe system	Charge sensor
Boom at nose of drone	Discharge sensors
Battery	Force sensors
Liquid cooling	Solenoid sensors
Lithium anode	Condition sensors
Nickel manganese cobalt cathode	
Structure	
Pratt truss with doubled diagonals	
Lattice skin support	

Table 12.2: Technical summary of the eCarus drone

Variable	Value	Unit	Variable	Value	Unit
Mission characteristics			**Battery characteristics**		
Cruise altitude	4572	m	Battery specific energy	600	Wh/kg
Cruise velocity	110	m/s	Battery energy density	900	Wh/L
Drone range	665	km	Total battery weight	4057	kg
Total weight	5413.76	kg	Total battery volume	602.377	L
Wing planform			**Power and propulsion**		
Centre of gravity	2.977	m	Cruise power	598 988	W
Aspect Ratio	6	-	Total energy	685.8375	kWh
Span	16.38	m	Cruise thrust	4048.3	N
Body sweep at quarter chord	30	degree	Maximum total thrust	9269.22	N
Wing sweep at quarter chord	28	degree	Engine weight	223	kg
Oswald efficiency factor	0.95	-	Propeller diameter	2.2	m
Root chord	6.73	m	Number of engines	2	-
Tip chord	0.767	m	Propeller efficiency	0.941	-
Surface area	44.698	m^2	Cruise noise	56.67	dB
MAC	3.65	m	Wing loading	1279.974	N/m^2
Tail planform			**Structures**		
Surface area	7	m^2	Factor of safety	1.3	-
Height	0.65	m	Maximum load factor	3.09	-
Moment arm about xcg	5.23	m	Minimum load factor	-1.23	-
Aspect Ratio	3	-	Maximum skin pressure	7290	MPa
Aerodynamic parameters			Maximum tensile stress	212.3	MPa
Cruise lift coefficient	1.269	-	Skin thickness	1	mm
Zero lift drag coefficient	0.00813	-	Lattice spacing	31.9	cm
Lift gradient	3.97	1/rad	Truss cross section	1.374	cm^2
Oscillatory half times			Highest internal load	64.44	kN
Short period	0.95	s	Maximum tip deflection	17.02	cm
Phugoid	70.6	s	Weight of trusses	733.8	kg
Dutch roll	30.5	s	Skin weight	136	kg
Sprial	0.45	s	Landing gear weight	275.75	kg

13 Verification and Validation

The verification and validation of the methods and codes used is described in this chapter. The chapter initiates by describing the procedure used in the Power and Propulsion chapter in section 13.2. Following this, the V&V methods used for Aerodynamics are described in section 13.3. The verification and validation performed for structures is noted in section 13.4. Finally, the compliance matrix is described in section 13.4. The Verification and Validation procedures implemented throughout the technical design tasks make team eCarus confident in the results obtained.

13.1. Docking Mechanism

This section presents how the verification and validation of the drogue-probe system is performed. The first step in validation is to check if the system complies to the imposed requirements. Some requirements function are design-driving requirements and others imposed mission requirements. The driving requirements in the compliance matrix in section 13.6.

Future validation plans

The drogue-probe system design requires testing for validation. Future plans include aerial tests to validate the upper bound of the recharging zone, as is described in section 5.1, wind tunnel testing to assess the drogue configuration's aerodynamic effects, and prototype testing to ensure a high probability of successful connections. Testing will cover diverse conditions as compliance is necessary with requirements [REQ-US-SR-06] *The system shall work in all weather conditions in which the target aircraft can operate* and [REQ-US-SR-01] *A drone shall dock an aircraft successfully 99.9% of all attempts.*.

Validated with experts

Since the connection between the probe and drogue is a complete new theory the use of experts opinions is crucial. an overview of the contacted experts and their expertise and outcome is shown Table 13.1. Most of the experts we have talked to did not have a large expertise on such a docking system since it is a completely new design. This is reason why testing of the probe-drogue system is crucial in future design phases.

Table 13.1: Experts interviews with their outcome

Expert	Function	Outcome
Tine Tomažič	Director of Engineering & Programs at Pipistrel	Discharge functioning, Electric system between drone battery and receiving battery.
Dr.ir. P. Bauer	Electrical Engineer at TU Delft	General proposed connection, input in electrical system.
Lior Zivan	Chief Engineer at Manna Drone Delivery	Proposed risk in terms of lightning, wet conditions and short circuit within system.

13.2. Power and Propulsion

For verification of the aerofoil A, γ and k_p values estimation, the procedure as described by Traub is performed on the aerofoil used in the paper to test whether the same results are obtained. The Clark Y aerofoil is analysed in XFLR5 using the same Reynolds numbers as described in the paper and at a Mach number of 0. The $c_{d_{min}}$ values for every respective Reynolds number are plotted in Figure 13.1. To obtain a formula for $c_{d_{min}}$ in terms of Re, a power curve is once again fitted to this data. The figure shows the power curve found in the paper in orange and the power curve that is obtained during verification in blue. The graph shows a strong resemblance, indicating that the procedure is correct and therefore verified.

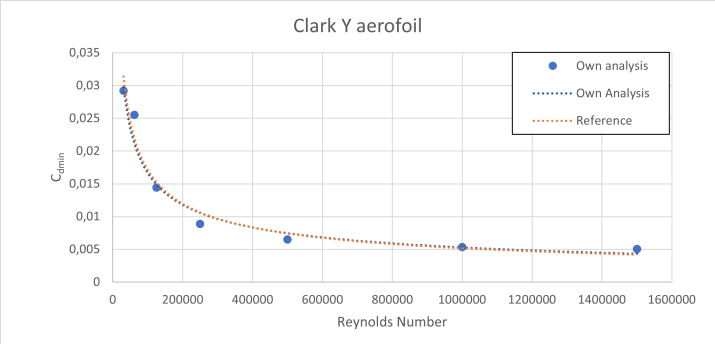

Figure 13.1: Reynolds numbers potted against their respective $c_{d_{min}}$ values for the Clark Y aerofoil for verification

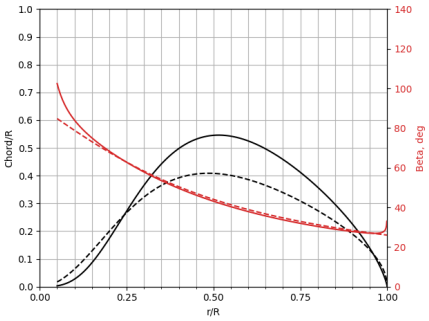

(a) Code results for 2 blades

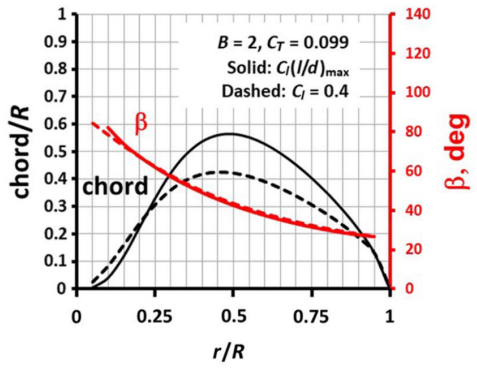

(b) Traubs results for 2 blades [38]

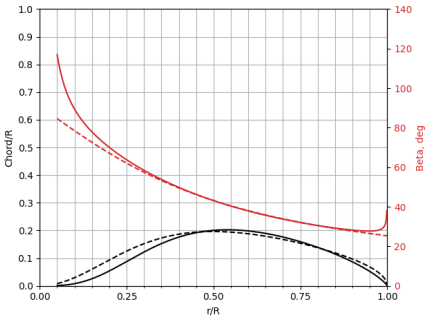

(c) Code results for 4 blades

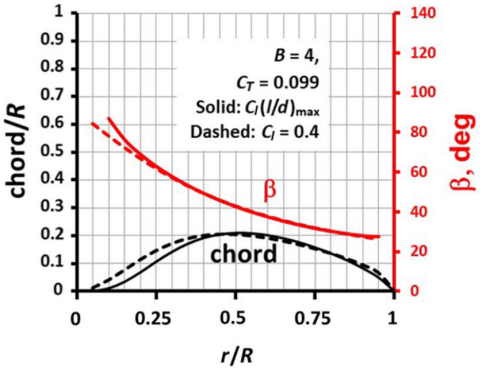

(d) Traubs results for 4 blades [38]

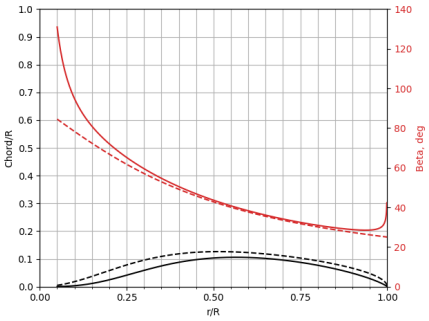

(e) Code results for 6 blades

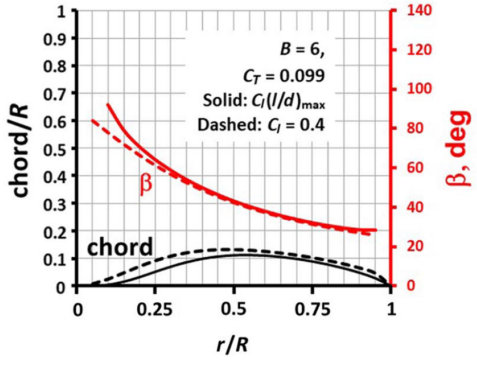

(f) Traubs results for 6 blades [38]

Figure 13.2: Comparison of code generated results and Traubs results for the Cessna Centurion 210 propeller at cruise conditions

Verification of the correct implementation of the induced loss procedure is done by comparing the generated results of the programme with the results presented by Traub [38]. Traub utilises the propeller from a Cessna Centurion 210 during cruise as a test case for the procedure. The values highlighted in Table 13.2 are used as inputs to the procedure. Figure 13.2 shows on the left-hand side the results generated by the written code and on the right-hand side the results obtained by Traub. Simple visual comparison reveals the resemblance of both obtained results. It can thus be concluded that the code is verified, as similar inputs give similar outputs to an already verified study. As the aforementioned study is also already validated, it is safe to conclude that the performed induced loss procedure presented here is validated as well since the same procedure is used and verified.

Table 13.2: Cessna Centurion 210 propeller design inputs

Parameter	Value	Unit
V_∞	99	m/s
RPM	2000	-
$T_{desired}$	2000	N
ρ	0.661 143	kg/m^3
D	2.29	m
A	783.44	-
γ	-0.846	-
k_p	0.042	-
c_{l_α}	0.1032	1/deg
$\alpha_{c_{l=0}}$	-3	deg
$c_{l_{d_{min}}}$	0.2	-
$c_{l_{(l/d)_{max}}}$	0.4	-

13.3. Aerodynamics

In this section the verification and validation of the aerodynamics departments will be discussed.

13.3.1. Aerodynamic Coefficients

First of all, as the aerodynamic coefficients are calculated through empirical methods, it is important to validate the correctness of the results. This was done by comparing the results of the BWB with the aerodynamic coefficient of a Cessna Citation shown in Table 13.3 and Table 13.4. The aerodynamics coefficient can be found in Table 7.3 and Table 7.4.

Table 13.3: Symmetric motion coefficients of Cessna Citation[54]

Coefficient	Value
C_{X_u}	-0.09
C_{X_α}	0.15
C_{X_q}	0

Coefficient	Value
C_{Z_u}	-0.90
C_{Z_α}	-5.9
C_{Z_q}	-7.36

Coefficient	Value
C_{m_u}	0
C_{m_α}	-0.80
C_{m_q}	-16.50

Table 13.4: Asymmetric motion derivatives

Coefficient	Value
C_{Y_β}	-0.90
C_{Y_p}	-0.23
C_{Y_r}	0.48

Coefficient	Value
C_{l_β}	-0.09
C_{l_p}	-0.60
C_{l_r}	0.23

Coefficient	Value
C_{n_β}	0.11
C_{n_p}	0.02
C_{n_r}	-0.14

When comparing the results, two things can be noticed. First although most coefficients have the same sign, the BWB regularly possess an inferior magnitude. This can be explained, by the lack of moment arm and contributing surfaces such as a fuselage or a horizontal stabiliser. The second observation is that two coefficients namely C_{Y_p} and C_{n_p} are positive where the comparison aircraft is negative. C_{Y_p} can be neglected for the moment, as no requirement is given on the sign of that coefficient. The sign of C_{n_p} can be explained by the high sweep and BWB configuration.

13.3.2. Pitch Moment Coefficient

During an interview with MTH Brown (Table 15.1), it was advised to use empirical methods to find the pitch moment. The result of this method is now compared to a VLM estimate of C_{m_0}. The comparison can be seen in Table 13.5.

Table 13.5: Pitching moment validation

Method	C_{m_0}
Empirical	0.01021
VLM	0.016

The comparison shows that the empirical methods gives a lower estimate of the pitching moment. This is preferable as this makes the design conservative. It can also be seen that VLM give a 60% increase in moment coefficient, which is in the same order of magnitude.

13.4. Structures

In this section, the verification and validation are described regarding the code used for structural design.

13.4.1. Landing Gear

The landing gear code is a Python class containing two methods. The first is to place the MLG and NLG and compute some relevant distances. To verify this instance method, a simple calculation was performed by hand using the same inputs of the class.

The second method assesses tip-over and the clearance criteria, and returns the height of the landing gear as well as the track width of the MLG. As for the previous method, using the same input values, all the computations in the method were performed by hand. The values were compared to the outputs of the method, and it became clear that they all returned the correct value. The code is thus deemed verified.

Regarding the validation, the only formulas used in the class are based upon simple geometric relations and thus do not require any further analysis. To perform some validation, a look can be taken at the assumptions made in the code. One is that the MLG is located at 15% MAC behind the centre of gravity. Another is that the NLG holds 15% of the take-off weight. Haiqiang Wang et al. stated in a research article on landing gear development that these are typical values, thus the assumptions are regarded valid [103].

13.4.2. Truss Geometry Design and Analysis

The truss geometry design utilises 5 numerical tools: an internal loading calculator based on aerodynamic coefficients provided by aerodynamic analyses, a discretisation tool for applying the distributed loads onto the nodes of the truss structure, a mesh coordinate geometry generation tool from parameters describing the truss and the planform, the truss and beam analysis software frame3dd [83] and a simulation results visualisation tool. These were separately verified and their combined results validated.
The internal loading calculator is verified by integrating backwards over the results and verifying whether they add up to the original loading. These are accurate to 1e-4 with meshes of resolution over 100 points. This was validated using a simple load case analysed by hand were the results matched to 1e-3. The confidence in this numerical method is high. The discretisation tool is verified by adding up the discretised forces and testing them against the integral of the distributed loads. These were accurate to 1e-2. This is an acceptable result regarding the simplifications made. The truss mesh generated is validated by verifying the angle of trusses to the horizontal and that all nodes lie within the platform section. The results are accurate for angles β between 0 and 90°. Frame3dd is validated by simulating a test case described and solved in the AE4ASM003 course [104]. The results obtained are checked for linear dependence between applied loads and deflection at the tip. The visualisation of these results was used as a visual check for proper definition of the mesh and credible deformation and loading (compressive/tensile) in the truss members.

13.5. Parameter Sensitivity Analysis

In this section, the sensitivity of the design is explored. Certain important design variables are subjected to a minor change, to indicate what the outcome of the design would have been in that case.

13.5.1. Battery Specific Energy
The first parameter included in the sensitivity analysis is the battery specific energy. Throughout the design, this parameter has been found to severely influence the design. Before any iterations were performed, the value used was $500\,\mathrm{Wh/kg}$. This resulted in a total drone weight of $19\,902\,\mathrm{kg}$. In a later iteration, the specific energy was increased with 20% to $600\,\mathrm{Wh/kg}$. This leaded to a drastic weight reduction, ending up at $6511.83\,\mathrm{kg}$. This is a decrease of 67.3%.

13.5.2. Zero Lift Drag Coefficient
Another parameter is the zero lift drag coefficient. An increase of this factor would lead to an increase in the wing loading, which would make the design heavier. An increase of 10% would lead to an increase of 1.27% for both the total drone weight and the required power.

13.5.3. Sweep Angle
The sweep angle also is a parameter with an influence on the design. The effects of this are shown in section 7.6. Increasing the body sweep increases the distance to the aerodynamic centre, while increasing the outer wing sweep reduces this distance. Thus the stability of the drone is sensitive to the sweep angle of both the body and the outer wing.

13.5.4. Conclusion
This sensitivity analysis proves that the robustness of the design varies with parameters. To some parameters, like the battery specific energy, the design is really sensitive. On the other hand, a variation in for example the zero lift drag coefficient only has a slight influence on other important parameters such as the total weight or the cruise energy consumption. It is of crucial importance that the sensitive parameters are identified and are correct.

13.6. Compliance Matrix
The compliance matrix on the A3 page summarises the requirements set in **??** and the if the design complies to those requirements. The compliance matrix specifies if the design complies with the requirement, doesn't comply or if the requirement was rephrased or removed and an explanation.

REQUIREMENT	DECRIPTION	STATUS
User and stakeholder requirements		
REQ-US-02	The cost per unit energy supplied to the aircraft shall be equal or less to 1.5 that of SAF assuming global wide-spread adaptation of the system.	The cost per unit energy supplied per hour is 2.017 times the cost of SAF fuel.
REQ-US-03	The system shall have a charge rate to allow for perpetual flight over the covered region.	A total charge of \$I(1246)(kWh)\$ is delivered. This is equivalent to 75 minutes of cruise flight excluding the 40-minute recharge allowing for perpetual flight
REQ-US-04	The on-aircraft system shall be adaptable to existing aircraft.	The aircraft only needs an adaption kit in the form a cable-drum unit
REQ-US-05	Under no condition shall a drone collide with an aircraft.	The drone uses avoid and detection sensors to ensure it will not collide with an aircraft or any other objects
REQ-US-06	The system shall transport energy produced by a sustainable method.	Batteries have been chosen to transport the green energy
REQ-US-07	The system shall operate on energy produced by a sustainable method.	Green energy PPA contracts will be secured at each hub location
REQ-US-09	The system shall declutter recharge logistics of electric aircraft at airports.	Regional hubs that are not busy have been chosen as hubs in order to declutter the busy airspace near international airports
REQ-US-10	The system shall make use of the technology available in 2030.	Done
REQ-US-PER-01	A drone shall dock the aircraft autonomously.	The drone uses computer vision to detect the drogue and adjust attitude, next to this the probe has trusters to adjust its attitude
REQ-US-PER-02	A drone shall detach autonomously from the aircraft after recharging the aircraft.	The AAR controller will detach the docking system when charging is complete
REQ-US-PER-03	A drone shall reach the aircraft within 20 minutes in case of an emergency.	The maximum distance between hub and passing aircraft has been sized to ensure that an emergency aircraft can reach the aircraft within 20 minutes of declaring a charging failure
REQ-US-PER-04	The system shall be able to meet electric aircraft demand by 2050.	Scalability of the system is evaluated and checked to ensure that the market demand is met
REQ-US-PER-05	A hub of the system shall be placeable on land and the sea.	A hub is only placeable on land
REQ-US-SR-01	A drone shall dock an aircraft successfully 99.9\% of all attempts.	The docking procedure is designed such that this success rate achieved
REQ-US-SR-02	A drone will return to base for inspection and will request another drone to come to the aircraft if docking has failed.	The UAV system recognises docking failure and engages the docking failure procedure returning to the base and requesting another drone.
REQ-US-SR-03	A drone shall only be able to charge an aircraft when it has docked successfully.	Contact sensors ensure that docking is secure before charging begins
REQ-US-SR-04	A drone shall stop recharging automatically when the aircraft is full.	Battery condition sensors monitor the battery charge
REQ-US-SR-05	A drone shall have sufficient energy after recharging the aircraft to return to its base.	The hub placement and the drones flightpath ensure that the drone can return to its base
REQ-US-SR-06	The system shall work in all weather conditions in which the target aircraft can operate.	The system has been sized to the worst wind conditions and gusts have been accounted for in the structural design
REQ-US-SR-07	Drones shall track when they need maintenance in addition to regular maintenance checks and will fly themselves to and from a maintenance hub when required.	The maintenance is tracked by a schedule and the curtrent design has no auto-diagnostic capabilities
REQ-US-SUS-01	The life-cycle impact of the system shall be minimal.	All technical design of the drone takes as objective minimising environmental impact of the system thus minimising life-cycle impact in energy usage and material usage. The end of life performance of the materials are an important design criteria.
REQ-US-SUS-02	The nominal lifetime of a drone shall be 30 years.	The fatigue from the expected number of flight cycles has been incorporated into the structural design.
REQ-US-SUS-03	The hub shall be capable of producing its renewable energy when placed at a remote location.	No remote location hub design was performed
REQ-US-EB-01	The system shall be able to deliver enough power for a range of 500 \(km\) for a 6-8 passenger aircraft upon disconnect.	The charge delivered to the aircraft is sufficient for 764 km of ideal cruise flight including the distance flown during recharging
REQ-US-EB-02	A drone shall be able to transfer its charge to the aircraft in no more than 40 minutes.	Charging time is fixed at 40 minutes
REQ-US-EB-03	A drone shall be recharged at the hub in no more than 60 minutes.	The recharging procedure design was not performed
REQ-US-EB-04	The airframe of the drone shall be such that it can carry either a hydrogen charge or a battery charge.	Requirement changed
REQ-US-EB-05	A drone shall not fly faster than Mach 0.9.	The maximum velocity is equal to 0.59 Mach at cruise altitude in ISA conditions
REQ-US-CST-01	The cost per unit energy supplied to the aircraft shall be equal or less to 1.5 that of SAF assuming global wide-spread adaptation of the system.	The cost per unit energy supplied per hour is 2.017 times the cost of SAF fuel.
REQ-US-MSC-01	For demonstration, the system shall be designed for use with the “Electric Commuter Aircraft with Perpetual Flight Capability” – DSE project 13.	Done
REQ-US-MSC-02	The system shall be scalable to megawatt-class aircraft.	The current demonstrator system is not designed for aircraft of megawatt-class.It is scalable to these aircraft as scalability is a design criteria in recharge system design and operations design.
REQ-US-MSC-03	The system shall be extendable to worldwide coverage.	Analysis shows that there are enough suitable regional airports to extend eCarus to worldwide coverage
REQ-US-VA-01	There shall be no mid-flight battery replacement operation during the in-flight charging procedure.	In-flight recharging uses a safer probe-and-droge connection system to charge up the batteries directly
REQ-US-VA-02	The drone shall not land on the Electrifly aircraft during the in-flight charging procedure.	See explantion above
REQ-US-VA-03	The drone shall provide 600 kWh to the Electrifly aircraft during the in-flight charging procedure.	1264 kWh of charge is delivered to the receiving aircraft
REQ-US-VA-04	The drone shall provide a higher Voltage than the Electrifly aircraft’s battery during the in-flight charging procedure.	The drone supplies the energy at 1000V and the Electrifly’s battery operates at 800V
REQ-US-VA-05	The drone shall charge the Electrifly aircraft at an altitude above 1000 ft.	In discussion with Electrifly, charging occurs at 15000 ft due to the extra convenience
REQ-US-VA-06	The drone shall charge the Electrifly aircraft at a speed above 45 m/s.	Recharging occurs at the cruise speed of 110 m/s

Sustainability ans Safety Requirements		
REQ-SUS-ENV-01	The system shall have recycling procedures in place for the end-of-life phase.	The end of life phase accounts for recycling of the structure materials
REQ-SUS-ENV-02	The greenhouse gasses emitted during the system’s operation shall be 0 grams.	The drone uses electric engines that operate on electric energy supplied by green PPA contracts from the hub
REQ-SUS-ENV-03	The energy efficiency of the entire system shall be at least 50%, from input to energy in the recharged aircraft, at any time.	The efficiency of charge/discharge of the batteries and energy transfer through cables is designed over 90%.
REQ-SUS-ENV-04	The system shall be built compactly.	The drones planform and internal design eliminate unused volume
REQ-SUS-ENV-05	The system shall not leak poisonous waste to its environment during production, life-cycle, and end-of-life.	Not applicable to the design made
REQ-SUS-ENV-06	The system shall not leak radioactive waste to its environment during production, life-cycle, and end-of-life.	Nuclear power is not used to ensure that there is no radioactive waste
REQ-SUS-ENV-07	The system shall not leak explosive waste to its environment during production, life-cycle, and end-of-life.	Not applicable to the design made
REQ-SUS-ENV-08	The system shall not leak carcinogenic waste (causing cancer) to its environment during production, life-cycle, and end-of-life.	Not applicable to the design made
REQ-SUS-ENV-09	The system shall not leak mutagenic waste (causing damage to chromosomes) to its environment during production, life-cycle, and end-of-life.	Not applicable to the design made
REQ-SUS-ENV-10	The system shall not leak teratogenic waste (causing birth defects) to its environment during production, life-cycle, and end-of-life.	Not applicable to the design made
REQ-SUS-ENV-11	The system shall not leak bioaccumulative waste (that is, increasing in concentration at the higher ends of food chains) to its environment during production, life-cycle, and end-of-life.	Not applicable to the design made
REQ-SUS-ENV-13	The system shall not leak waste containing dangerous pathogens to its environment during production, life-cycle, and end-of-life.	Not applicable to the design made
REQ-SUS-ENV-14	The system shall not emit fine particles during operations.	The system uses electric engines that don’t emit any pollutants during operation
REQ-SUS-ENV-15	The system shall not emit mono-nitrogen oxides.	See explanation above
REQ-SUS-EC-01	The total cost of recharging mid-air, taking into account time saved and alternative recharging logistics, shall be lower or equivalent to a recharging stop in an airport or recharging station.	A recharge stop would cost around 672 USD while a inflight recharging costs 2408 €
REQ-SUS-EC-03	The budget shall account for and cover the total maintenance and operational costs of the drone and hub.	The financial budget takes these aspects into account for the financial budget
REQ-SUS-EC-06	The system’s operations cost increase shall be less or equal to the inflation rate.	Future predictions on operation costs were not analysed in the current design
REQ-SUS-SOC-02	The system’s production, maintenance, and operation shall not make use of any type of forced labor, child labor, or discrimination.	The production of the drone does not utilise child labour, forced labour and discrimination is forbidden by the project sustainability requirements
REQ-SUS-SOC-03	The system shall not fly over residential areas at an altitude of less than 305m	The system uses regional hubs and drones will follow already established flightpaths until at high enough altitude
REQ-US-SUS-01	The life-cycle impact of the system must be minimal.	The life cycle of the design is analysed and the impact on sustainability of the system is an important design criteria
REQ-US-SUS-01	The life-cycle impact of the system must be minimal.	The life cycle of the design is analysed and the impact on sustainability of the system is an important design criteria

Sustainability ans Safety Requirements (cont)		
REQ-US-SUS-02	The nominal lifetime of a drone shall be 30 years.	The batery choice and material and structureare designed for a 30 year lifetime
REQ-US-SUS-03	The hub is capable of producing its renewable energy when placed at a remote location.	Local airports are chosen as hubs. Purpose built hubs in remote locations are deemed financialy infeasable for the inital implemetation of eCarus.
REQ-US-CST-01	The cost per unit energy supplied to the aircraft shall be equal or less to 1.5 that of SAF assuming global wide-spread adaptation of the system.	The cost per unit energy supplied per hour is 2.017 times the cost of SAF fuel.

Top-level Requirements		
REQ-SYS-PR	The system shall provide sufficient thrust for all operations.	The engines have been sized to account for the different thrusts needed during all
REQ-SYS-PW	The system shall provide electrical power to all subsystems.	The power of the batteries is sufficient to supply all the subsystems of the drone
REQ-SYS-ST	The system’s structure shall support all subsystems.	The structure has been designed according to a load analysis that incorporates the significant loads of all subsystems
REQ-SYS-PL	The system shall ensure the operation of the payload.	The payload is delivered safely and in-time to the recieving aircraft
REQ-SYS-FP	The system shall enable flight performance for all operations.	The drone has sufficient flight performance to conduct all operations. The flight performance needed in emergency situations have also been considered
REQ-SYS-UAV	The system shall operate an autonomous UAV system.	A high-level design has been made of the autonomous UAV system
REQ-SYS-OP	The system shall have operational logistics.	The system logistics are designed to be operational with contingencyies planend

REQUIREMENT	DECRIPTION	STATUS
Electrical Power System Requirements		
REQ-SYS-PW-01	The electrical power system shall provide sufficient power to the systems of the drone.	The power of the batteries is sufficient to supply all the subsystems of the drone
REQ-SYS-PW-02	The system shall have separate energy storage for power used by propulsion and for power used by auxiliary power and operating systems.	The drone has two batteries. One for its own propulsion and one to carry the energy that will delivered
REQ-SYS-PW-03-01	The electrical power system shall provide a minimum DC voltage of 28 [V].	The battery is capable of providing 800V of charge meaning with the correct converter 28V of DC power can be achieved
REQ-SYS-PW-03-02	The electrical power system shall provide a minimum AC voltage of 115 [V].	The same explanation as above applies
REQ-SYS-PW-03	The electrical power system shall be able to deplete the entire reserve of energy for propulsion of its energy storage in case of emergency.	In nominal operation only 90% to 10% of the battery capacity is used. The last 10% can be used in case of emergency
Structural Requirements		
REQ-SYS-ST-01	The structure shall not fail under the expected loads during all operational phases with an applied safety factor of 1.5.	The safety factor used is 1.3. This is in complaince with NATO UAV drone certification
%REQ-SYS-ST-02	The structure shall ensure a rigid drone.	Deformation in the structure has been analysed and is limited
REQ-SYS-ST-03	The structure shall ensure proper load paths between different subsystems.	Loadpaths go through the nodes in the truss structure
REQ-SYS-ST-04	The nominal lifetime of a drone shall be 30 years.	The batery choice and material and structureare designed for a 30 year lifetime
REQ-SYS-ST-05	The structures shall have a safe-life of 45 years. [REQ-SYS-ST-01]	The drone has an operational life of 30 years
REQ-SYS-ST-06	The structure shall have corrosion control.	Material selection has accounted for corrosion performance
REQ-SYS-ST-07	The structure shall have a fatigue cycle life of 100,000 mission cycles.	30,000 mission cycles have been factored into the fatigue analysis and design
REQ-SYS-ST-08	The structure shall be able to endure a positive load factor of 2.5g.	The maximum positive load factor that the drone can endure is 3.06g
REQ-SYS-ST-09	The structure shall be able to endure a negative load factor of -1g.	The maximum negative load factor that the drone can endure is -1g
REQ-SYS-ST-10	The structure shall endure the ultimate load for at least 3 seconds. [CS 25.305]	The design certifications of the structure are respected and contain this criteria
Propulsion System Requirements		
REQ-SYS-PR-01	The propulsion system shall provide a minimum power-over-weight ratio of 10.	The drone has a power-over-weight ratio of 11.27
REQ-SYS-PR-05	The propulsion system shall provide cruise thrust with an efficiency of at least 80%.	The propulsion system has an theoretical efficiency of 93.6% durring cruise
Payload Requirements		
REQ-SYS-PL-01	The system shall enable docking to the aircraft to transfer energy.	In-flight recharging uses a safer probe-and-droge connection system to charge up the batteries directly
REQ-SYS-PL-03	The payload shall have a power transfer capacity of 1.5 MW.	The drone supplied 1.7 MW of power to the recieving aircraft
REQ-US-EB-02	A drone shall be able to transfer its charge to the aircraft in no more than 40 minutes.	Charging time is fixed at 40 minutes
REQ-US-SR-04	A drone shall stop recharging automatically when the aircraft is full.	Sensors and communication links are designed to signal the UAV system to stopcharging at full charge
REQ-US-EB-01	The system shall be able to deliver enough power for a range of 750 km for a 6-8 passenger aircraft upon disconnect.	The system payload battery size is designed to charge the ElectriFly aircraft for an additional range of 750 km
Autonomous UAV System Requirements		
REQ-SYS-UAV-01	The system shall be able to communicate	The drone uses a communication system that is capable of data transfer with external systems, being other drones, the hubs, and the electric aircraft
REQ-SYS-UAV-01-01	The system shall be able to communicate with the aircraft.	See the explantion above
REQ-SYS-UAV-01-02	The drone system shall be able to communicate with the hub.	See the explantion above
REQ-SYS-UAV-01-03	The drone system shall be able to communicate with other drone systems.	See the explantion above
REQ-SYS-UAV-01-04	The system shall be able to communicate with aircraft control.	See the explantion above
REQ-SYS-UAV-02	The drone shall return to the hub when maintenance is required.	The drone returns to the hub when maintenance is sheduled
REQ-SYS-UAV-03	The system shall be able to locate the aircraft.	See the explantion above
REQ-SYS-UAV-04	The drone system shall not collide with its environment.	The drone uses avoid and detection sensors to ensure it will not collide with an aircraft or any other objects
REQ-SYS-UAV-05	The UAV system shall have the ability to autonomously fly itself to a determined location and altitude.	The UAV system uses autonomous flight and control systems and GPS sensors to locate and fly to the aircraft
REQ-SYS-UAV-06	The drone shall be able to manoeuvre to the designated take-off area.	The drone can use its landing gear and thrust to taxi
REQ-SYS-UAV-07	The drone shall be able to abort the take-off procedure.	Done
REQ-SYS-UAV-08	The drone shall be able to determine the reason for a take-off abortion.	The drone diagnoses the type of charging failure that happenned
REQ-SYS-UAV-09	The drone shall be able to determine its geographical location.	The drone UAV system utilises GPS localisation
REQ-US-SR-02	A drone will return to base for inspection if docking has failed.	The drone is ableto return to the hub if charging fails. It travels from hub to hub to reach the hub that has the proper maintenance equipement
REQ-US-PER-01	The drone shall dock the aircraft autonomously.	The drone uses computer vision to detect the drogue and adjust attitude, probe thrusters maintain probe altitude.
REQ-US-PER-02	A drone shall detach autonomously from the aircraft after recharging the aircraft.	The drone recharging system does it autonomously

Recharging system

Identifier	requirements	Status
REQ-PD-MS-01	The drogue-probe system shall have a communication system in terms of system status to both the drone and aircraft.	ECU + PSD integrated in system
REQ-PD-MS-04	The probe/drogue system shall have a clearance of 8 m.	Clearance is 8-11 meter.
REQ-PD-MS-05	The drogue-probe system should have a system that allows a discharge of 300 kV between the aircraft and the drone [19].	Designed for discharge handling
REQ-PD-MS-06	The drogue and probe shall have communication in the form of IR sensors and reflectors.	PSD integrated
REQ-PD-MS-07	The drone shall redock in case of tension/compression cut-off.	Recharge procedure
REQ-PD-MS-08	The drone shall have 5 minutes to connect.	Imposed by the recharge procedure
REQ-PD-PR-01	The structure of the probe/drogue system shall withstand loads induced during an engagement of 3 m/s.	Designed for 5.6 kN, 9.2 kN in tension, compression.
REQ-PD-PR-03	The prope nozzle are capable of an off-center disconnects of 22.5 degrees maximum [19].	Due to designed ball joint.
REQ-PD-CB-01	Cable length should provide a stable droque/cable configuration and shall provide the drone/aircraft of enough clearance.	8-11 m clearance
REQ-PD-CB-02	The Drogue + Cable should be inherently stable.	designed dragnet to be tested
REQ-PD-CB-03	Th drogue+coupling should not spin. In addition the coupling swivel ball should not be mechanically clamped.	Designed rotating coupling
REQ-PD-CB-04	At full trail the vertical and lateral oscillations should not exceed half the diameter of the drogue canopy. These oscillations should dampen out to 1/3 amplitude after 3 cycles [19].	to be tested
REQ-PD-CB-05	The cable tension/compression should not exceed 6.7 kN / 11 kN.	Designed for
REQ-PD-DR-01	The drogue shall be aerodynamically stable.	Implemented drogue net
REQ-PD-DR-02	The drogue shall aim towards the probe using thrusters and or rotary connections.	Implemented thrusters
REQ-PD-DR-03	The probe/drogue system should not interfere with the air data sensors of the drone.	Air data sensors not leading edge
REQ-PD-CU-01	The cable unit shall provide air/liquid to fulfill thrusters.	Implemented in cable
REQ-PD-CU-03	The cable unit shall be able to extend and bring in the cable.	Cable Drum Unit used
REQ-PD-CU-04	The cable unit shall include a rotation spring and damper to mitigate oscillations in the distance between the plane and drone.	implemented by ElectriFly group

REQUIREMENT	DECRIPTION	STATUS
Flight Performance Requirements		
REQ-SYS-FP-01	The drone system shall sustain steady flight.	The lift has been sized to counteract the weight
REQ-SYS-FP-01-01	The drone system shall fly steadily at velocities up to 413 km/h.	The maximum velocity of the drone 121 meters per second which is equal to 436 km/h
REQ-SYS-FP-01-02	The drone system shall sustain steady flight in every weather condition acceptable to operate the aircraft.	The control surfaces can handle disturbances that can be encountered durring flight
REQ-SYS-FP-01-03	The drone system shall sustain steady flight during launch phase conditions.	The max lift coefficient is sufficient for take-off
REQ-SYS-FP-01-04	The drone system shall sustain steady flight during recovery phase conditions.	The max lift coefficient is sufficient for landing
REQ-SYS-FP-04	The drone system shall handle subsonic aerodynamic effects.	The design has been made using calculations for subsonic conditions since the
REQ-SYS-FP-05	The aerodynamic interference effect of the drone shall not induce instability of the aircraft.	The drone flies behind the recieving aircraft so that it does not cause any aerodynamic interference
REQ-SYS-FP-06	The drone system shall be statically stable.	The center of gravity is infront of the neutral point. Directional stability is also sufficient
REQ-SYS-FP-07	The control of the drone system shall ensure dynamic stability.	The eigenmotions are stable, control dampers have been implemented, this has increased the dynamic stability to acceptable levels
REQ-SYS-FP-08	The noise generated shall not be more than 65 dB at places with people present.	The designed duckted fan reduces the noise by half. During taxi this is below the limit but durring take-off the 65db is realistically unachievable by any flying object. A simple pleasure quadcopter drone generates between 70 and 80 db. At cruise the eCarus engine generates only 56.67db.
REQ-SYS-FP-09	The drone system shall not fly faster than Mach 0.9.	The maximum velocity is equal to 0.59 Mach at cruise altitude in ISA conditions.
REQ-SYS-FP-10	The drone shall fly along with the Electrifly design group’s aircraft during recharge.	The drone flies roughly 10m behind and 5m underneath Electrifly during rechargeing. The distances will be finetuned in testing later.
REQ-SYS-FP-10-01	The drone system shall cruise with the aircraft at a cruise velocity of 396 km/h.	The cruise speed of the drone is 396 km/h
REQ-SYS-FP-10-02	The drone shall remain controllable and manoeuvrable during the entire recharge under any condition.	The cable of the drogue-probe recharging allows the drone to fly freely within the recharging zone. The control surfaces enable this manouvrebility.
REQ-SYS-FP-10-03	The drone system shall cruise with the aircraft at an altitude of 4572 m.	The cruise altitude during rechargeing 4572m
REQ-SYS-FP-11	The drone system shall have a maximum bank angle of 60 degrees.	At low speeds the drone can handle bank angles of 60 degrees
REQ-SYS-FP-12	The drone system shall have a climb gradient of at least 8.3% in every condition.	The propulsion systemis is designed to comply with this requirement
REQ-SYS-FP-13	The drone system shall be able to perform a 'go-around' manoeuvre.	The drone will be able to increase its thrust during landing to perform a go-around
REQ-SYS-FP-14	The drone system shall be able to distance the aircraft by 40 m in 5 seconds in case of an emergency.	The drone is capable of decelerating at 8 meters per second safely. The drone could also manouvre to the left, right, or bottom of the aircraft easily.
REQ-SYS-FP-15	The drone system shall have a maximum turn rate of 2 degree per second	The load factor durring a 2 degree per second turn will be 1.07 which is within the operational limits of the drone

Operational Requirements		
REQ-SYS-OP-01	The system shall allow maintenance facilities at the hub.	Maintenance facilities at or near the local airports are used for drone maintenance
REQ-SYS-OP-02	The system shall be able to determine weather conditions at the aircraft location.	Communication systems between the aircraft and the hub will convey weather data
REQ-SYS-OP-03	The system shall be able to determine weather conditions at the hub.	The hub is at a local airport with readily available weather data
REQ-SYS-OP-04	The system shall be able to make a 'go' or 'no go' launching decision.	The drone is able to fly in all conditions in which a recieving aircraft would fly. It will adhere to the advice of the airport tower on whether flying is allowed or not.
REQ-SYS-OP-05	The system shall track when it needs maintenance in addition to regular maintenance checks.	The maintenance is tracked by a schedule and the curtrent design has no auto-diagnostic capabilities
REQ-SYS-OP-06	The system shall determine the landing and launching locations.	Optimal hub locations can be determined using the hub placement code
REQ-SYS-OP-07	A hub shall be able to determine the specific drone to be sent to a certain aircraft.	All drones are the same meaning that the system only has to determine which drone is sufficiently charged to conduct the operation.
REQ-SYS-OP-08	The hub shall be able to produce its renewable energy.	The hub will operate on green energy supplied by local PPAs
REQ-US-PER-03	A drone shall reach the aircraft within 20 minutes in case of an emergency.	The maximum distance between hub and passing aircraft has been sized to ensure that an emergency aircraft can reach the aircraft within 20 minutes of declaring a charging failure
REQ-US-PER-04	The system shall be able to meet electric aircraft demand by 2050.	The design is made to operate a test flight in 2030, 2050 demand is not taken into account in the current design
REQ-US-PER-04-01	A hub shall be able to store all the drones used for charging simultaneously.	Hangers at the local airport can be rented for storage of the drones
REQ-US-EB-03	A drone shall be recharged at the hub in no more than 60 minutes.	The recharge time of the batteries is not analysedin the current design. However, due to the drone having two split high-voltage batteries this requirement is likely achievable.
REQ-US-SR-06	The system shall operate in all weather conditions.	The system has been sized to the worst wind conditions and gusts have been accounted for in the structural design

Resource Requirements		
REQ-SYS-RES-03	The system shall be designed with the available TU Delft facilities.	Done
REQ-SYS-RES-04	The system shall be designed with a total of 4000 man-hours.	Done
REQ-SYS-RES-05	The system shall be designed within 10 weeks.	Done
REQ-SYS-RES-06	The system shall be designed with 10 full-time members.	Done
REQ-SYS-RES-07	The total costs per charge shall not be more than € 6,800.	The cost per recharge is 2629$ which is equal to €2408

Safety Requirements		
REQ-US-SR-07	Under no condition shall the drone collide with the aircraft.	The drone uses avoid and detection sensors to ensure it will not collide with an aircraft or any other objects
REQ-US-SR-01	A drone shall dock an aircraft successfully 99.9\% of all attempts.	The docking procedure is designed such that this success rate achieved
REQ-US-SR-02	A drone will request another drone to come to the aircraft if docking has failed.	A new drone is launched after 5 minutes of failed docking
REQ-US-SR-03	A drone shall only be able to charge an aircraft when it has docked successfully.	The docking procedure is designed so that an unsuccessful docking aborts recharge
REQ-SYS-SAF-01	The drone shall not collide with any of the ground systems.	The drone uses avoid and detection sensors to ensure it will not collide with an aircraft or any other objects

Regulations and Legislation Requirements		
REQ-SYS-LEG-01	The system shall adhere to airspace regulations.	The system operates at altitudes, speeds, and locations, in complaince with airspace regulations
REQ-SYS-LEG-02	The system shall adhere to safety regulations.	UAV regulations specified by the NATO have been used to design the drone structure
REQ-SYS-LEG-03	The system shall be certifiable.	See the reason above
REQ-SYS-LEG-04	The system shall respect the international charter of human rights.	Done. Does not apply to the design made

Objectives		
OBJ-SUS-SOC-01	The price of the implementation of the system for customers shall be minimized.	Minimizing cost has been a criteria in every relevant trade-off
OBJ-SUS-EC-01	The production, maintenance, and operation cost of the system shall be minimized.	Minimizing cost has been a criteria in every relevant trade-off

14 Financial Analysis

This chapter elaborates on the financial feasibility of the project. It is of utmost importance to analyse not only the operational and manufacturing costs but also the potential market. In section 14.1, the operational and manufacturing costs are discussed. Then an analysis is performed for a testflight and the return on investment is assessed. In section 14.2, the market analysis is assessed to further verify feasibility.

14.1. Cost Analysis

In order to perform a cost analysis of the eCarus aircraft. Operational and manufacturing costs are estimated using equations prescribed in Roskam [105]. As the eCarus is an innovative aircraft design, various modifications to this method are made in order to more realistically assess the total costs.

14.1.1. Operational Costs

For the operational costs, equations concerning crew, passengers, or aviation fuel have been omitted or modified to fit the specifics of the eCarus aircraft. Operational costs are first divided into direct and indirect operating costs. For calculating operational costs Roskam uses data from between 1970 and 1989. However, current wages, electricity prices, and manufacturing costs have been used as a basis for many of the equations. As a compromise, the costs have been upscaled with the inflation rate of 1989 to today which is 245.3% [106]. Manufacturing costs have been estimated using the current estimations of key subsystems.

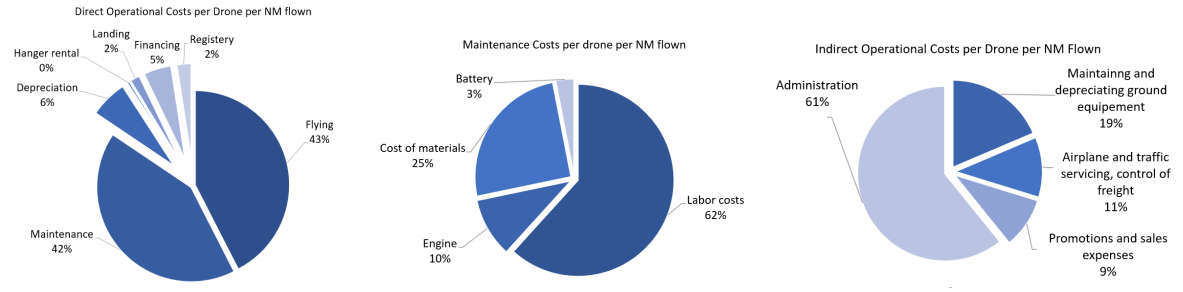

(a) Direct operational costs **(b)** Direct operational maintenance costs **(c)** Indirect operational costs

Figure 14.1: Idirect operational cost breakdown

Table 14.1: Operating costs

Operating costs per NM	
Total per drone per year	2 894 032 USD
Lifetime costs per drone	86 820 967 USD

Table 14.2: Price breakdown

Price breakdown	
Price per recharge	3405.4 USD
Total costs per recharge	2628.8 USD
Payload energy cost	672.8 USD
Profit margin	103.5 USD

Indirect costs encompass the many costs needed to operate a business. The largest cost is the salary of workers that would need to work in the office to be able to manage a vast network of drones. For the indirect cost, the cost is split over all the drones in operation. Although the indirect costs also scale up with a larger network of drones, the price per drone decreases the more drones are active. The cost

requirements assume a global adoption of the system. Therefore the indirect costs have been split over 100 drones.

The average profit margins in the airline industry, pre-corona, hovered around 5.5% [107]. Applying this rate and incorporating the cost of the energy being delivered yields a total price for the customer of 3405.4 USD. These results are visualised in Table 14.2
Requirement [REQ-US-02] states that "The cost per unit energy supplied to the aircraft shall be equal or less to 1.5 that of SAF assuming global wide-spread adaption of the system. The price of sustainable aviation fuel (SAF) fuel is 1.1 USD per litre [108]. A Cessna Citation CJ4 (8-person business jet) uses 659 litres of fuel per hour [109]. Multiplying this by the 1.5 factor results in a maximum cost of 1087.4 USD per hour of flight.

An electric aircraft using a single recharge with characteristics similar to Electrifly would spend 442 USD on charging its own batteries on the ground. Then, it would spend 3405 USD on a full recharge mid flight. In total, the flight would take 2.56 hours meaning that per hour this would cost 1503 USD. If the profit margin of eCarus is discarded, this decreases to 1462 USD per hour of flight. This is equivalent to 2.017 times the cost of SAF, meaning the requirement is not satisfied. However, the margin of a few hundred USD per hour does seem to indicate that the requirement could be satisfied with the future refinement of the eCarus system. How this could be done will be elaborated on in section 14.4.

14.1.2. Manufacturing Costs

According to Leeham, the replacement cost of batteries is projected to be 400 USD - 500 USD per KWh at the end of the decade [110]. As the flight test is not taking place before 2035, the optimistic value of 400 USD is used. This implies that the replacement costs of the payload battery (1246 kWh) and the primary battery (749.95 kWh) are 623 160 USD and 299 980 USD, respectively. This comes down to a total cost for the batteries of 923 140 USD. According to Pipistrel CTO Tine Tomažič, a reasonable assumption for engine costs is 300 EUR per kWh. Using the current conversion rate of 1.09 USD/EUR, this comes down to 327 USD per kWh. Thus, both the two engines that use 374.98 kWh, cost 122 616.825 USD. Roskam's method for estimating manufacturing costs is deemed inaccurate when applied to a BWB structure with electric propulsion and no fuselage. Therefore, it is decided to use the reliable costs of the engines and of the batteries to scale the costs of the other major components of the drone. Using the distribution of costs per component for existing aircraft as a reference the estimation of the breakdown of manufacturing costs is shown in **??**. The relative importance of the wing and structure has been increased due to the BWB design, the major cost of the batteries has been added, and the importance of systems has also been increased due to the costs of operating UAV system as well as the extensive thermal management system.

Figure 14.2: Manufacturing cost breakdown

Manufacturing Cost Breakdown	
Total Cost	2 305 842 USD
Battery	923 140 USD
Wing and structure	830 826 USD
Systems	323 099 USD
Engines	122 616 USD
Empennage	43 849 USD
Landing gear	62 312 USD

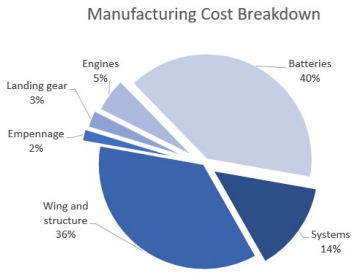

Figure 14.3: Manufacturing costs

14.1.3. Return on Investment

The total operating costs of one drone is 86 820 967 USD over a lifetime of 30 years as fixed by requirement [REQ-US-SUS-02] stating that "the nominal lifetime of a drone shall be 30 years". New airlines have a downtime of one average 3 weeks per 18 months. Large maintenance checks like this increase with the age of the aircraft. However, the eCarus drone combines many novel technologies and will therefore need far more maintenance than the reliable airliners of today. Therefore it is assumed that the eCarus drone will fly 300 days a year. It is also assumed that the demand for the eCarus drone on

the days that it operates will be high due to the optimal placement of hubs. A drone can fly roughly four times a day when accounting for the charging time it needs on the ground. This yields 1200 flights a year. Each flight makes a 5.5% profit margin. The drone will therefore compensate the total operating investment of 86 820 967 USD plus the 2 305 842 USD manufacturing investment with a 9 139 878 USD profit. The operational cost and the depreciation the drone are both incorporated into the operational cost meaning that the 9.14 million dollar profit is pure profit.

For the eCarus system to properly function a sizeable network of hubs must first be developed. A larger network yields a larger profit but it also requires a large initial investment.

The drone 2 305 842 USD to build and returns a 304 662 USD in profit per year of operation. This yields a return on investment of 7.57 years. However, the true return on investment is longer due to the capital needed to start up production, build the offices, and secure the first clients.

Due to the use of existing local airports as hubs, the initial investment is kept lower than expected and is mainly comprised of acquiring drones. Costs such as setting up an office, hanger rental, and ground services have been incorporated into the operational costs of the drone.

14.2. Market Analysis

Doing a proper market analysis is key for assessing if the solution is viable. The baseline report focused on analysing the pros and cons of an eCarus-like solution in the global market. Now that a final design has been made, the larger assumptions and conclusions drawn in the baseline can be evaluated against the design. Therefore this chapter will briefly summarise the main conclusions mentioned in the baseline report and then continue to assess the feasibility of the final design in a future market.

14.2.1. Market Volume and Timing

The aviation industry is expected to grow with the high demand for new aircraft. While there are ongoing developments in hybrid and electric aircraft, they are still in the early stages and have not been widely adopted. However, the support from major players in the industry indicates a strong drive to develop this technology. The market for electric or hybrid aircraft recharging is currently extremely small but expected to grow significantly with the push for electric air travel and overall market expansion.

The development of electric aircraft creates an ideal opportunity for in-flight recharging. Eviation's 9-seater aircraft, Alice, demonstrates the feasibility of electric passenger planes flying worthwhile distances. The market for electric in-flight recharging is almost entirely unexplored, with only a few players in the early development stages (technology readiness levels (TRL) of 2 or 3). This presents a new market with potential military applications and growth that mimics the growth of in-flight refuelling in the 1920s.

14.2.2. Market Opportunities

Analysis reveals opportunities in sustainability and infrastructure for a mid-flight UAV recharging system. The growing demand for sustainable air travel, driven by emission reduction goals set by the International Civil Aviation Organisation [111], creates a compelling investment opportunity. The limited range of current electric aircraft emphasises the need for a recharging system to enable such aircraft to properly compete with current fossil-fuel or even hydrogen-power variants. The recent developments by aircraft such as the Eviation Alice show their potential to perform missions traditionally reserved for fossil-fuel aircraft. The eCarus system could make optimal use of the boom in electric aircraft development making the timing of an eCarus system another great opportunity.

14.2.3. Challenges and Competitors

To compete in the market, assessing challenges and opportunities is crucial. As battery technology progresses the increase in electric aircraft range could potentially make in-flight recharging unnecessary. On the flip side, eCarus can remain relevant by considering its role in extending the range of electric aircraft allowing them to carry smaller batteries and thus operate more efficiently. A smaller, more weight-efficient battery combined with a widespread network of hubs could make in-flight recharg-

ing more favourable than carrying a heavy battery throughout the entire flight. The added costs of an eCarus also pose a challenge in making the service competitive with a saturated flight market.

14.2.4. Flight Distance

The baseline report made an analysis of the distribution of flight lengths around the world with the intention of highlighting that there is a band of ranges that are more popular, and thus have more clients for eCarus. This analysis is now extended and evaluated against the capabilities of eCarus.

The range an aircraft can fly by itself is critical for optimal hub spacing. To be able to extend the range as far as possible, hubs should be placed near the ends of the aircraft's own range. Therefore, when examining the goal of extending the range of electric aircraft, examining the ranges that aircraft would like to fly is critical to understanding the market.

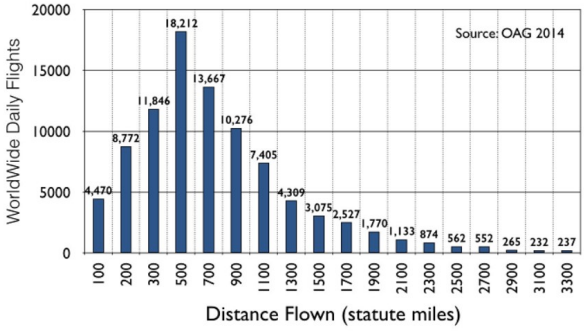

(a) Number of worldwide daily flights per distance flown in 2014. Provided by Official Online Guide (OAG) [112]

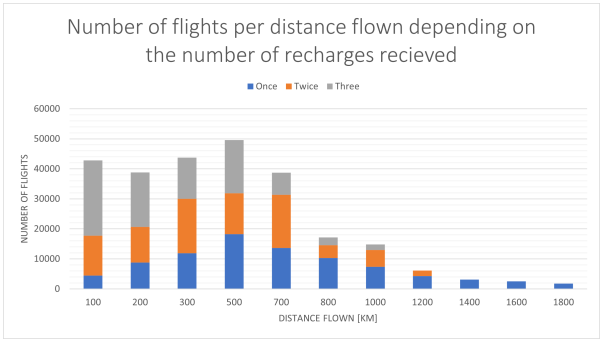

(b) Flights per distance flown per recharge

Figure 14.4: Flight statistics

The figure 14.4a shows the distances that flights around the world flew in 2014. The peak is clearly around 500 NM which is equivalent to 926 km. For the purposes of recharging, this means that the optimal aircraft range to recharge is 463 km which would need one recharge. However, more recharges can also be supplied, which would open up longer-range markets. Breaking up the data into multiple recharges yields the following figure:
Figure Figure 14.4b shows the number of flights optimally match with a set number of recharges due to their distances. More recharges could be less popular due to the added expense but it could also open up new longer-range markets for electric aircraft. Therefore, if assuming that these two factors roughly cancel out, the graph above can be used to see what range of aircraft are best serviced by eCarus. The best flightpaths to service are flights with a distance around 500 km. The combined market for 500 km, 1000 km, and 1500 km range is thus apparently larger than intervals at other ranges.

It is key to note that ranges below or above 500 km can also be serviced by eCarus. However, from a perspective of extending the range of electric aircraft, and allowing as many flightpaths as possible to convert to electric flying, a 500 km range aircraft are best. Coincidentally, the eCarus system has been designed to service the ElectriFly aircraft which has a design range of 500 km. This falls perfectly within the range zone with the largest demand. Therefore the eCarus system is well-positioned to enter the market.

14.2.5. Additional Income Streams

Aside from extending the range of electric aircraft, another business model is based on using in-flight recharging to reduce aircraft downtime. If the time to charge an electric aircraft is longer than the turnaround time for the passenger or cargo, then the charging would be the limiting factor in turn-over time. This would drastically increase the total costs of a turnaround since every minute on the ground counts. Assuming a short-haul aircraft that performs 2-hour flights 7 times a day with a turnaround time of an hour, a decrease in turnaround time of only 14.3% or 17.2 minutes means that an extra flight can be flown per day [113]. This would significantly increase the airline's profits for that aircraft.

For this to be another profit stream for the product, in-flight recharging would have to be cheaper than the extra turnaround time on the ground as well as the electricity available at the airport. The reality of this is now investigated.

If choosing to recharge at the destination, then the aircraft will have to pay for the charging infrastructure including the electricity and the parking time needed during charging. Immaterial losses must also be factored in such as the downtime penalty on how many flights can be flown per day. If the recharge is done at an intermediate airport, then the cost of extending the flight time and its effect on how much customers are willing to pay must also be factored in.

Schiphol airport charges no parking fees for parking times shorter than 6.5 hours [114] therefore this component of the cost is disregarded. The costs of electricity at airports are not much more than charging up an electric car in the city according to an employee of Rotterdam Airport Table 15.1. The cost of recharging in Amsterdam varies around 0.54 cents per kWh [115]. It is also key to understand that eCarus delivers the charge used up by flying during recharge on top of a full battery charge. This amounts to a 153% charge. Therefore, to make a fair comparison, the total charge that eCarus delivers of 1246 kWh must be considered instead of the smaller charge the Electrifly could receive on the ground. 1246 kWh is equivalent to 673 USD. No significant direct costs are associated with the ground recharging.

The fastest that this recharge can be done is in 40 minutes. The mean distance the Electrifly flies is 400 km at a cruise speed of 396 km. Taking into account boarding, taxi, lift-off, and landing this means a total flight time of roughly 2 hours. Adding charging this becomes 3 hours. This means that on a very busy day, Electrifly could perform roughly 5 flights a day in a 15-hour window. If the charging was done during the flight, this would increase to 7 to 8 flights a day. A 40-60% increase. Two to three extra margins could be earned.

When recharging using eCarus, the electricity price remains roughly the same since electricity prices do not vary significantly. The price of the eCarus service is 3405 USD per recharge including electricity costs. This leaves a 2732 USD gap.

Factors such as the indirect costs of increasing the total flight time account for some of this increase. The Electrifly aircraft costs 781 EUR per hour of operation [3]. Using the pre-corona industry average of 5.5% profit margin [107], this amounts to 43 EUR of profit per hour of flight. In-flight recharging allows the aircraft to nearly continuously operate yielding a 15-hour operation day. On the ground, recharging reduces this to 10. The extra 5 hours amount to 215 EUR.

The remaining 2517 EUR price difference cannot be completely justified by logical business decisions. With a 5.5% margin, Electrifly would charge a total of 824 EUR per hour of flight which is 103 EUR per passenger. The 2517 EUR eCarus price adds an extra 314.6 EUR to the ticket price quadrupling the ticket price per hour of flight. Therefore the eCarus system in its current state will be heavily reliant on the drive towards flying sustainably both by passengers and through the subsidies of governments to reduce or justify the price.

14.2.6. Potential Market Share and Return on Investment

To evaluate if the eCarus system would be a feasible system in the real world. The return on investment must be estimated. More importantly, the break-even point must be found. Due to the complex nature of building a global network of hubs and the massively varying number of flights this can service, performing a break-even analysis of the global system could quickly become complete and unreliable. Therefore, the break-even point for a smaller system will be estimated and later extrapolated to worldwide coverage.

The test-flight from Amsterdam to Madrid, discussed in section 14.3, requires two hubs: Aéroport Orléans Loire-Valley and Arcachon – La Teste-de-Buch Aéroport. These hubs are strategically posi-

tioned in overlap zones, allowing three specific flight paths within the EU to utilise them for their routes. The routes benefiting from these hubs are Madrid to Amsterdam, Madrid to Brussels, and Madrid to Paris. In 2021, the number of passengers flying between Madrid and Amsterdam was 918 751, Madrid and Brussels was 820 916, and Madrid and Paris were 1 110 630 [100]. It's important to mention that while there are 707 707 flights from Madrid to Amsterdam, the return flight is not listed in the top 50. Therefore, we assume that the return flight falls just outside the top 50 and consider the lowest value, 402,923. Notably, the Madrid-Paris route exclusively utilises the Arcachon – La Teste-de-Buch Aéroport hub.

With an average of 100 passengers per flight, this means that there are 17,397 that could be recharged by the hub at Aéroport Orléans Loire-Valley and 28,503 flights that could be serviced by the hub at Arcachon – La Teste-de-Buch Aéroport. This is of course conservative since flightpaths outside the top-50 busiest could also be serviced by one of the two hubs. It is also key to note that the hub at Aéroport Orléans Loire-Valley would only be 126 km away from Paris Charles de Gaulle airport which means it could be used for the turn around time business model. This would increase the traffic to the hub even further.

Adoption rate estimation

Over the next two decades, more than 44 000 new aircraft are expected to be placed on the market. The potential market volume for zero-emission aircraft has been estimated at 26 000 by 2050 according to a press release of the European Union in June 2022 [116].

This is equivalent to 59.1% of all new aircraft. The average aircraft lifespan is between 20 and 30 years indicating Over the 27 years left until 2050 most old aircraft will have been cycled out. This leads to the assumption that 50% of all aircraft flying in 2050 are zero-emmision. The 9.1% is left out to take into account the small fleet of old aircraft still flying in 2030.

The two largest players in the zero-emission aircraft market are electric and hydrogen aircraft. Therefore, assuming that 40% of all new zero-emission aircraft are electric, it predicts 10,400 electric aircraft in 2050 which could all be fitted to be compatible with eCarus. The adoption rate of eCarus is hard to predict, therefore three different values will be used so that the results can be compared: 2%, 5%, 10%. These adoption rates lead to 208, 520, 1040 aircraft respectively.

If 50% of the aircraft flying in 2050 are zero-emission aircraft and of that roughly 40% are electric then 20% of aircraft flying in 2050 are estimated to be compatible. Using the same 2, 5, or 10% adoption rates and multiplying them together with the 20% results in that 0.4%, 1%, and 2% of all aircraft flying in 2050 will be using eCarus. Having this value as a percentage allows it to be reasonably applied to the number of flights between two locations to estimate how many eCarus fitted aircraft will fly that route.

This percentage can be applied to the 17 397 that could be recharged by the hub at Aéroport Orléans Loire-Valley and 28 503 flights that could be serviced by the hub at Arcachon – La Teste-de-Buch Aéroport. This results in that 70, 174, 348 flights per year for the Loire-Valley hub and 114, 285, 570 flights per year for the Arcachon hub. The yearly numbers for 2 and 5% adoption rates are low meaning that an adoption rate of at least 10% of compatible electric aircraft is likely required for the system to be financially sustainable. Factors such as servicing more routes per hub and servicing nearby international airports with recharge to reduce turnaround time could alleviate the high adoption rate.

14.3. Business Case: Test Flight

In order to assess the economic viability of the eCarus system, the total cost for a reference flight is estimated. As discussed in chapter 11, there are multiple viable flight routes in Europe as well as in the US. The test flight considered is an electric aircraft taking off from Amsterdam (The Netherlands) and landing in Madrid (Spain).

Overflight fee

The overflight fee is a fee for using the air traffic control (ATC) of a certain geographical region. In Figure 14.5, the test flight is mapped over the different ATC regions of EUROCONTROL. As stated above, for the test flight from Amsterdam to Madrid, the drones would take-off and land from two hubs (indicated in green in Figure 14.5). These hubs are Aéroport Orléans Loire-Valley (LFOZ, near Orleans, France) and Arcachon – La Teste-de-Buch Airport (LFCH, southwest of Bordeaux, France), respectively. As can be seen in Figure 14.5 for these locations, the drone only operates in the Paris (LFFF) aerodrome and the Bordeaux (LFBB) aerodrome, respectively. Both of these regions use French fees.
Eurocontrol takes into account three factors for the overflight fee calculations [117];

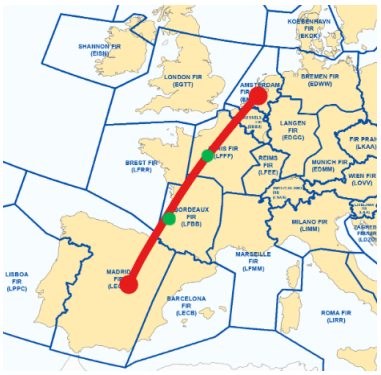

Figure 14.5: Test flight mapped on ATC regions

$$\text{Overflight fee} = \text{Distance factor} \cdot \text{Weight factor} \cdot \text{Unit rate of charge} \tag{14.1}$$

The distance factor is defined as the distance in kilometres divided by 100. As our operational range per drone is on average 608 km, this factor becomes 6.08. The weight factor is calculated as $\sqrt{\text{MTOW}/50}$ with MTOW in metric tons. For a MTOW of 5413.76 kg, this becomes 0.36. Lastly, the unit rate of charge is determined every month by EUROCONTROL and is currently (June 2023) given for France as 73.69 USD [117]. For the test flight from Amsterdam to Madrid, two drones are required, so the total overflight fee becomes: $2 \times (6.08 \times 0.36 \times 73.69) = 161.54$ USD.

Total cost

For the cost of using the eCarus system for the flight from Amsterdam to Madrid, two recharges are required. Next to this, the total overflight fee is added. This adds up to a total price of 6972.34 USD. From private jet charter data, the cost of chartering an 8-passenger private business jet from Amsterdam to Madrid is around 16 742.4 USD.

14.4. Price Conclusion

The price of 3405 USD per recharge is high. For an 8 person aircraft, this is equivalent to an increase in ticket price of roughly 426 USD. In exchange for this the passenger gets a 500 km longer flight that is fully powered by green electric energy.

A future implementation of eCarus that is looking to decrease costs should focus its efforts on decreasing the price of electricity and maintenance costs. Together these account for 79.41% of the direct operating costs. The maintenance could be decreased by optimising the use of a hub-and-spoke system for maintenance which would require fewer maintenance hubs. Increasing the number of flights per year per drone would increase the maintenance costs but would increase the profit margins even further. This could be done by looking at faster charging of the drones on the ground or by increasing the operating hours.

15
Project Organisation

This chapter provides an overview of the project group structure and the available resources allocated to support the group's activities. Additionally, the chapter includes an approximate estimate of the project's timeline, demonstrated through a project design and logic diagram and a project Gantt chart.

15.1. Group Organisation

Designing a complex system requires strong organisation and a broad understanding of diverse engineering fields. This section discusses the steps taken to ensure a smooth and efficient design process as well as the resources used during the project.

15.1.1. Role division

Assigning roles is a crucial part of a project of such complexity. It ensures efficient division of tasks and, most importantly, guarantees the completion of the project in its entirety. The division of the roles is done at the start of the project and has as a goal that every member of the team carries a part of the total responsibility. Two categories of roles are considered, ow which the first is the category management roles. The purpose of these roles is to contribute to the inner working of the team on a mostly non-technical level. The roles are the following:

- **Chairman**: This person is mainly in charge of representing the team to the external stakeholders. This could manifest itself during business pitches with companies or during meetings with customers. The person is also in charge of leading discussions and making sure that everybody's opinion is voiced.
- **Project Manager**: The main responsibility of the project manager is to keep the team on track in order to deliver what is expected of the project. The person also organises and checks the calendar and sets up meetings.
- **System Engineer**: The role of the systems engineer is to be the communication channel between all the technical departments of the projects. The system engineer makes sure all the systems are well integrated and are designed to work together.
- **External communication**: As the project involves working with several stakeholders, the external communication manager sets up the necessary communication channels between the people.
- **Secretary** The main role of the secretary is to record everything that is said during meetings. It is also responsible to archive all that data in order to review it at a later time.
- **Sustainability and Risk Manager**: This person is in charge of the sustainability approach and risk management of the project.
- **Quality Assurance**: The role of quality assurance is to control that the deliverables meet the required quality standard.
- **Resource Manager**: The resource manager is in charge of all the resources that are used in during the project and makes sure they are correctly organised and maintained.

Next to the management roles, the project group was also divided into multiple technical departments. The purpose of these departments is to organise the workload in work packages that require a similar area of expertise. The technical departments are:

- **Aerodynamics, flight performance & control**
- **Structures**
- **Power & Propulsion**
- **Payload**
- **Operations**

15.1.2. Available Resources

Tutors

Throughout the whole span of the project, the group is followed by a tutor as well as two coaches. The tutoring is set up to implement an opportunity for continuous feedback and possible help with advanced concepts. It is planned into the project in the form of communication channels, weekly meetings and monthly reviews and is deemed as crucial towards a favourable project outcome.

Experts

Next to the tutors, the group made use of the many experts available at the TU Delft. Due to the abundance of highly talented individuals at the TU Delft, the university benefits from a remarkable pool of intellect. This pool is made available as long as it is used reasonably while taking into account the busy schedule of the experts. In Table 15.1 a list of all the experts that were solicited until this stage of the project can be seen.

Table 15.1: List of experts

Name	Expertise
Daan van Dijk	Airport Innovation
T. Tomažič	Electric Aviation
E.J. van den Bos	CAD Software
C.D. Rans	Structural analysis
S. Teixeira De Freitas	Adhesive Bonding
J. Dong PhD	Capacitors
D.M.J. Peeters	FEM Validation
Dr. X. Wang	Aerospace Computational Mechanics
Dr.ir. P. Bauer	Electrical Engineering
Lior Zivan	Chief Engineer at Manna Drone
MTH Brown	Blended-wing-body
T. Sinnige	Propeller Design
Dr. S.J. Hulshoff	Advanced Aerodynamics

Available literature

Lastly, the group is also given a list of available literature. These are valuable books and publications, which were used extensively during the whole project. A list the used literature is noted below:

- Aircraft Design: A Conceptual Approach - D.P. Raymer [118]
- Aircraft Structure for Engineering Student: A Conceptual Approach - T.H.G. Megson [80]
- Airplane Design Part II - Dr.J.Roskam [88]
- Airplane Design Part V - Dr.J.Roskam [57]
- Airplane Design Part VI - Dr.J.Roskam [51]
- Airplane Design Part VIII - Dr.J.Roskam [105]

15.2. Future of the Project

As the project is not yet finished, it is important to look at further steps that shall be taken in the future. As was stated in section 14.3, a demonstration flight is planned to happen in the year 2030. This means that all that a prototype shall be ready to fly in approximately seven years. In order to better visualise the large steps to be taken, a project design and development logic plan is constructed.
Looking at Figure 15.1, it can be concluded that three main phases must be completed in order to be ready for the demonstration flight. The phases are the in-depth design phase, the prototyping phase and the testing phase. Furthermore it is assumed that the demonstration flight will take place on the first of July 2030. Comparing this to the development timeline of the A380, the following table of the time budget can be created.

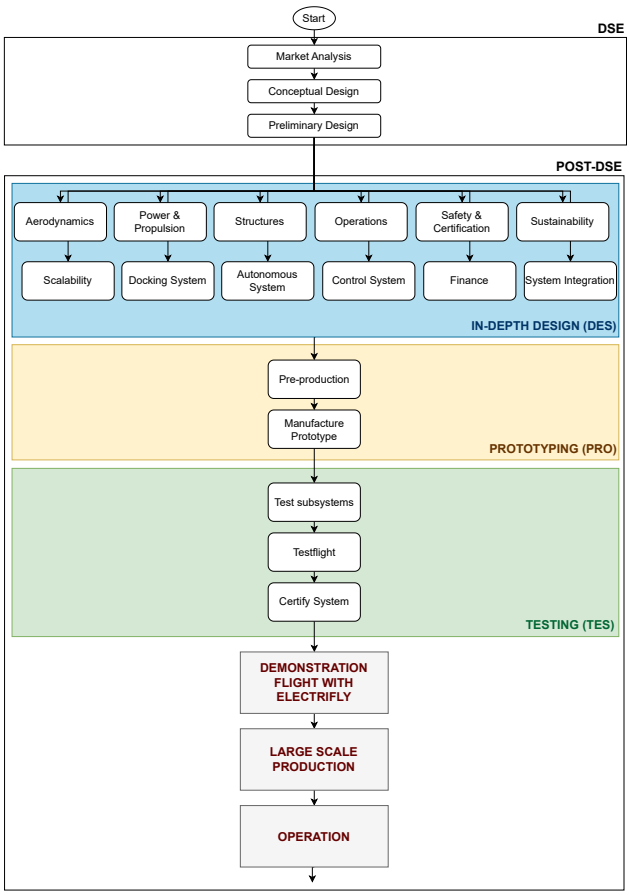

Figure 15.1: PD&D diagram

Table 15.2: Predicted development

Phases	Baseline A380	eCarus
In-depth design	64%	1636
Prototyping	24%	614
Testing	12%	307
Total	100%	2557 days

From the data in Table 15.2, a Gantt chart can be constructed with all the high-level tasks that are in order until the demonstration flight. The Gantt chart is shown on the next pages.

15.3. Functional Analysis

In this section the functional analysis of the system is performed. This analysis ensures that the system is capable of executing all its required functions. First, a functional breakdown structure was constructed in order to identify all of the functions and afterwards, a functional flow diagram is created to structure those functions. The diagrams can be seen in the figures located behind the Gantt Chart.

	Name	Duration	Start	Finish
1	**Post-DSE**	**2,555.472 ...**	**01/07/23 08:00**	**29/06/30 11:46**
2	**Development**	**1,636 days**	**01/07/23 08:00**	**22/12/27 17:00**
3	**Power & propulsion**	**1,308.944 ...**	**01/07/23 08:00**	**29/01/27 16:33**
4	Design of the duct	818.24 days	01/07/23 08:00	26/09/25 09:55
5	Design of propellers	818.24 days	01/07/23 08:00	26/09/25 09:55
6	Propeller wing interf...	490.944 days	26/09/25 08:00	29/01/27 16:33
7	Design of engine	818.24 days	01/07/23 08:00	26/09/25 09:55
8	Design of batteries	818.24 days	01/07/23 08:00	26/09/25 09:55
9	Design of power con...	490.944 days	26/09/25 08:00	29/01/27 16:33
10	Noise analysis	163.648 days	26/09/25 08:00	08/03/26 14:11
11	Design power supply	818.24 days	01/07/23 08:00	26/09/25 09:55
12	Simulation of thrust	327.296 days	01/07/23 08:00	23/05/24 10:22
13	Create testbed	163.648 days	26/09/25 08:00	08/03/26 14:11
14	**Aerodynamics**	**1,636 days**	**01/07/23 08:00**	**22/12/27 17:00**
15	Optimise planform	1,636 days	01/07/23 08:00	22/12/27 17:00
16	Compute airflow cha...	327 days	01/07/23 08:00	22/05/24 17:00
17	Design of wing	818 days	01/07/23 08:00	25/09/25 17:00
18	Design of stabiliser	818 days	01/07/23 08:00	25/09/25 17:00
19	Design control surfaces	818 days	26/09/25 08:00	22/12/27 17:00
20	Design of high lift de...	654 days	26/09/25 08:00	11/07/27 17:00
21	Design of remaining ...	490 days	01/07/23 08:00	01/11/24 17:00
22	Investigate all aerod...	490 days	26/09/25 08:00	28/01/27 17:00
23	Complete CFD analysis	1,309 days	01/07/23 08:00	29/01/27 17:00
24	Wind tunnel testing	327 days	01/01/26 08:00	23/11/26 17:00
25	**Structures**	**1,634 days**	**01/07/23 08:00**	**20/12/27 17:00**
26	Optimisation of truss...	981 days	01/07/23 08:00	07/03/26 17:00
27	Design of skin	981 days	01/07/23 08:00	07/03/26 17:00
28	Complete structural ...	1,309 days	01/12/23 08:00	01/07/27 17:00
29	Design of structural ...	654 days	19/02/24 08:00	03/12/25 17:00
30	Design of remaining ...	818 days	01/07/23 08:00	25/09/25 17:00
31	Design of Landing gear	818 days	01/07/23 08:00	25/09/25 17:00
32	Investigation of failu...	654 days	22/05/24 08:00	06/03/26 17:00
33	Material selection	1,309 days	19/02/24 08:00	19/09/27 17:00
34	Develop production ...	1,145 days	01/11/24 08:00	20/12/27 17:00
35	**Operations**	**1,636 days**	**01/07/23 08:00**	**22/12/27 17:00**
36	Choose hub placement	490 days	19/08/26 08:00	21/12/27 17:00
37	Design energy trans...	654 days	08/03/26 08:00	21/12/27 17:00
38	Design hub logistics	1,309 days	22/05/24 08:00	21/12/27 17:00
39	Incorporate sustaina...	1,636 days	01/07/23 08:00	22/12/27 17:00
40	Market Anlaysis	981 days	01/07/23 08:00	07/03/26 17:00
41	Create building prod...	818 days	25/09/25 08:00	21/12/27 17:00
42	Schedule test flight	490 days	19/08/26 08:00	21/12/27 17:00
43	Design maintenance ...	981 days	15/04/25 08:00	21/12/27 17:00
44	**Safety and certifica...**	**1,636 days**	**01/07/23 08:00**	**22/12/27 17:00**
45	Design of safety pro...	818 days	25/09/25 08:00	21/12/27 17:00
46	Verify and validate e...	1,309 days	22/05/24 08:00	21/12/27 17:00
47	Certify components	654 days	08/03/26 08:00	21/12/27 17:00
48	Identify and counter...	1,636 days	01/07/23 08:00	22/12/27 17:00
49	**Docking System**	**1,309 days**	**01/07/23 08:00**	**29/01/27 17:00**
50	Design aircraft comm...	1,309 days	01/07/23 08:00	29/01/27 17:00
51	Design of probe and ...	1,309 days	01/07/23 08:00	29/01/27 17:00
52	Design of batteries	1,309 days	01/07/23 08:00	29/01/27 17:00
53	Design thermal mana...	1,309 days	01/07/23 08:00	29/01/27 17:00
54	Design electrical syst...	818 days	03/11/24 08:00	29/01/27 17:00
55	Design required sens...	981 days	23/05/24 08:00	28/01/27 17:00
56	Design cooling inlets	654 days	23/05/24 08:00	07/03/26 17:00
57	**Autonomous System**	**1,495 days**	**01/07/23 08:00**	**03/08/27 17:00**
58	Design computer	1,309 days	01/07/23 08:00	29/01/27 17:00
59	Design electrical syst...	1,309 days	01/01/24 08:00	01/08/27 17:00
60	Design sensors	1,309 days	02/01/24 08:00	02/08/27 17:00
61	Design autonomous ...	1,309 days	03/01/24 08:00	03/08/27 17:00
62	**Control**	**1,636 days**	**01/07/23 08:00**	**22/12/27 17:00**
63	Design control comp...	818 days	01/01/24 08:00	28/03/26 17:00
64	Design control softw...	1,636 days	01/07/23 08:00	22/12/27 17:00
65	Design control surfaces	818 days	01/07/23 08:00	25/09/25 17:00
66	Optimise stability an...	1,636 days	01/07/23 08:00	22/12/27 17:00
67	Design electrical syst...	818 days	01/01/24 08:00	28/03/26 17:00
68	**Finance**	**1,636 days**	**01/07/23 08:00**	**22/12/27 17:00**
69	Advertise product	818 days	25/09/25 08:00	21/12/27 17:00
70	Search customers	1,636 days	01/07/23 08:00	22/12/27 17:00
71	Find investors	1,636 days	01/07/23 08:00	22/12/27 17:00
72	Create branding	163 days	13/07/27 08:00	22/12/27 17:00
73	Asses operatlonal cost	1,472 days	12/12/23 08:00	22/12/27 17:00
74	Set up budget	327 days	30/01/27 08:00	22/12/27 17:00
75	**Systems Integration**	**1,636 days**	**01/07/23 08:00**	**22/12/27 17:00**
76	Optimise planform fo...	1,636 days	01/07/23 08:00	22/12/27 17:00
77	Iterate design config...	1,309 days	23/05/24 08:00	22/12/27 17:00
78	Integrate componen...	818 days	26/09/25 08:00	22/12/27 17:00
79	Create digital clone	981 days	16/04/25 08:00	22/12/27 17:00
80	Organise subsystem ...	1,636 days	01/07/23 08:00	22/12/27 17:00
81	Produce small scale c...	654 days	09/03/26 08:00	22/12/27 17:00
82	**Sustainability**	**1,636 days**	**01/07/23 08:00**	**22/12/27 17:00**
83	Set-up sustainability ...	1,636 days	01/07/23 08:00	22/12/27 17:00
84	Set-up end of life pr...	1,636 days	01/07/23 08:00	22/12/27 17:00
85	Asses the sustainabil...	1,636 days	01/07/23 08:00	22/12/27 17:00
86	Optimise sustainabilit...	1,636 days	01/07/23 08:00	22/12/27 17:00
87	**Scalability**	**1,309 days**	**23/05/24 08:00**	**22/12/27 17:00**
88	Investigate scalabilit...	654 days	09/03/26 08:00	22/12/27 17:00

	Name	Duration	Start	Finish
89	Investigate future te...	1,309 days	23/05/24 08:00	22/12/27 17:00
90	Make design future p...	654 days	09/03/26 08:00	22/12/27 17:00
91	**Prototyping**	**1,227.68 d...**	**18/04/26 08:00**	**27/08/29 14:26**
92	**Pre-Production**	**613.84 days**	**18/04/26 08:00**	**22/12/27 15:43**
93	Create production plan	613.68 days	18/04/26 08:00	22/12/27 14:26
94	Collect necessary ma...	245.472 days	21/04/27 08:00	22/12/27 11:46
95	Acquire required facil...	306.84 days	19/02/27 08:00	22/12/27 15:43
96	Acquire assembly line	306.84 days	19/02/27 08:00	22/12/27 15:43
97	Find suppliers	306.84 days	19/02/27 08:00	22/12/27 15:43
98	Set-up logistics	368.208 days	19/12/26 08:00	22/12/27 09:39
99	Choose for most sus...	613.68 days	18/04/26 08:00	22/12/27 14:26
100	**Manufacture protot...**	**613.68 days**	**23/12/27 08:00**	**27/08/29 14:26**
101	Produce aerodynami...	490.944 days	23/12/27 08:00	26/04/29 16:33
102	Produce docking syst...	490.944 days	23/12/27 08:00	26/04/29 16:33
103	Produce batteries	490.944 days	23/12/27 08:00	26/04/29 16:33
104	Produce propulsion s...	490.944 days	23/12/27 08:00	26/04/29 16:33
105	Produce control system	490.944 days	23/12/27 08:00	26/04/29 16:33
106	Produce UAV-system	490.944 days	23/12/27 08:00	26/04/29 16:33
107	Produce structures c...	490.944 days	23/12/27 08:00	26/04/29 16:33
108	Produce operational ...	552.312 days	23/12/27 08:00	27/06/29 10:29
109	Assemble sub-assem...	122.736 days	26/04/29 08:00	26/08/29 14:53
110	Test components	245.472 days	23/12/27 08:00	24/08/28 11:46
111	Maintain supply chain	613.68 days	23/12/27 08:00	27/08/29 14:26
112	Maintain facilities, to...	613.68 days	23/12/27 08:00	27/08/29 14:26
113	Manage work-force	613.68 days	23/12/27 08:00	27/08/29 14:26
114	**Testing**	**306.472 da...**	**27/08/29 08:00**	**29/06/30 11:46**
115	**Test subsystems**	**61.368 days**	**27/08/29 08:00**	**27/10/29 10:56**
116	Test structures	61.368 days	27/08/29 08:00	27/10/29 10:56
117	Test engines	61.368 days	27/08/29 08:00	27/10/29 10:56
118	Test payload	61.368 days	27/08/29 08:00	27/10/29 10:56
119	Test autonomous sy...	61.368 days	27/08/29 08:00	27/10/29 10:56
120	Test control system	61.368 days	27/08/29 08:00	27/10/29 10:56
121	**Testflight**	**245.472 da...**	**27/10/29 08:00**	**29/06/30 11:46**
122	Test performance goals	245.472 days	27/10/29 08:00	29/06/30 11:46
123	Test emergency situ...	245.472 days	27/10/29 08:00	29/06/30 11:46
124	Test prolonged flight...	245.472 days	27/10/29 08:00	29/06/30 11:46
125	Test extreme weath...	245.472 days	27/10/29 08:00	29/06/30 11:46
126	Test meeting proced...	245.472 days	27/10/29 08:00	29/06/30 11:46
127	Test docking with air...	245.472 days	27/10/29 08:00	29/06/30 11:46
128	Test autonomous sy...	245.472 days	27/10/29 08:00	29/06/30 11:46
129	Certify Aircraft	245.472 days	27/10/29 08:00	29/06/30 11:46
130	**Certification**	**306.472 da...**	**27/08/29 08:00**	**29/06/30 11:46**
131	Certify components	122.736 days	27/08/29 08:00	27/12/29 14:53
132	Certify aircraft	245.472 days	27/10/29 08:00	29/06/30 11:46

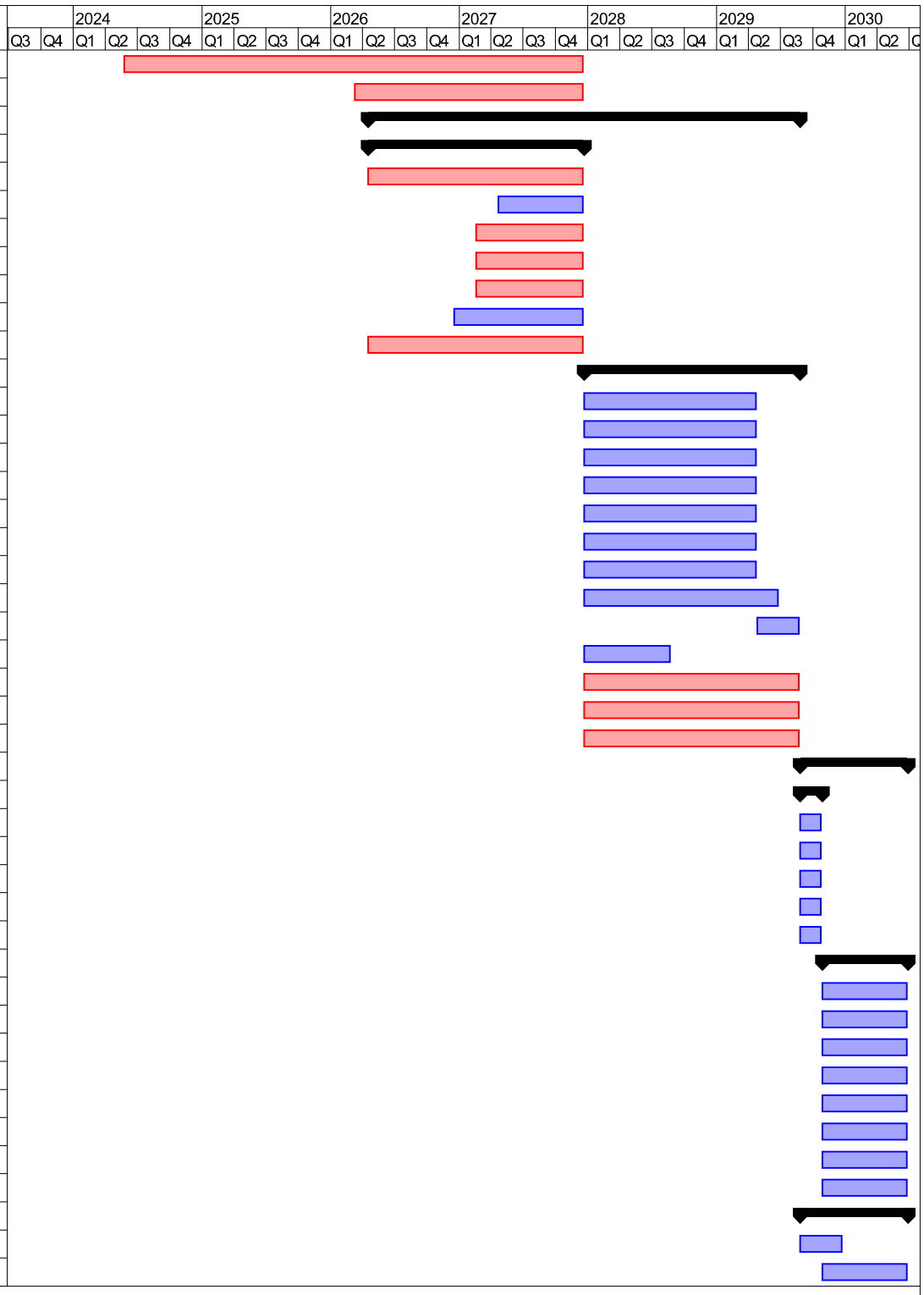

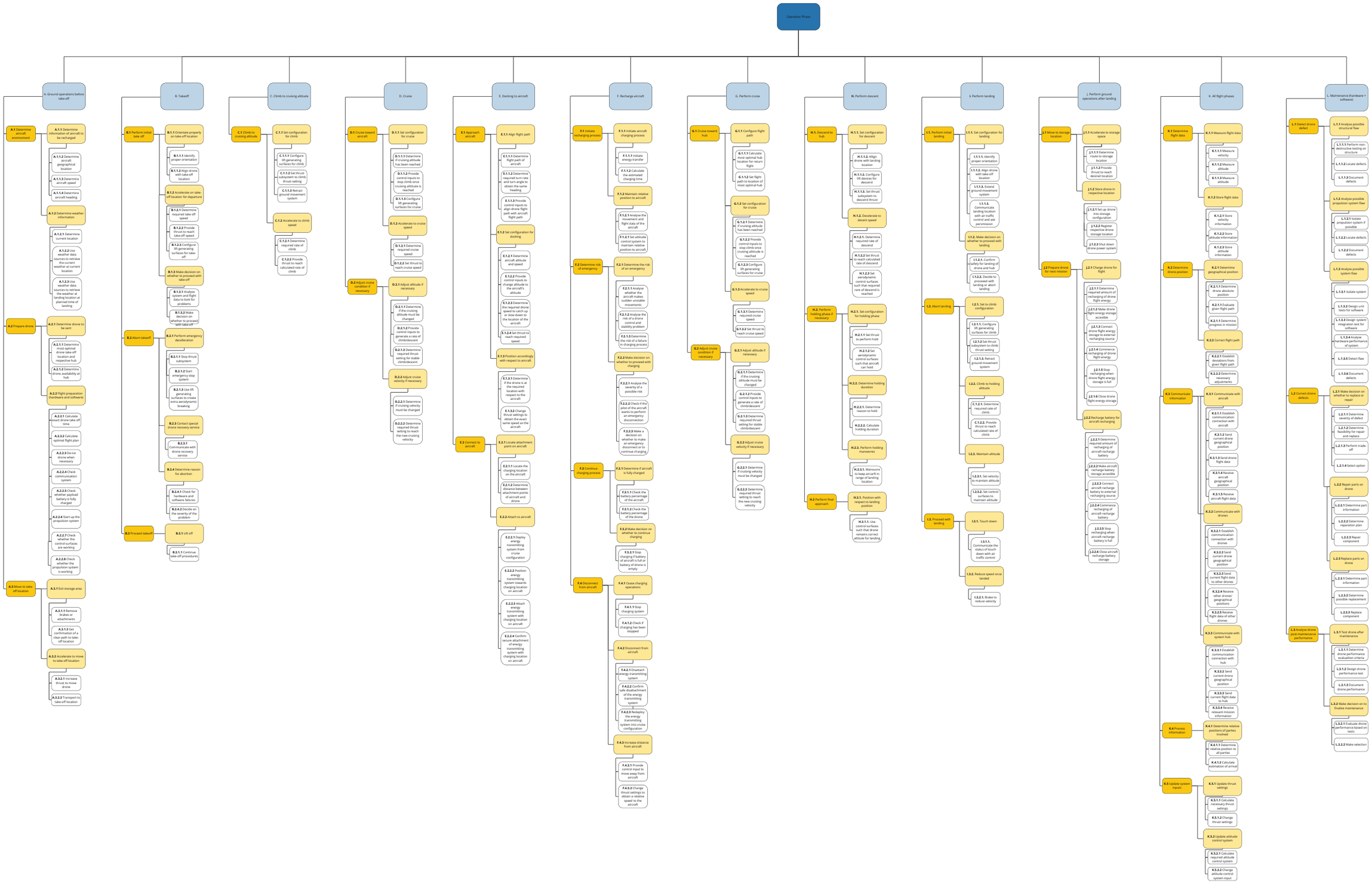

Figure 16.2: Functional Breakdown Structure

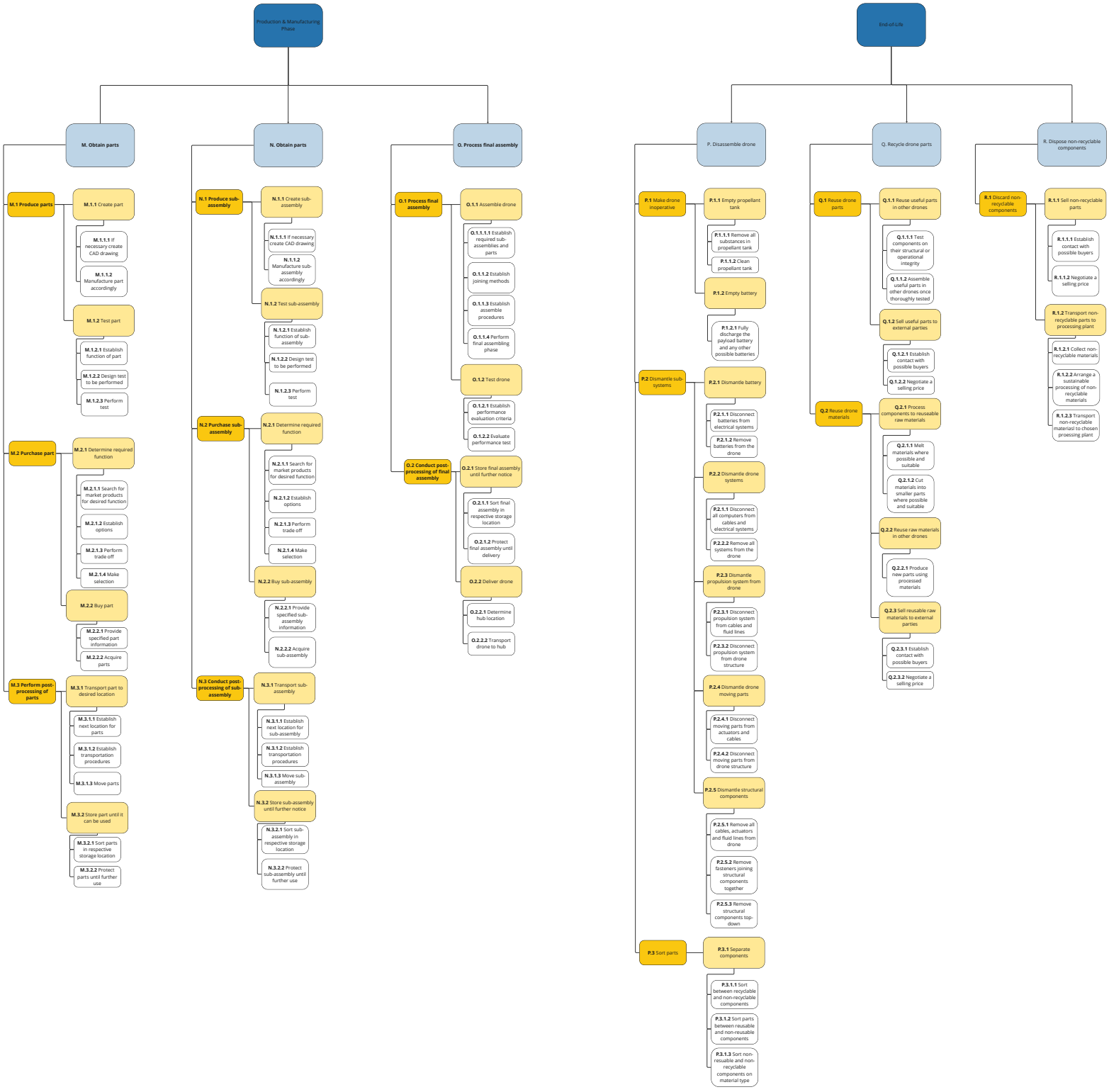

Figure 16.3: Functional Breakdown Structure ctd

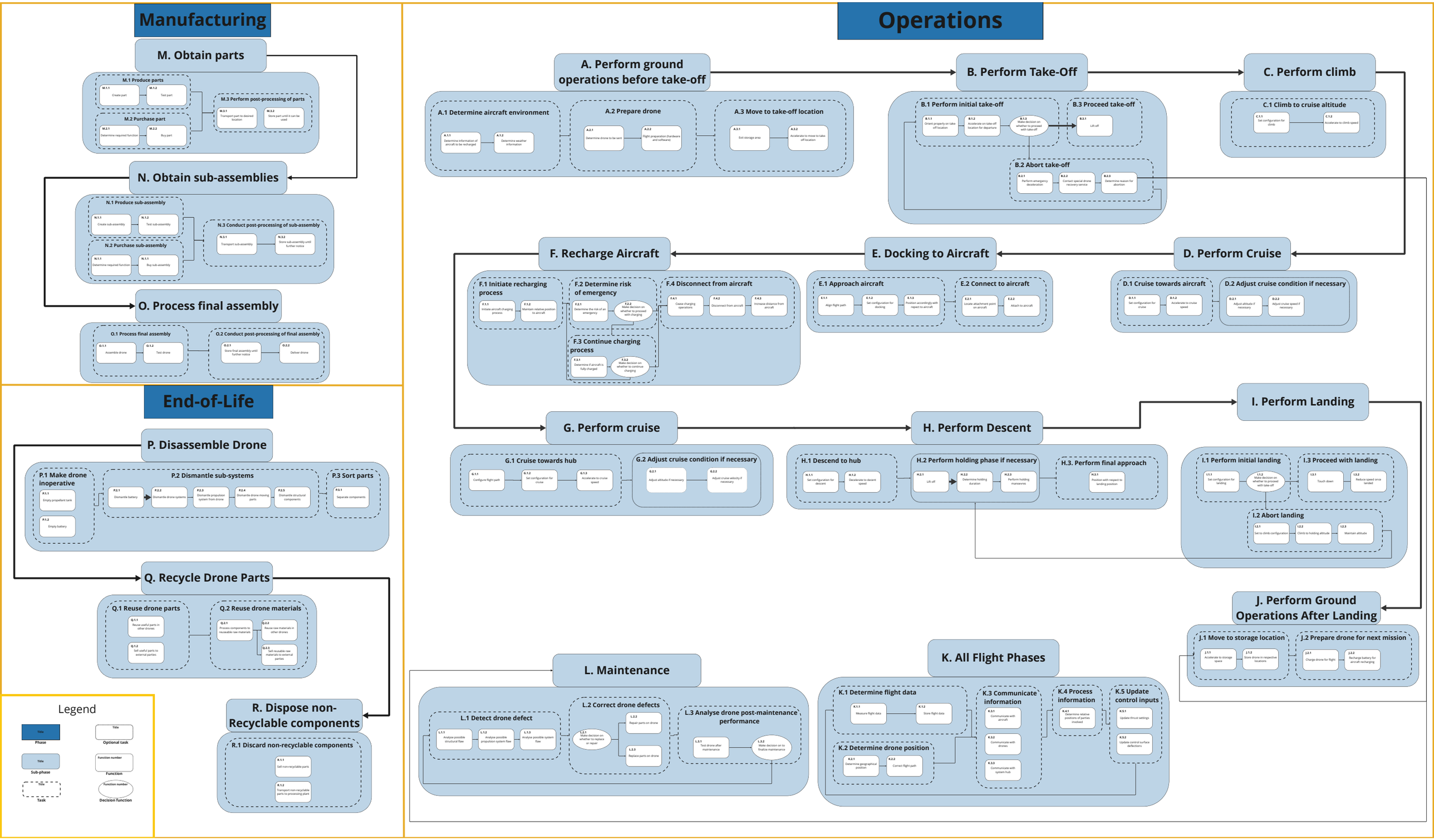

Figure 16.4: Functional Flow Diagram

16
Risk Analysis

A complex design and a complex system such as the one in this report brings a lot of potential risks that can occur. Thus, a proper risk assessment needs to be done in order to prevent unexpected occurrences.

Several risks were identified in the midterm and baseline report, and these risks are still applicable towards the current design. But as the design developed into more detail, more risks arise that are more specific to the design. Thus, the risks need to be further assessed.

In the chapter, new risks identified as well as the mitigation plans for it will be discussed. Risks that occurred during design, risks that need to be updated, and critical risks from that were identified before will also be discussed,

16.1. RAMS Analysis of the System

This section addresses the characterisation of the system using the RAMS methodology.

Reliability

The first in this characterisation is the reliability of the system. It indicates the ability of a system to function without failure, for a required time and in a specified environment [**reliability**]. A requirement that flows directly from this is [REQ-US-SR-01]: *A drone shall dock an aircraft successfully 99.9% of all attempts* [4]. The system is designed to fulfil this requirement. In order to meet these requirements, the docking system is designed such that docking is successful in 99.9% due to a fixed low speed of 3 m/s during the docking approach. In cases of missed docking, a series of mitigations are devised to ensure no other system failures occur as a result of different failure modes of docking.

Availability

Closely related to reliability is availability. This describes the proportion of time the system is able to perform the required function. At the hub, a redundancy principle is applied. In case one drone fails in any way to perform its function, there is another to take its place. According to [REQ-US-PER-04]: *The system shall be able to meet electric aircraft demand by 2050* [4]. As stated in chapter 11 docking failures are made imperceptible to the client by ensuring a second drone can be present at the aircraft within 20 minutes. Emergency procedures only happen after two docking fails. The range of the operating hub is chosen such that this second drone recharge attempt can be made within this time frame in detail design.

Maintainability

As stated in [REQ-US-SR-08]: *Drones shall track when they need maintenance in addition to regular maintenance checks and will fly themselves to and from a maintenance hub when required*. To ensure this requirement is complete, sensors are placed on critical truss members of the structure and are easily accessed through the non-load-carrying skin designed in chapter 8. These sensors ensure that if an issue is detected by the drone, an inspection is arranged and maintenance is conducted.

Safety

[REQ-US-SR-07] states that *Under no condition shall a drone collide with an aircraft* [4]. Various considerations have been made to ensure the system's safety. The docking mechanism was carefully chosen, with a cable design being selected. Next to this, the drone shall be capable of maintaining a safe distance by flying behind and below the aircraft. Additionally, a battery is selected over hydrogen to enhance safety performance. For these decisions, multiple factors were taken into account, with safety being a significant determinant.

16.2. Risk Identification

This section focuses on reviewing the risks associated with the baseline and midterm reports [4] and identifying any new risks that may have emerged. The collected risks are presented in the table below. Updated risks are indicated by blue identifiers, while green identifiers represent newly identified risks. Aside from critical risks from previous assessments, the table excludes risks that have remained unchanged. In the operational risk category, high-level risks are still depicted in black, shedding light on the newly identified sub-risks. Moreover, each new risk is assigned an impact and probability score ranging from 1 to 5. Within the table, probability is denoted by "P", and impact is denoted by "I".

Table 16.1: Risk Mitigation and Effect

ID	Risk	Mitigation	P	I
Design				
R-DES-09	Lack of understanding of current technology and regulations	Reconsidering of design for catapult launching	4	1
R-DES-09-01	Energy density of 600 Wh/kg isnt possible	Battery needs to be larger, aircraft gets heavier	2	3
R-DES-10	Budget overrun	Product cannot be completed and produced	3	3
R-DES-10-01	Catapult too expensive to develop	Product not economically viable	5	3
R-DES-10-01	Arrested landing gear too expensive to develop	Product not economically viable	5	3
R-DES-13	Errors in design estimations	Sub-optimal or infeasible design	4	3
R-DES-13-01	cg assumptions not valid	Error in cg results	2	4
R-DES-13-02	MOI assumptions not valid	Error in MOI results	2	4
R-DES-13-03	Semi-empirical methods not valid for design	Error in aerodynamic results	3	4
Verification and validation				
R-VV-02	Inaccurate simulation models	Simulation not reflective of the real world, so analysis not valid	2	3
R-VV-02-01	Design configuration not within CFD software limits	Invalid results	4	2
Operational				
R-OPE-01	Operational hub failure	Region becomes unoperational and repair is required	2	4
R-OPE-01-01	Risk of airport closure	Drones cannot take-off and land from the designated airport	2	4
R-OPE-02	Structural failure	Recovery and repair required, potential loss of drone	2	3
R-OPE-02-01	Too large cracks present in the skin.	Skin will fail in fracture before yielding	3	5
R-OPE-02-02	Duct skin experiences more severe loading than aircraft skin	Part may deform during operation	1	2
R-OPE-04	Payload failure	Drone cannot perform function	3	1
R-OPE-04-01	Drone failed to manoeuvre the probe in the drogue (miss mode).	Miss Mode is started within recharge procedure	3	4
R-OPE-04-02	Tension/Compression forces exceeds maximum	Disconnection of the drogue-probe system	2	3

Continuation of Table 16.3

ID	Risk	Consequence	P	I
R-OPE-04-03	Failure of locking solenoids unable to connect	Unable to connect with the aircraft	3	4
R-OPE-04-04	Failure of locking solenoids unable to disconnect	Drone is stuck to drogue of the aircraft.	2	4
R-OPE-06	Propulsion system failure	Recovery and repair required	2	3
R-OPE-06-01	Propulsion system uses energy during landing	Primary battery too small to deliver required energy	1	3
R-OPE-06-02	RPM setting is too close to max RPM	No margin for thrust setting in case of one engine failure	2	2
R-OPE-08	The drone damages the aircraft	Recovery and repair required for both aircraft and drone. Potential loss of both and endangers passengers.		
R-OPE-08-01	Drone inflicts impact damage	Severe damage could lead to unable to charging by the drone/probe system	2	2
R-OPE-08-02	Short circuit in recharge system	The Aircraft/drone system may get damaged.	2	3
R-OPE-08-03	Discharge effect through other part of the drogue-probe system	electrical systems fail within aircraft	2	5
R-OPE-09	System failure is a hazard for environment	Damage of property. Can cause injury or loss of life if it hits a person	3	5
R-OPE-12	Conventional MRO companies not skilled enough to ensure safety of drone	Drone is not certified to fly	2	4
R-OPE-13	A take-off distance of 1130 m is not enough	Aircraft overruns the runway	2	3
R-OPE-14	A landing distance of 1130 m is not enough	Aircraft overruns the runway	2	3
R-OPE-15	Design point for wing loading diagram is on the limit case	W/S and W/P are overestimated	3	2

16.3. Risk Mitigation Methods

To avoid risks from happening and compromising the project, mitigation plans have to be done. Mitigations reduce either the probability or impact of the risks, thus making the risk safer. First, a pre-mitigation risk map is shown to give a visual of the severity of all risks.

Table 16.2: Pre-mitigation risk map

		Probability				
		1	2	3	4	5
Impact	5		**R-OPE-08-03**	**R-OPE-02-01,R-OPE-09**		
	4		**R-DES-13-01,R-DES-13-02, R-OPE-01,R-OPE-01-01, R-OPE-12**	**R-DES-13-03,R-OPE-04-01, R-OPE-04-03**		
	3	…	…	**R-DES-13**	**R-DES-13**	**R-DES-10-01, R-DES-10-02**
	2		…	…	**R-VV-02-01**	
	1			…	**R-DES-09**	

It can be seen from Table 16.2 that there are a lot of critical risks that can occur. Critical risks are characterised by risks that have a score of 9 or above. The score of a risk can be found from

Equation 16.1

$$\text{Score} = I \cdot P \tag{16.1}$$

Thus, methods to mitigate need to be created. These mitigation will change wither the probability P or impact I. THe mitigation methods are shown in Table 16.3

Table 16.3: Risk Mitigation and Effect

ID	Mitigation	P	I
	Design		
R-DES-09			
R-DES-09-01	In-depth analysis on battery development	2 to 1	
R-DES-10	Better budget breakdown and managment	3 to 2	
R-DES-10-01	Reconsider design choice	5 to 0	
R-DES-10-02	Reconsider design choice	5 to 0	
R-DES-13	Regularly update of estimations, use of literature	4 to 3	
R-DES-13-01	Validation by modelling	2 to 1	
R-DES-13-02	Validation by modelling	2 to 1	
R-DES-13-03	Validation by testing or comparison with other methods	3 to 2	
	Verification and validation		
R-VV-02	Spend more time on research of models	2 to 1	
R-VV-02-01	Validation by testing or comparison with other methods	4 to 3	
	Operational		
R-OPE-01	Backup systems for the hub		4 to 2
R-OPE-01-01	Carefully select airport and keep in constant with airports	2 to 1	
R-OPE-02	Quality assurance	2 to 1	
R-OPE-02-01	Ultrasonic inspection will be performed to ensure cracks are no larger than 3 mm and panel will yield before fracture.	3 to 1	
R-OPE-02-02			
R-OPE-04	Quality assurance	3 to 2	
R-OPE-04-01	Drone will manoeuvre to pre-contact position and restart coupling procedure	3 to 2	4 to 3
R-OPE-04-02	Damping in cable drum unit to mitigate oscillation and the use of recharging zone.	2 to 1	4 to 3
R-OPE-04-03	Use of multiple locking solenoids creating redundancy	3 to 2	4 to 2
R-OPE-04-04	Weakpoint in the solenoids resulting in breakage of the solenoids		4 to 2
R-OPE-06	Quality assurance	2 to 1	
R-OPE-06-01	Depth of discharge reserve in case of energy requirement		3 to 2
R-OPE-06-02	Use no more than 92% of max RPM setting	2 to 1	
R-OPE-08	Automatic avoidance system or damage minimisation system	2 to 1	5 to 4
R-OPE-08-01	Fixed closer rate set to 2-3 m/s	2 to 1	2 to 1
R-OPE-08-02	Both aircraft are equiped with an ECU consisting of a safety switch and fuses in case of short circuit.	2 to 1	3 to 1
R-OPE-08-03	ECU will be equipped with discharge wiring switch to the aircraft	2 to 1	
R-OPE-09	Inclusion of large safety factors, and redundant systems	3 to 1	5 to 4
R-OPE-12	Train maintenance personall and use autonomous software for detection	2 to 1	
R-OPE-13	Additional power setting for faster acceleration	2 to 1	
R-OPE-14	Design approach speed closer to stall speed	2 to 1	
R-OPE-15	Use conservative values for creation of wing loading diagram	3 to 2	

A few mitigations need to be explained further. R-OPE-10-01 and R-OPE-02 were deemed too critical and the risk occuring would create an unfeasible design. Thus, the entier catapult launching and

arrested landing gear system was changed to conventional take-off and landing as explained in section 11.1. Thus, the entire risk was omitted and tthe probability was set to 0.

R-OPE-09 was a critical risk previously even after mitigation, and a contingency of a self destruct syste was implemented. This was deemed not viable and thus the design was changed to include more safety factors and redundancied, thus changing the probability from 3 to 1, making the risk not critical anymore. With methods for mitigation created, the post mitigation risk map can be made.

Table 16.4: Post-mitigation risk map

		Probability				
		1	2	3	4	5
Impact	5	**R-OPE-02-01,R-OPE-08-03**				
	4	**R-DES-13-01,R-DES-13-02, R-OPE-01-01,R-OPE-09, R-OPE-12,**	**R-DES-13-03**			
	3	**…**	**…**			
	2		**…**			
	1			**…**	**R-DES-09**	

It can be seen that all of the new risks were not critical anymore after mitigation. The most critical risk is R-DES-13-03 with a score of 8. This risk, although still not critical, should be given more attention to prevent it from happening as it is close to being critical.

17 Sustainability

Sustainability remains an integral part of the design and was considered throughout the project. This chapter will give an overview of all sustainability considerations done throughout the design, and future sustainability plans. Sustainability is comprised of three pillars, namely the environmental, social and economic pillars. It is important to consider all of them in order to have a fully sustainable design.

17.1. Impact of Design on Sustainability

The system possesses great potential towards making air travel more sustainable. Failing to realise this potential, will lead to an unoptimised design and a commercial failure.

The primary benefit of the system is the improvement in the electric passenger aircraft range. As was discussed in chapter 11, a conventional flight from Rotterdam to Malaga could be converted from a burden to the environment and social sustainability to a trip completely free of emissions. Next to that end-of-life possibilities in section 8.8 will contribute to the transition towards green energy by enabling the energy storage of fluctuating energy sources like solar panels. These examples are only some of the many benefits that the system could bring to tomorrow's society.

17.2. Sustainable Approach on the Design

In this section, an overview of the design choices relating to sustainability is presented as well as their position in the report.

17.2.1. Aerodynamics

It is fair to say that the sustainability criterion has been the most important driver of the aerodynamic design for the whole project. Starting with the configuration selection, the choice for a BWB was mainly determined by its high aerodynamic efficiency. For the remaining of the design, the aerodynamic shape was continuously optimised in order to maximise efficiency.

Another consideration for sustainability was that the volume within the drone was maximised in section 7.2. This minimises the waste of resources as it maximises the use of available space within the drone.

17.2.2. Power and Propulsion

The propulsion system is one of the main energy consumers. Low efficiency in energy usage would have a disastrous effect on economic and environmental sustainability. Thus, it is important to correctly design the whole subsystem while optimising for sustainability. Social aspects have to be taken into account as the propulsion system creates a great amount of noise.

The following design decision were taken as a result of sustainability:

- Noise was a criteria considered during thrust generation resulting in the selection of a ducted fans (subsection 6.2.2)
- Optimisation of the number of propellers to maximise efficiency reduce used materials (section 6.7)
- Higher energy density for the battery to reduce battery size (subsection 6.1.3)
- Less noise by using two engines instead of distributed propulsion (subsection 6.3.2)
- Less structural weight due to two big engines close to the centre line instead of distributed propulsion. (subsection 6.3.2))
- Noise is lower than 65 dB at ground level when aircraft is at cruise altitude (subsection 6.4.2)

- Carbon-graphite and kevlar composite propeller blades with foam core to reduce noise (section 6.6)
- Carbon-graphite and kevlar composite propeller blades to reduce maintenance (section 6.6)

17.2.3. Battery

The battery contains a lot of heavy metal, and also makes up most of the weight of the drone. Thus, an efficient battery needs to be design in order to reduce waste, and end of life needs to be properly planned.

- Life cycle was maximised in the design of the bettery (chapter 4)
- Batteries arranged in modules to ease manufacturability and maintenance (chapter 4)
- 600 Wh/kg required to decrease battery weight and thus use less energy (chapter 4)
- At the end of life, batteries will be reused as power storage at hubs or remanufactured for new usage in the drone or other applications (section 8.8)

17.2.4. Structures

The structural design greatly determines the sustainability of the system. The structure includes the material choice, as well as end-of-life procedures that must be analysed. Thus, the sustainability of the structures is essential and should always be considered.

Sustainability plans for further design:

- C_{0_2} production in manufacturing and end-of-life is considered in trade-off for skin material and truss material (section 8.3)
- Use of recycled aluminium 6061 for skin, recycled aluminium takes 95% less energy in production (section 8.3)
- At the end of life, aluminium skin is recycled (section 8.8)
- At the end of life, SiC reinforced trusses are recycled (section 8.8)

17.2.5. Operation

Once again the sustainability needs to be assessed. The operations of the aircraft have large impacts on social and environmental sustainability, as the drone might create excessive noise or disrupt wildlife. In this section, the sustainability considerations for operations will be summarised.

The sustainability approaches taken comprise of:

- Adding electric drones to regional and local airports will add less noise pollution than conventional aircraft (chapter 11)
- Airports are selected based on sustainable factors such as noise pollution and area occupation (chapter 11)
- Energy consumption is limited and shared because of use of regional airports (chapter 11)
- Drones can fly from hub to hub which allows the maintenance procedures to be optimised by using a hub-and-spoke system. Fewer hubs need to be capable of maintaining and servicing drones (chapter 11)

17.3. Overall Sustainability of Design

As a conclusive note, sustainability is an integral part of the project. Great efforts have been made in order to push the system towards full sustainability. Looking at the sustainability requirements, it can be seen that the great majority of the key sustainability requirements have been met.

18 Scalability

The eCarus system must be scalable to remain economically sustainable for the coming decades. In section 18.1, drone scalability is discussed. The current eCarus system is designed to recharge an electric 8-passenger business aircraft. As the aviation industry continues to innovate and constantly changes, the system must be adaptable to larger electric aircraft as well. This follows from the requirement, [REQ-US-MSC-02]: *"The system shall be scalable to megawatt-class aircraft."* [16]. Next to drone scalability, the operational scalability is assessed in section 18.2. Following from requirement [REQ-US-MSC-03], *"The system shall be extendable to worldwide coverage."* [16]. This implies that in addition to scalable drones, the entire system, including take-off and landing locations, needs to be scalable as well.

18.1. Drone Design Scalability

This section discusses the scalability of the eCarus drone design. In order to evaluate the required improvements to be scalable to a megawatt-class aircraft, the Airbus A320 is used for comparison. It is assumed in this section that the aviation industry continues to invest in and expand the electric aircraft market. Next to that, it is assumed that at some point in the future megawatt-class aircraft such as the A320 will be electric and would be interested in using the eCarus system for range extension.

18.1.1. Drone Design Limitations

An A320 uses approximately $3\,\mathrm{kg/km}$ of Jet A-1 fuel [119]. The currently designed drone adopts a charging strategy for a range of $764\,\mathrm{km}$, resulting in a required payload battery energy of $1161.28\,\mathrm{kWh}$ or $4181\,\mathrm{MJ}$. On the other hand, an A320 consumes $100\,848\,\mathrm{MJ}$ over a distance of $764\,\mathrm{km}$. This results in the following possible combinations for scalability to megawatt-class aircraft.

Table 18.1: Possible combinations for scaling to megawatt-class aircraft

Amount of drones	24	12	6	4	2
Scaling factor of drone payload battery	1.005	2.010	4.020	6.030	12.060

A preliminary assessment, keeping in mind the span width and safety regulations, immediately rules out charging with more than four drones at the same time because of interference and safety regulations. However, at this stage, scaling the drone payload battery with a factor of 12.060 is also deemed less feasible than a payload battery scaled with a scaling factor of 6.030. Important to note is that a more in-depth analysis of the possible combinations needs to be performed in future design plans. For now, charging with four drones is deemed the most optimal. This means that a scaling factor of 6.030 is required. Still, this means that the payload battery either needs to increase in volume and weight or needs to have improved specific energy. This is again an optimisation issue. The following payload battery combinations are possible in order to comply with the 6.030 scaling factor.

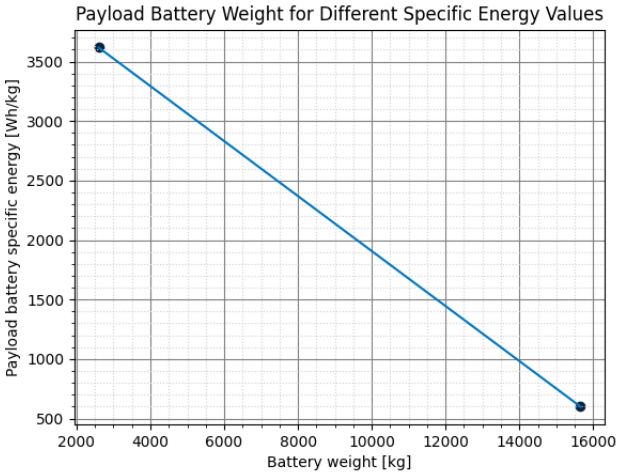

Figure 18.1: Possible combinations for scaling the payload battery

As can be observed in Figure 18.1, there are various combinations of battery improvement possible. The dark blue dots indicate the design point for the current battery weight (3596.51 kg), and the design point for the current specific energy (600 Wh/kg) from left to right, respectively. Every point on the line in between these two points is a possible combination to comply with the scaling factor requirement. As can be seen, in order to not massively impact the design of the drone by increasing the payload battery weight, major advancements in battery technology are required. Next to this, it is important to keep in mind that increasing the specific energy also implies that the charge rate needs to increase in order to comply with the requirement that the energy shall be transferred within 40 minutes. This again has an effect on thermal management and battery voltage. Vice-versa, increasing the weight has an effect on every design step from the first weight estimation onward.

18.2. System Scalability

This section discusses the scalability of the eCarus system as a whole. It is assumed that the demand for range extension for electric 6-8 passenger business aircraft increases over the coming decades. The system is designed to be scalable to comply with the requirement of meeting the electric aircraft demand of 2050.

18.2.1. Airport Selection

The current eCarus system uses regional airports. These airports are selected on the following criteria; the runway length must be between 1300 m and 2000 m. Secondly, the runway must be made out of asphalt or concrete. The selected airports, however, impose limitations on the scalability of the system because of runway length and possibly because of energy and charge capacity. It is therefore important to select regional airports with more criteria regarding these limiting factors. The following extra airport selection criteria are identified to ensure system scalability.

- **Runway length**: the runway length requirement should be increased in order to be usable for larger drones.
- **Number of runways**: to meet the electric aircraft demand multiple drones should be able to take off at the same time. Therefore, at least more than one runway needs to be available.
- **Drone storage capacity**: As the system increases, every take-off location needs to store more drones.
- **Energy and charge capacity**: More charging operations per take-off location requires more energy at the hub and more charging capabilities.
- **Accessibility for logistics and maintenance**: As drone usage increases, more maintenance is required. The take-off locations need to be perfectly accessible via public routes to ensure that maintenance parties and other logistic parties can reach the location easily.

18.2.2. Scalability of the Hub placememt

Lastly, concerning the selection of hub locations, consideration has to be given to how future-proof the hub selection method is and how compatible it is with other potential business models. In the midterm report [6], the system was optimised to extend the range of electric aircraft. The best optimisation is achieved when hubs are located near the maximum ranges of aircraft. Another interesting application of this system is reducing turnaround time at airports. This can be accomplished by recharging near the destination airport, allowing the aircraft to land and take off again without ground recharging. This section will explore this usage of the system.

As battery technology continues to improve, the range of electric aircraft will also increase. Consequently, the optimal placement of hubs near the end of aircraft ranges will change. Hubs placed at optimal locations for 2030's battery technology may become obsolete by 2050, as aircraft will be able to bypass them to reach the next hub. This implies that hub placement based solely on a range extension model is not entirely future-proof.

A possible solution is to design hubs placed slightly outside the aircraft's range. In the initial years, the drone can fly more towards the incoming plane, charging it slower but for a longer duration. This can later transition to optimal symmetric placement and eventually to a slanted flight triangle in the opposite direction.

Recharging to reduce turnaround time is also impacted by technological progress, albeit to a lesser extent. A hub can be placed relatively close to each major airport to top up an aircraft's charge before landing or after takeoff. If the aircraft's range increases, the hub can be positioned further from the airport, but this introduces complications regarding its placement. Placing the hub further away limits which flight paths can utilise it due to increased deviations aircraft would have to make. Placing it closer allows any flight to use the facility, making this usage more future-proof.

A combination of both use cases is possible without severely compromising their effectiveness. A hub can be placed near a major airport and subsequently located at optimal intervals dictated by the range-increasing model. If hubs are placed near enough large airports, their collective coverage could encompass all routes in the area. Thus, the final design proposes a hub placed within range of every major airport, along with optimal interval points between hubs if airports' nearby hubs do not already cover them.

19
Conclusion & Recommendations

19.1. Conclusion

The objective of the DSE project was to develop an automated in-flight recharging system for carbon-neutral aviation, with the dual aims of expanding the capabilities of electric aircraft and streamlining airport logistics. The present report represents the result of the collaborative efforts of ten students in the field of Aerospace Engineering, who dedicated the past ten weeks to the final design of a new revolutionary and innovative system, subsequently named eCarus.

The eCarus project is extra unique due to the collaboration with the ElectriFly Design Group [3] with their goal to design a 6-8 electric passenger aircraft for regional transport that is capable of mid-flight recharging [3]. Both our teams worked in close correlation together which led in turn to design choices due to their presence.. The eCarus system is designed for the Electrifly application but the scalability of the system is tested for the MW aircraft class.

The eCarus system consist of 3 different systems namely the hub, drone and docking system. Initially, the placement of the hub was deemed unfeasible. As a result, there was a shift in hub locations from remote areas to regional airports, primarily driven by the risk of financial infeasibility. The current hubs have a operating range of 764 km distance between the aircraft and the hub. The drone is required to manoeuvre towards the aircraft, recharge it and return to the hub all in one charge.Thus it is of utmost importance that the drone operates as efficient as possible. Therefore one of our main design choices regarding the aerodynamic body resulted in a blended wing body. ($b = 16.38m$, $Sweep = 28,30[deg]$, $S = 44.7m$) This design choice resulted in improved structural and aerodynamic efficiency, despite the inherent challenges. The same efficiency combined with the risk of cable collision, imposed by the ElectriFly group, led to the design choice of engine placement, being two ducted fans at the trailing edge. The recharging procedure is composed out of 8 modes controlled by the AAR controller. A new design is proposed where the system connection transfers 1.7 MW of charge through a conducting probe-drogue connection to the receiving battery. However, since this technology is newly designed, it needs to be thoroughly tested in future design phases to ensure successful docking.

All the subsystems of the drone are integrated within the BWB structure. The performed iteration converted to the following major values for the eCarus design: MTOW of 5414 kg, surface area of $44.7\,m^2$, CL of 1.27, W_{bat} of 4057 kg. This iteration is performed multiple times and verified using a sensitivity analysis for the obtained values. This gives insight due to what values our design is prone to change. As is the case for electric aviation in general, the drone is mostly bound to the specific energy of our battery.

The integration of all subsystems of the drone within the Blended Wing Body structure has resulted in the following major design values for the eCarus Design: a MTOW of 5414 kg, a wing surface area of $44.7\,m^2$, a CL of 1.27 and a W_{bat} of 4057 kg. To ensure accuracy, this iterative design process was conducted multiple times and subjected to a sensitivity analysis to assess potential variations in design values. This analysis provides valuable insight into the factors that influence our design. As with electric aviation in general, the eCarus design is heavily reliant upon the specific energy density of its battery. current drone scalability of the eCarus system to the MW class aircraft results in a scalability factor of the drone of 6 with the use of 4 simultaneous drones. The usage of more than 4 drones is limited by safety and regulations and 2 drones results in a upscale factor of 12. Improved technology has also a beneficial effect on the hub placement in terms of scalability. The range between the hubs can be increased and the system can be more optimised. Concluding, scalability is challenging for the current designed system. It greatly depends on the increase potential of batteries in the future making the

system scalability more feasible.

Throughout the design of the project, a great amount of effort has been put in order to make the design as sustainable as possible. Multiple design choices have been made with as main goal to achieve great sustainability levels. An example of such a choice is the use of a ducted fan in order to achieve high efficiency and low noise levels. Looking at the sustainability requirements it can be seen that the great majority of requirements have been met through those design choices.
For the financial conclusion of the eCarus system both the market and cost analysis are addressed. Implementing such a high-tech system comes at a prices which concludes to a recharge cost of 3.405 USD. The proposed test flight of 4 hours from Amsterdam to Madrid requires 4 drone flight hours to service this route. The main contributing factors to these costs are the electricity (36.5%) and the maintenance (42%). By securing PPA contracts and investments the electricity costs can be reduced. In addition, over time the drone will be fine-tuned and more reliable making the maintenance more streamlined and lest costly.

19.2. Recommendations

The aim of the DSE project was to conduct a feasibility study, investigating the limits of mid-flight recharging, and stimulating innovation. Nonetheless, during the design phase not all analysis were performed to a final extend due to some constraints. Moreover some detailed design concepts require further research or analysis since they were imposed in a later design stage. In order to make the eCarus design reality it is essential to note that additional recommendations must be considered in the future. These recommendations are listed below:

- The concept of liquid cooling lines running through the leading-edge functioning as de-icing systems is something that needs to be explored in terms of feasibility.
- The concept of combining multiple BTMS and thus temporarily transferring energy from the propulsion batteries during recharge can be further researched to improve thermal management.
- The drogue-probe system connection has to be thoroughly tested in terms of stability and connection failure. Furthermore, the influence of water within the connection needs to be analysed in the future.
- The stabilising effects of the voluminous engine ducts shall be investigated in order to minimise the vertical tailplane surface.
- Capabilities of the autonomous control systems shall be investigated in more detail in order to improve the control surface sizing.
- The aerodynamic effects of the discontinuities on the drone surface needs to be investigated.
- Simulation of the aircraft dynamics with control inputs could be done to investigate the effect of inputs.
- The lattice structure should be designed into more detail, assessing the geometry and the material.
- A more in-depth analysis needs to be performed regarding the charging of MW aircraft with the use of 2-4 drones.
- Upgrade the hub placement code to take into account the local price of green energy.

References

[1] Dr ir Julien van Campen. *Project Guide Mid-flight Aircraft Recharging System*. 2023.

[2] Ryan Dibley, Michael Allen, and NASA Dryden Flight Research Center. *Autonomous Airborne Refueling Demonstration, Phase I Flight-Test Results*. 2007. URL: https://ntrs.nasa.gov/api/citations/20080003275/downloads/20080003275.pdf.

[3] Group 13. *Final Report Design Synthesis Exercise Group 13*. June 2023.

[4] Group 10. *Baseline Report Design Synthesis Exercise Group 10*. May 2023.

[5] Group 10. *Mid-Term Report Design Synthesis Exercise Group 10*. June 2023.

[6] B Boer et al. “Midterm Report: Design Synthesis Exercise Group 10”. In: (2023).

[7] Boaretto Nicola et al. “Lithium solid-state batteries: State-of-the-art and challenges for materials, interfaces and processing”. In: *Journal of Power Sources* 502 (Aug. 2021), p. 229919. DOI: 10.1016/j.jpowsour.2021.229919.

[8] Abdul Ghani Olabi et al. “Battery thermal management systems: Recent progress and challenges”. In: *Elsevier* 15 (Aug. 2022), p. 100171. DOI: 10.1016/j.ijft.2022.100171. URL: https://doi.org/10.1016/j.ijft.2022.100171.

[9] Sheng Wang et al. “An extra-wide temperature all-solid-state lithium-metal battery operating from −73 □ to 120 □”. In: *Energy Storage Materials* 39 (Aug. 2021), pp. 139–145. DOI: 10.1016/j.ensm.2021.04.024. URL: https://doi.org/10.1016/j.ensm.2021.04.024.

[10] W Affronso. *System architectures for thermal management of hybrid-electric aircraft*. 2022. URL: https://iopscience.iop.org/article/10.1088/1757-899X/1226/1/012062/pdf.

[11] George Bower. “Tesla Model 3 Battery Can Transfer Twice The Heat Of Model S P100D”. In: (Aug. 2018). URL: https://insideevs.com/news/339220/tesla-model-3-battery-can-transfer-twice-the-heat-of-model-s-p100d/.

[12] *Specific Heat Formula*. URL: https://www.softschools.com/formulas/physics/specific_heat_formula/61/.

[13] Dafen Chen et al. “Comparison of different cooling methods for lithium ion battery cells”. In: *Applied Thermal Engineering* 94 (Feb. 2016), pp. 846–854. DOI: 10.1016/j.applthermaleng.2015.10.015. URL: https://doi.org/10.1016/j.applthermaleng.2015.10.015.

[14] Nicolas Fezans and Thomas Jann. “Modeling and Simulation for the Automation of Aerial Refueling of Military Transport Aircraft with the Probe-and-Drogue System”. In: June 2017. DOI: 10.2514/6.2017-4008.

[15] Mark S. Jurkovich and Christopher J. Hummer. *Understanding the Flowfield Behind a Tanker Aircraft*. 2018. URL: https://arc.aiaa.org/doi/pdf/10.2514/6.2018-0536.

[16] group 10. “Baseline Report: Design Synthesis Exercise Group 10”. In: (2023).

[17] AERIAL REFUELING SYSTEMS ADVISORY GROUP. *AERIAL REFUELING SYSTEMS ADVISORY GROUP*. Oct. 2018. URL: https://apps.dtic.mil/sti/pdfs/AD1064517.pdf.

[18] *MIL-A-19736 A AIR REFUELING SYSTEMS*. URL: http://everyspec.com/MIL-SPECS/MIL-SPECS-MIL-A/MIL-A-19736A_17611/.

[19] Jinrui Ren et al. “Docking control for probe-drogue refueling: An additive-state-decomposition-based output feedback iterative learning control method”. In: *Chinese Journal of Aeronautics* 33.3 (Mar. 2020), pp. 1016–1025. DOI: 10.1016/j.cja.2019.11.007. URL: https://doi.org/10.1016/j.cja.2019.11.007.

[20] United States Patent Application Publication. *Hose and drogue inflight refuelling system*. Jan. 2012. URL: https://patentimages.storage.googleapis.com/06/91/47/40dea221758545/US20060065785A1.pdf.

[21] Incore cables. *XLPE kabel-isolatie*. 2023. URL: https://www.incore-cables.com/xlpe-kabel-isolatie/?lang=nl.

[22] Peter Thomas et al. “Advances in air to air refuelling”. In: *Progress in Aerospace Sciences* 71 (Nov. 2014), pp. 14–35. DOI: 10.1016/j.paerosci.2014.07.001.

[23] Mario Luca Fravolini et al. “Development of Modelling and Control Tools for Aerial Refueling for Uavs”. In: Aug. 2003. DOI: 10.2514/6.2003-5798. URL: https://doi.org/10.2514/6.2003-5798.

[24] Mario Luca Fravolini et al. “Modeling and control issues for autonomous aerial refueling for UAVs using a probe–drogue refueling system”. In: *Aerospace Science and Technology* 8.7 (Oct. 2004), pp. 611–618. DOI: 10.1016/j.ast.2004.06.006.

[25] Giampiero Campa et al. “Autonomous Aerial Refueling for UAVs Using a Combined GPS-Machine Vision Guidance”. In: June 2004. DOI: 10.2514/6.2004-5350. URL: https://doi.org/10.2514/6.2004-5350.

[26] Xunhua Dai, Zi-Bo Wei, and Quan Quan. “Modeling and simulation of bow wave effect in probe and drogue aerial refueling”. In: *Chinese Journal of Aeronautics* 29.2 (Feb. 2016), pp. 448–461. DOI: 10.1016/j.cja.2016.02.001. URL: https://doi.org/10.1016/j.cja.2016.02.001.

[27] *Global Hawk UAV-to-UAV Refueling Demonstration*. URL: https://www.nasa.gov/centers/dryden/multimedia/imagegallery/Global_Hawk/ED12-0012-36.html.

[28] R. Vos, M.F.M. Hoogreef, and B.T.C. Zandbergen. *Lecture 3: Generation of Wing and Thrust/Power Loading Diagrams*. AE1222-II Aerospace Design Systems Engineering. 2021.

[29] D.M. Black, C. Rohrbach, and H.S. Wainauski. “Shrouded Propellers - a comprehensive performance study”. In: *5th Annual Meeting and Technical Display* (Oct. 1968). DOI: 10.2514/6.1968-994.

[30] Snorri Gudmunsson and Snorri Gudmunsson. “Chapter 15 - Thrust Modeling for Propellers”. In: *General Aviation Aircraft Design: Applied Methods and procedures*. Butterworth-Heinemann, 2022, pp. 597–656.

[31] G.N. Barakos. “Review on ducted fans formpound rotorcraft”. In: *The Aeronautical Journal* 124.1277 (2020), pp. 941–974. DOI: 10.1017/aer.2019.164.

[32] National Aeronautics and Space Administration. *Boundary Layer Ingestion Propulsion*. 2023. URL: https://www1.grc.nasa.gov/aeronautics/bli/.

[33] Hyun D. Kim, Aaron T. Perry, and Phillip J. Ansell. "A Review of Distributed Electric Propulsion Concepts for Air Vehicle Technology". In: *AIAA Propulsion and Energy Forum* (July 2018). DOI: 10.2514/6.2018-4998.

[34] Reynard de Vries and Roelof Vos. "Aerodynamic Performance Benefits of Over-the-Wing Distributed Propulsion for Hybrid-Electric Transport Aircraft". In: *AIAA Scitech 2022 Forum* (Jan. 2022). DOI: 10.2514/6.2022-0128.

[35] Stephen A. Rizzi et al. "Annoyance to Noise Produced by a Distributed Electric Propulsion High-Lift System". In: *23rd AIAA/CEAS Aeroacoustics Conference* (June 2017). DOI: 10.2514/6.2017-4050.

[36] P. Schmollgruber et al. "Multidisciplinary Exploration of DRAGON: an ONERA Hybrid Electric Distributed Propulsion Concept". In: *AIAA Scitech 2019 Forum* (Jan. 2019). DOI: 10.2514/6.2019-1585.

[37] Huiling Li and Kun Liu. "Aerodynamic Design Optimization and Analysis of Ducted Fan Blades in DEP UAVs". In: *Aerospace* 10.153 (Feb. 2023). DOI: 10.3390/aerospace10020153.

[38] L W. Traub. "Considerations in optimal propeller design". In: *Journal of Aircraft* 58.4 (July 2021), pp. 950–957. DOI: 10.2514/1.c036258.

[39] Gerrit JJ Ruijgrok. *Elements of aviation acoustics*. Delft University Press, 1993.

[40] Airfoil Tools. *Airfoils A to Z*. 2023. URL: http://airfoiltools.com/ (visited on 06/19/2023).

[41] L.W. Traub. "Simplified propeller analysis and design including effects of stall". In: *The Aeronautical Journal* 120.1227 (May 2016), pp. 796–818. DOI: 10.1017/aer.2016.31.

[42] F Marc De Piolenc and George E Wright Jr. *Ducted Fan Design, Volume 1: Volume 1-Propulsion Physics and Design of Fans and Long-Chord Ducts*. Vol. 1. Marc de Piolenc, 2001.

[43] Serdar Yilmaz, Duygu Erdem, and Mehmet Kavsaoglu. "Effects of Duct Shape on a Ducted Propeller Performance". In: *51st AIAA Aerospace Sciences Meeting including the New Horizons Forum and Aerospace Exposition* (Jan. 2013). DOI: 10.2514/6.2013-803.

[44] Anwar MN Malgoezar et al. "Experimental characterization of noise radiation from a ducted propeller of an unmanned aerial vehicle". In: *International Journal of Aeroacoustics* 18.4-5 (2019), pp. 372–391. DOI: 10.1177/1475472X19852952.

[45] Hatzell Propeller. *Composite Propellers: Why Make the Switch?* 2023. URL: https://hartzellprop.com/composite-propellers-why-make-the-switch/ (visited on 06/19/2023).

[46] V.E. Zetterlind, S.E. Watkins, and M.W. Spoltman. "Fatigue testing of a composite propeller blade using fiber-optic strain sensors". In: *IEEE Sensors Journal* 3.4 (2003), pp. 393–399. DOI: 10.1109/JSEN.2003.815795.

[47] Jorrit van Dommelen and Roelof Vos. "Conceptual design and analysis of blended-wing-body aircraft". In: *Proceedings of the Institution of Mechanical Engineers, Part G: Journal of Aerospace Engineering* 228 (Dec. 2013), pp. 2452–2474. DOI: 10.1177/0954410013518696.

[48] P. Panagiotou, S. Fotiadis-Karras, and K. Yakinthos. "Conceptual design of a Blended Wing Body MALE UAV". In: *Aerospace Science and Technology* 73 (2018), pp. 32–47. ISSN: 1270-9638. DOI: https://doi.org/10.1016/j.ast.2017.11.032. URL: https://www.sciencedirect.com/science/article/pii/S1270963817315870.

[49] S. Kapsalis, P. Panagiotou, and K. Yakinthos. "CFD-aided optimization of a tactical Blended-Wing-Body UAV platform using the Taguchi method". In: *Aerospace Science and Technology* 108 (2021), p. 106395. ISSN: 1270-9638. DOI: 10.1016/j.ast.2020.106395.

[50] Geoffrey Larkin and Graham Coates. "A design analysis of vertical stabilisers for Blended Wing Body aircraft". In: *Aerospace Science and Technology* 64 (2017), pp. 237–252. ISSN: 1270-9638. DOI: https://doi.org/10.1016/j.ast.2017.02.001. URL: https://www.sciencedirect.com/science/article/pii/S1270963816310434.

[51] J. Roskam and University of Kansas. *Airplane Design: Part 6 - preliminary calculation of aerodynamic, thrust and power characteristics*. DARcorporation, 1985. URL: https://books.google.nl/books?id=S3HVmgEACAAJ.

[52] Mark Drela. "XFOIL: An analysis and design system for low Reynolds number airfoils". In: *Lecture Notes in Engineering* (1989), pp. 1–12. DOI: 10.1007/978-3-642-84010-4_1.

[53] Joseph Katz and Allen Plotkin. *Low-speed aerodynamics*. Cambridge University Press, 2010.

[54] J.A. Mulder, W.H.J.J. van Staveren, J.C. van der Vaart, E. de Weerdt, C.C. de Visser, A.C. in 't Veld, E. Mooij. *AE3202 Flight Dynamics Lecture Notes*. 2023.

[55] R. Vos, M.F.M. Hoogreef, and B.T.C. Zandbergen. *Aerospace Design and Systems Engineering Elements - AE1222-II: Wing and Propulsion System Design*. 2020.

[56] Department of Defense of the United States of America. *MIL-F-8785C, Military Specification: Flying Qualities of Piloted Airplane*. 1969.

[57] J. Roskam. *Airplane Design*. Airplane Design 5. DARcorporation, 1985. ISBN: 9781884885501. URL: https://books.google.nl/books?id=mMU47Ld7yQkC.

[58] *NSO NSDD*. URL: https://nso.nato.int/nso/nsdd/main/standards/stanag-details/9175/EN.

[59] Ansys. *Grante Edupack 2022 R1*. 2022. URL: https://www.ansys.com/products/materials/granta-edupack.

[60] Phillip John Doorbar and Stephen Kyle-Henney. "4.19 Development of Continuously-Reinforced Metal Matrix Composites for Aerospace Applications". In: 2018.

[61] Shiping Li et al. "Structural design and compression-bending test of ultra-lightweight carbon-fiber-reinforced polymer truss structures". In: *Composite Structures* 313 (2023), p. 116909. ISSN: 0263-8223. DOI: https://doi.org/10.1016/j.compstruct.2023.116909. URL: https://www.sciencedirect.com/science/article/pii/S0263822323002532.

[62] Alaa M. Almushaikeh et al. "Manufacturing of carbon fiber reinforced thermoplastics and its recovery of carbon fiber: A review". In: *Polymer Testing* 122 (2023), p. 108029. ISSN: 0142-9418. DOI: https://doi.org/10.1016/j.polymertesting.2023.108029. URL: https://www.sciencedirect.com/science/article/pii/S0142941823001095.

[63] Meddaikar Yasser M. et al. “Skin Panel Optimization of the Common Research Model Wing Using Sandwich Composites”. In: *Journal of Aircraft* (Nov. 2021), pp. 1–14. DOI: 10.2514/1.c036551. URL: https://doi.org/10.2514/1.c036551.

[64] M. P. Sreejith and R.S. Rajeev. *Fiber reinforced composites for aerospace and sports applications*. Jan. 2021, pp. 821–859. DOI: 10.1016/b978-0-12-821090-1.00023-5. URL: https://doi.org/10.1016/b978-0-12-821090-1.00023-5.

[65] Raphael Gerard et al. *Updated Fatigue Test Methods for Structural Foams and Sandwich Beams*. Mar. 2015. URL: https://www.researchgate.net/profile/Fahmi-Alila/publication/274081361_UPDATED_FATIGUE_TEST_METHODS_FOR_STRUCTURAL_FOAMS_AND_SANDWICH_BEAMS/links/55157aa10cf2f7d80a3300e4/UPDATED-FATIGUE-TEST-METHODS-FOR-STRUCTURAL-FOAMS-AND-SANDWICH-BEAMS.pdf.

[66] Patel Kishan et al. “Development of FRC Materials with Recycled Glass Fibers Recovered from Industrial GFRP-Acrylic Waste”. In: *Advances in Materials Science and Engineering* 2019 (June 2019), pp. 1–15. DOI: 10.1155/2019/4149708. URL: https://doi.org/10.1155/2019/4149708.

[67] Kim Garam and Sterkenburg Ronald. “Investigating the effects aviation fluids have on the flatwise compressive strength of Nomex® honeycomb core material”. In: *Journal of Sandwich Structures and Materials* 23.1 (Jan. 2021), pp. 365–382. DOI: 10.1177/1099636219836645. URL: https://doi.org/10.1177/1099636219836645.

[68] Kamalieva Rumiya N. and Charkviani Ramaz V. “Creation of Ultra-light Spacecraft Constructions Made of Composite Materials”. In: *Procedia Engineering* (Jan. 2017). DOI: 10.1016/j.proeng.2017.03.337. URL: https://doi.org/10.1016/j.proeng.2017.03.337.

[69] Saevarsdottir Gudrun, Kvande Halvor, and Welch Barry J. “Aluminum Production in the Times of Climate Change: The Global Challenge to Reduce the Carbon Footprint and Prevent Carbon Leakage”. In: *JOM* 72.1 (Nov. 2019), pp. 296–308. DOI: 10.1007/s11837-019-03918-6. URL: https://doi.org/10.1007/s11837-019-03918-6.

[70] Al Ashraf Abdullah. *Energy Consumption and the CO2 footprint in aluminium production*. June 2014. URL: https://www.researchgate.net/publication/263085263_Energy_Consumption_and_the_CO2_footprint_in_aluminium_production/link/00463539c23961f2a1000000/download.

[71] Subodh K. Das and J. Gilbert Kaufman. *Recycling Aluminum Aerospace Alloys*. 2007. URL: https://secat.net/wp-content/uploads/Recycling-Aluminum-Aerospace-Alloys.pdf.

[72] Zhou Bo et al. “Microstructure evolution of recycled 7075 aluminum alloy and its mechanical and corrosion properties”. In: *Journal of Alloys and Compounds* 879 (Oct. 2021), p. 160407. DOI: 10.1016/j.jallcom.2021.160407. URL: https://doi.org/10.1016/j.jallcom.2021.160407.

[73] Kuchariková Lenka, Tillová Eva, and Bokůvka Otakar. “RECYCLING AND PROPERTIES OF RECYCLED ALUMINIUM ALLOYS USED IN THE TRANSPORTATION INDUSTRY”. In: *Transport Problems* 11.2 (Jan. 2016), pp. 117–122. DOI: 10.20858/tp.2016.11.2.11. URL: https://doi.org/10.20858/tp.2016.11.2.11.

[74] Zudova L. A. et al. “Hybrid structural layout of wing box for small aeroplane”. In: *MATEC web of conferences* (Jan. 2019). DOI: 10.1051/matecconf/201930401018. URL: https://doi.org/10.1051/matecconf/201930401018.

[75] Shanygin Alexander et al. “Designing pro-composite truss layout for load-bearing aircraft structures”. In: *Fatigue Fracture of Engineering Materials Structures* 40.10 (Oct. 2017), pp. 1612–1623. DOI: 10.1111/ffe.12695. URL: https://doi.org/10.1111/ffe.12695.

[76] Sandu Marin et al. “Possibilities to reduce the stress concentration in adhesive bonded joints”. In: *ResearchGate* (Jan. 2009). URL: https://www.researchgate.net/publication/289052509_Possibilities_to_reduce_the_stress_concentration_in_adhesive_bonded_joints.

[77] Gursel Ali. “FUNDAMENTALS IN ADHESIVE BONDING DESIGN FOR COMPLEX STRUCTURES AND CONDITIONS”. In: *ResearchGate* (May 2019). URL: https://www.researchgate.net/publication/333220995_FUNDAMENTALS_IN_ADHESIVE_BONDING_DESIGN_FOR_COMPLEX_STRUCTURES_AND_CONDITIONS/link/5d8a864f92851c33e938a131/download.

[78] Gooch D J. *Remnant Creep Life Prediction in Ferritic Materials*. Jan. 2003, pp. 309–359. DOI: 10.1016/b0-08-043749-4/05122-3. URL: https://doi.org/10.1016/b0-08-043749-4/05122-3.

[79] W A Timmer and S J Elsloo. *AE2111-I Work Package 4 5*. Nov. 2021.

[80] T H G Megson. *Aircraft Structures for Engineering Students*. 1st ed. Elsevier, 2007, pp. 226–235. ISBN: 978-0-7506-6739-5.

[81] C.D. Rans and J. Melkert. *Structural analysis and design week 7 lecture notes*. 2021.

[82] SkyCiv Engineering. “What is a Truss? Common Types of Trusses in Structural Engineering”. In: *SkyCiv* (2023).

[83] H. P. Gavin. “Static and Dynamic Structural Analysis of 2D and 3D Frames.” In: *Duke University* (2023). URL: https://frame3dd.sourceforge.net/.

[84] Barot R P, Desai R P, and Sutaria Mayur. “Recycling of Aluminium Matrix Composites (AMCs): A Review and the Way Forward”. In: *International Journal of Metalcasting* (Nov. 2022). DOI: 10.1007/s40962-022-00905-7. URL: https://doi.org/10.1007/s40962-022-00905-7.

[85] Hu Qiushi and Xu Linghong. “An overview on Lithium-ion batteries recycling processes”. In: *Journal of physics* 1885.3 (Apr. 2021), p. 032031. DOI: 10.1088/1742-6596/1885/3/032031. URL: https://doi.org/10.1088/1742-6596/1885/3/032031.

[86] Heimes Heiner et al. “RECYCLING OF LITHIUM- ION BATTERIES”. In: *ResearchGate* (Sept. 2021). URL: https://www.researchgate.net/publication/354653006_RECYCLING_OF_LITHIUM-_ION_BATTERIES.

[87] Kampker Achim et al. “Battery pack remanufacturing process up to cell level with sorting and repurposing of battery cells”. In: *Journal of remanufacturing* 11.1 (June 2020), pp. 1–23. DOI: 10.1007/s13243-020-00088-6. URL: https://doi.org/10.1007/s13243-020-00088-6.

[88] Roskam Jan. *Part II: Preliminary Configuration Design and Integration of the Propulsion System*. 4th ed. Design Analysis and Research Corporation, 2004, pp. 217–234. ISBN: 1-884885-43-8.

[89] Malcom Brown and Roelof Vos. “Conceptual Design and Evaluation of Blended-Wing Body Aircraft”. In: Jan. 2018. DOI: 10.2514/6.2018-0522. URL: https://doi.org/10.2514/6.2018-0522.

[90] E. Gill and Fabrizio Oliviero. *AE3211-I Systems Engineering Aerospace Design*. 2023.

[91] iNews. *How expensive is the carrier-based aircraft arrest cable? CCTV disclosed the high cost and only two countries in the world can make*. URL: https://inf.news/en/military/71c485ba3ba7cd8e45ff30b8a8a005f9.html (visited on 06/06/2023).

[92] TMP Staff. *Video: Why Aircraft Carriers Lost One Arresting Wire*. URL: https://themaritimepost.com/2021/06/video-why-aircraft-carriers-lost-one-arresting-wire/ (visited on 06/06/2023).

[93] Mrs. Janet McGovern. *Advanced Cable for Arresting Aircraft*. URL: https://www.navysbir.com/n08_2/N082-136.html (visited on 06/06/2023).

[94] "MK 7 AIRCRAFT RECOVERY EQUIPMENT". In: (). URL: https://www.globalsecurity.org/military/library/policy/navy/nrtc/14310_ch3.pdf.

[95] Federal Aviation Administration. *Airport Categories*. URL: https://www.faa.gov/airports/planning_capacity/categories (visited on 09/06/2023).

[96] Michál Červinka. "Is a regional airports business a way to make a profit?" In: *Transportation Research Procedia* 43 (2019), pp. 84–92.

[97] Gerald L Dillingham PhD. *FAAs and Industry s Cost Estimates for Airport Development*. United States Government Accountability Office. URL: https://www.gao.gov/assets/gao-17-504t.pdf.

[98] Jean-Paul Rodrigue. "The Geography of Transport Systems". In: 5 (2020), pp. 200–240.

[99] David Megginson. *Open Data Downloads - airports.csv*. URL: https://ourairports.com/data/.

[100] European Union. *Data/Statistical themes/Transport/Data/Database/Airtransport*. URL: https://ec.europa.eu/eurostat/web/transport/data/database (visited on 09/06/2023).

[101] Simple Flying. *What Are Minimum Fuel Requirements And How Are They Defined*. URL: https://simpleflying.com/minimum-fuel-requirements-definitions-guide/ (visited on 02/06/2023).

[102] Alan Hobbs PhD and Stanley R Herwitz PhD. *Human Factors in the Maintenance of Unmanned Aircraft*. Federal Aviation Administration. NASA Research Park Moffett Field CA. URL: https://www.faa.gov/about/initiatives/maintenance_hf/library/documents/media/human_factors_maintenance/maint_uav_nasa.pdf..

[103] Haiqiang Wang, Yue Wang, and Min Wang. *On the development of a landing gear design method in aircraft multidisciplinary design environment*. Oct. 2016. DOI: 10.1109/AUS.2016.7748083. URL: https://ieeexplore.ieee.org/abstract/document/7748083.

[104] D. Peters. *Lecture Notes 2022, AE4ASM003 Linear Modelling*.

[105] J. Roskam and University of Kansas. *Airplane Design: Part 8 - airplane cost estimation: design, development, manufacturing and operating*. DARcorporation, 1985. URL: https://books.google.nl/books?id=p12pzQEACAAJ.

[106] *Inflation Calculator*. URL: https://www.usinflationcalculator.com/.

[107] Statista Research Department. *EBIT margin of commercial airlines worldwide from 2010 to 2022, by region*. URL: https://www.statista.com/statistics/225856/ebit-margin-of-commercial-airlines-worldwide/.

[108] Gaurav Joshi Sumit Singh. *How SAF Can Become Cost Competitive Against Conventional Fuel*. URL: https://simpleflying.com/saf-cost-competitive-jet-fuel/#:~:text=I%5C%202020%5C%2C%5C%20the%5C%20overall%5C%20cost,price%5C%20of%5C%20conventional%5C%20jet%5C%20fuel..

[109] aeroaffaires. *CITATION CJ4 PRIVATE JET HIRE*. URL: https://aeroaffaires.com/private-jet-hire/midsize-jets/citation-cj4/.

[110] Leeham News and Analysis. *The true cost of Electric Aircraft*. 2023. URL: https://leehamnews.com/2021/07/01/the-true-cost-of-electric-aircraft/ (visited on 06/15/2023).

[111] IEA. *IEA aviation report*. URL: https://www.iea.org/reports/aviation (visited on 2023).

[112] Ty Marien et al. *Short-Haul Revitalization Study Final Report*. NASA, 2018.

[113] K. Ciesluk. *Turnaround Time: Why It's Important And How Airlines Can Speed It Up*. URL: https://simpleflying.com/turnaround-time-importance/ (visited on 2023).

[114] *Schiphol Airport Charges and Conditions*. Schiphol Airport, 2022.

[115] *Charging your electric car at Schiphol*. URL: https://www.schiphol.nl/en/parking/electric-vehicle-ev-charge-points/ (visited on 2023).

[116] European Commission. *Zero-Emission Aviation: Commission launches new Alliance to make hydrogen-powered and electric aircraft a reality*. 2023. URL: https://ec.europa.eu/commission/presscorner/detail/en/ip_22_3854 (visited on 06/15/2023).

[117] EUROCONTROL. *EUROCONTROL customer guide to charges*. URL: https://www.eurocontrol.int/sites/default/files/2022-11/eurocontrol-customer-guide-to-charges.pdf.

[118] Daniel P. Raymer. "Thrust-to-Weight Ratio and Wing Loading". In: *Aircraft design: A conceptual approach*. American Institute of Aeronautics and Astronautics, Inc., 1999, pp. 87–112.

[119] *Energy efficiency of Airbus A320*. Dec. 2020. URL: https://aiimpacts.org/energy-efficiency-of-airbus-a320/.